PROTON CAPTURE ON ^{34}S IN THE ASTROPHYSICAL ENERGY REGIME

by

Matthew A. Lovely

A thesis submitted to the Faculty and the Board of Trustees of the Colorado School of Mines in partial fulfillment of the requirements for the degree of Doctor of Philosophy (Applied Physics).

Golden, Colorado

Date _____

Signed: _____
Matthew A. Lovely

Signed: _____
Dr. Uwe Greife
Thesis Advisor

Golden, Colorado

Date _____

Signed: _____
Dr. Uwe Greife
Professor and Head
Department of Physics

ABSTRACT

Novae are unique environments for nucleosynthesis, fueled by the thermonuclear runaway of material accreted onto the surface of the white dwarf component of a close binary system. In order to properly model these systems, precise knowledge of the nuclear reactions in the complex reaction networks is required. Many of the reaction rates, often preceding via narrow resonances, are theoretically calculated, leading to large uncertainties which have been shown to be able to drastically alter the expected production of novae material. The uncertainties in theoretical calculations of the radiative proton capture strengths of ^{34}S in novae conditions with peak temperatures, T = 0.145-0.418 GK have been shown to cause deviations in the production of ^{35}Cl and ^{36}Ar by factors up to 20 and 7 respectively [1]. Previous measurements of the $^{34}\mathrm{S}(p,\gamma)^{35}\mathrm{Cl}$ reaction only went down to $E_p = 400$ keV and saw no notable features below 510.6 keV [2]. In order to properly model the nova phenomenon, the strength of various resonances of the $^{34}\mathrm{S}(p,\gamma)^{35}\mathrm{Cl}$ reaction needed to be measured directly and the uncertainties needed to be better constrained. Simulations show evidence of the production of ^{35}Cl through proton capture in Gamma-Ray Burst (GRB) x-ray afterglows [3] and Type 1a supernova [4]. Cl and S isotopic ratios are also an important tool in determining the potential nova or supernova source of pre-solar meteoritic grains [5], so a precise knowledge of the potential novae source of these isotopes is needed. The resonance strength of proton capture on ^{34}S was measured directly at DRAGON using the electromagnetic mass separator at center of mass energies from 272 to 495.5 keV in inverse kinematics.

In addition, a ^{21}Ne + p calibration reaction was evaluated and the analysis of several years of accumulated energy loss and charge state distribution data was done to provide a realistic means of access for this information and to update a semi-empirical formula for predicting the charge state distributions of ions passing through gas.

TABLE OF CONTENTS

LIST OF FIGURES

LIST OF TABLES

LIST OF SYMBOLS

Solar mass . . . . . $M_\odot = 1.989\times10^{30}$[kg]

Center of mass energy . . . . . E_{CM}

Giga Kelvin . . . . . GK = 10^9 Kelvin

Q value . . . . . Q

Proton mass . . . . . 1.673×10^{-27}[kg]

Neutron mass . . . . . 1.675×10^{-27}[kg]

Mass defect . . . . . Δm

Speed of light . . . . . c = 2.998×10^{8}[m/s]

Lab kinetic energy . . . . . T_{lab}

Lorentz factor . . . . . γ

Reduced mass . . . . . μ

Plank's constant . . . . . h = $\hbar 2\pi = 6.626\times10^{-34}$m^{2}kg/s

Cross section . . . . . σ

de Broglie wavelength . . . . . λ

Avogadro's number . . . . . N_A

Atomic charge . . . . . Z

Neutron number . . . . . N

Mass number . . . . . A

Kronecker delta . . . . . δ

Resonance width . . . . . Γ

Resonance strength . . . . . $\omega\gamma$

Spin and parity . . . . . J^{π}

Azimuthal quantum number l

Spin . . . . . $\vec{s}$

Yield . . . . . Y

Beam normalization coefficient . . . . . R

Efficiency of detector i . . . . . η_i

Elementary charge . . . . . e=4.803×10^{-10}[statC]

LIST OF ABBREVIATIONS

Gamma-Ray Bursts	GRB
Proton Proton Chain	pp chain
Carbon Nitrogen Oxygen	CNO
Carbon Oxygen	CO
Oxygen Neon	O-Ne
Triangle Universities Nuclear Laboratory	TUNL
ISAC Beam Operations	OPS
Isotope Separator and Accelerator	ISAC
TRI University Meson Facility	TRIUMF
Multi Charge Ion Source	MCIS
Low Energy Beam Transport	LEBT
Radio Frequency Quadrupole	RFQ
Drift Tube Linac	DTL
Detector of Recoil And Gammas Of Nuclear astrophysics	DRAGON
Micro-Channel Plate	MCP
Dual Sided Silicon Strip Detector	DSSSD
Ionization Chamber	IC
Bismuth Germanate	BGO
Time of Flight	TOF
Full Width at Half Maximum	FWHM

Surface Barrier . . . . . SB

Stopping Range of Ions in Matter . . . . . SRIM

Data AcQuisition system . . . . . DAQ

Charge State Distribution . . . . . CSD

Magnetic Dipole 1 . . . . . MD1

Particle IDentification . . . . . PID

Time to Amplitude Converter . . . . . TAC

Convolution Approximation for Swift Particles . . . . . CASP

FOREWARD

"It's a dangerous business, Frodo, going out your door. You step onto the road, and if you don't keep your feet, there's no telling where you might be swept off to.

-J.R.R. Tolkien The Fellowship of the Ring

I don't think I could ever properly explain how grateful I am for the people around me who supported me throughout my degree, though I will attempt to do so. First and foremost, my advisor, Uwe Greife, without his support during my undergraduate degree and the opportunity he gave me to be his graduate student, I may never have even pursued a PhD. Our lighthearted conversations reminded me to not take myself so seriously and to enjoy my time as a student. Your knowledge and insight have been invaluable to me over the last 4 years and I could never thank you enough for all that you have done. I would also like to thank Jonathan Karpesky and everyone else in the Mines community who taught me so much along the way. Additionally I would like to thank Devin Connolly, Annika Lennarz, Chris Ruiz, and everyone else at TRIUMF for teaching me all I know about DRAGON and making this work actually possible. Of course, I'm forever grateful for the support from my family: my mother and father, and their never-ending support of all that I have done. And finally, I'd like to thank my partner, Alyx, without her love and encouragement, through the late nights and stress, I know I could not have achieved any of this. Thank you for all that you have done and continue to do.

CHAPTER 1

INTRODUCTION

The production of ^{35}Cl in explosive nucleosynthesis environments, particularly novae, has been shown to be sensitive to the $^{34}\mathrm{S}(p,\gamma)^{35}\mathrm{Cl}$ reaction rate. These sensitivity studies have shown that by varying the current resonance strengths within the bounds of the uncertainty for the $^{34}\mathrm{S}(p,\gamma)^{35}\mathrm{Cl}$ reaction, the production of direct products ^{35}Cl and ^{36}Ar can vary up to a factor of 20 and 7 respectively [1]. Simulations also show evidence of the production of ^{35}Cl in Gamma-Ray Bursts (GRB) x-ray afterglows [3]. While ^{34}S has been shown to be an important product in Type Ia Supernova simulations [4]. Cl and S isotopic ratios are also an important method of helping to determine the source of pre-solar meteoritic grains [5]. The strength of proton capture on ^{34}S has been previously measured using indirect and relative methods but considerable uncertainties still exist due to unknown target stoichiometries and stopping powers. There exist several previous measurements of the E_{CM}=1177 keV resonance strength [6–8] stating absolute values which vary by as much as a factor of 5. The 1177 keV state has then been used as the reference point in the determination of the relative resonance strengths of lower energy resonances. This is problematic because any strengths measured relative to this state will have the same discrepancy. In order to properly understand the processes that underlie nova reactions these uncertainties must be decreased. Many resonances of potential astrophysical significance exist below the previously measured threshold of E_{CM}=388 keV and their strengths were estimated theoretically based off the results from a recent transfer measurement, $^{34}\mathrm{S}(^{3}\mathrm{He,d})^{35}\mathrm{Cl}$, conducted by Gillespie et al. [9]. During the Gillespie measurement, several new potential resonances in the relevant energy region for novae nucleosynthesis were proposed based on the excited states populated.

1.1 Stellar Evolution

After the primordial hydrogen began to condense and form the first stars, the heat generated in the contraction from the gravitational potential energy soon caused the stars to reach core temperatures of several 10^6 K [10]. This allowed the hydrogen to begin to fuse together in a series of successive reactions in what is known as the proton-proton chain (pp chain) [11] and later the carbon nitrogen oxygen (CNO), cycle which uses carbon, nitrogen, and oxygen as a catalyst in the production of helium. After burning began, a hydrostatic equilibrium was reached between the gravitational forces and the energy released from the nuclear reactions. As the star continues to burn, it exhausts its supply of hydrogen in the core and the star then starts to contract again under the massive gravitational forces. The star then heats up due to the contraction, which causes the burning of hydrogen in layers surrounding the core and the star begins to expand becoming a red giant [12]. If the mass of the star is M$\geq$0.4 $M_\odot$, then, during contraction, the core will reach temperatures of >0.1GK and will ignite the burning of the helium produced by previous stages of hydrogen burning.

Helium burning proceeds through what is known as the triple alpha process. Two helium ions combine to form the short lived ^{8}Be, which has a half-life of 6.7x10^{-17} s in the decay back to 2 helium ions [13]. Over time an equilibrium is reached between the production and decay of ^{8}Be and a third helium ion can then begin fusing with the ^{8}Be to form ^{12}C, which is stable. Helium burning can continue through subsequent alpha captures on the ^{12}C, producing ^{16}O, ^{20}Ne, and other heavier elements until the supply of helium in the core is diminished and the hydrostatic equilibrium again ends, causing contraction of the red giant. For lower mass stars, 0.4 to 2.0 $M_\odot$, the core has become electron degenerate and the ignition of helium burning causes a thermonuclear runaway until the degeneracy has been lifted in what is known as a core helium flash [14]. Once the helium in the core is exhausted and the star again begins to contract, the star can ignite helium and hydrogen burning in shells surrounding the carbon oxygen core. This will happen in a series of pulses as subsequent layers are ignited. These thermal pulses can begin to destabilize the outer

layers and eventually much of the mass of the star will be lost due to stellar winds, revealing the interior layers of the star. The intense radiation from the interior will heat up and eventually ionize the ejected material, causing the formation of a planetary nebula and the star will become a carbon and oxygen rich white dwarf (CO).

A more massive star, $2M_{\odot}$<M<$9M_{\odot}$, will proceed in the same manner, until it has depleted the core of hydrogen. The star will then begin to contract and because the core is not electron degenerate, a helium flash will not occur. Instead the helium in the core begins burning quiescently until the star ends its life by creating a planetary nebula and a CO white dwarf [15].

1.2 Heavy Ion Burning

For a star with original mass $9M_{\odot}$<M<$11M_{\odot}$, once the helium has been depleted, the star will begin to contract and the partially electron degenerate, carbon and oxygen rich core, will ignite in carbon burning [16] as two carbon ions fuse into products like neon and magnesium. This leads to thermonuclear runaway that occurs in a series of flashes similar to helium burning. It will continue until the carbon has been depleted and the star will again contract which will ignite the still existing hydrogen and helium shells for a final round of burning. As further stages of burning occur, the star develops a shell structure which can be seen in Figure 1.1. Eventually, the outer layers will be ejected by stellar winds, leaving behind a white dwarf rich in oxygen and neon (O-Ne) and a planetary nebula.

If the original mass of the star is $>11M_{\odot}$, further stages of heavy ion burning can occur. These consist of neon, oxygen, and silicon burning and proceed in a slightly different manner compared to carbon burning. After the carbon has been depleted, contraction causes the temperature to rise above about 1GK and this leads to the photodisintegration of ^{20}Ne, which releases alpha particles. These alpha particles are then captured by the remaining ^{20}Ne and lead to the production of magnesium and silicon [12]. After the neon fuel has been depleted, the star again contracts and ignites oxygen burning. The Coulomb barrier for the ^{16}O+^{16}O reaction is lower compared to other available reactants, and this is the first reaction to take

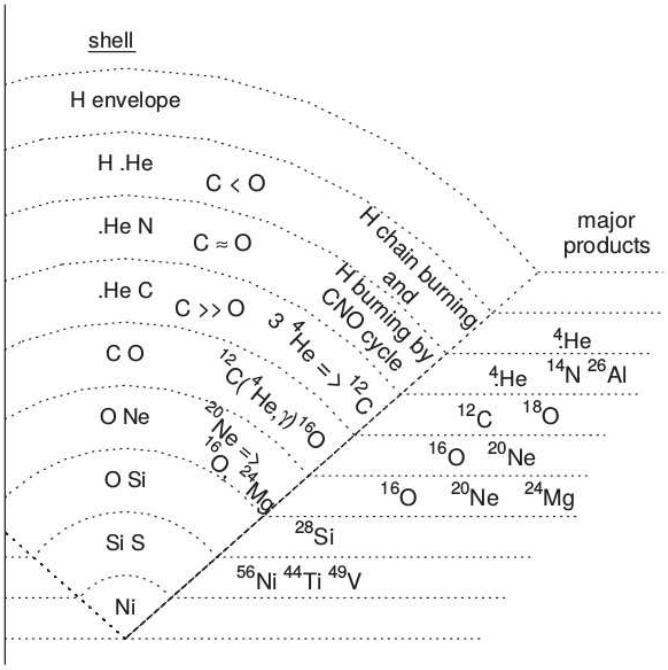

Figure 1.1: Diagram of the various burning shells from [17] and their main products.

place. This can lead to the production of ^{34}S via the reaction chain ^{16}O(^{16}O,2p)^{30}Si(α,γ)^{34}S [18]. Once the oxygen has been depleted the contraction again heats the core and ignites silicon burning. It proceeds via photodisintegration of less tightly bound nuclei and the subsequent alpha capture on the remaining tightly bound nuclei until the production of iron peak nuclides occurs. Once the silicon burning has ceased, this will eventually lead to the collapse of the core and what is known as a supernova, which will be discussed in the next section.

1.3 Explosive Nucleosynthesis

1.3.1 Supernovae

As mentioned before, supernovae are explosive events occurring in massive stars that result in a unique environment for nucleosynthesis. There are two main types of supernovae and several sub classes depending on observed spectral lines. The first to be discussed is classified as a Type 1a supernova and leading theories state that these can occur either by

thermal runaway caused by accretion onto a white dwarf star in close binary orbit with a main sequence star or by the merging of two white dwarf stars or two more massive compact remnants. In both scenarios, the core approaches the Chandrasekhar limit, the maximum mass of a stable white dwarf star [19], until carbon burning takes off, causing the temperature to increase until the degeneracy of the core is lifted [20]. By this point the energy generation rate is so high that an explosion takes place. This can only occur in stars whose core is rich in carbon as the temperatures required to ignite oxygen burning are too high and a core collapse will take place instead.

The other types of supernovae are classified as Type Ib, Type Ic, and Type II. These are known as core collapse supernovae and occur when the core of the massive star reaches the Chandrasekhar limit due to loss of nuclear fuel and begins to collapse in on itself. The star will continue to collapse until the repulsive short range nuclear forces rebound and cause a shock wave to propagate outward [21]. This shock wave can cause what is known as explosive nucleosynthesis and leads to the production of iron peak elements in the interior layers, while the outer layers are ejected into the interstellar medium. Type II occur in stars with $9M_{\odot} < M < 12M_{\odot}$, which still have a hydrogen rich envelope and have a metallicity greater than that of our sun. These are characterized by the presence of hydrogen spectral lines. Type Ib and Ic occur in stars which no longer have a significant hydrogen envelope, either due to stellar winds or accretion onto a companion star. Type Ib contain significant helium and are characterized by the presence of helium spectral lines where Type Ic contain very little helium, again, reflected by the spectral lines [22]. Supernovae leave behind a dense core known as a neutron star or even a black hole depending on the progenitor mass. Black holes form either from direct collapse into a black hole which usually results in a failed supernova or from fallback onto the neutron star remnant after the supernova event [23]. Supernovae are relevant for the current work because ^{34}S and ^{35}Cl are expected to be important products of Type Ia supernovae [4].

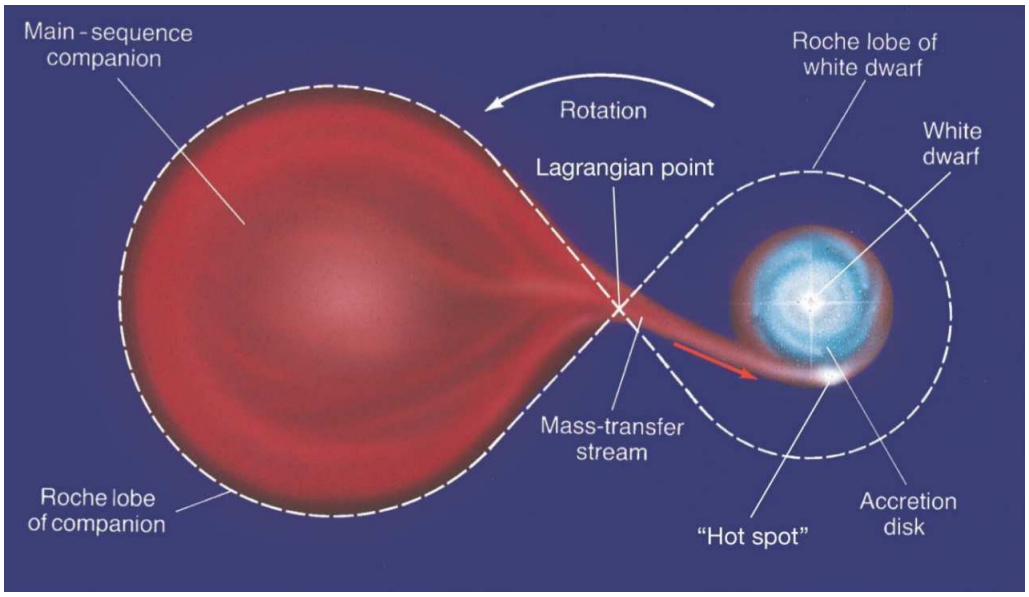

Figure 1.2: Artists depiction of a classical nova [24].

1.3.2 Novae

Novae are the result of thermonuclear runaway on the surface of a compact white dwarf in a close binary system with a main sequence star. Once the main sequence star enters the Roche lobe of the binary system the strong gravitational forces will begin to pull the outer envelope of the main sequence star through the inner Lagrangian point and into the accretion disk of the white dwarf. Typical accretion rates are of the order of 10^{-10}-$10^{-9} M_{\odot}$ per year [10]. Eventually, some of the hydrogen rich material in the accretion disk will fall to the surface of the white dwarf where it is heated and compressed by the strong surface gravity until it becomes electron degenerate. The accreted hydrogen begins fusing via the pp chain until mixing with the white dwarf leads to the ignition of the CNO cycle. This provides additional heat and due to the electron degeneracy, thermonuclear runaway takes place. The accreted material continues to be heated until an explosion occurs, which ejects the newly formed material into the interstellar medium. Typically, novae eject about $2{\times}10^{-5} M_{\odot}$ per outburst [25], which can provide a significant source of isotopic enrichment for the interstellar medium. Novae are different from Type Ia supernovae as the white dwarf

in the novae event does not reach the Chandrasekhar limit and therefore does not collapse in on itself. This results in a less energetic explosion that does not destroy the white dwarf star. Novae can also be classified as recurrent if they have multiple recorded novae events. These are ordinary nova but have a recurrence time of less than about a century so multiple events have been recorded over the observational history of the nova. The time between events is determined by the mass and the accretion rate onto the white dwarf [26]. Novae are a unique environment for nucleosynthesis because the strong mixing of the accreted material with the white dwarf leads to proton and alpha capture on the various elements that compose the white dwarf [27]. As a result they are the main source of isotopes like ^{13}C, ^{15}N, and ^{17}O [28]. Depending on the mass of the white dwarf progenitor and what stages of burning were reached before formation, a white dwarf may either be rich in carbon and oxygen or in oxygen and neon which determines the type of reactions that will take place and the material that will subsequently be ejected due to the nova. This unique environment leads to an overproduction of specific isotopes compared to solar concentrations, such as ^{35}Cl through proton capture on the existing ^{34}S. A schematic of a nova can be seen in Figure 1.2.

The production of ^{34}S is mainly seen in the later stages of heavy ion burning, namely oxygen burning, that occurs in more massive stars after the conclusion of hydrogen and helium burning. A number of reactions can lead to ^{34}S but the most common is the alpha capture on ^{30}Si, see Figure 1.3, which itself is the product of several different subsequent reactions occurring during the oxygen burning process [16]. The reaction chain can be expressed as ^{16}O(^{16}O,2p)^{30}Si(α,γ)^{34}S. The results of core oxygen burning can be seen in Figure 1.4, which shows the abundances relative to solar for a 4 $M_{\odot}$ star. A strong overproduction of ^{34}S can be seen which leads to ideal conditions for this reaction to proceed as this star is likely to end up as a O-Ne white dwarf and potentially a nova system.

1.3.3 Gamma Ray Bursts

Another source of explosive nucleosynthesis is known as a gamma ray burst, which is thought to be caused by the production of a black hole from a supermassive progenitor

Figure 1.3: Chart of nuclides outlining most common production method of ^{35}Cl, image from [29].

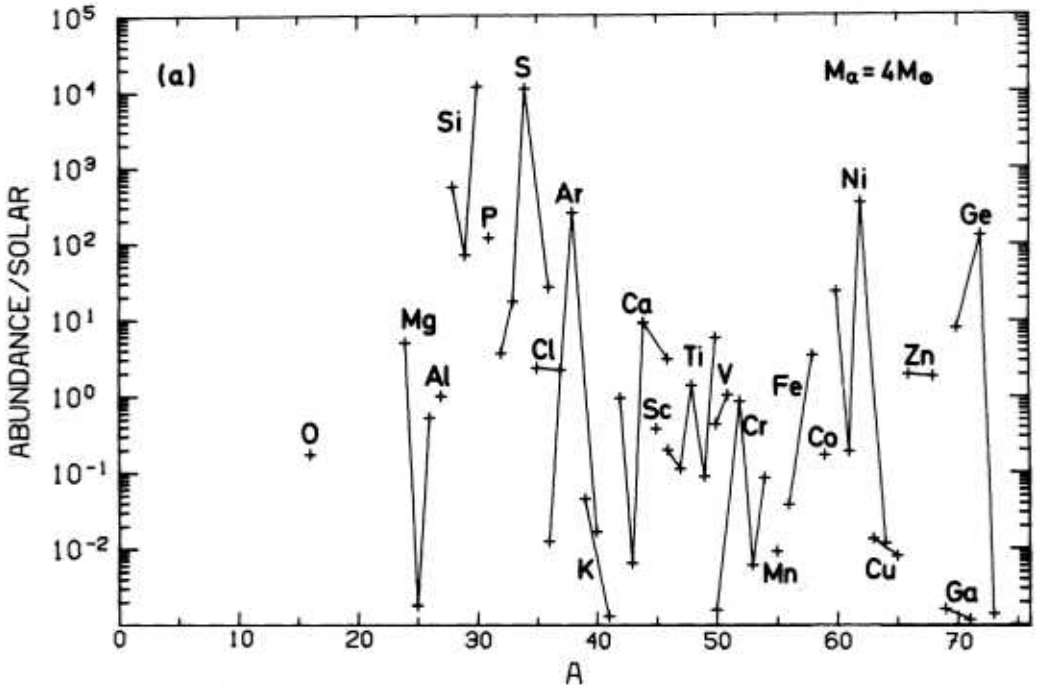

Figure 1.4: Isotopic abundances relative to solar for a 4 $M_\odot$ post core oxygen burning star from [30]. ^{34}S is overproduced compared to solar by a factor of 10000.

system. The length of the burst is determined by the progenitor of the burst itself. The formation of a black hole by the merging of two neutron stars or a neutron star and black hole [3] or more recently theorized the merging of two black holes [31] create what are known as short gamma ray bursts. These typically last less than 2 seconds in which they release energy on the order of what the sun emits throughout its entire lifetime. Long gamma ray bursts are caused by the core collapse of a supermassive star into a black hole. This is known as the collapsar model and can be broken up into two types [32]. In type I collapsars, the progenitor is a rapidly spinning low metallicity supermassive star M$\geq$40M$_\odot$ and once its core reaches the Chandrasekhar limit it collapses in on itself to directly form a black hole. These events are known as failed supernovae as there is no associated supernova explosion. The rapid spinning provides angular momentum such that the remaining material forms into a high density accretion disk that is then pulled into the black hole [33]. This accretion causes jets of material to be ejected perpendicularly to the accretion disk which interact with the

interstellar medium to produce the long gamma ray burst lasting up to several minutes. Type II collapsars are thought to be caused by supermassive stars with $20M_{\odot} \leq M \leq 40M_{\odot}$ which collapse into a proto-neutron star and result in a small supernova explosion. The ejecta eventually fall back into the collapsed core which then forms a black hole [34]. Gamma ray bursts are followed by x-ray afterglows which can last several hours. These events are relevant for this work because simulations suggest that ^{35}Cl can be produced in the accretion disk during the x-ray afterglow of some long gamma ray bursts via proton capture on ^{34}S [35, 36] .

1.4 Pre-Solar Grains

Pre-solar meteoritic grains are small (micron sized) grains of dust that formed prior to the formation of the solar system. These can be created by various sources, including novae and supernovae, and can have a unique signature on the resulting grain that can vary drastically from solar isotopic expectations. They are recognized by isotopically anomalous samples caused by the production and subsequent decay of short lived radionuclides which are contained within these grains such as the decay of ^{22}Na into ^{22}Ne which then leaves an overproduction of ^{22}Ne and large ^{22}Ne/^{20}Ne ratios [37, 38]. The analysis of presolar meteoritic grains requires the precise knowledge of the nuclear reactions that lead to the production of these grains along with accurate models of the underlying processes. It has been shown that novae and supernovae can produce low ^{12}C/^{13}C and ^{14}N/^{15}N ratios that can't be currently explained by other sources [39], see Figure 1.5. For grains coming from novae sources the ratios of ^{26}Al/^{27}Al are expected to be large and ^{30}Si/^{28}Si ratios are expected to be small. More recently, it has been shown that ^{34}S/^{32}S ratios can also be used to distinguish grains from novae from those of supernovae. One reaction of particular importance, proton capture on ^{34}S which leads to the production of ^{35}Cl, has large uncertainties below the peak energy range relevant for novae nucleosynthesis, 0.1-0.4 GK. This reaction fuels the production of ^{36}Ar and ^{35}Cl and the destruction of ^{34}S which are all used in the various methods of cosmochemistry analysis of presolar meteoritic grains. Models have shown that novae

overproduce ^{35}Cl compared to solar levels by up to a factor of 80 which could be used as a marker to determine a possible nova source [5]. The age of the grain can be determined using ^{36}Cl which is known as a cosmological clock due to its long half life. By analyzing the concentrations of the daughter products ^{36}Ar and ^{36}S, the original concentration of ^{36}Cl can be determined and the age can be calculated. A rough schematic of the production of these grains can be seen in Figure 1.6.

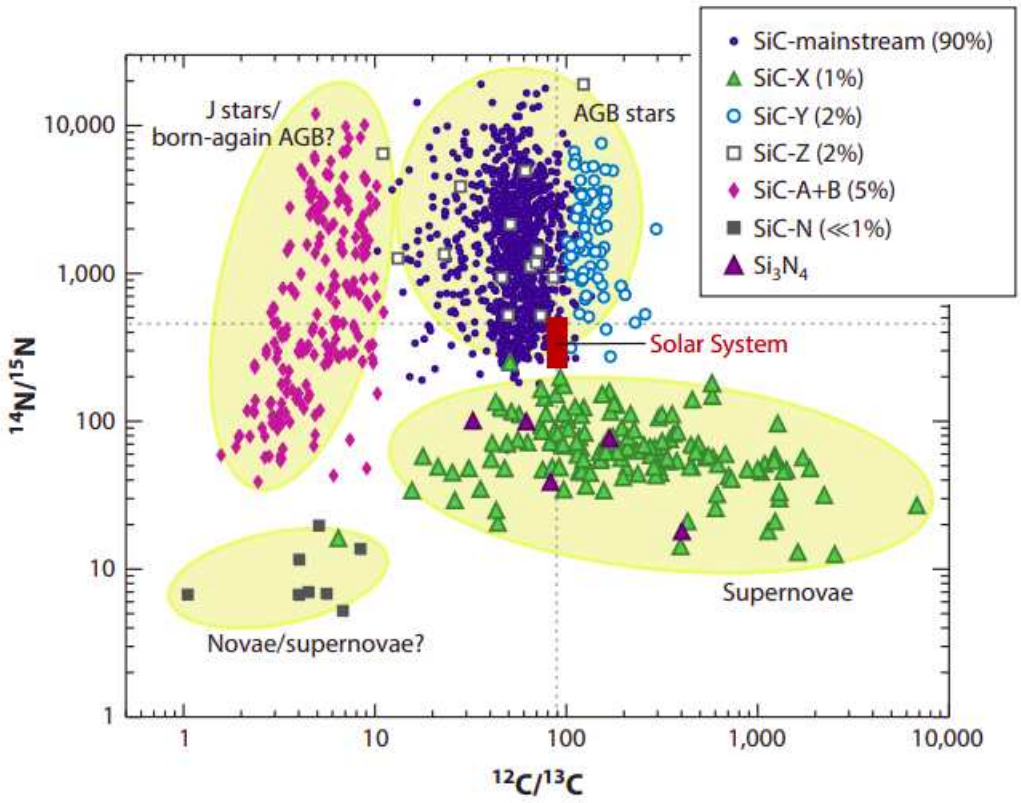

Figure 1.5: Figure of samples of isotopic ratios and associated stellar sources from various presolar meteoritic grains from [39].

1.5 Motivation/Previous Data

There have been several previous measurements of the resonance strengths of the ^{34}S(p,γ) ^{35}Cl reaction at energies relevant for nova nucleosynthesis. For the E$_{CM}$=1177 keV resonance, which has been used as the absolute reference in relative measurements, separate measure-

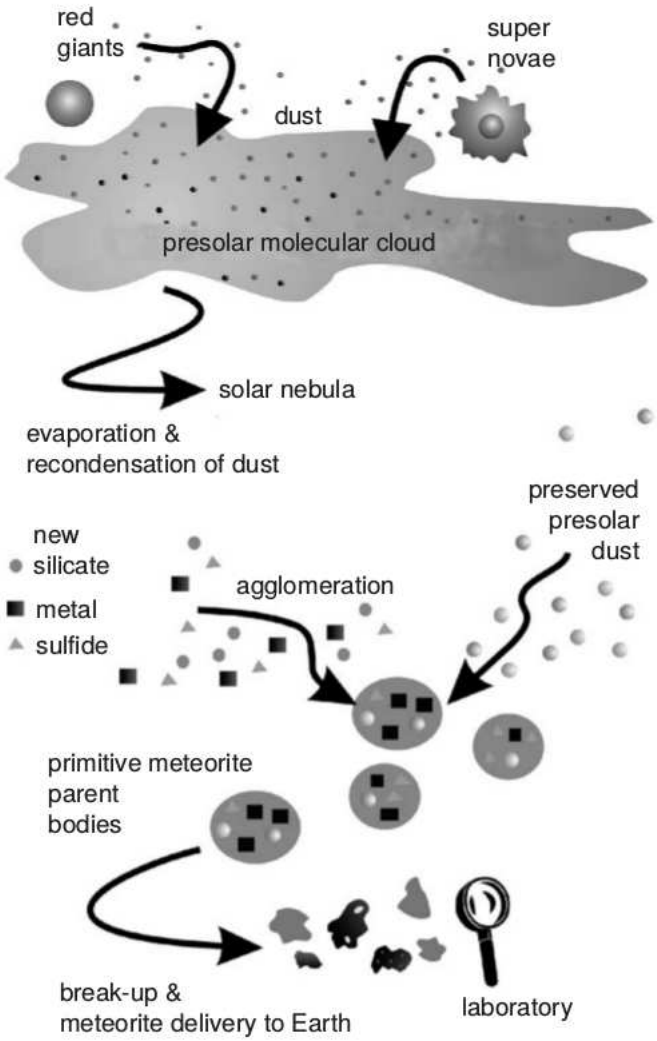

Figure 1.6: Diagram outlining the general process for production of presolar grains [17].

ments have yielded results that vary by considerable amounts. Hazewindus et al. measured this state in 1963 to have a strength of 2 eV [6], while a measurement in 1966 by Engelbertink et al. resulted in a resonance strength of 10.5(15) eV [7]. Another measurement done in 1974 by Aléonard et al. yielded a strength of 4.9(5) eV [40]. This strength was again measured in 1979 by Paine et al. [8] which yielded a resonance strength of 4.7(9) eV which agreed well with the most recent measurement by Aléonard. Several subsequent relative measurements have used the results from the possibly incorrect Engelbertink measurement as the reference state strength to determine the strength of new lower energy resonances, such as the measurement done by Meyer et al. in 1976 [41] where the resonance at 695 keV was measured relative to the 1177 keV state. This leads to even further confusion as in 1988 Pruissen measured the strength of the 495 keV state relative to the 695 keV state, which had previously been measured relative to the 1177 keV state [2]. Since the results of the relative measurements are directly related to the strength of the reference state, any errors in the reference state measurement propagate directly into the relative measurement.

The reduction of the uncertainties in the ^{34}S$(p,\gamma)^{35}$Cl reaction is important for understanding O-Ne novae nucleosynthesis. Sensitivity studies [1] have shown the need to better constrain the uncertainties in many of the resonances. Many of the strengths have been calculated using the value obtained by Engelbertink which leads to significant uncertainties in the resulting resonance strengths. Several excited states which could yield resonances between 272 and 495.5 keV center of mass energy were found using an indirect measurement of the ^{34}S(^{3}He,d)^{35}Cl reaction conducted by Gillespie et al [9], a level diagram of some of these states can be seen in Figure 1.7. This reaction has been measured previously by Graue et al. [42] in 1969 but only up to excitation energies of 5.8 MeV which is much too low to be relevant to this work. Many of these potential resonant states seen in the measurement by Gillespie had never been observed before and confirmation of their existence was needed along with direct measurements of the resonance strengths and astrophysical impact of the individual states. A table of the results from the measurement by Gillespie can be

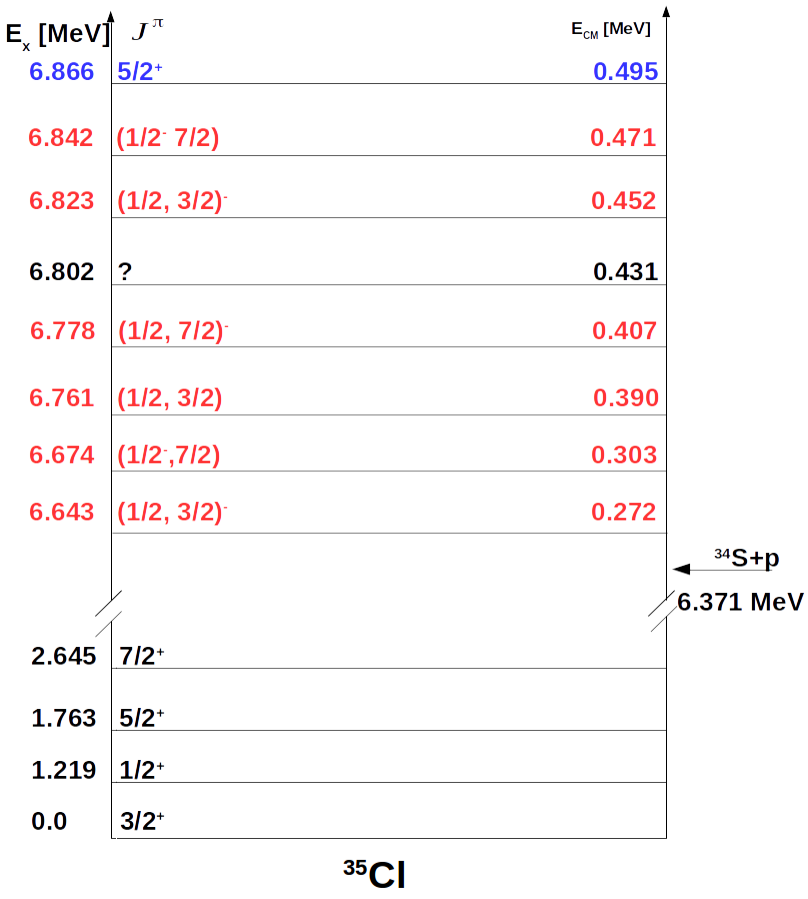

Figure 1.7: Partial level diagram for 35Cl. States in blue have been previously directly measured. States in red have been indirectly populated by Gillespie et al..

seen below in Figure 1.8. Most of the potential new resonant states fall within the Gamow window, or the relevant energy region for Novae nucleosynthesis, as discussed more in detail in the Theory section. Looking at the strengths attributed to these potential states and the resulting astrophysical reaction rate, it appears the $E_{CM} = 272$ keV could be the dominant state for most of the peak nova burning temperatures (T= 0.1-0.4 GK) and therefore could solely determine the production of ^{35}Cl. The astrophysical reaction rates, using the upper limit resonant strengths found by Gillespie, can be seen in Figure 1.9 and the rates using

Adopted E_x (keV)	E_r (keV)	J^π	$\omega\gamma$ (eV)	Present work $\omega\gamma_{min}$ (eV)	$\omega\gamma_{max}$ (eV)
6427(2)	56(2)	$(5/2, 7/2)^-$	–	$6.5(2) \times 10^{-24}$	$2.2(1) \times 10^{-22}$
6468(2)	97(2)	$(1/2, 3/2)^-$	–	$4.2(5) \times 10^{-14}$	$4.7(5) \times 10^{-14}$
6491.5(8)	120.6(5)	$(3/2, 5/2)^+$	–	$3.7(1) \times 10^{-13}$	$4.1(1) \times 10^{-13}$
6545(2)	174(2)	(1/2, 3/2)	–	$7.4(13) \times 10^{-10}$	$4.1(1) \times 10^{-9}$
6643(2)	272(2)	$(1/2, 3/2)^-$	–	$8.5(10) \times 10^{-6}$	$8.9(10) \times 10^{-6}$
6674(2)	303(2)	(1/2 - 7/2)	–	$2.4(2) \times 10^{-8}$	$4.1(8) \times 10^{-6}$
6761(2)	390(2)	(1/2, 3/2)	–	$2.4(3) \times 10^{-4}$	$1.5(1) \times 10^{-3}$
6778(2)	407(2)	$(1/2, 3/2)^-$	–	$9.4(12) \times 10^{-4}$	$1.0(1) \times 10^{-3}$
6823(2)	452(2)	$(1/2, 3/2)^-$	–	$2.7(3) \times 10^{-3}$	$2.7(3) \times 10^{-3}$
6842(2)	471(2)	(3/2 / 7/2)	–	$3.3(1) \times 10^{-5}$	$7.0(3) \times 10^{-4}$
6866.4(6)	495.5(6)	$5/2^+$	$2.5(12) \times 10^{-2}$	$3.0(3) \times 10^{-2}$	$4.7(5) \times 10^{-2}$
7065.9(10)	695.1(10)	$5/2^+$	$7.0(40) \times 10^{-2}$	$2.2(1) \times 10^{-2}$	$2.2(1) \times 10^{-2}$
7103.3(10)	732.5(10)	$3/2^-$	0.23(12)	$6.0(3) \times 10^{-2}$	1.30(7)
7178.6(10)	807.8(10)	$1/2^+$	$8.1(4) \times 10^{-2}$	–	–
7185(1)	814(1)	$5/2^+$	–	–	–
7194.1(10)	823.3(10)	$1/2^-$	0.38(19)	–	–
7224.5(10)	853.7(10)	5/2	$7.6(38) \times 10^{-2}$	–	–
7233.5(10)	862.7(10)	$(3/2, 5/2)^+$	0.52(10)	–	–
7272.8(10)	902.0(10)	$1/2^-$	0.59(12)	11(2)	34(3)
7361.9(10)	991.1(10)	$3/2^-$	0.85(17)	0.30(4)	3.0(6)
7397.4(16)	1026.6(16)	$7/2^-$	0.19(10)	0.18(1)	0.19(1)

Figure 1.8: Results from ^{34}S(^{3}He,d)^{35}Cl measurement [9].

the lower limits strengths can be seen in Figure 1.10.

A follow-up measurement to the measurement by Gillespie was conducted at Triangle Universities Nuclear Laboratory (TUNL) via a ^{32}S(α,p) reaction which populated excited states of ^{35}Cl [43]. The results of this work saw confirmation of 6 of the states found by Gillespie. TUNL did not see the 272 keV state, likely due to the selection rules for this particular reaction, as discussed more thoroughly in the Theory section. The ^{32}S(α,p) reaction preferentially populates high spin states which could explain why the 272 keV state was not seen as Gillespie attributed a spin of $\frac{1}{2}^-$ or $\frac{3}{2}^-$ to this state. Also worth noting, is that the TUNL work saw a potential state at 431 keV which was not seen in the work by Gillespie but had been previously listed in a compilation by Endt [44]. This state was one of the states covered by this work and will be discussed further in the Analysis section. It should be noted that the results by TUNL were not published until after the measurements for this present work had concluded and therefore did not influence the states that were measured.

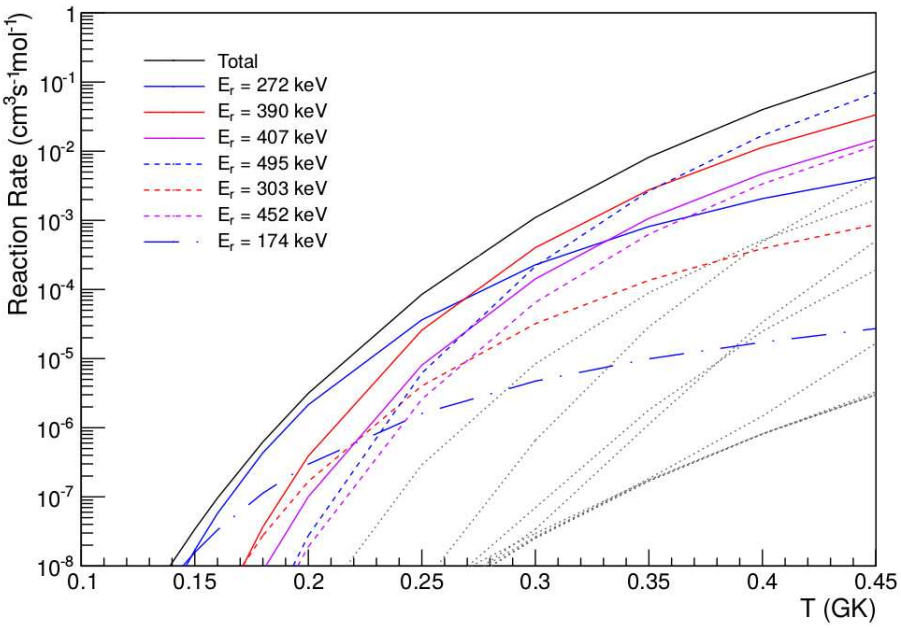

Figure 1.9: Astrophysical reaction rates calculated using the upper limit strengths found by Gillespie [9]. It can be seen that the 272 keV state dominates the reaction rate until about 0.25 GK.

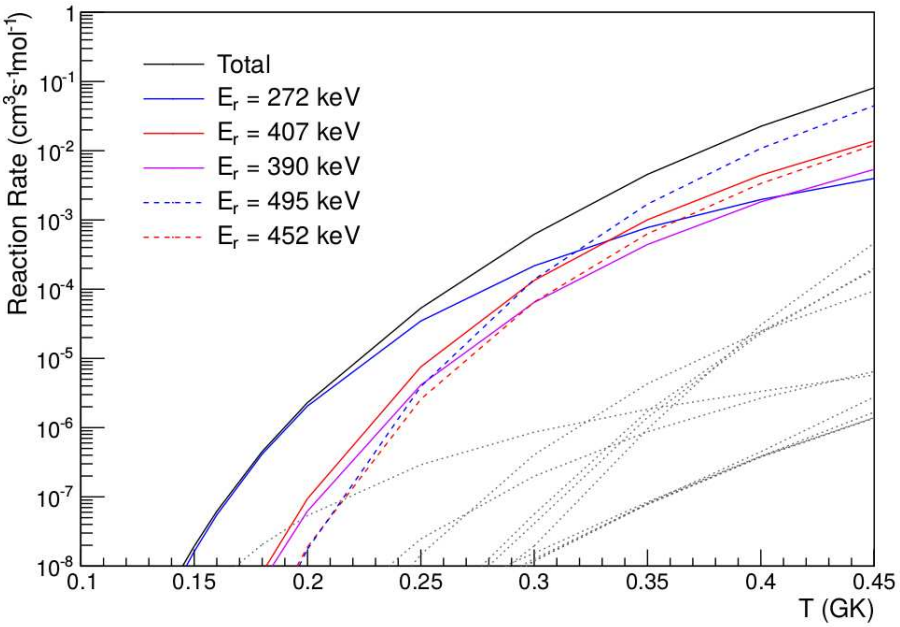

Figure 1.10: Astrophysical reaction rates calculated using the lower limit strengths found by Gillespie [9]. It can be seen that the 272 keV state dominates the reaction rate until about 0.3 GK.

CHAPTER 2

NUCLEAR CAPTURE REACTION THEORY

The following section outlines the theory of radiative capture nuclear reactions with specific focus on experiments conducted in inverse kinematics at recoil separators. Most of the derivations can be found in [10] unless otherwise noted.

2.1 Kinematics

Consider a reaction between two particles labeled A and B, of masses m_A and m_B, which collide and fuse to form particle C and emit(s) a gamma(s).

$$A + B \rightarrow C + \gamma \quad or \quad A(B, \gamma)C \tag{2.1}$$

The two particle reaction liberates energy, which is known as the reaction Q-value, and is found by,

$$Q_{AB} = (m_A + m_B - m_C)c^2. \tag{2.2}$$

The mass of the individual nuclei is one of its most fundamental properties and is defined by,

$$m_{nuc} = Zm_p + Nm_n - \Delta m, \tag{2.3}$$

where Z is the atomic number, N is the neutron number and Δm is the mass defect, which is the difference between the mass of the individual nucleons of a nucleus and the measured mass and relates to the binding energy of the nucleus. The Q value, the energy required or liberated from the reaction, can then be represented in terms of the atomic mass.

$$Q = Z_A m_p + N_A m_n - \Delta m_A + Z_B m_p + N_B m_n - \Delta m_B - Z_C m_p + N_C m_n - \Delta m_C \tag{2.4}$$

$$\begin{aligned} Q = m_p(Z_A + Z_B - Z_C) + m_n(N_A + N_B - N_C) - \Delta m_A - \Delta m_B + \Delta m_C \\ = -\Delta m_A - \Delta m_B + \Delta m_C. \end{aligned} \tag{2.5}$$

Particle accelerators can accelerate particles to speeds approaching that of the speed of light and using non-relativistic approximations can lead to an unnecessary source of error. For the experiments done for this work, the highest measured incoming beam energy used was E_{lab} = 518.6 keV/u which corresponds to T_{lab} = 17.627 MeV, where T_{lab} refers to the particles total kinetic energy in the lab frame of reference. If we assume this is the correct relativistic kinetic energy then the lab frame of reference kinetic energy, T_{lab}^{rel}, can be defined by Einstein's theory of special relativity as,

$$T_{lab}^{rel} = mc^2(\gamma - 1) \tag{2.6}$$

solving for γ, which is known as the Lorentz factor, yields,

$$\gamma = \frac{T_{lab}^{rel}}{mc^2} + 1 \tag{2.7}$$

and for the highest beam energy used in this work yields a $\gamma = 1.00054$. The Lorentz factor can also be expressed in terms of β, the ratio of the particles velocity to the speed of light,

$$\gamma = \frac{1}{\sqrt{1-\beta^2}} \quad => \quad \beta = 0.0334 \tag{2.8}$$

Which means the particle's velocity is 3.3% the speed of light. The classical kinetic energy can next be solved for using,

$$T_{lab}^{class} = \frac{1}{2} m\beta^2 c^2 = 17.612 \text{ MeV} \tag{2.9}$$

The classical approximation differs from the relativistic result by only 15 keV or 0.44 keV/u, to see the extent of the effect of the classical approximation we'll look at the percent deviation in beam energy,

$$\Delta T_{percent} = \frac{T_{lab}^{rel} - T_{lab}^{class}}{T_{lab,rel}} * 100\% = 0.0835\%. \tag{2.10}$$

The non-relativistic approximation has an effect of at most about 0.1% error. When compared to the other sources of error for the beam energy such as as 0.17% error in the energy measured at DRAGON's charge slits and a spread in the beam energy delivered from the beam operators (OPS) corresponding to an error of 0.19%. These two sources, added in

quadrature, result in an error in the measured beam energy of 0.254%, which is significantly more than the error from the non-relativistic approximation. From these calculations it is apparent that the relativistic corrections can be ignored without introducing a significant source of error.

Most accelerator facilities utilize a light ion beam impinging on a solid target in what is known as regular kinematics. This provides a wide variety of reaction possibilities due to the wide range of energies available and the simplicity of making solid targets. Issues arise with these methods due to the uncertainty in target composition and stoichiometry. Also, important values such as the stopping power are difficult to measure because the beam is generally stopped in the target backing. The energy of the incoming beam is generally not high enough to release the recoil nuclei from the atomic bonds and the recoils remain in the target as well. Both experiments described in this thesis were done at the DRAGON facility, which utilizes what is known as Inverse Kinematics, meaning a heavy ion beam at energies between 0.153 to 1.53 MeV/u [45] impinge on a hydrogen or helium gas target. This allows for an adjustable target thickness that permits the beam and recoil nuclei to exit the target and be separated by a series of electric and magnetic dipoles. Experiments done in inverse kinematics are most easily understood when expressed in the center of mass frame of reference which is defined as,

$$\vec{R}_{CM} = \frac{\Sigma_i m_i \vec{r}_i}{\Sigma_i m_i} = \frac{m_A \vec{r}_A + m_B \vec{r}_B}{m_A + m_B}, \tag{2.11}$$

where $\vec{R}_{CM}$ is the center of mass position, $\overline{r}_i$ is the position of particle i, and m_i is the mass of particle i. When Equation 2.11 is differentiated with respect to time, this gives the center of mass velocity,

$$\vec{V}_{CM} = \frac{d}{dt}\vec{R}_{CM} = \frac{d}{dt}\Big(\frac{m_A \vec{r}_A + m_B \vec{r}_B}{m_A + m_B}\Big) = \frac{m_A \vec{v}_A + m_B \vec{v}_B}{m_A + m_B}, \tag{2.12}$$

where $\vec{v}_i$ is the velocity of particle i. The center of mass momentum for particle A can be found using,

$$\vec{p}_{CM,A} = m_A(\vec{v}_A - \vec{V}_{CM}) = m_A\vec{v}_A - m_A\frac{m_A\vec{v}_A + m_B\vec{v}_B}{m_A + m_B}, \tag{2.13}$$

and can be rearranged to yield,

$$\frac{m_A\vec{v}_A(m_A + m_B) - m_Bm_B\vec{v}_B - m_A^2\vec{v}_A}{m_A + m_B} = m_Am_B\vec{v}_A - m_Am_B\vec{v}_B = m_Am_B(\vec{v}_A - \vec{v}_B), \tag{2.14}$$

which ultimately yields the end result of the center of mass momentum.

$$\vec{p}_{CM,A} = \mu\vec{v}_{CM}, \tag{2.15}$$

where $\mu = \frac{m_A * m_B}{m_A + m_B}$ is the reduced mass of the compound system and $\vec{v}_{CM} = \vec{v}_A - \vec{v}_B$ is the relative velocity of the compound system. The same can be done for $\vec{p}_{CM,B}$,

$$\vec{p}_{CM,B} = m_B(\vec{v}_B - \vec{V}_{CM}) = m_B\vec{v}_B - m_B\frac{m_A\vec{v}_A + m_B\vec{v}_B}{m_A + m_B} \tag{2.16}$$

and again rearranged to yield,

$$\frac{m_B\vec{v}_B(m_A + m_B) - m_Am_B\vec{v}_A - m_B^2\vec{v}_B}{m_A + m_B} = m_Am_B\vec{v}_B - m_Am_B\vec{v}_A = \frac{m_Am_B(\vec{v}_B - \vec{v}_B)}{m_A + m_B} \tag{2.17}$$

giving us,

$$\vec{p}_{CM,B} = -\mu\vec{v}_{CM}. \tag{2.18}$$

The total kinetic energy of the system before the collision can be expressed as such,

$$E = \frac{1}{2}(m_A\vec{v}_A^2 + m_B\vec{v}_B^2) \tag{2.19}$$

and rearranging the previous equations 2.13 and 2.16 for the individual velocities,

$$\vec{v}_A = \vec{V}_{CM} + \frac{m_B}{m_A + m_B}\vec{v}_{CM} \tag{2.20}$$

$$\vec{v}_B = \vec{V}_{CM} - \frac{m_A}{m_A + m_B}\vec{v}_{CM} \tag{2.21}$$

then substituting in the velocities that were just derived into the energy equation,

$$E = \frac{1}{2}\big[m_A(\vec{V}_{CM} + \frac{m_B}{m_A + m_B}\vec{v}_{CM})^2 + m_B(\vec{V}_{CM} - \frac{m_A}{m_A + m_B}\vec{v}_{CM})^2\big]. \tag{2.22}$$

Which, when expanded and simplified, yields the total energy in the center of mass frame,

$$E_{CM} = \frac{1}{2}(m_A + m_B)\vec{V}_{CM}^2 + \frac{1}{2}\mu\vec{v}_{CM}^2. \tag{2.23}$$

To determine the energy of the emitted gamma(s) we must acknowledge that the total energy before and after the collision will be conserved. This means the gamma energy E_γ and the total energy of particle C must sum to the initial energy of both particle A and B. This can be written as follows,

$$E_i = E_f = E_{CM} + (m_A + m_B)c^2 = E_\gamma + m_C c^2, \tag{2.24}$$

then by rearranging for the energy of the emitted gamma ray,

$$E_\gamma = E_{CM} + (m_A + m_B)c^2 - m_C c^2 \tag{2.25}$$

and substituting in the Q value yields,

$$E_\gamma = E_{CM} + Q. \tag{2.26}$$

It is also useful to have a conversion between the lab frame of reference energy and the center of mass frame energy. To do so, we will set $\vec{v}_b = 0$, which assumes the gas is stationary relative to the incoming beam, and is a valid assumption given their relative velocities.

$$\vec{V} = \frac{m_A\vec{v}_A + m_B\vec{v}_B}{m_A + m_B}, \quad \vec{v}_B = 0 \quad => \quad \vec{V}_{CM} = \frac{m_A}{m_A + m_B}\vec{v}_A \tag{2.27}$$

and using the previous results from equations 2.20 and 2.21,

$$\vec{v}_{CM,A} = \vec{v}_A - \vec{V}_{CM} = \Big(1 - \frac{m_A}{m_A + m_B}\Big)\vec{v}_A = \frac{m_B}{m_A + m_B}\vec{v}_A \tag{2.28}$$

$$\vec{v}_{CM,B} = \vec{v}_B - \vec{V}_{CM} = \frac{m_A}{m_A + m_B}\vec{v}_A = -\frac{m_B}{m_A + m_B}\vec{v}_A. \tag{2.29}$$

Then solving for the individual energies in the center of mass frame of reference,

$$E_{CM,A} = \frac{1}{2}m_A\Big(\frac{m_B}{m_B + m_B}\vec{v}_A\Big)^2 = \Big(\frac{m_B}{m_A + m_B}\Big)^2 E_A \tag{2.30}$$

$$E_{CM,B} = \frac{1}{2}m_B\Big(\frac{m_A}{m_A + m_B}\vec{v}_A\Big)^2 = \frac{m_A m_B}{(m_A + m_B)^2}E_A. \tag{2.31}$$

Then combine both energies together to get the total center of mass energy,

$$E_{CM} = E_{CM,A} + E_{CM,B} = \Big(\frac{m_B}{m_A + m_B}\Big)^2 E_A + \frac{m_A m_B}{(m_A + m_B)^2} E_A = \frac{m_B}{m_A + m_B} E_A. \quad (2.32)$$

When the fusion occurs, the beam and recoil nuclei have the same momentum. The recoil will be in an excited state and decays via gamma emission(s) to the ground state. This gamma can be emitted isotropically or with a specific angular distribution and imparts a small amount of momentum into the recoil nuclei. The result is the recoil exits the gas target with a small angular deviation relative to the beam axis in what is called a recoil cone. Due to the small angular acceptance of DRAGON, this needs to be taken into account to ensure that any recoil nuclei lost in the separating stages are included in the final analysis. The maximum cone angle will result from a direct to ground state transition gamma emitted perpendicular to the beam axis and can be solved for as follows.

Conservation of momentum demands that,

$$\vec{p}_i = \vec{p}_f = m_A \vec{v}_A + m_B \vec{v}_B = (m_A + m_B)\vec{v}_C + \vec{p}_\gamma = m_C \vec{v}_C + \vec{p}_\gamma \quad (2.33)$$

and we know that,

$$\vec{p}_\gamma = \hbar \vec{k} = \frac{E_\gamma}{c} = \frac{Q + E_{CM}}{c}. \quad (2.34)$$

To better see the effect of the momentum from the recoil gamma, we will break the equation up into the x and y components. We will align the axes so the z direction is perpendicular to the beam axis and the recoil gamma and can be excluded from these considerations.

$$p_{C,x} = p_A - p_\gamma \mathrm{Cos}(\theta) \quad (2.35)$$

$$p_{C,y} = -p_\gamma \mathrm{Sin}(\theta) \quad (2.36)$$

$$Tan(\phi) = \frac{p_{C,y}}{p_{C,x}} = \frac{\frac{1}{c} E_\gamma \mathrm{Sin}(\theta)}{\sqrt{2 m_A E_A} - \frac{E_\gamma}{c}\mathrm{Cos}(\theta)} \quad (2.37)$$

$$\phi = tan^{-1}\Big(\frac{E_\gamma \mathrm{Sin}(\theta)}{\sqrt{2 m_A c^2 E_A} - E_\gamma \mathrm{Cos}(\theta)}\Big) \quad (2.38)$$

The recoil cone angle ϕ, is maximum at $\theta = \frac{\pi}{2}$ or $\theta = \frac{3\pi}{2}$, when the gamma is emitted perpendicular to the beam axis. Any other emission angles will yield a value of ϕ that will be contained within this cone. A diagram of the reaction process can be seen in Figure 2.1.

$$\phi_{max} = \tan^{-1}\Big(\frac{E_\gamma}{\sqrt{2m_A c^2 E_A}}\Big) \tag{2.39}$$

Any gammas emitted at angles other than $\theta = \frac{\pi}{2}$ or $\theta = \frac{3\pi}{2}$ will cause a change in the x component of the momentum, and as a result the recoil nuclei will have a range of energies which can be solved for via,

$$p_{C,x} = p_A - p_\gamma \mathrm{Sin}(\theta) \tag{2.40}$$

Where θ is again the angle of the emitted gamma with respect to the beam axis. The momentum of the recoil nuclei is maximally affected at emission angles of 0 and π or when the gamma emission is aligned or anti-aligned with respect to the beam axis. Inserting both values of θ into the momentum equation yields,

$$p_{C,x} = p_A \pm p_\gamma = \sqrt{2m_A E_A} \pm \frac{E_\gamma}{c} \tag{2.41}$$

which gives the energy of the recoils as,

$$E_{C,x} = \frac{1}{2m_C}\Big(\sqrt{2m_A E_A} \pm \frac{E_\gamma}{c}\Big)^2 \tag{2.42}$$

Expanding the square and simplifying yields,

$$E_{C,x} = \frac{1}{2m_C}\Big(2m_A E_A + \frac{E_\gamma^2}{2m_A c^2 E_A} \pm \frac{2E_\gamma}{\sqrt{2m_A E_A c^2}}\Big) = \frac{m_A}{m_C} E_A\Big(1 + \frac{E_\gamma^2}{2m_A c^2 E_A} \pm \frac{2E_\gamma}{\sqrt{2m_A E_A c^2}}\Big) \tag{2.43}$$

2.2 Stellar Reaction Rate/Cross Section

Classically, the cross section is a function of the physical sizes of the two objects in question and can be expressed as such.

$$\sigma = \pi(r_0 + r_1)^2 \tag{2.44}$$

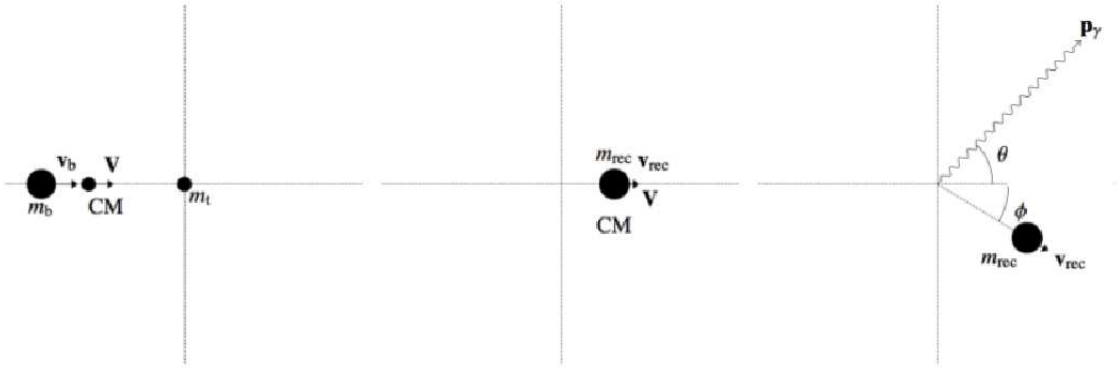

Figure 2.1: Diagram of recoil cone due to collision in inverse kinematics. (a) Beam nuclei with velocity v_b interacts with stationary target nuclei. (b) Beam nuclei and target nuclei fuse to form compound recoil nuclei in excited state. (c) Recoil nuclei emits gamma ray(s) with momentum p_γ as it decays to the ground state, resulting in recoil nuclei exiting the target into a cone with half angle ϕ_{max}. Figure taken from [46].

Where r_i is the radius of particle i and σ is the reaction cross section. In this section we will switch from the particle labels A and B to 0 and 1 to avoid confusion with Avogadro's number, N_A, in the stellar reaction rate. When considering nuclear reactions one must include effects from the quantum nature of things, such as the dependence on energy. For a nuclear reaction, the cross section may be written as,

$$\sigma = \frac{1}{4\pi}\lambda^2. \tag{2.45}$$

Where λ is known as the de Broglie wave length and is defined for a two particle reaction as such,

$$\lambda^2 = \frac{m_0 + m_1}{m_0 m_1}\frac{h^2}{2E_{CM}}, \tag{2.46}$$

where h is known as Planck's constant. The cross section can be expressed as,

$$\sigma = \frac{\text{(number of interactions per time)}}{\text{(number of incident particles per area per time)(number of target nuclei within beam)}} \tag{2.47}$$

Or in terms of symbols,

$$= \frac{(N_r/t)}{[N_b/(tA)]N_t}. \tag{2.48}$$

We can then write the reaction rate per volume,

$$\frac{N_r}{Vt} = (\sigma N_t)\Big(\frac{N_b}{VAt}\Big) = \sigma\frac{N_t}{V}\frac{N_b}{At} = \sigma\frac{N_t}{V}v\frac{N_b}{V}, \tag{2.49}$$

where the current density $j_b = \frac{N_b}{At} = v\frac{N_b}{V}$ is used. This can now be seen as a function of v, the relative velocity of the compound system. The reaction rate is defined as the number of reactions per unit time and per unit volume and can then be expressed in terms of a particle induced reaction via,

$$r_{01} = N_0 N_1 v\sigma(v), \tag{2.50}$$

where N_i are the number densities N/V of the respective particle, either the target or the beam. For the case of a stellar plasma, the velocity of the individual particles is not constant, which means the relative velocity between the particles is not constant as well. The relative velocity takes the form of a distribution described by the probability function P(v). P(v) is defined as the probability that the relative velocity is between v and v + dv and obeys the property that,

$$\int_0^\infty P(v)dv = 1. \tag{2.51}$$

The reaction rate can be rewritten using this property to be,

$$r_{01} = N_0 N_1 \int_0^\infty vP(v)\sigma(v)dv = N_0 N_1 \langle\sigma v\rangle_{01}, \tag{2.52}$$

where $\langle\sigma v\rangle_{01}$ is the reaction rate per particle pair and N_0N_1 is the total number density of pairs of nonidentical nuclei 0 and 1. This can be generalized to include identical particles via,

$$r_{01} = \frac{N_0 N_1 \langle\sigma v\rangle_{01}}{1+\delta_{01}}, \tag{2.53}$$

where δ_{01} is the usual Kronecker delta.

As mentioned before, the reaction rate depends on the relative velocities between the two particles, which are generally described by a Maxwell-Boltzmann distribution. The probability density for this distribution is given by,

$$P(v)dv = \left(\frac{m_{01}}{2\pi kT}\right)^{3/2} e^{-m_{01}v^2/(2kT)} 4\pi v^2 dv, \tag{2.54}$$

where k is the Boltzmann constant, T is the temperature and m_{01} is the reduced mass of the compound system. This probability distribution gives the probability that the relative velocity is between v and v+dv. By making the substitutions $E = m_{01}v^2/2$ and $dE/dv = m_{01}v$ we can then write,

$$P(v)dv = P(E)dE = \left(\frac{m_{01}}{2\pi kT}\right)^{3/2} e^{-E/kT} 4\pi \frac{2E}{m_{01}} \frac{dE}{m_{01}} \sqrt{\frac{m_{01}}{2E}} = \frac{2}{\sqrt{\pi}} \frac{1}{(kT)^{3/2}} \sqrt{E} e^{-E/kT} dE. \tag{2.55}$$

The distribution of velocities has a maximum value at $v_T = \sqrt{2kT/m_{01}}$, which corresponds to E = kT, while the energy distribution has a maximum at E = kT/2. For the reaction rate per particle pair we can write,

$$\langle \sigma v \rangle_{01} = \int_0^\infty vP(v)\sigma(v)dv = \int_0^\infty vP(E)\sigma(E)dE = \left(\frac{8}{\pi m_{01}}\right)^{1/2} \frac{1}{(kT)^{3/2}} \int_0^\infty E\sigma(E)e^{-E/kT}dE. \tag{2.56}$$

This can then be represented in terms of the stellar reaction rate, $N_A\langle \sigma v \rangle_{01}$, and for a given temperature, T_9, now in units of GK,

$$N_A\langle \sigma v \rangle_{01} = \frac{3.7318 \times 10^{10}}{T_9^{3/2}} \sqrt{\frac{m_0 + m_1}{m_0 m_1}} \int_0^\infty E\sigma(E)e^{-11.605E/T_9}dE. \tag{2.57}$$

2.3 Non-resonant Reaction

Due to the quantum mechanical nature of capture reactions, there is always a non-zero probability to have the reaction occur via tunneling, regardless of the energy. Cross sections vary smoothly with respect to energy outside of resonances and tend to have a 1/E dependence, which makes it convenient to introduce the astrophysical S-factor, S(E). This is defined as,

$$\sigma(E) = \frac{1}{E} e^{-2\pi\eta} S(E), \tag{2.58}$$

where $e^{-2\pi\eta}$ is known as the Gamow factor and represents the probability for an s-wave transition through the Coulomb barrier and is equal to $\exp[-\frac{2\pi}{\hbar}\sqrt{\frac{m_{01}}{2E}} Z_0 Z_1 e^2]$. Now, using the previous result from Equation 2.57, we can write,

$$N_A\langle\sigma v\rangle_{01} = \left(\frac{8}{\pi m_{01}}\right)^{1/2} \frac{N_A}{(kT)^{3/2}} \int_0^\infty e^{-2\pi\eta} S(E) e^{-E/kT} dE. \tag{2.59}$$

By examining the two exponentials in the integrand it can be seen that they have the opposite effect. At high energies the $e^{-E/kT}$ factor causes the transition probability to drastically decrease and at low energies the $e^{-2\pi\eta}$ factor does the same. As a result, there is a confined interval where the integrand is significant, which is referred to as the Gamow window and can be seen in Figure 2.2. If we approximate the S-factor as constant, meaning S(E) = S_0,

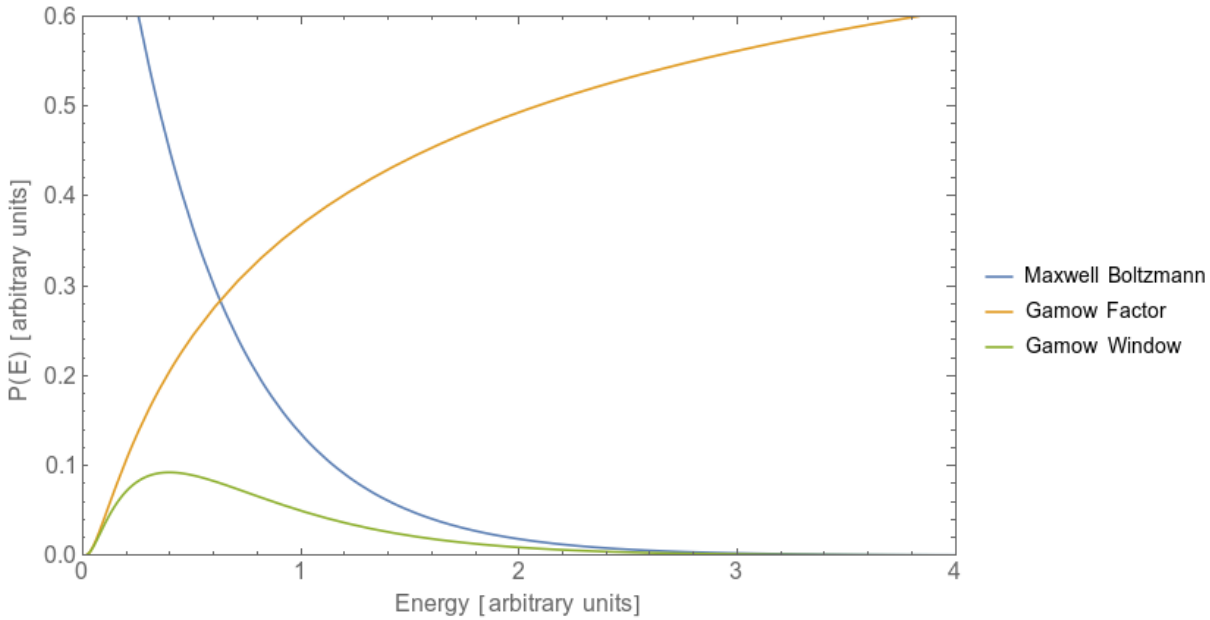

Figure 2.2: Gamow window(green) from the Maxwell Boltzmann factor(blue) and Gamow factor(orange) shows the range of energies where radiative capture reactions can proceed.

we can then write,

$$N_A\langle\sigma v\rangle_{01} = \left(\frac{8}{\pi m_{01}}\right)^{1/2} \frac{N_A}{(kT)^{3/2}} S_0 \int_0^\infty e^{-2\pi\eta} e^{-E/kT} dE, \tag{2.60}$$

where the integrand is referred to as the Gamow Peak. The Gamow Peak can be maximized by taking the derivative with respect to energy and setting it equal to 0.

$$\frac{d}{dE}Exp\Big[-\frac{2\pi}{\hbar}\sqrt{\frac{m_{01}}{2E}}Z_0Z_1e^2-\frac{E}{kT}\Big]_{E=E_0}=\frac{\pi}{\hbar}Z_0Z_1e^2\sqrt{\frac{m_{01}}{2}}\frac{1}{E_0^{3/2}}-\frac{1}{kT}=0 \tag{2.61}$$

Solving for E_0 yields,

$$E_0=\Big[\big(\frac{\pi}{\hbar}\big)^2\big(Z_0Z_1e^2\big)^2\big(\frac{m_{01}}{2}\big)(kT)^2\Big]^{1/3}. \tag{2.62}$$

The Gamow Peak can be approximated by a Gaussian function that has its maximum at E_0 and the same curvature at E_0 as well. We can write the Gaussian as such,

$$\mathrm{Exp}\big[-\frac{2\pi}{\hbar}\sqrt{\frac{m_{01}}{2E}}Z_0Z_1e^2-\frac{E}{kT}\big]=\mathrm{Exp}\big[-\frac{2E_0^{3/2}}{\sqrt{E}kT}-\frac{E}{kT}\big]\approx\mathrm{Exp}\big[-\frac{3E_0}{kT}\big]\mathrm{Exp}\Big[-\big(\frac{E-E_0}{\Delta/2}\big)^2\Big]. \tag{2.63}$$

The width of the Gaussian distribution, Δ, can be found by setting the second derivatives equal at $E=E_0$,

$$\frac{d^2}{dE^2}\Big(\frac{2E_0^{3/2}}{\sqrt{E}kT}-\frac{E}{kT}\Big)_{E=E_0}=\frac{3}{2}\frac{1}{E_0kT} \tag{2.64}$$

$$\frac{d^2}{dE^2}\Big(\frac{E-E_0}{d/2}\Big)^2_{E=E_0}=\frac{2}{(\Delta/2)^2} \tag{2.65}$$

which, when set equal and solved for Δ, the result is as follows,

$$\Delta=\frac{4}{\sqrt{3}}\sqrt{E_0kT}. \tag{2.66}$$

Combining the previous results gives us the Gaussian approximation for the Gamow peak,

$$G(E)=\mathrm{Exp}[-\frac{3E_0}{kT}]\mathrm{Exp}[-\frac{3(E-E_0)^2}{4E_0kT}]. \tag{2.67}$$

2.4 Reaction Rate Resonant

In this section we will outline the formalism for the case that the S-factor varies strongly as the result of a narrow and isolated resonance. A resonance is considered to be narrow if the corresponding partial widths are approximately constant over the total resonance width.

We will start with the one level Breit-Wigner formula which is as follows,

$$\sigma(E)_{BW} = \frac{\lambda^2}{4\pi}\frac{(2J+1)(1+\delta_{01})}{(2j_0+1)(2j_1+1)}\frac{\Gamma_a\Gamma_b}{(E_r-E)^2+\Gamma^2/4}, \tag{2.68}$$

where j_i is the target and projectile spin, Γ_i is the entrance and exit partial widths, Γ is the total resonance width, and λ is the de Broglie wavelength. The Kronecker delta term is included because the cross section doubles for identical particles. The narrow isolated resonance reaction rate can then be calculated using the reaction rate formula derived earlier.

$$< \sigma\nu >_{01} = \int_0^\infty d\nu P(\nu)\sigma(\nu) = \int_0^\infty dE\nu\sigma(E)P(E) \tag{2.69}$$

Where the probability density P(E) is the Maxwell-Boltzmann distribution,

$$P(E) = \frac{2}{\sqrt{\pi}}\frac{1}{(kT)^{3/2}}\sqrt{E}e^{-E/kT}. \tag{2.70}$$

Using these together with the Breit-Wigner formula, we have the stellar reaction rate for narrow isolated resonances,

$$N_A < \sigma\nu > = \Big(\frac{8}{\pi m_{01}}\Big)^{\frac{1}{2}}\frac{N_A}{(kT)^{\frac{3}{2}}}\int_0^\infty dE\sigma(E)_{BW}Ee^{-\frac{E}{kT}}. \tag{2.71}$$

If we then define,

$$\omega = \frac{(2J+1)(\delta_{01}+2)}{(2j_0+1)(2j_1+1)}, \tag{2.72}$$

we can make the substitution into the stellar reaction rate,

$$N_A < \sigma\nu > = N_A\frac{\sqrt{2\pi}\hbar^2}{(m_{01}kT)^{\frac{3}{2}}}\omega\int_0^\infty dE\frac{\Gamma_a\Gamma_b}{(E_r-E)^2+\frac{\Gamma^2}{4}}e^{-\frac{E}{kT}}. \tag{2.73}$$

Where we have already replaced λ with the expression for the de Broglie wavelength, Equation 2.46. If the resonance is sufficiently narrow, the Maxwell-Boltzmann factor and the partial widths Γ_i are approximately constant over the total width of the resonance. This means we can replace them with their value at E_r and can calculate the integral analytically, see Appendix A for a more detailed derivation.

$$N_A < \sigma\nu > = N_A\frac{\sqrt{2\pi}\hbar^2}{(m_{01}kT)^{\frac{3}{2}}}e^{-\frac{E_r}{kT}}\omega\frac{\Gamma_a\Gamma_b}{\Gamma}2\int_0^\infty dE\frac{\Gamma/2}{(E_r-E)^2+\frac{\Gamma^2}{4}} \tag{2.74}$$

Where the result of the integral is,

$$N_A < \sigma\nu >= N_A \frac{\sqrt{2\pi}\hbar^2}{(m_{01}kT)^{3/2}} e^{-E_r/kT} \omega \frac{\Gamma_a \Gamma_b}{\Gamma} 2\pi = N_A \Big(\frac{2\pi}{m_{01}kT}\Big)^{\frac{3}{2}} \hbar^2 e^{-\frac{E_r}{kT}} \omega\gamma. \tag{2.75}$$

The replacement $\omega\gamma = \frac{\omega\Gamma_a\Gamma_b}{\Gamma}$ was made and $\omega\gamma$ is known as the resonance strength and is proportional to the area under the resonance cross section. Reaction rates for narrow resonances depend on the energy and strength of the resonance only, which makes measuring the reaction rate easier because most partial and total widths are not known experimentally. The total reaction rate for several narrow isolated resonances can be calculated by just summing the individual contributions from each resonance.

2.5 Selection Rules

Considering the ^{34}S$(p,\gamma)^{35}$Cl reaction, where the proton has a ground state spin of $\frac{1}{2}^+$ and the ^{34}S has a ground state spin of 0^+, then via the equation for conservation of total angular momentum J,

$$\vec{J} = \vec{l} + \vec{j}_p + \vec{j}_{^{34}S} = \vec{l} + \vec{s} \tag{2.76}$$

where $\vec{s}$ can be found using

$$|j_p - j_{^{34}S}| \leq s \leq j_p + j_{^{34}S}. \tag{2.77}$$

This results in a value for $\vec{s}$ of $\frac{1}{2}$, which is then added together with the possible l values in the same manner as Equation 2.77. Then, one can use the following equation to determine the corresponding parities,

$$\Pi = (\pi_p)(\pi_{^{34}S})(-1)^l. \tag{2.78}$$

This means the spin J^π can be written in terms of the orbital angular momentum l, which for various values of l the accessible states in ^{35}Cl can be seen in table Table 2.1.

Meaning at low energies, we expect the ^{34}S$(\mathrm{p},\gamma)^{35}$Cl reaction to populate states in ^{35}Cl with spins of $\frac{1}{2}^+$,$\frac{3}{2}^-$ or $\frac{1}{2}^-$, $\frac{5}{2}^+$ or $\frac{3}{2}^+$, $\frac{7}{2}^-$ or $\frac{5}{2}^-$ with decreasing probability as l increases.

Table 2.1: Table of allowable populated spins in ^{35}Cl.

Selection Rules	
l	J^π
0	$\frac{1}{2}^+$
1	$\frac{3}{2}^-, \frac{1}{2}^-$
2	$\frac{5}{2}^+, \frac{3}{2}^+$
3	$\frac{7}{2}^-, \frac{5}{2}^-$

We can also use selection rules for gamma transitions to determine the possible allowed transitions from the initially populated excited states of ^{35}Cl. Again, from conservation of angular momentum, we know that,

$$J_r = L + J_f, \tag{2.79}$$

where J_r is the spin of the initial excited state, L is the spin of the emitted gamma, and J_f is the spin of the state after the gamma transition. We know the parity of the emitted gamma obeys the following equations,

$$\Pi_E = \pi_i(-1)^L \tag{2.80}$$

$$\Pi_M = \pi_i(-1)^{L+1}. \tag{2.81}$$

Where the subscripts E and M denote electric or magnetic transitions respectively and π_i is the parity of the initially populated excited state of the recoil nuclei. We expect the nuclei to favor direct to ground state transitions if that is allowed by the selection rules.

CHAPTER 3

EXPERIMENTAL SETUP

The experiment was conducted in the Isotope Separator and ACcelerator I (ISAC) experimental hall of the TRIUMF facility in Vancouver Canada. A diagram of the experimental hall can be seen in Figure 3.1. Ions are produced by the Supernanogan multi-charge ion

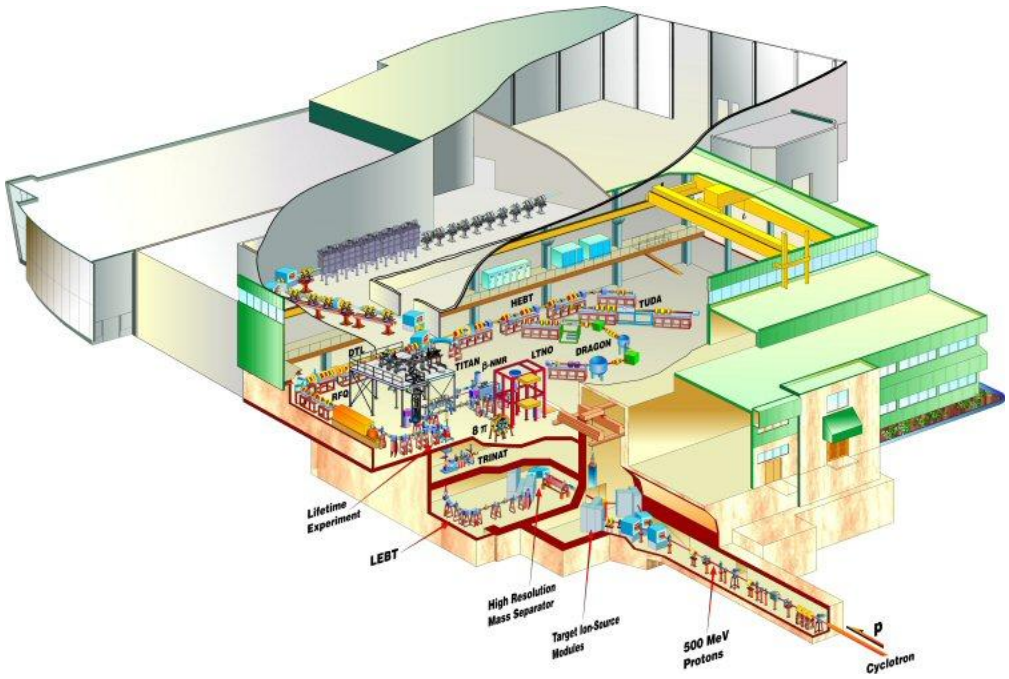

Figure 3.1: Diagram of the ISAC experimental hall showing various stages of the beam line leading to DRAGON [47].

source (MCIS), for a more detailed description see [48]. The ions are transported from the MCIS to a switching station then fed into an 11.8 MHz pre-buncher, then through the low energy beam transport line (LEBT) into a 35.4 MHz Radio Frequency Quadrupole (RFQ) which can accelerate ions of $A/q \leq 30$ from 2 to 153 keV/u which then can be further accelerated by the 106 MHz drift tube linear accelerator (DTL) up to energies of 1.53 MeV/u. The DTL is only capable of accelerating ions of $3 \leq A/q \leq 6$ [45]. The beam for this experiment

was ^{34}S delivered at an average intensity of 10^{11} s^{-1} with a charge of 7+, which gives an A/q of 4.86. A figure of the ISAC accelerating stages can be seen in Figure 3.2.

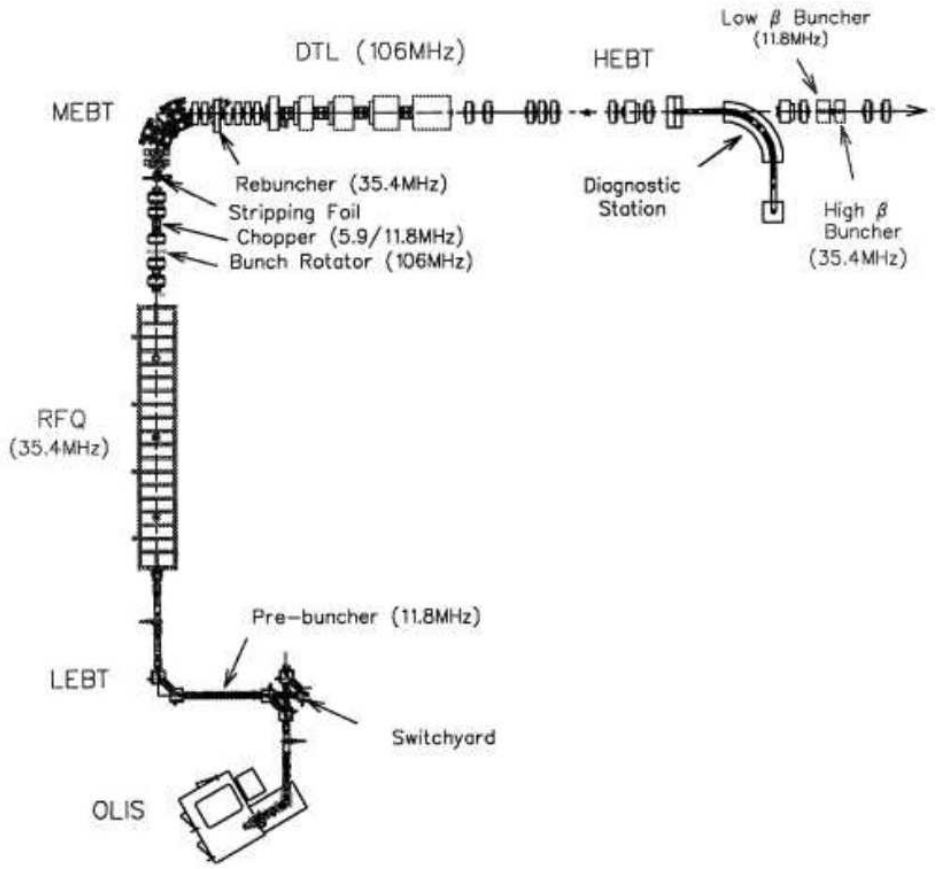

Figure 3.2: Diagram of the ISAC accelerator line from the ion source to the β bunchers directly upstream of DRAGON [45].

3.1 DRAGON Overview

DRAGON (Detector of Recoil And Gammas Of Nuclear astrophysics) is a 21 m long recoil separator composed of a series of magnetic and electrostatic dipoles used to select ions with specific charge to mass ratios and magnetic rigidities, a diagram of which can be seen in Figure 3.3. DRAGON is composed of three main components, the head, the electromagnetic separator (EMS) and the tail. The head consists of the windowless gas target and surrounding BGO array. The EMS consists of the bending magnets and electric dipoles

as well as several beam diagnostic and monitoring components. The tail detectors consist of two micro-channel plate (MCP) detectors and dual sided silicon strip detector (DSSSD) or Ionization Chamber (IC) or the newly installed Hybrid detector which combines both the DSSSD and IC detectors. The Hybrid Detector was chosen for this experiment to provide the position and energy resolution of the DSSSD and the energy loss measurements of the IC for optimal particle identification.

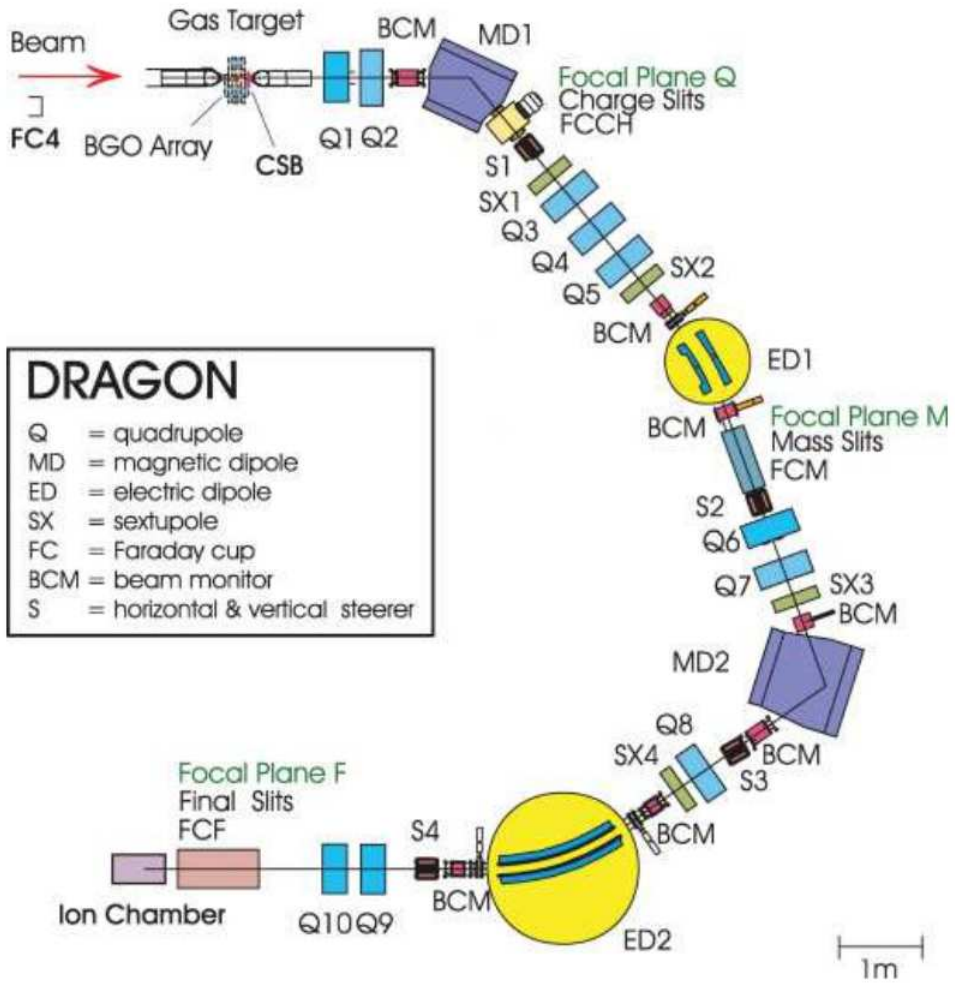

Figure 3.3: Diagram of the DRAGON with magnetic dipoles in purple and electric dipoles in yellow [49].

3.2 DRAGON Head

The head of DRAGON is composed of the windowless gas target, a diagram can be seen in Figure 3.4. Connected directly up and downstream of the gas target are a series of differential pumping boxes and the pressure within each box is regulated by a series of 7 turbomolecular pumps connected as can be seen in Figure 3.5. Pressures between 0.2 and 10 Torr [50] of H_2, ^{4}He, and ^{3}He, are possible within the gas target at an effective target length of 12.3(4) cm and a physical length of 11 cm. Any gas that leaks through the target's flow limiting apertures is pumped out by a combination of 5 roots blower pumps and recirculated through a LN2 cooled Zeolite trap which is used to remove contaminants and preserve the gas purity. The combination of pumps maintain a vacuum on the order of $<10^{-6}$ Torr outside of the gas target which is particularly important downstream of the target to prevent any further charge changing reactions that would distort the charge state distribution and diminish the quality of the beam suppression, the ratio of the number of incoming beam particles to the number of beam particles detected in the end detectors, through secondary scattering reactions.

The target has an entrance aperture of 6 mm and an exit aperture of 8 mm due to the expected beam size and angular spread caused by the emitted recoil gamma rays discussed in the Theory section. The pumping tubes downstream are tapered to allow for the recoil cone to pass through unaltered, see Figure 3.6. This gives an angular acceptance through the separating stages of DRAGON of $\pm$20 mRad [50].

The gas target is surrounded by 30 Bismuth Germanate (BGO) scintillation detectors, see Figure 3.7, with a hexagonal cross section, which are placed in a closely packed array that provides a 92% solid angle coverage from the center of the gas target [51, 52]. These are used in combination with the tail heavy ion detectors to provide further means of particle identification via global time of flight (TOF). Monte Carlo simulations predict a total efficiency of 45% to 60% for gamma rays with energies ranging from 1-10 MeV for the array [46, 51, 52]. The average gamma energy resolution for 6.13 MeV gamma rays is 7% full

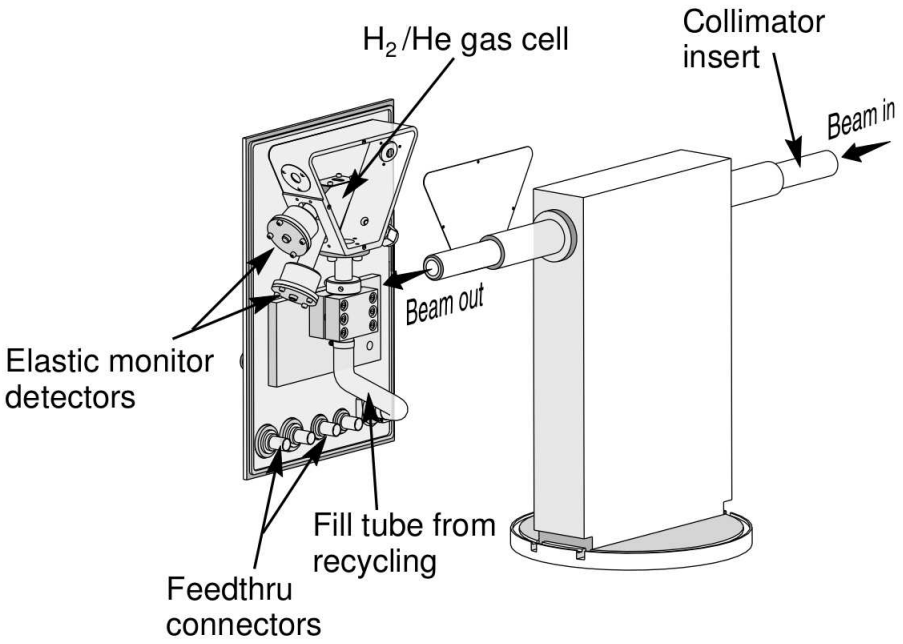

Figure 3.4: DRAGON gas target showing the exterior and interior components [49].

width at half maximum (FWHM). The beam current is passively monitored by the use of 2 silicon detectors located within the gas target at angles of 30° and 57°. These monitor the elastically scattered protons or alpha particles during the course of the run and are used to normalize out any fluctuations in beam intensity that may occur.

3.3 EMS

To properly measure the yield of reactions with small cross sections relevant to novae nucleosynthesis, DRAGON needs to have online beam suppression up to the order of 10^{13}, this is primarily accomplished using DRAGON's EMS. DRAGON's EMS consists of a two stage mass and charge separator used to separate the unreacted beam and the recoil ions. The optical components of the EMS are a series of magnetic dipoles (M) for recoil separation, magnetic quadrupoles (Q) for focusing, magnetic sextupoles (S) for focusing, and electric dipoles (E) for recoil separation. These are arranged in the order QQMSQQQSE-QQSMQSEQQ. The EMS also contains several beam diagnostic components such as Faraday

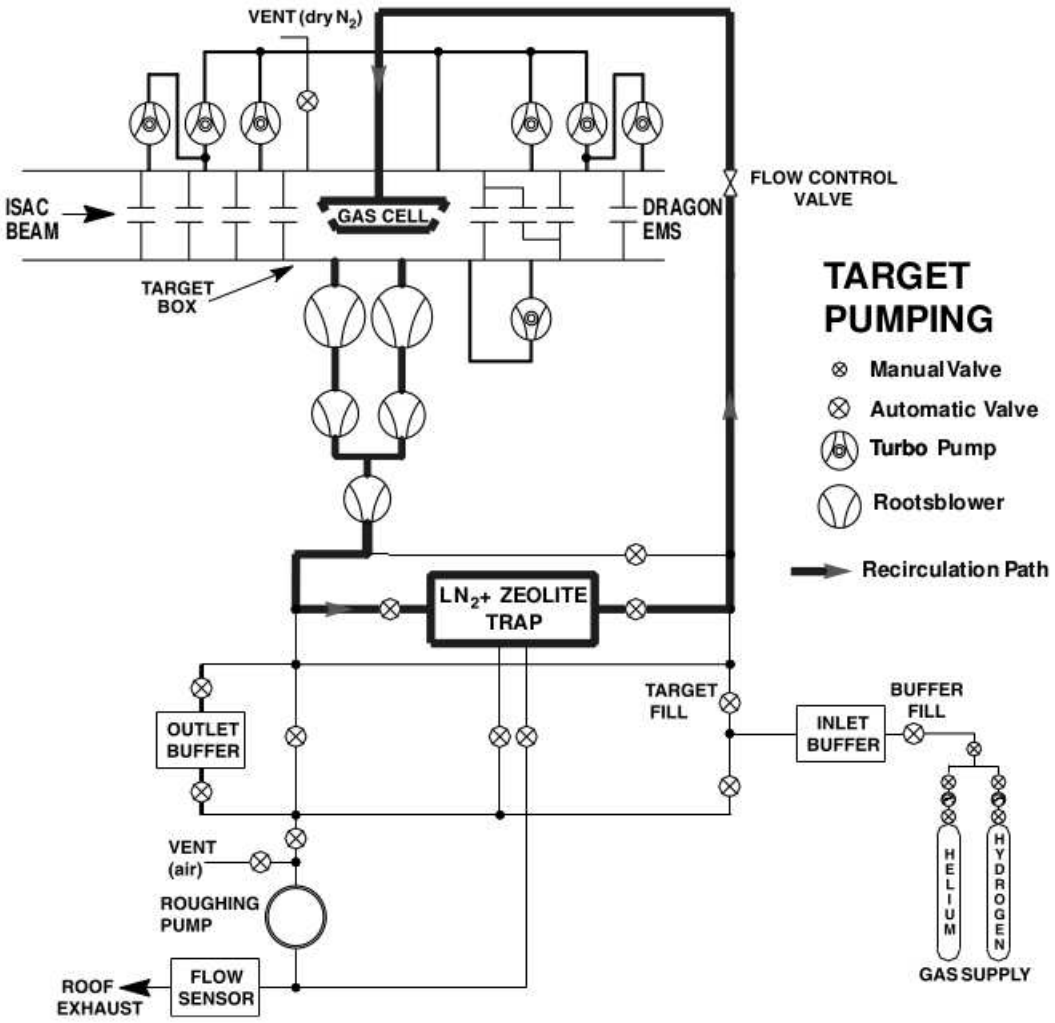

Figure 3.5: Target vacuum and gas recirculation system. Gas enters from the gas supply into the target and any leaked gas is recirculated into the zeolite trap to maintain purity [49].

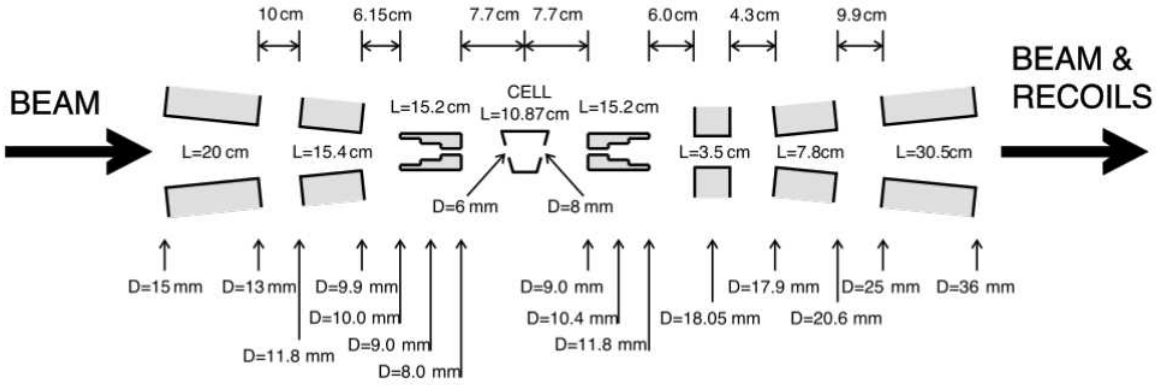

Figure 3.6: Tapered pumping stages surrounding the gas target to compensate for recoil cone angle [49].

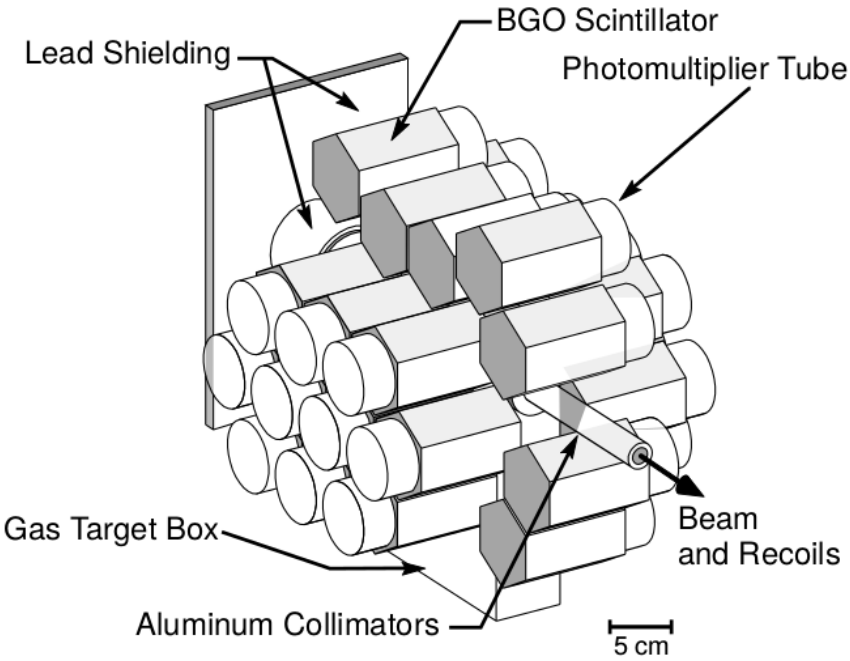

Figure 3.7: Diagram showing arrangement of BGO array which surrounds the center of the gas target [49].

cups to measure the beam current, a CCD camera used to check the beam position in the gas target, and beam centering monitors used to check the alignment of the beam leaving the gas target [53]. The beam centering monitors consist of a grid of wires which are used to measure the deviation of the beam by turning on and off the focusing quadrupoles located directly upstream and downstream of the gas target.

Apart from the small variations due to the recoil gamma rays the unreacted beam and recoil nuclei will exit the target with the same momentum but a different energy per nucleon,

$$p_{rec} = p_{beam} = \sqrt{2T_{rec}m_{rec}} = \sqrt{2T_{beam}m_{beam}} \tag{3.1}$$

which results in,

$$T_{rec} = \frac{m_{beam}}{m_{rec}} T_{beam}. \tag{3.2}$$

The first magnetic dipole allows for the selection of a specific charge state through the ion's magnetic rigidity,

$$R_M = r|B| = \frac{p}{q}. \tag{3.3}$$

This means the charge may be chosen by selecting the field strength and ions without the selected charge will be steered into the charge slits located directly after the magnetic dipole. The beam enters the target in a single charge state but due to a series of charge changing reactions the beam and recoils will exit the target in a distribution of charge states. Generally, the highest probable charge state, approximately 40% of the recoils, is chosen to maximize the number of recoils detected in the heavy ion detectors. After the charge is selected, the mass can be chosen through the particle's electric rigidity,

$$R_E = r|E| = \frac{mv^2}{q} \propto \frac{T}{q}. \tag{3.4}$$

If you insert Equation 3.2 into Equation 3.4 you can solve for the recoil magnetic rigidity,

$$R_{E,rec} = r_{rec}|E| = \frac{m_{beam}}{m_{rec}} \frac{T_{beam}}{q} \tag{3.5}$$

where as the beam magnetic rigidity is,

$$R_{E,beam} = r_{beam}|E| = \frac{T_{beam}}{q}. \tag{3.6}$$

Since the ions which make it to the first electric dipole, see Figure 3.8, should be primarily of the chosen charge state, the ion's trajectory through the electric dipole will be determined by the ion's mass. The recoil nuclei have picked up an additional proton, or an alpha particle depending on the particular reaction and therefore have a different mass than the beam. The beam is steered into a set of mass slits while the recoils are allowed to pass through. The entire process is repeated again through the second stage of the EMS. This allows the beam to be suppressed relative to the recoils and later analysis is greatly simplified by the removal of unnecessary background.

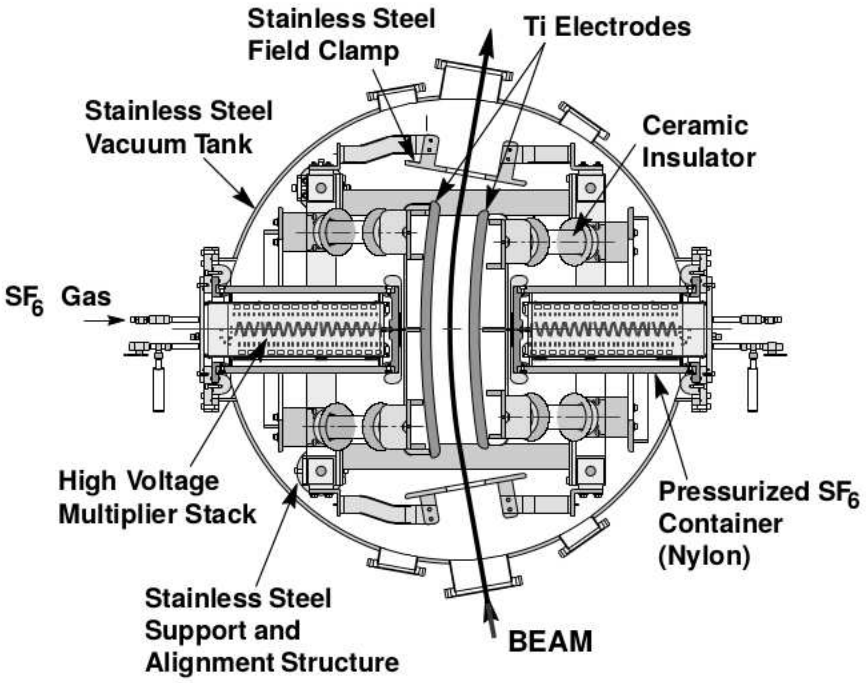

Figure 3.8: Diagram showing electric dipole configuration at DRAGON [49].

3.4 Dragon Tail

The tail end of DRAGON consists of two MCP detectors, and in the case of this experiment a hybrid detector which consists of an IC and DSSSD working in conjunction,

Figure 3.9. The hybrid detector allows E vs ΔE comparisons for better particle identification than either detector individually. The IC portion consists of two anodes and the chamber is filled with isobutane up to pressures of 30 Torr. The chamber is separated from the beam line by a thin mylar window, Figure 3.10. This allows the beam to enter the IC with minimal interaction and the energy loss within the chamber can be measured, giving energy loss vs energy measurements. Ions lose energy based on the nuclear charge and velocity. This allows the recoils to be identified relative to the beam as they have an additional proton for (p,γ) reactions. The DSSSD is located at the back of the IC and is composed of 3 mm active silicon strips aligned vertically in the front and horizontally in the back to see the 2D hit position of the ion [50]. The silicon detector provides a precise measurement of the ion energy and has high detection efficiency, >90%. The optimal particle identification can be achieved by selecting the isobutane pressure which will maximize the energy difference between the leaky beam and recoil ions by the time they reach the DSSSD portion of the detector. DRAGON's MCP detectors detect secondary electrons emitted when the beam

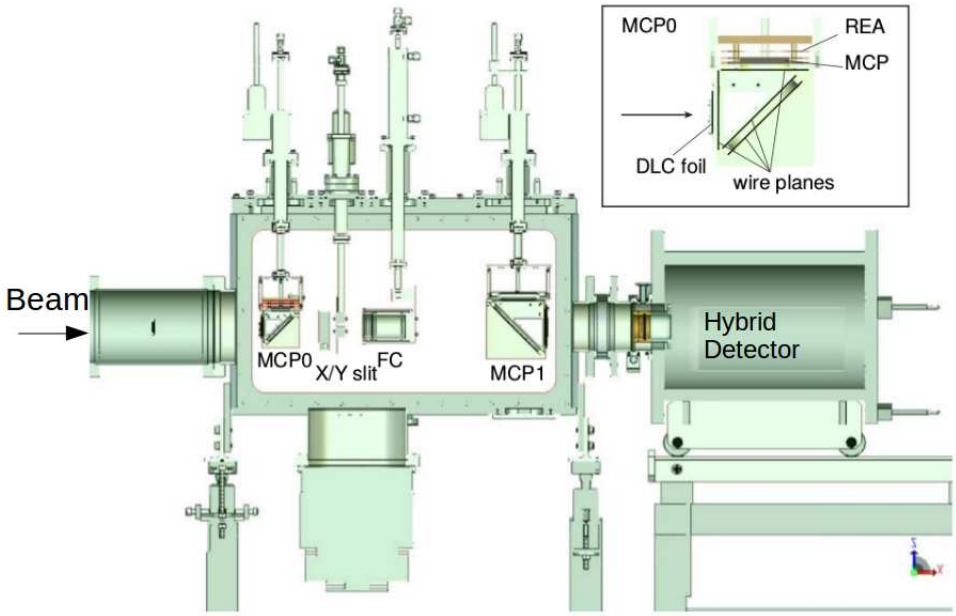

Figure 3.9: Diagram showing arrangement of the hybrid detector and MCP detectors at the tail end DRAGON [46].

passes through a thin carbon foil. An electrostatic mirror directs these electrons away from the beam axis and into the MCP detectors [53]. The detectors are located 59 cm apart and are used to produce a local TOF parameter to further distinguish the leaky beam and recoils via their different velocities. The velocities vary because the recoils and leaky beam have the same momentum but the recoils have a slightly larger mass. The larger the relative difference between the recoil and leaky beam mass the better the separation seen in the MCP detectors. This is one of the best means of particle identification for DRAGON as it can be used to do both singles and coincident analysis, which will be discussed more in the Analysis section.

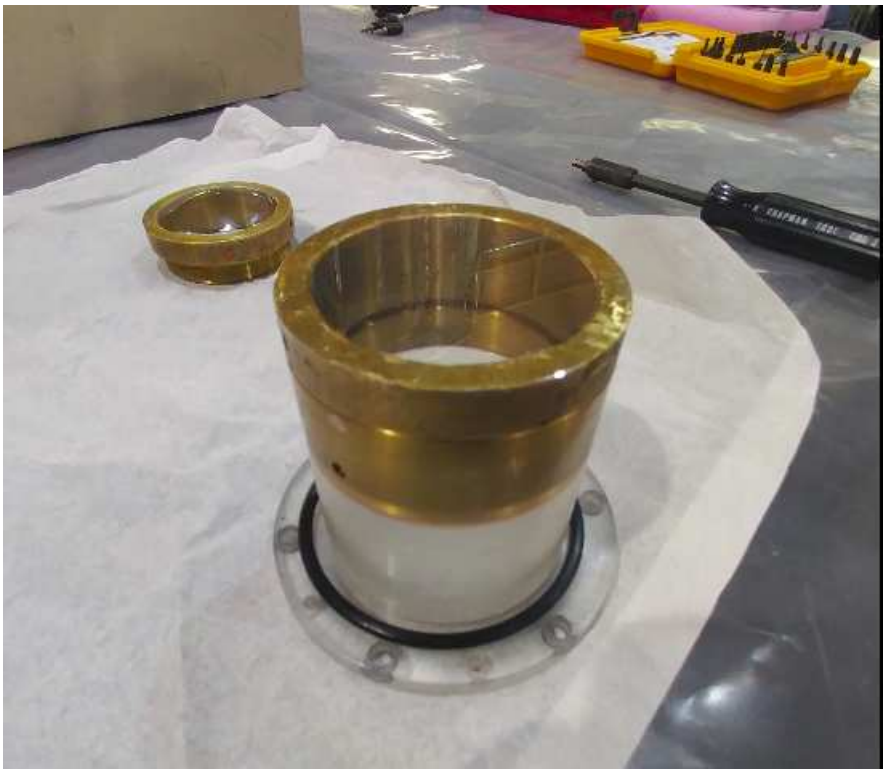

Figure 3.10: Image of the IC window before installation into the hybrid detector.

CHAPTER 4

ANALYSIS METHODS

This next chapter will focus on the methods of analysis used during the course of this work. During the ^{34}S(p,γ)^{35}Cl measurements, which will be referred to from now on as S1686, 8 potential resonances were measured from center of mass energies 272 keV to 495 keV. For the ^{21}Ne(p,γ)^{22}Na measurement, which will now be referred to as S1363, the E_{CM}=258.6 keV resonance was measured with several yield measurements with varying parameters in order to confirm or deny a discrepancy from a previous commissioning calibration measurement.

4.1 Yield

The primary quantity measured during radiative capture reactions is what is known as the yield and is defined as,

$$Y = \frac{N_{rxn}}{N_b}. \tag{4.1}$$

Where Y is the yield, N_{rxn} is the number of reactions that occurred, and N_b is the number of incoming beam particles. Experiments at DRAGON measure the number of recoils detected in the heavy ion detectors and using the efficiencies and transmissions associated with the given kinematics, the original number of reactions that occurred in the gas target can be determined. This can be represented as,

$$Y = \frac{N_{rec}}{\eta_{rec} N_b}. \tag{4.2}$$

Where η_{rec} is the combined efficiency and transmission and N_{rec} is the number of detected recoils. We now need to relate the yield to the desired quantity, the resonance strength. Consider a beam with incoming energy, E_b, which is incident on a target with thickness Δx. The thickness can be divided into slices labeled Δx_i, over which the stopping power, ϵ_i, and cross section, σ_i, are constant. The yield can then be rewritten as,

$$\Delta Y_i = \frac{N_{rxn,i}}{N_{b,i}} = \frac{\sigma_i N_{t,i}}{A} = \sigma_i N_i \Delta x_i. \tag{4.3}$$

If we want the yield across the total length of the target we can integrate over that length,

$$Y(E_o) = \int_{\Delta x} dx N(x)\sigma(x). \tag{4.4}$$

In the above integral we have assumed that the number density, N, is constant over the width of the target. If we consider the expression for the stopping power for a target with number density N, we can express the yield in terms of the energy,

$$S_N(E) = -\frac{1}{N}\frac{dE}{dx} = -\epsilon(E) \tag{4.5}$$

Assuming that the beam particle only loses a small amount of its total energy, then we can express the target width Δx as,

$$\Delta x = \int_{E_o - \Delta E}^{E_o} \frac{dE}{dE/dx} = \frac{\Delta E}{(dE/dx)_{E_o}}, \tag{4.6}$$

where ΔE is the total energy loss across the target. In the third expression we have made the assumption that the stopping power remains constant over the width of the target. Then multiply the expression by N/N and rearrange to yield,

$$N\Delta x = \frac{\Delta E}{(\frac{1}{N}\frac{dE}{dx})_{E_o}} = \frac{\Delta E}{\epsilon}. \tag{4.7}$$

This can then be inserted into the earlier equation for the experimental yield,

$$Y(E_o) = \int_{\Delta x} dx N\sigma(x)\frac{dE}{dx}\frac{1}{dE/dx} = \int_{E_o - \Delta E}^{E_o} dE\frac{\sigma(E)}{\epsilon(E)}. \tag{4.8}$$

4.1.1 Resonant Yield

If we take the previous results for the yield and utilize the one-level Breit-Wigner formula for narrow isolated resonances we can rearrange to give,

$$Y(E_o) = \int_{\Delta x} dE\frac{1}{\epsilon(E)}\frac{\lambda^2}{4\pi}\frac{(2J+1)(\delta_{01}+1)}{(2j_0+1)(2j_1+1)}\frac{\Gamma_a\Gamma_b}{(E_r-E)^2+\frac{\Gamma^2}{4}}. \tag{4.9}$$

If we consider the width of the resonance Γ relative to the width of the target and $\Gamma << \Delta$E and the parameters Γ_a, Γ_b, λ and ϵ have only a small energy dependence over the width of

the target then we can replace them with their values at E_o.

$$Y(E_o) = \frac{\lambda_r^2}{2\pi}\omega\gamma\frac{m_p + m_t}{m_t}\frac{1}{\epsilon_r}\frac{\Gamma}{2}\int_{E_o-\Delta E}^{E_o}\frac{dE}{(E_r - E)^2 + \frac{\Gamma^2}{4}} \tag{4.10}$$

The factor $\frac{m_p+m_t}{m_t}$ is introduced because the stopping power is typically measured in the lab frame of reference and the desired resonance strength is in the center of mass frame. The integral resembles Equation 2.74 and can then be integrated similarly but with different integral limits, resulting in,

$$Y(E_o) = \frac{\lambda_r^2}{2\pi}\omega\gamma\frac{m_p + m_t}{m_t}\frac{1}{\epsilon_r}\big[\tan^{-1}\Big(\frac{E_o - E_r}{\Gamma/2}\Big) - \tan^{-1}\Big(\frac{E_o - E_r - \Delta E}{\Gamma/2}\Big)\big]. \tag{4.11}$$

The above equation is at its maximum when,

$$\frac{d}{dE_o}\big[\tan^{-1}\Big(\frac{E_o - E_r}{\Gamma/2}\Big) - \tan^{-1}\Big(\frac{E_o - E_r - \Delta E}{\Gamma/2}\Big)\big] = 0 \tag{4.12}$$

$$\frac{2/\Gamma}{1 + (\frac{E_o - E_r}{\Gamma/2})^2}\frac{2/\Gamma}{1 + (\frac{E_o - E_r - \Delta E}{\Gamma/2})^2} = 0 \tag{4.13}$$

$$\Big(\frac{E_o - E_r}{\Gamma/2}\Big)^2 - \Big(\frac{E_o - E_r - \Delta E}{\Gamma/2}\Big)^2 = 0 \tag{4.14}$$

$$(E_o - E_r)^2 - (E_o - E_r - \Delta E)^2 = 0 \tag{4.15}$$

$$\big[(E_o - E_r) - (E_0 - E_r - \Delta E)\big]\big[(E_o - E_r) + (E_0 - E_r - \Delta E)\big] = 0. \tag{4.16}$$

The portion in the first set of square brackets gives a trivial solution of $\Delta E = 0$ and the second portion gives a non-trivial solution,

$$E_o^{max} = E_r + \frac{\Delta E}{2}. \tag{4.17}$$

Which can be reinserted back into the equation.

$$Y_{max} = \frac{\lambda^2}{2}\omega\gamma\frac{m_p + m_t}{m_t}\tan^{-1}\Big(\frac{\Delta E}{\Gamma}\Big) \tag{4.18}$$

We can then take the limit as $\Delta E >> \Gamma$ which results in the thick target yield for a narrow Breit-Wigner resonance [54],

$$Y_\infty = \frac{\lambda_r^2}{2}\omega\gamma\frac{m_p + m_t}{m_t}, \tag{4.19}$$

where $\omega\gamma$ is the resonance strength and λ_r is the center of mass de Broglie wavelength. If we solve for $\omega\gamma$ we have the expression for the center of mass resonance strength,

$$\omega\gamma = 2\frac{Y_\infty}{\lambda_r^2}\epsilon_r\frac{m_t}{m_p + m_t}. \tag{4.20}$$

4.2 Beam Normalization

To determine the number of beam particles incident on the gas target, we have to normalize out any fluctuations of beam intensity that may have occurred during the run. This is done using the silicon detectors or surface barrier detectors (SB), located inside of the gas target, described previously in the Experimental Setup section, to detect elastically scattered protons. The rate of scattered protons is directly proportional to the incoming beam intensity and by comparing to the beam intensities of Faraday Cup readings done before and after the 1 hour run, the beam intensity during the run can be determined. This is done by calculating the beam normalization coefficient R, which is defined as,

$$R = \frac{I}{qe}\frac{\Delta t}{N_p}\epsilon_{tgt}, \tag{4.21}$$

where N_p is the number of scattered protons in the surface barrier detector energy peak, Δt is the time window chosen, 120 seconds in this case, q is the beam charge, e is the elementary charge, and ϵ_{tgt} is the target transmission. The R coefficient is calculated for each run of a given yield set, see Figure 4.1, and an average for the entire yield measurement, $\overline{R}$, is then calculated and the total number of incoming beam particles, N_b, can be calculated using,

$$N_b = \overline{R}N_p. \tag{4.22}$$

This is generally done separately for both of the silicon detectors in the gas target due to different collomator settings, angles, and path lengths, which usually provides a redundancy in the determination of the number of particles on target. During the course of the S1686 experiment, it was seen that the second detector, SB1, was detecting significantly less scat-

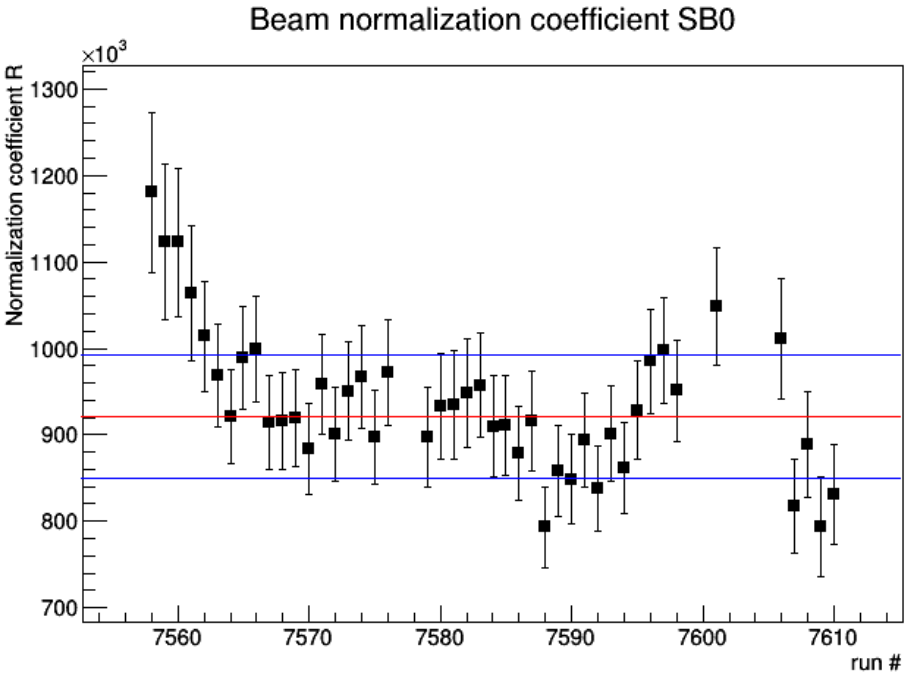

Figure 4.1: Beam normalization coefficient from SB0 for all 272 keV runs. The red line is the weighted arithmetic mean and the blue line is the associated error in the mean.

tered protons, likely due to the threshold settings of that individual detector. As a result, this detector had very little statistics and provided a poor estimation of the number of beam particles on target and was excluded from analysis. The resulting number of particles per run determined using SB0 can be seen in the Figure 4.2

This analysis incurs error in $\overline{R}$, which will be added in quadrature, of $\sqrt{N_p}$, statistical error of 2-3% due to current fluctuations, 3% systematic error in current measurements, and an average of 2% in target transmission due to fluctuations in beam position. For a given function, $F(x_i)$, the associated error can be found by adding in quadrature using,

$$\Delta F(x_i) = \sqrt{\Sigma_i^n \Big(\frac{dF(x_i)}{dx_i}\Big)^2 \Delta x_i^2}. \tag{4.23}$$

After calculating the R coefficients for each run an average is found by using a weighted arithmetic mean found by,

$$\overline{R} = \frac{\Sigma_i^n (\sigma_i^{-2} R_i)}{\Sigma_i^n \sigma^{-2}}, \tag{4.24}$$

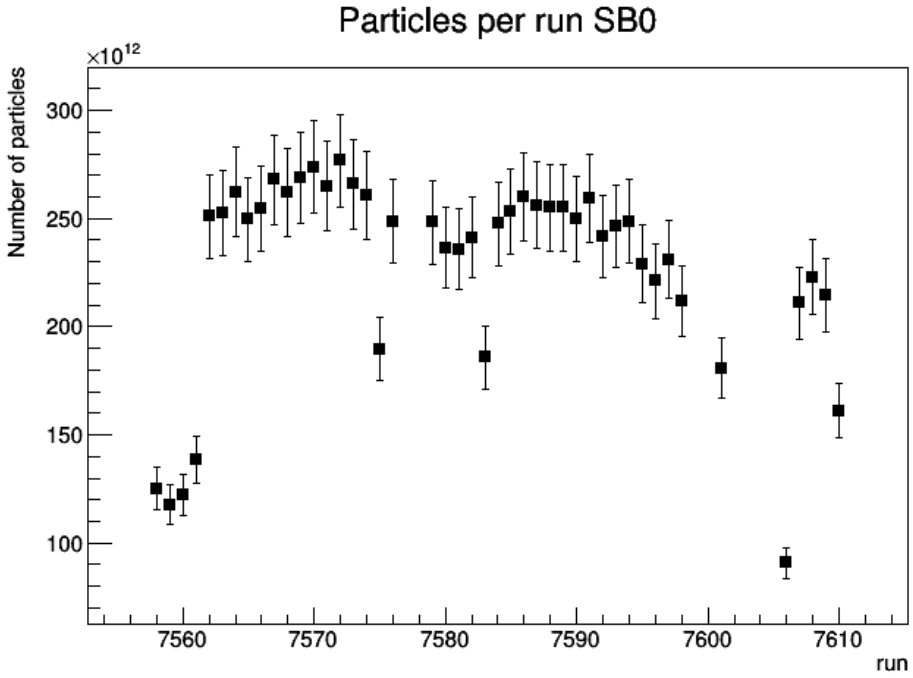

Figure 4.2: Particles per run from SB0 for all 272 keV runs. Most variations in particles per run are due to run length.

where i iterates from 1 to n, which is the number of runs, and σ_i is the error for each run. The associated error in that mean is found by [55],

$$\sigma_{\overline{R}} = \sqrt{\frac{n}{n-1}\frac{\Sigma_i^n \frac{1}{\sigma_i^2}(R_i - \overline{R})}{\Sigma_i^n \sigma_i^{-2}}} \tag{4.25}$$

The magnitude of the error in $\overline{R}$, and the resulting N_b, depends on the number of runs, the statistics available for the calculations, and variations between individual beam normalization coefficients, but typically is about 5%.

4.3 Stopping Power

Stopping power is calculated using the beam energy before and after the gas target. The energy is measured with the charge selecting magnetic dipole and is done so by centering the beam after a 50° bend on the charge slits. The centering is done by changing the magnetic field strength of the magnetic dipole until equal currents are read on each side of the slits

and the energy can be calculated using,

$$E_b = c_{mag}\left(\frac{qB}{m}\right)^2, \tag{4.26}$$

where E_b is the beam energy in keV/u, q is the beam charge or charge state of interest if the target contains gas, B is the magnetic field strength in Gauss, m is the beam mass in amu, and c_{mag} is the magnetic constant of the bending magnet. This was calculated theoretically and confirmed through calibration measurements to be 0.0004815 keV*amu/G^2. The calibration measurements will be discussed more in Section 4.8. The incoming beam energy is measured by removing the gas from the target and then centering the beam on the charge slits. By adding enough gas to the target to cause a noticeable energy loss, ΔE in units of keV/u, the stopping bower can be calculated. This process is outlined more thoroughly in [56]. The stopping power can be calculated using the formula,

$$S(E) = \frac{\Delta E}{\Delta A} m_b 10^{18}, \tag{4.27}$$

where S(E) is the stopping power in $\frac{\text{eV}}{(10^{15}/\text{cm}^2)}$, ΔA is the change in area target density between measurements, and m_b is the beam mass in amu. A can be found using,

$$A = 9.66 * 10^{18} \nu \frac{P}{T * l}, \tag{4.28}$$

where ν is the gas type, 2 for diatomic, T is the temperature in K and l is the target length in cm. The stopping power can also be calculated by linearly fitting the energy vs area target density for various values of target pressure with a straight line. The slope from this fit is then the stopping power in $\frac{\text{keV}}{(10^{15}/\text{cm}^2)}$. The result is in keV only because the energy used in the fit was in keV instead of eV. An example of this method can be seen in Figure 4.3. For the 3 most important resonance measurements, 495 keV, 272 keV, and 407 keV several different pressures were measured to improve the quality of the fit. This incurs error in the stopping power from the energy measurements of 0.254% as discussed in the Theory section, T of 2.5 K or about 1%, P of 0.5% in statistical uncertainty and 1% systematic uncertainty, and l of 0.4 cm [57]. This gives about 5% error when added in quadrature, in the stopping

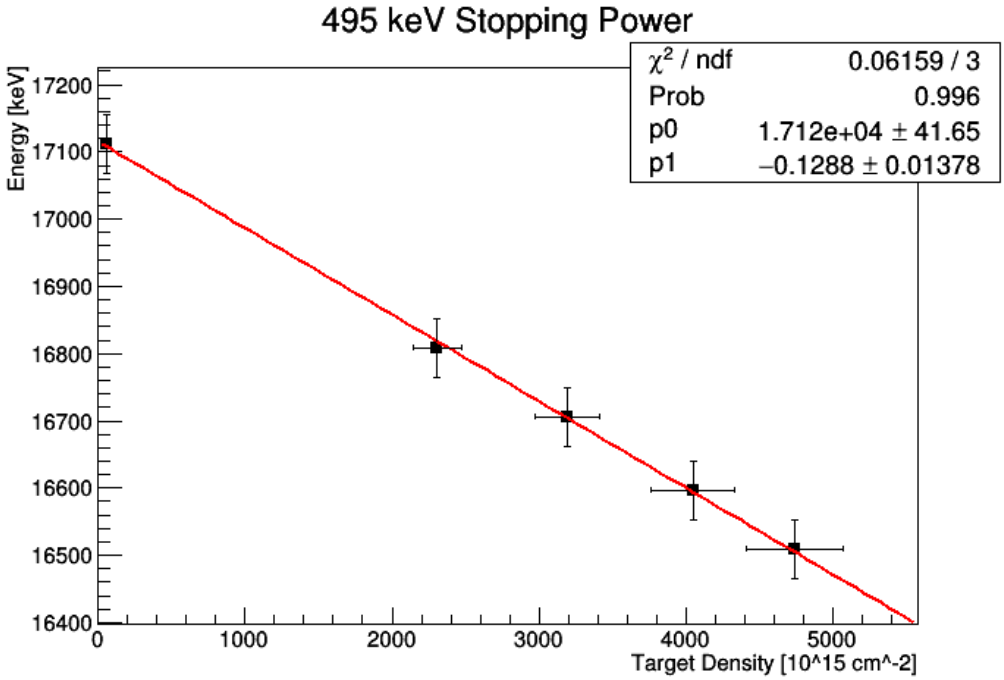

Figure 4.3: Plot of fit to determine the stopping power. The slope is the stopping power in keV/(10^{15}/cm^2).

power and can be seen to deviate from the values calculated with the code Stopping Range of Ions in Matter (SRIM) [58] significantly. These values can be seen, along with the calculated values, in the Table 4.1. SRIM typically agrees within about 5% of the measured values of the stopping power but close to the stopping power maximum these values can deviate by up to 10-15% [57]. For the measurements done during this work, the average deviation from the SRIM value was 23%, which is larger than expected. The direct measurement of these stopping powers could be the focus of a future measurement to reduce the uncertainty caused by using a semi-empirical code, such as SRIM, for sulfur in hydrogen gas.

4.4 Recoil Detection Efficiency

As was mentioned previously, DRAGON only detects what are known as recoils, i.e. the reaction products that make it to and are properly detected by the tail end heavy ion detectors. In order to calculate the total number of reactions that occurred, the efficiency and transmission of each component must be taken into account. Analysis can be done in two

Table 4.1: Stopping power measurements for all measured energies for S1686. Stopping power is in units of $[eV/(10^{15}/\mathrm{cm}^2)]$.

S1686 Stopping Power ^{34}S in H_2					
$E_{CM,rxn}$ [keV]	$E_{lab,rxn}$ [keV/u]	$E_{in,lab}$ [keV/u]	$E_{out,lab}$ [keV/u]	S(E)	SRIM
495.5	505.7	518.6	499.6	128.8(130)	166.8
272	277.9	287.3	271.7	106.5(87)	138.3
390	398.5	409.7	392.7	125.1(117)	159.2
407	415.8	426.7	410.1	115.6(120)	160.8
303	309.6	318.7	303.2	114.4(95)	145.4
452	461.8	472.5	454.8	122.4(126)	164.5
471	481.2	492.5	473.6	133.2(134)	165.6
431	440.3	451.6	435.1	113.8(119)	162.9

ways, namely singles or coincidence, which can provide means to compare the results of each individual analysis. Singles analysis uses all recoils detected by the tail end detectors and does not rely on the BGO array, while coincidence analysis is done using only the recoils that had an associated gamma ray detected within a preset time window of the recoil detection. This requires the knowledge of the BGO array total efficiency but allows for better particle identification as a new method of particle discrimination can be introduced, specifically the separator time of flight. The leaky beam background has also been severely reduced as only leaky beam events that accidentally coincided with a background gamma detection are included and because these events are uncorrelated, the background is expected to be constant. During the course of the measurements for S1686, the MCP detectors were not functioning properly and the MCP time of flight parameter could not be used for particle identification. As a result, in order to properly identify the recoils, the separator time of flight parameter had to be used and therefore singles analysis could not be done. The coincident efficiency for this experiment is as follows,

$$\eta_{coin} = \eta_{BGO}\ \eta_{CSF}\ \eta_{sep}\ \eta_{MCP}^{trans}\ \eta_{live,c}\ \eta_{H}. \tag{4.29}$$

Where η_{BGO} is the BGO detection efficiency, η_{CSF} is the fraction of recoils in the charge state selected, η_{MCP}^{trans} is the geometric transmission through the MCP frame, η_{sep} is the

separator transmission or the percentage of recoils that make it through the separating stages of DRAGON, $\eta_{live,c}$ is the live time percentage for the DAQ (Data Acquisition system), and η_H is the efficiency of the hybrid detector. The overall detection efficiency can then be put into the equation for coincident yield to give,

$$Y_{coinc} = \frac{N_c}{N_b\ \eta_{BGO}\ \eta_{CSF}\ \eta_{Sep}\ \eta_{MCP}^{trans}\ \eta_{live,c}\ \eta_H}, \tag{4.30}$$

where N_c is the number of detected coincidence recoils. Most efficiencies can be directly calculated or measured for DRAGON, except the BGO efficiency, which requires the use of a GEANT3 simulation of DRAGON, which will be discussed in the next section.

The separator transmission, η_{Sep}, is determined by the recoil cone angle and the location of the resonance within the gas target. DRAGON has an angular acceptance of $\pm$20 mRad. For the S1686 measurements the largest cone angle is 8.60 mRad which is well within the angular acceptance of DRAGON and the canonical value of the transmission $\eta_{Sep} = 0.999(1)$ was used for this analysis.

The DAQ dead time is different for each run of the experiment and can be found by taking the ratio of the sum of the busy times for the coincident electronics to the total runtime. The live time can then be found by subtracting the dead time from 1. The error in this value is determined by the statistics available and is typically less than 1%.

Even though the hybrid detector provided only minimal particle identification, we still have to determine its efficiency to calculate the total yield because the hybrid was used in combination with the BGO array to produce the global TOF or separator TOF. This is done by comparing the number of valid events in the IC portion of the detector to the number of valid events that fall in both the IC and the DSSSD portions of the hybrid. This is because the ionization chamber has approximately 100% detection efficiency and will have detected nearly every recoil that interacts with the detector. The resulting hybrid efficiency is reliant primarily on the DSSSD efficiency. To solve for the hybrid efficiency, consider the total efficiencies of events detected by the IC and the DSSSD.

$$N_{rxn} = \frac{N_{IC}}{\eta_{BGO}\ \eta_{CSF}\ \eta_{Sep}\ \eta_{MCP}^{trans}\ \eta_{live,c}\ \eta_{IC}} \tag{4.31}$$

$$N_{rxn} = \frac{N_{DSSSD}}{\eta_{BGO}\ \eta_{CSF}\ \eta_{Sep}\ \eta_{MCP}^{trans}\ \eta_{live,c}\ \eta_{DSSSD}} \tag{4.32}$$

When η_{IC} is set to 1 and η_{DSSSD} is set to η_H the two equations can be set equal and rearranged to yield the hybrid efficiency.

$$\eta_H = \frac{N_{DSSSD}}{N_{IC}} \tag{4.33}$$

Each of the values N_{IC} and N_{DSSSD} are determined from examining the peaks in Figure 4.4 and Figure 4.5. All counts within the range of bins 231 and 454 were summed for the N_{DSSSD} value and all counts in the range of bins 1669 and 2692 were summed for the N_{IC} value. These ranges roughly encapsulate the entirety of the peaks but vary for each beam energy. The efficiency for the hybrid detector was calculated separately for each energy and the average efficiency was calculated to be 0.897(43).

Also of importance is determining the MCP transmission which can be done by comparing the results of attenuated beam runs with and without the MCPs in the beam line. These two runs were performed at each energy after the recoil runs had been completed and were done right after one another to minimize the effect from beam fluctuations. Taking into account the relative efficiencies and runtimes the MCP transmission can be found as follows,

$$\eta_{MCP,trans} = \frac{N_{in}}{N_{out}} \frac{T_{out}\eta_{live}^{out}}{T_{in}\eta_{live}^{in}}. \tag{4.34}$$

Where N refers to the number of valid counts in the respective peaks and the subscripts in and out refer to the position of the MCP detectors relative to the beam line. The measured MCP transmission for this experiment was 0.766(9), which agrees very nicely with the previously measured value for the transmission of 0.769(6) [46]. A table of the individual efficiencies for each set of recoil runs can be seen below in Table 4.2. It should be noted that η_{coinc} is the total coincident detection efficiency and includes the BGO efficiency and charge state fraction which will be discussed in the remainder of this chapter.

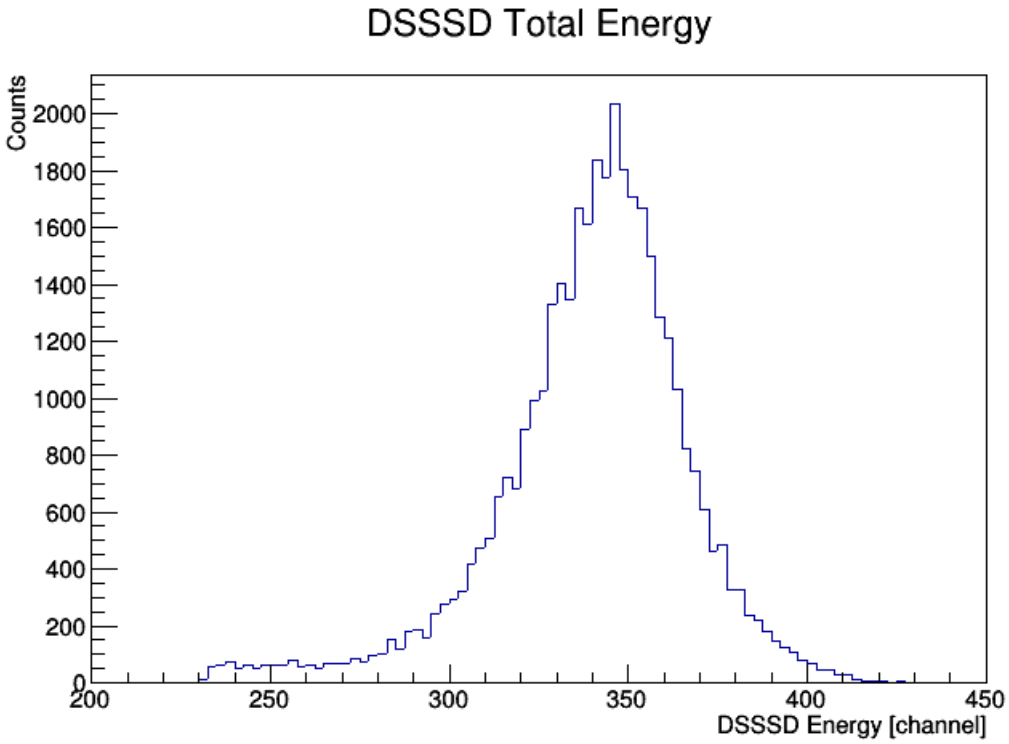

Figure 4.4: DSSSD plot used to determine hybrid efficiency. All counts between bins 231 and 454 were summed to calculate the hybrid efficiency.

Table 4.2: Total efficiencies for S1686

E_{CM} [keV]	τ_{tgt}	$\eta_{live,c}$	η_H	η_{coinc}
495.5	0.940(18)	0.745(7)	0.900(7)	0.118(22)
272	0.914(3)	0.745(7)	0.890(6)	0.155(36)
390	0.907(19)	0.746(5)	0.897(22)	0.153(74)
407	0.927(13)	0.827(4)	0.949(44)	0.168(34)
303	0.921(14)	0.735(11)	0.904(10)	0.141(53)
452	0.950(12)	0.735(10)	0.946(44)	0.078(57)
471	0.926(17)	0.740(23)	0.882(55)	0.091(24)
431	0.943(21)	0.757(14)	0.833(70)	0.055(44)

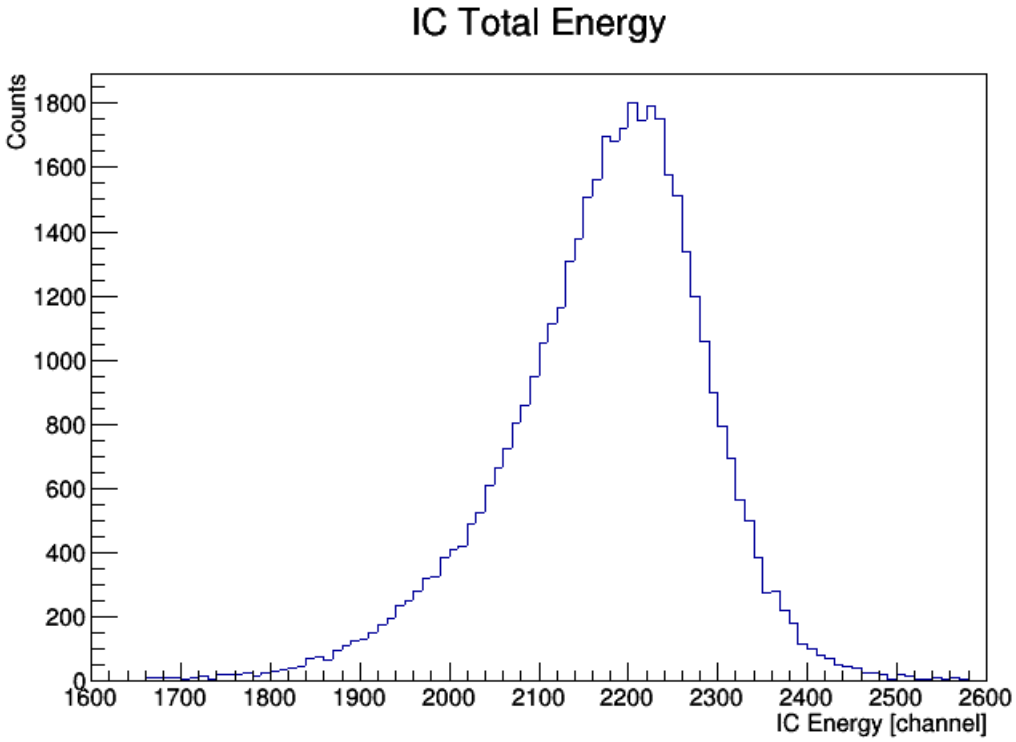

Figure 4.5: IC plot used to determine hybrid efficiency. All counts between bins 1669 and 2692 were summed to calculate the hybrid efficiency.

4.5 BGO Simulation

For this experiment the BGO efficiency could not be experimentally determined in the usual manner of comparing the number of coincident events to the number of singles events because we were unable to do singles analysis. The BGO efficiency was therefore calculated using a GEANT3 simulation of DRAGON, which required an input file for the specific reaction detailing the branching ratio for the excited state of the recoil. Since many of the states examined had no experimental branching ratios, two simulations had to be done to determine the range of possible efficiencies.

The first was the lower limit and was done by assuming 100% transmission directly to the ground state and the second was the upper limit which assumed 100% transmission through a 3 gamma decay to spin and parity allowed states all with gamma energies over 1.5 MeV. The resulting BGO efficiency was the average of these two simulations. The expected

error for each simulation was found by using the total range of the upper and lower limit simulations and came to be 17.5% on average. An experimental branching ratio and decay scheme was found for the 495 keV state [2] after completing the initial BGO simulations and another simulation, using this new information, was performed and the results agree within error of the result of the previous method of simulating the BGO efficiency. For the 495 keV state, the error in the BGO efficiency was taken to be 10%, which is the expected upper limit for the error in the direct simulations. A table of the resulting simulated BGO efficiencies can be seen in Table 4.3.

Table 4.3: BGO simulation results for the S1686 experiment

Simulated BGO Efficiencies			
E_{CM} [keV]	$\eta_{BGO,up}$ [%]	$\eta_{BGO,low}$ [%]	η_{BGO} [%]
495.5	88.1	61.6	73.6(74)
272	88.0	62.0	75.0(130)
390	88.6	63.2	76.0(127)
407	88.2	61.0	75.0(136)
303	87.3	62.3	75.0(125)
452	88.1	62.3	75.0(129)
471	88.3	61.9	75.0(132)
431	88.6	61.5	75.0(136)

4.6 Charge State Distributions

As previously mentioned, the separating stages of DRAGON allow only one charge state to pass through to the end detectors and as the singly charged beam passes through the gas target a series of charge changing reactions occur, which leave the outgoing beam and recoils in a distribution of charge states. This distribution cannot currently be exactly calculated theoretically due to the complexity of these reactions and must either be directly measured or estimated using a semi-empirical formula such as the one developed by Liu et al. [59, 60]. Other semi-empirical methods of determining the charge state distribution can be found in [61–64]. The setup of DRAGON allows the charge state distribution (CSD) to be directly

measured. This entails receiving a beam of the recoil element, for the $^{34}S(p,\gamma)^{35}Cl$ reaction this would be Cl, and passing it through a gas target which leaves the outgoing beam energy equal to the outgoing beam energy of the recoils created during the actual experiment. As the beam leaves the gas target it has reached an equilibrium charge state distribution and by selecting a single charge state with the first magnetic dipole (MD1), the beam currents before and after the gas target can be compared. This allows the charge state fraction to be measured and by repeating over all measurable charge states a full distribution can be found. This was done after the experiment was conducted so an approximate charge state fraction was needed to estimate the most populated recoil charge state during the experiment. For this, the semi-empirical formula developed by Liu et al. was used. Liu's formula is based on a Gaussian with its center at $\overline{q}$,

$$\overline{q} = Z_p\Big(1 - \mathrm{Exp}[-\frac{A}{Z_p^{\gamma}}\sqrt{\frac{E}{E'}} + B]\Big) \tag{4.35}$$

and standard deviation,

$$d = d_1 Z_p^w. \tag{4.36}$$

Where Z_p is the projectile charge, E is the energy in MeV/u, and E' is a reduced expression for the electron velocity but is equal to 0.067635 MeV/u. The parameters γ, A and B are the best fit parameters from a series of direct measurements which for a hydrogen target are equal to γ=0.44515, A=1.4211 and B=0.4495. For a helium target, these parameters are equal to γ=0.44515, A=1.1326 and B=0.3449. This formula is not completely accurate but provides a good approximation when experimental data is not available and generally provides error less than that of our other sources. Liu's formula does not have an associated error but for these charge state fractions the error is expected to be around 10%. An example CSD can be seen in Figure 4.6.

In a follow-up beam time the Cl in hydrogen gas CSD was measured for the 495.5, 407, and 272 keV recoils as these were the states with the highest impact on the astrophysical

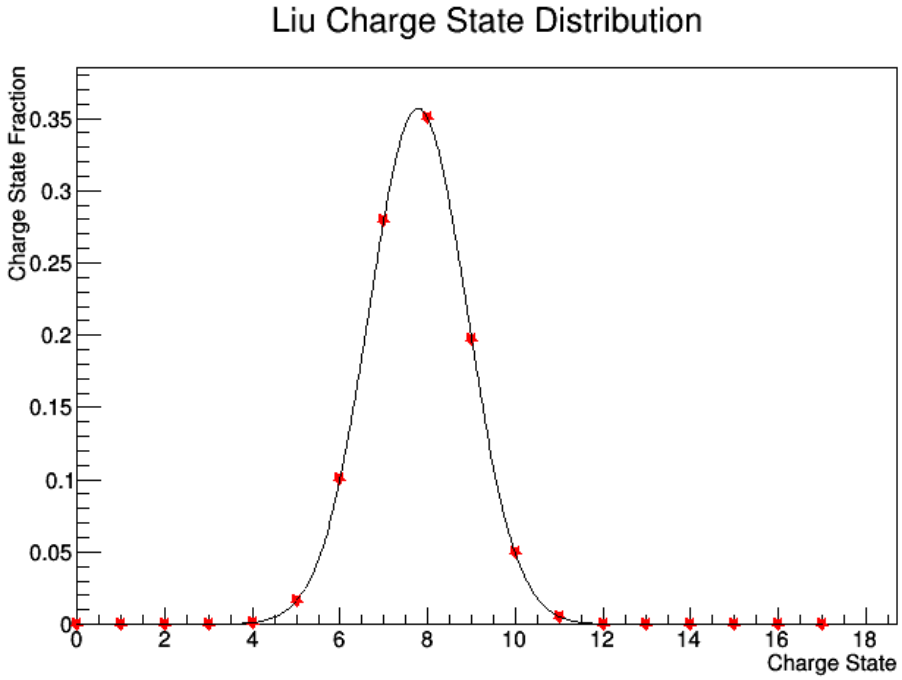

Figure 4.6: Results from Liu's semi-empirical CSD formula for Cl+H_2 at 471 keV/u.

reaction rate. The results compared to Liu's semi-empirical formula can be seen in Figure 4.7 for each energy, as labeled by the outgoing recoil energy.

Due to differences in the measured recoil stopping power from the values obtained by SRIM, the energies of the measured Cl CSD's are slightly different from the actual recoil energies. To interpolate to the required energies we plotted the mean charge state as a function of energy for the 3 measured Cl CSD's along with 2 other Cl in hydrogen CSD's found from previous DRAGON experiments. We then did a linear fit to interpolate the expected charge state mean as can be seen in Figure 4.8. For the distribution widths we fit the measured distribution widths with a constant line as they appeared roughly equal, see Figure 4.9. Liu's formula also approximates the width as constant for any given atomic charge. These were then used to calculate the charge state distributions for the recoil products and the resulting charge state fractions for the chosen charge state can be seen in Table 4.4.

Liu's semi-empirical formula was established in 2003 and the parameters were fit with limited data. Since then, many CSD's have been measured at DRAGON and the semi-

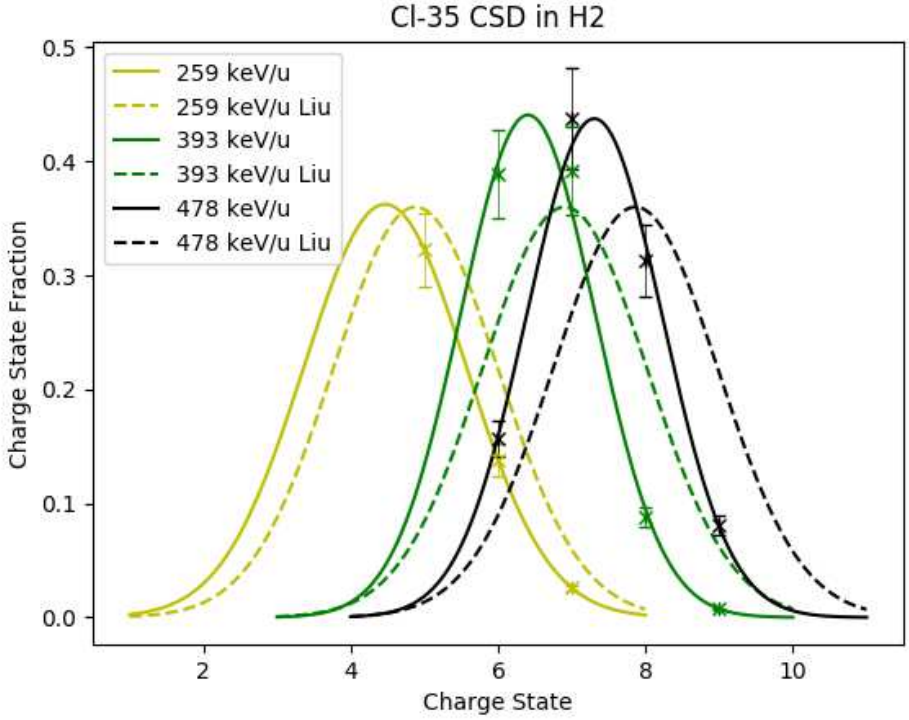

Figure 4.7: Comparison between experimentally measured CSD's (solid lines) and Liu's formula (dashed lines) for Cl+H_2.

Table 4.4: Charge State Fractions used for recoil calculations

E_{CM} [keV]	$E_{out,rec,lab}$ [keV/u]	Charge State	Fraction [%]
495.5	471.4	8	30.7(17)
272	255.3	5	42.7(42)
390	368.4	6	42.9(40)
407	385.8	6	41.0(16)
303	284.0	5	42.4(47)
452	425.9	8	16.9(27)
471	444.2	8	22.3(22)
431	407.7	8	12.3(34)

empirical formula has not been updated. An additional part of this thesis will be to condense and fit the more recently measured CSD's at DRAGON for a set of updated parameters. This will be discussed in the Results section but all listed Liu values before this point were calculated using the original Liu parameters.

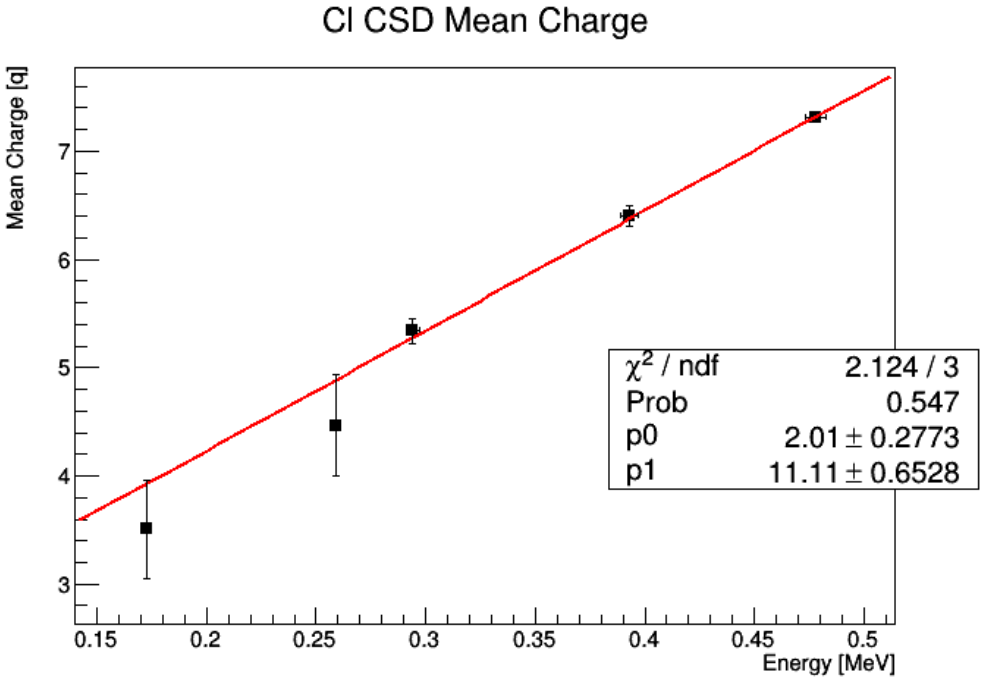

Figure 4.8: Interpolation fit for Cl CSD mean charge in hydrogen.

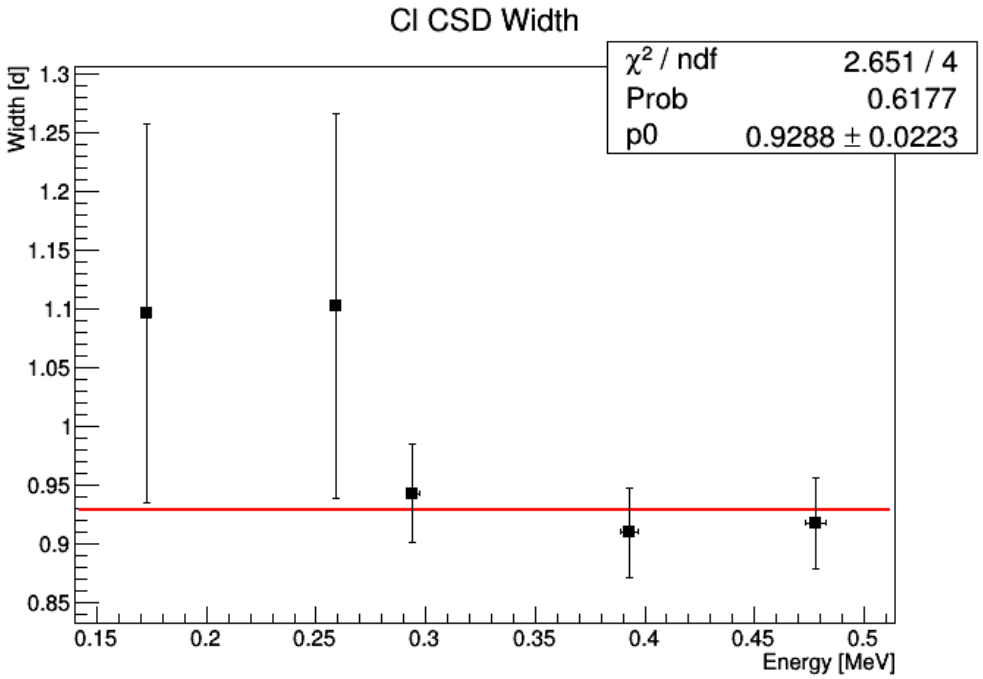

Figure 4.9: Cl CSD experimental distribution widths.

4.7 Particle Identification

For this experiment, particle identification (PID) was done only using coincidence events as the MCPs weren't able to produce a reliable signal and the hybrid detector only provided minimal means of PID. The MCP detectors had an excessive amount of electronic noise which caused the detection efficiency to be below 50% and the coincident efficiency to be less than 1%. There also appeared to be a ringing effect as can be seen in Figure 4.10. The expected MCP TOF for the recoils at this energy is approximately 96 ns but peaks can be seen at 96, 93, 89 and 86. This caused the recoil events to overlap the leaky beam events and meant no PID could be performed using the MCP TOF. This meant PID was done by

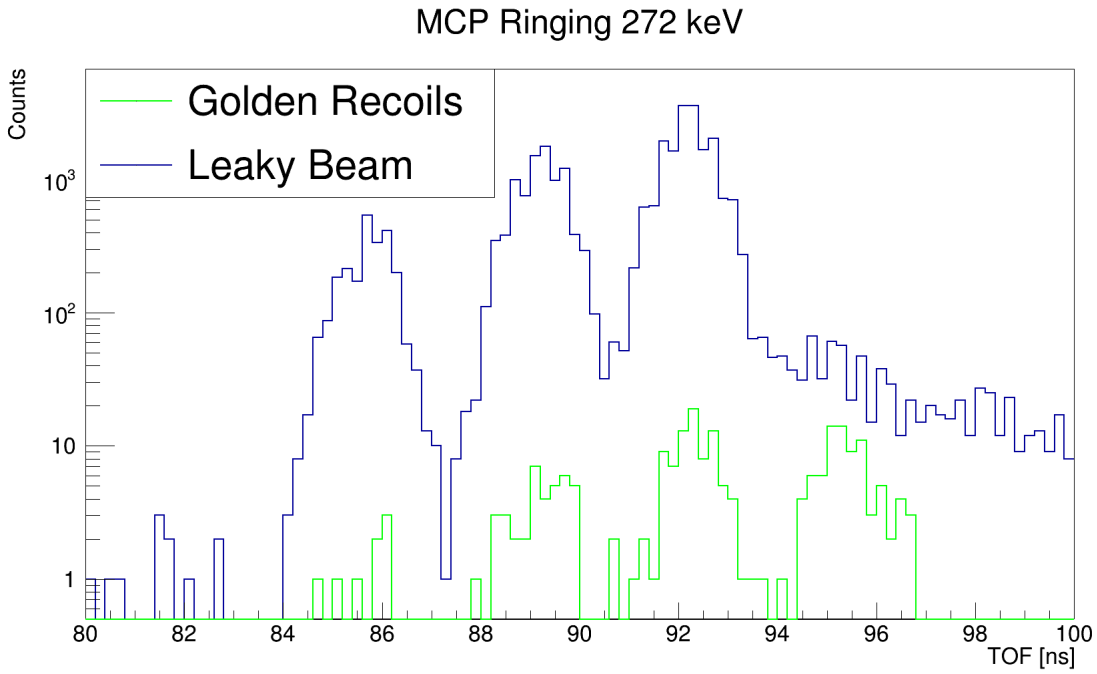

Figure 4.10: Ringing feature in the MCPs seen in both leaky beam(blue) and recoil events(green).

plotting the separator TOF signal which is the amount of time between the detection of a gamma ray in the BGO array and the detection of a heavy ion in the end detectors. This produces a spectrum that can be seen in Figure 4.11, which has three distinct recoil peaks due to the problems with the MCP electronics. The DAQ was left in a setup that triggered

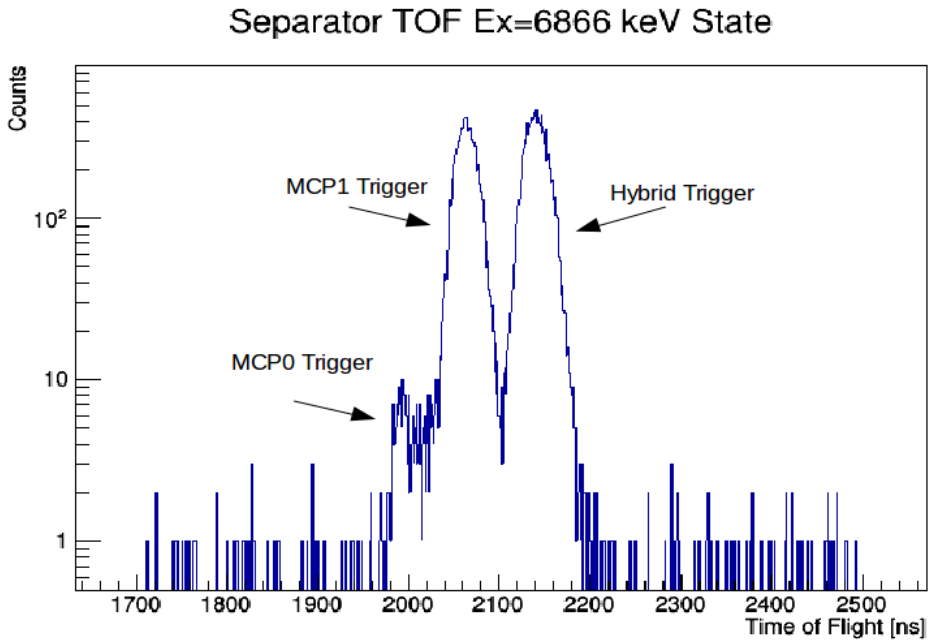

Figure 4.11: Separator TOF plot showing means of PID. The 3 peaks are a result of the electronics setup and correspond to different combinations of the heavy ion detector triggers. The spacing reflects partly the TOF between each component but also electronics and cable delays.

separately for each of the end detectors but did not double or triple count any events. The result was a small peak from MCP0 which was approximately 0.5% of the total counts from events that triggered MCP0 and the hybrid. The first of the larger peaks are from events that triggered MCP1 and the hybrid, and the final peak triggered only the hybrid. The spacing between the peaks is due partly to the TOF between the individual detectors plus delays in electronics and cables. The smallest peak was only visible for the 495 keV resonance as this had the highest statistics and the peak only accounts for 0.5% of the total events. To ensure these events are included for all energies the recoil signal region was extended an additional 50 ns. There is also a constant random background which is caused by the accidental coincidence between a leaky beam particle in the end detector and a gamma from the room background. Since these events are uncorrelated, the resulting background should be constant and easy to account for. Cuts were also placed on the detected gamma ray energy to ensure only events which are energetically possible from the excited state of the

recoil particle are included. A lower energy threshold was also placed to ensure a distinct cutoff existed to determine the BGO efficiency. Cuts were also placed on the hybrid detector energy but only very minimal PID could be done with this detector.

The total recoil number was determined by taking the counts in the separator TOF peak and subtracting a constant background. The background was found for each yield measurement by determining the number of background counts across the entire non-signal region of the separator TOF spectra in segments of 100 bins. This is then fit with a constant value and adjusted for the size of the signal region, see Figure 4.12, resulting in the expected background contribution across the signal region. It should be noted that the binning for the sideband analysis is not equal to the binning in the separator TOF plot.

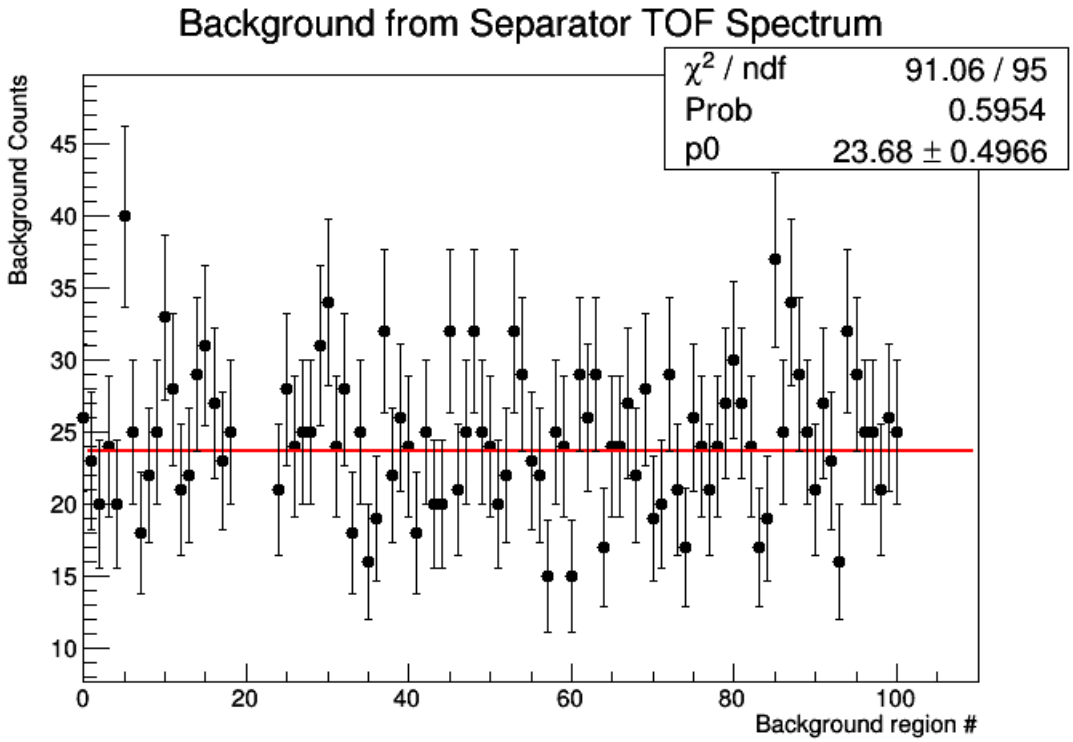

Figure 4.12: Sideband analysis to determine the background contribution in the separator TOF signal region.

During this experiment the hybrid detector was installed which utilizes both the IC and DSSSD heavy ion detectors, in order to take advantage of the DSSSD's superior energy

resolution and the IC's superior charge separation. However, during operation, the hybrid detector offered minimal means of PID, likely because the IC portion generally only provides charge separation when the ion is stopped within the gas volume and the interactions with the gas produced an energy spread that washed out any energy separation that may have been present in the DSSSD spectra.

For recoil runs where there were no definite recoil peaks in the expected signal region of the separator TOF spectra an upper limit of the number of recoils was determined using Bayesian statistics. Since the recoil region could not be visually determined a 200 ns range was taken, with the center calculated using the expected recoil energy from that measurement. Given a result with 0 signal events (recoils) and b background events, the upper limit in the number of counts for a confidence interval of α, s, can be determined by the equation,

$$\alpha = \frac{\Sigma_{r=0}^{s+b} e^{-(s+b)}(s+b)^r/r!}{\Sigma_0^{s+b} e^{-b} b^r/r!}. \tag{4.37}$$

An attempt at singles analysis of the 495 keV state data was done. As can be seen in Figure 4.13, there is a small amount of separation between the coincident recoils and the singles leaky beam in the DSSSD portion of the hybrid. If we just focus on the DSSSD spectra, Figure 4.14, we can see two peaks which can be fit with a double Gaussian. Using the fit to calculate a rough estimate of the singles recoils we get approximately 2×10^5 singles recoil counts. Using our coincident number of approximately 2×10^4 and an expected BGO efficiency of 74% the number of expected singles counts is roughly 2.7×10^4.

This fit overestimates the number of singles recoil counts due to the large amount of background and interference from the leaky beam peak. Normally this background could be taken into account using the MCP TOF as a method of gating but since we've excluded the MCP detectors from analysis we are unable to do singles analysis. For all other energies the separation between the recoils and leaky beam peak in the DSSSD spectra is even less and no PID can be done using the singles data.

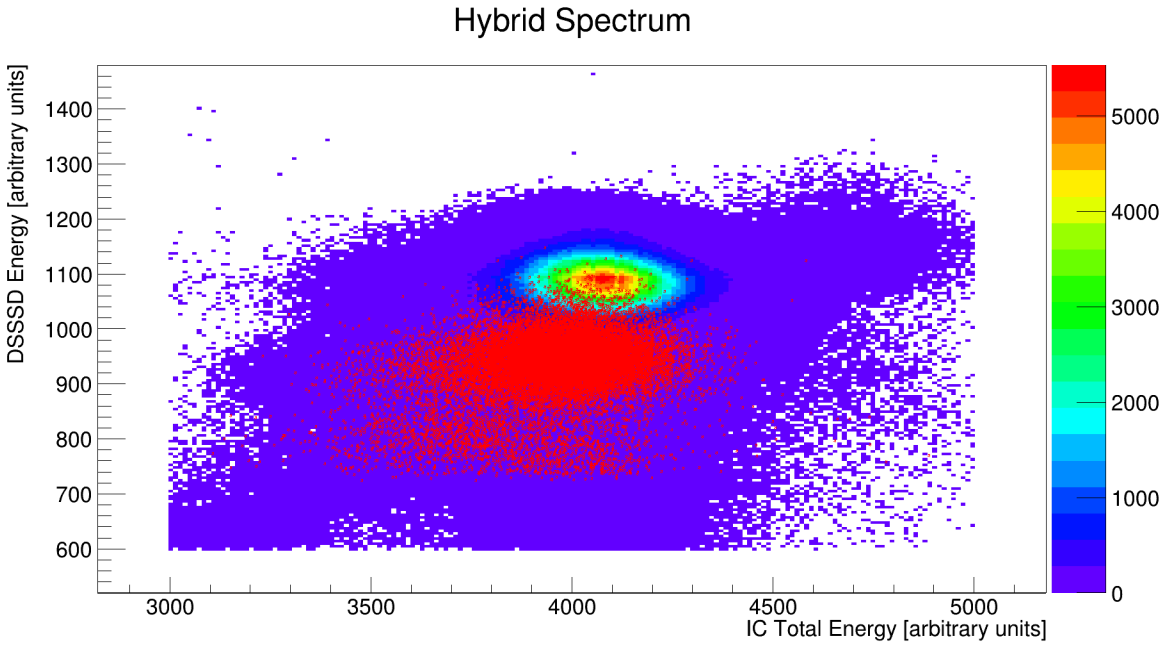

Figure 4.13: Hybrid spectrum with all singles events in color scale and all coincident recoil events in red stars.

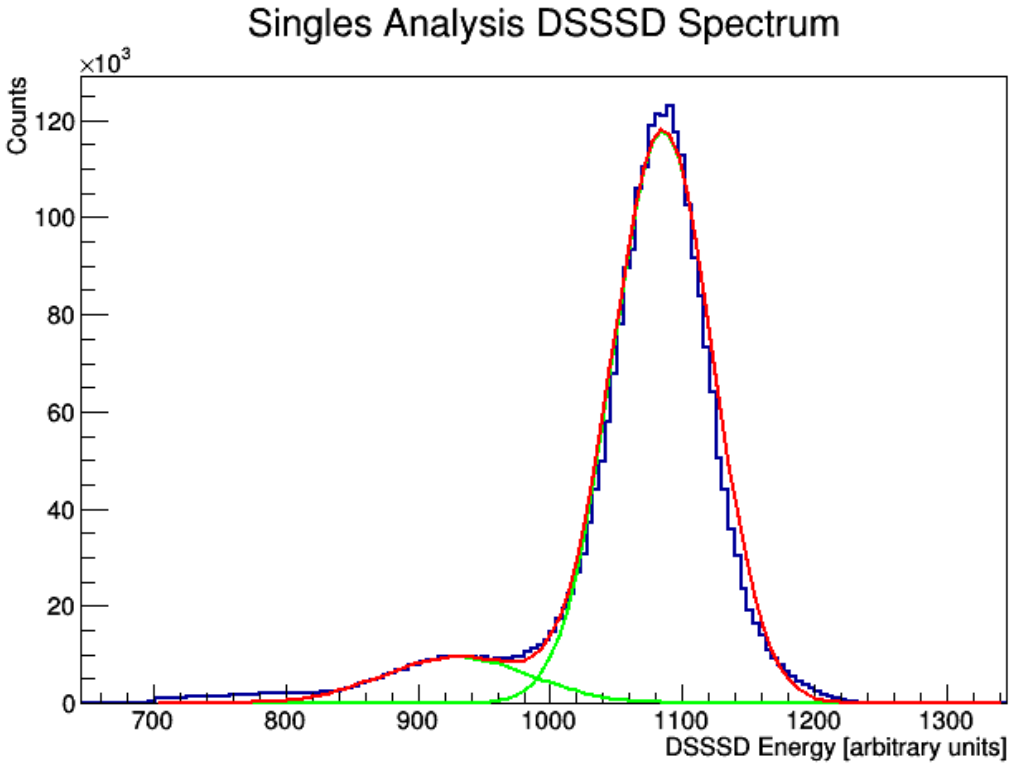

Figure 4.14: DSSSD spectrum for all singles events fit with a double gaussian.

4.8 Calibration Measurement Confirmation

The $^{21}\mathrm{Ne}(p,\gamma)^{22}\mathrm{Na}$ experiment was conducted in 2013 and required slightly different analysis methods due to the variations in experimental setup. During the experiment the MCP detectors were functioning properly which allows analysis to be done in singles and coincidence. Also, only the DSSSD was used as the heavy ion detector and PID was achievable with the DSSSD's energy resolution. The resulting detection efficiencies are,

$$\eta_{coin} = \eta_{BGO}\ \eta_{CSF}\ \eta_{sep}\ \eta_{MCP}^{trans}\ \eta_{MCP}^{det}\ \eta_{live,c} \tag{4.38}$$

$$\eta_{sing} = \eta_{DSSSD}\ \eta_{CSF}\ \eta_{sep}\ \eta_{MCP}^{trans}\ \eta_{MCP}^{det}\ \eta_{live,s} \tag{4.39}$$

where η_{MCP}^{det} is the MCP detection efficiency, and $\eta_{live,s}$ is the singles live time. This allows us to then express the singles and coincident yield for this experiment as,

$$Y_{coinc} = \frac{N_{coinc}}{N_b\ \eta_{BGO}\ \eta_{CSF}\ \eta_{Sep}\ \eta_{MCP}^{det}\ \eta_{MCP}^{trans}\ \eta live, c} \tag{4.40}$$

$$Y_{sing} = \frac{N_{sing}}{N_b\ \eta_{DSSSD}\ \eta_{CSF}\ \eta_{Sep}\ \eta_{MCP}^{det}\ \eta_{MCP}^{trans}\ \eta live, s} \tag{4.41}$$

where N_{sing} is the number of singles recoils. Given that the singles and coincidence yields should be equal we can set the expressions equal and solve for an experimental BGO efficiency,

$$\eta_{BGO}^{exp} = \frac{N_{coinc}}{N_{sing}} \frac{\eta_{DSSSD}\eta_{live,s}}{\eta_{live,c}}. \tag{4.42}$$

Excited states of ^{22}Na have been previously studied in depth and experimental branching ratios were available [13]. This allowed us to simulate the BGO efficiency for this experiment using the GEANT3 simulation of DRAGON and provided a check of the experimental BGO efficiency found during analysis. The GEANT3 simulations resulted in a BGO efficiency of 59.9% and by using Equation 4.42 the experimentally measured BGO efficiency was measured to be 63.2%.

Since the MCP detectors were functioning properly and the heavy ion detector provided a viable means of PID, the analysis methods were slightly different. For singles analysis the

1-D time to amplitude converter (TAC) signal between the two MCP detectors was plotted and two obvious peaks were seen, one from the recoils and one from the leaky beam. Due to the kinematics of these experiments, the recoils have a lower velocity and therefore a larger TAC signal, while the leaky beam has a higher velocity and smaller TAC signal. Further cuts were made on the DSSSD energy spectra to exclude events that did not deposit the full energy due to hitting the detector in between the active portion of the strips. This additional cut then allowed the two peaks in the TAC spectra to be isolated. The MCP TAC spectra can be seen for singles and coincident events in Figure 4.15. It can be seen that enforcing the coincident gate reduces the leaky beam contribution by about two orders of magnitude with minimal effect on the recoil peak, mostly due to the BGO detection efficiency of approximately 60%.

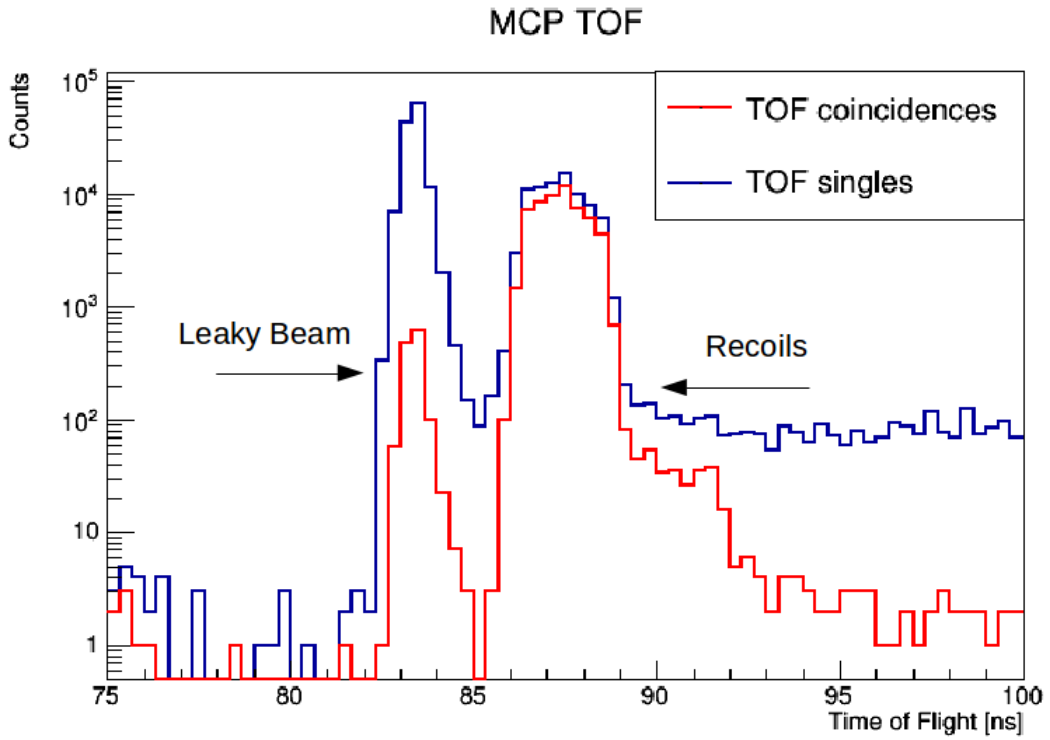

Figure 4.15: MCP TAC for singles and coincident events.

For coincident analysis the 2-D MCP TAC vs separator TOF was plotted and an obvious grouping was seen, see Figure 4.16. A generous gate was made around this grouping in what

is referred to as a golden recoil gate. Leaky beam contamination is also severely diminished as only events that are accidentally in coincidence with the detection of a background gamma ray are included in the coincidence analysis. Cuts were also placed on the DSSSD energy to include only events at the peak energy and gamma ray energy to ensure all included events were energetically possible from the ^{22}Na excited state.

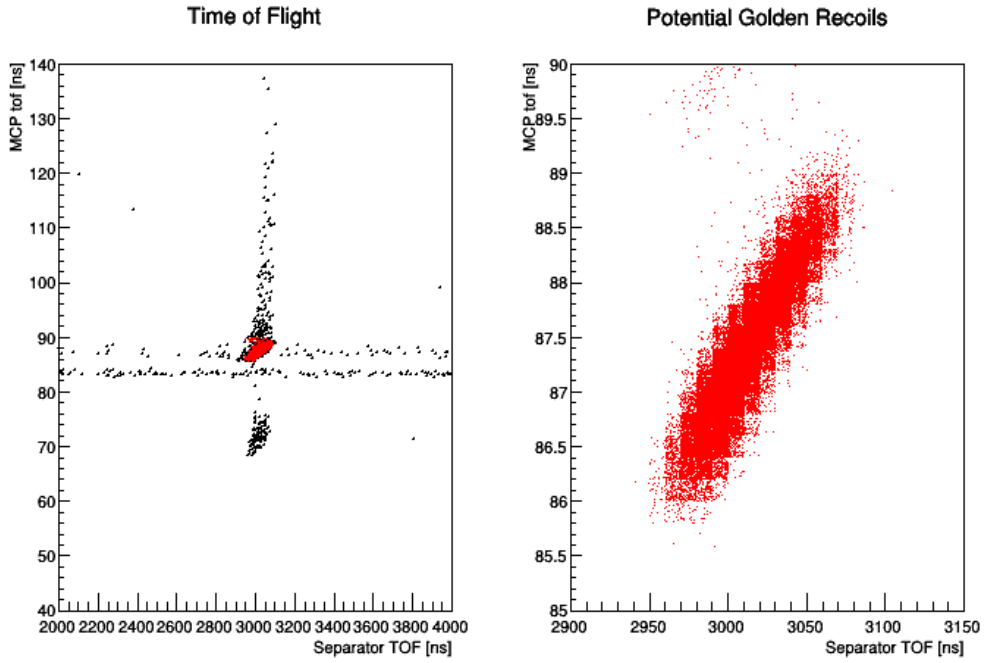

Figure 4.16: Spectrum showing recoil events in "Golden Recoil Gate" in red overtop all events in black.

In order to determine the MCP detection efficiency the effects of including the MCP in the analysis must be taken into account. This is done by considering the number of recoils that fall into the DSSSD full energy peak and the number of recoils that fall into the DSSSD full energy peak and the MCP TOF recoil peak. By taking the ratio of the two, the result is the MCP detection efficiency and can be seen in the equations below,

$$N_{DSSSD} = N_{tot}\eta_{DSSSD} \tag{4.43}$$

$$N_{MCP,DSSSD} = N_{tot}\eta_{MCP}\eta_{DSSSD} \tag{4.44}$$

by dividing the second equation by the first an expression for the MCP detection efficiency is found. This is as follows,

$$\eta_{MCP} = \frac{N_{MCP,DSSSD}}{N_{DSSSD}}. \tag{4.45}$$

The purpose of the original measurement of the ^{21}Ne(p,γ)^{22}Na resonance was to use a well known reaction as a means of calibrating the DRAGON setup and verifying its functionality. The calibration process is done by measuring the position of the resonance in the gas target and the resulting magnetic field needed to center the outgoing beam for several values of pressure after the first magnetic dipole. This information can then be fit to determine the magnetic coefficient for the magnet. The calibration process is detailed more thoroughly in [65]. During the initial DRAGON calibration measurements the resonance strength, here to be remeasured, was measured to be about 2.5 times the previous literature value measured by Görres et al. [66] and required this resonance to be remeasured to confirm the actual resonance strength. The results for the original measurement in 2001 compared to the literature values for all of the resonance strength measurements can be seen in Figure 4.17 with the addition of the results from the present work. The previous literature value for the ^{21}Ne(p,γ)^{22}Na resonance was 82.5(125) meV while the current re-measurement conducted in 2013 yielded a value of 81.9(135) meV, which agrees almost perfectly. The discrepancy in the calibrating measurements of DRAGON could possibly be explained by a large contribution of leaky beam leading to the resonance strength being overestimated.

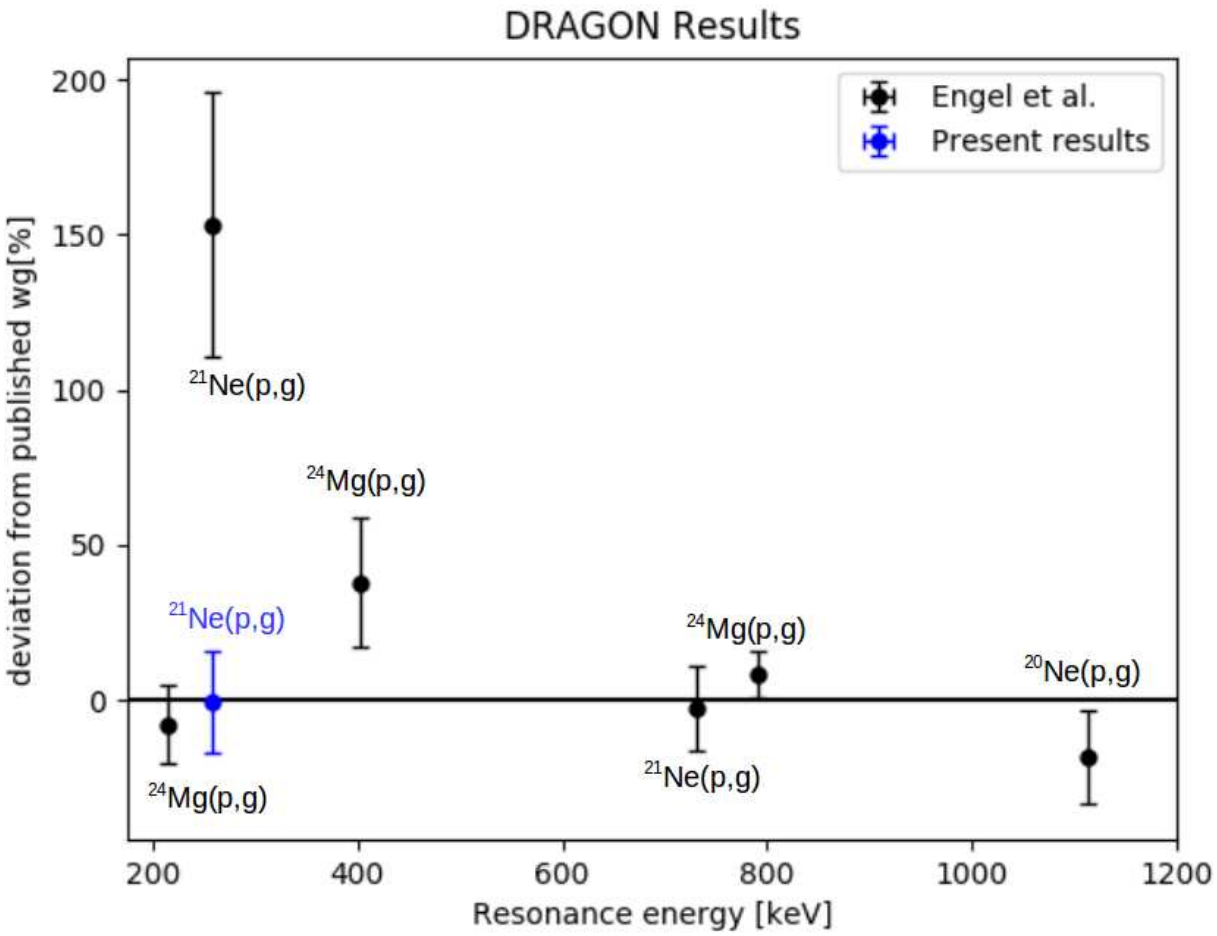

Figure 4.17: Deviation from literature value from initial DRAGON calibration measurements [65]. The result from the present remeasurement is in blue.

CHAPTER 5

RESULTS

5.1 S1686

During the course of the S1686 experiment, 8 potential resonances were examined between 272 and 495 keV center of mass energies. One of these states had been previously determined to be a resonant state through direct measurement, while the remaining states had been seen to exist in previous indirect measurements by Gillespie but have not been confirmed as resonant states with relevant strengths. The E_{CM}=495.5 keV state had been previously measured relative to a reference state so no independent direct measurement exists. The E_{CM}=431 keV state was listed in a previous excited state compilation by Endt et al. [44] and due to the higher than expected beam intensities there was enough time to investigate the potential astrophysical impact of this resonance.

5.1.1 495 keV ($\mathbf{E}_x$ = 6.866 MeV)

The 495 keV state had been previously measured relative to the 695 keV state, which itself was measured relative to the 1177 keV state's resonance strength, which has had several discrepancies in subsequent measurements. The original resonance strength for this state had been determined to be 25(12) meV and had been measured by Pruissen et al. in 1988 [2]. During our measurements this state was used as a benchmark to confirm the operation of the DRAGON facility due to the need to exclude the MCPs from analysis. Also, due to the discrepancies in the original measurements, this was used to provide insight into the reliability of the previous 1177 keV measurements.

The target was maintained at pressures of approximately 6 Torr during the course of the measurements. The beam intensity was about 1.5×10^{11} pps of ^{34}S in the 7+ charge state, which provided currents on the order of 100 nA. In total the beam on target was $6.47(12)\times10^{15}$ over the course of the approximately 12 hours of yield measurements. Using

Liu's CSD formula it was determined the 8+ charge state would have the highest charge state fraction at 35.1%, this was experimentally measured to be 30.7(17)%. Due to the previously mentioned issues with the MCP detectors, only coincident analysis could be done by viewing the separator TOF as can be seen in Figure 4.11 which is located in the Analysis section. After calculating the background contribution for the separator TOF signal region, 1950 to 2200 ns, to be 59.2 counts we are left with 23116.8 coincident recoil counts.

The branching ratio for this excited state in ^{35}Cl has been previously experimentally measured [2] so the BGO efficiency could be simulated directly from these values. The resulting efficiency from this simulation was 0.736 to which is assigned 10% uncertainty. The uncertainty is roughly how much this value is trusted and also encapsulates most of the range of efficiencies found by the upper and lower limit efficiency simulations. Since all other states had no branching ratio information an upper and lower limit simulation was also done for this state as was described in the Analysis section. The average for the two simulations was 0.749 which agrees well with the previous simulation. This shows that using this method for the BGO efficiency of all other states will likely not affect the results beyond the error currently assigned.

Looking at the 2D DSSSD energy versus IC energy spectra for the hybrid detector in Figure 5.1, it can be seen that the hybrid offers no reliable means of particle identification. As a result the separator TOF is our only means of reliable particle identification.

Using Equation 4.20 to determine the resonance strength, we end up with an $\omega\gamma$ = 13.8(23) meV. This result is roughly half the value measured by Pruissen et al. with a factor of 5 less uncertainty. The discrepancy in the current results to literature could be explained due to the relative methods used in the measurement by Pruissen. The strength of the 495 keV state was measured relative to the strength of the 695 keV state, which itself had been measured relative to the 1177 keV state. They used a strength of 10.5 eV for the strength of the 1177 keV reference state but if they replaced the strength with a more recently measured value of 4.9 eV the resulting strength for the Pruissen measurement would be 11.7 meV and

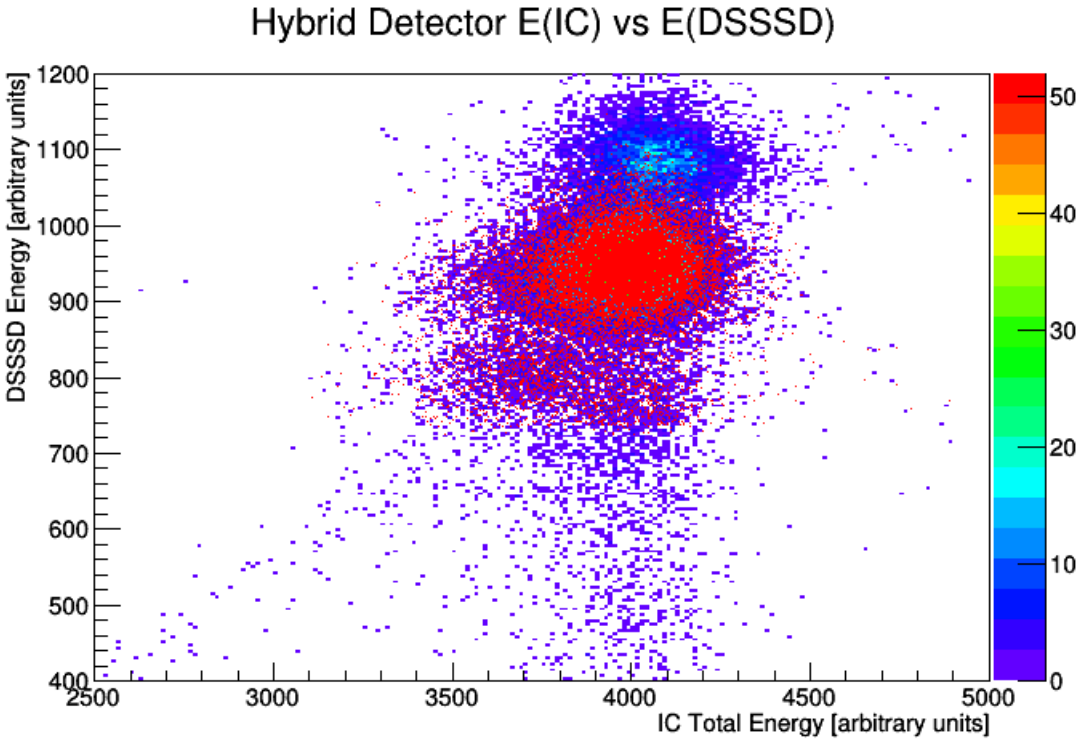

Figure 5.1: 2D spectra of hybrid energy showing minimal PID for 495 keV where the recoil events are the red dots over all coincident events

would agree very nicely with our measured value of 13.8(23) meV. This shows the need for the first absolute measurement of the 695 keV state and a remeasurement of the 1177 keV state at DRAGON in order to confirm our inferences on previous data. It should be noted that all the DRAGON measurements constitute absolute resonances strengths and the effect of the change in reference state strength will be discussed more later in this section.

5.1.2 272 keV (E_x = 6.643 MeV)

The 272 keV state has previously not been measured directly but was seen as an excited state and potential resonant state by the indirect measurements conducted by Gillespie et al. and a range of 8.5-8.9 μeV was expected for the resonant strength of this state. During our measurements beam intensities averaged about 7×10^{10} pps and target pressure was constant at 6 Torr. This energy was measured for approximately 2 days due to the weak expected resonance strength. The recoil charge state was 5+, which was experimentally measured to

have 42.7(42)% of the recoils. As can be seen in the separator TOF Figure 5.2, there again is a constant accidental background and a clear signal region. For this energy there is only one distinguishable peak due to the low resonance strength and resulting scarcity of statistics but to encapsulate this and the potential additional peaks a separator TOF signal region of 2770 to 2920 was used. The background contribution was largest for this energy and estimation was done in the same manner of sideband analysis and can be seen in Figure 5.3. The result was after $1.02(8) \times 10^{16}$ incoming beam particles, 103.7 coincident recoils were detected. The resulting resonance strength was found to be $\omega\gamma$=12.6(32) μeV.

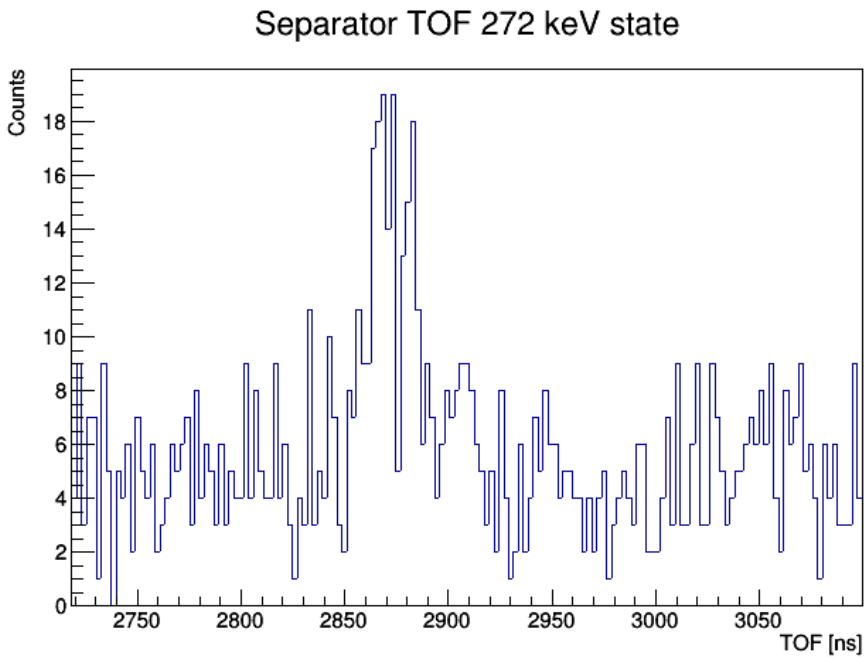

Figure 5.2: Separator TOF spectra for 272 keV runs with one obvious recoil peak due to the low resonance strength and resulting scarcity of statistics.

5.1.3 390 keV (E_x = 6.761 MeV)

The 390 keV state has no previous direct measurements but was seen as a possible resonant state in the experiment by Gillespie. For this work the resonance strength was postulated to be in the range of 0.24-1.5 meV. Beam intensities were approximately 8×10^{10} and in total we had about $2.60(0.07) \times 10^{15}$ particles into the target. The recoil charge state

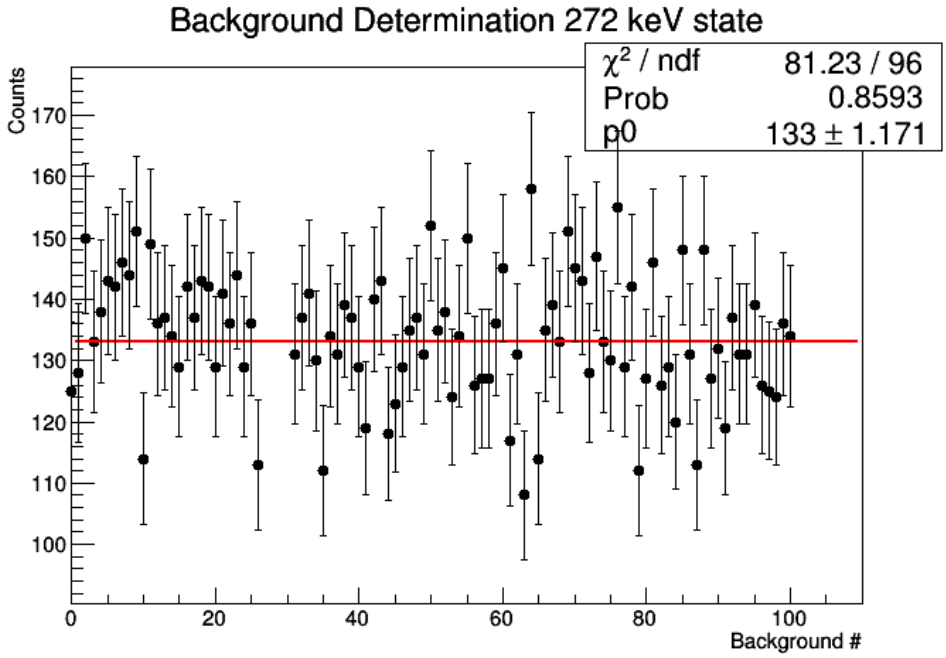

Figure 5.3: Background sideband analysis to determine background contribution in 272 keV separator TOF spectra.

was set to 6+, which was measured to have 42.9(40)% of the recoils. When we performed PID we saw no evidence of a peak in the separator TOF spectrum, Figure 5.4, which was expected around 2400 ns due to the recoil kinematics. In this region there was a background contribution of 10.47 counts per 100 bins as seen in Figure 5.5. We assumed a signal region of 200 ns to match the region used in both the 495 keV and 272 keV states, resulting in 21 background counts. From this an upper limit of 4.74 counts was attributed to the region based on the results of Equation 4.37 using a 1σ confidence interval. For all states with no positive recoil detection a 1σ interval was used. This puts a 1σ upper limit on the resonance strength of the 390 keV state at 5.63 μeV.

5.1.4 407 keV (E_x = 6.778 MeV)

There have been no previous direct measurements of this state but the Gillespie experiment extracted a possible resonance strength for this state of 0.94-1.0 meV. During our measurements we had approximately $5.2(3)\times10^{14}$ incoming beam particles over the course

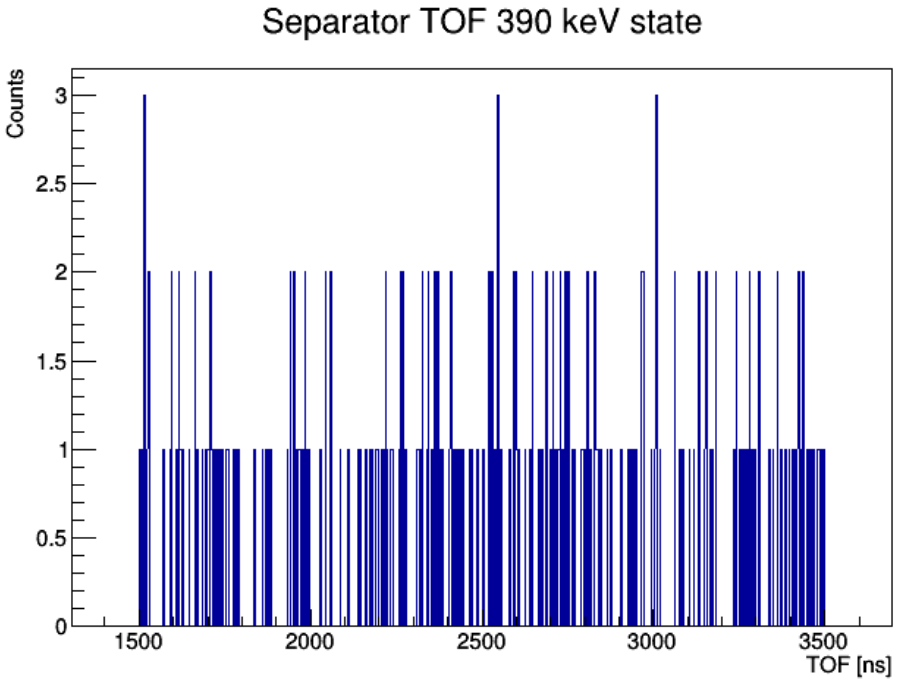

Figure 5.4: Separator TOF spectra for 390 keV runs with no obvious recoil peak in the expected TOF region.

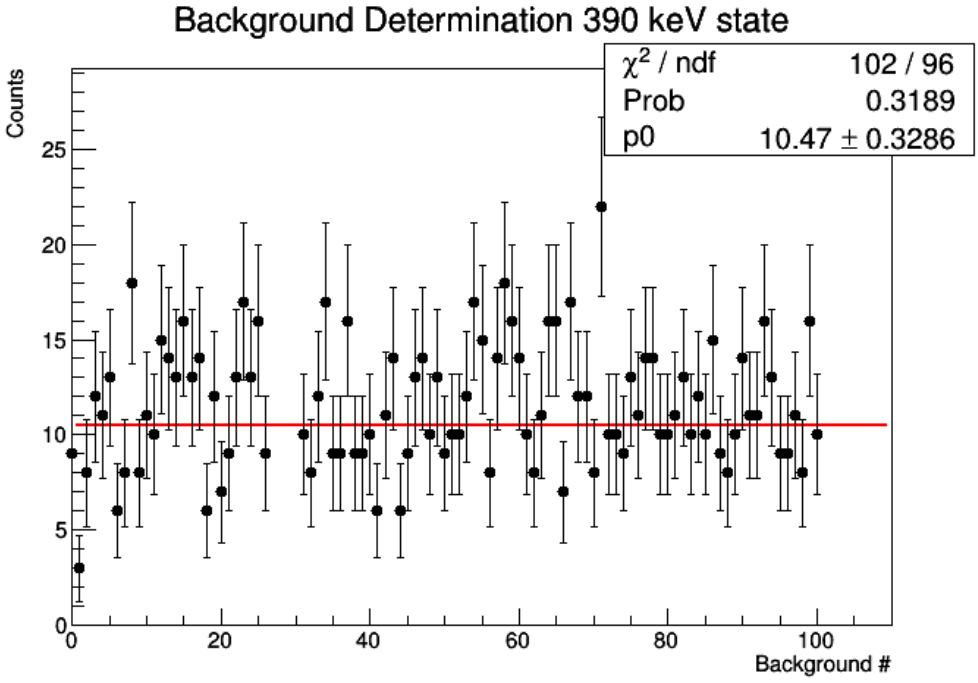

Figure 5.5: Background sideband analysis for 390 keV runs.

of about two hours of measurements. The 7+ charge state was expected to have a slightly higher fraction but due to the incoming beam being in the 7+ charge state the quality of the leaky beam suppression was diminished. As a result the 6+ charge state was chosen, which was measured to have 41.0(16)% of the recoils. PID was done in the same manner as previous states and two peaks could be seen in the separator TOF spectra, Figure 5.6, which were attributed to the recoil nuclei of the resonant state. Again, the two peaks are the result the electronic's settings, resulting in the MCP's providing a separate trigger from the hybrid. After background subtraction from Figure 5.7, 225.5 recoil counts remained, which resulted in a resonance strength of $\omega\gamma = 0.811(193)$ meV for this resonant state. Significantly more statistics could have been collected for this state to reduce the uncertainty but when compared to the energetically close 495 keV resonance, this state's astrophysical significance is of minimal impact.

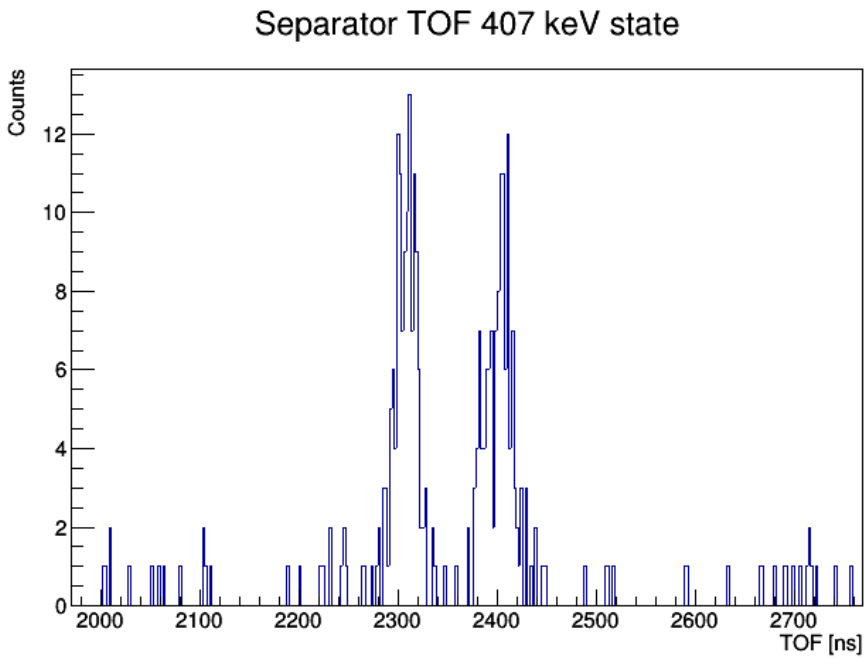

Figure 5.6: Separator TOF spectra for 407 keV runs with two obvious recoil peaks due to troubleshooting the electronics and having the MCP and hybrid detectors trigger separately. The space between peaks is due to the MCP to hybrid TOF plus cable and electronic delays.

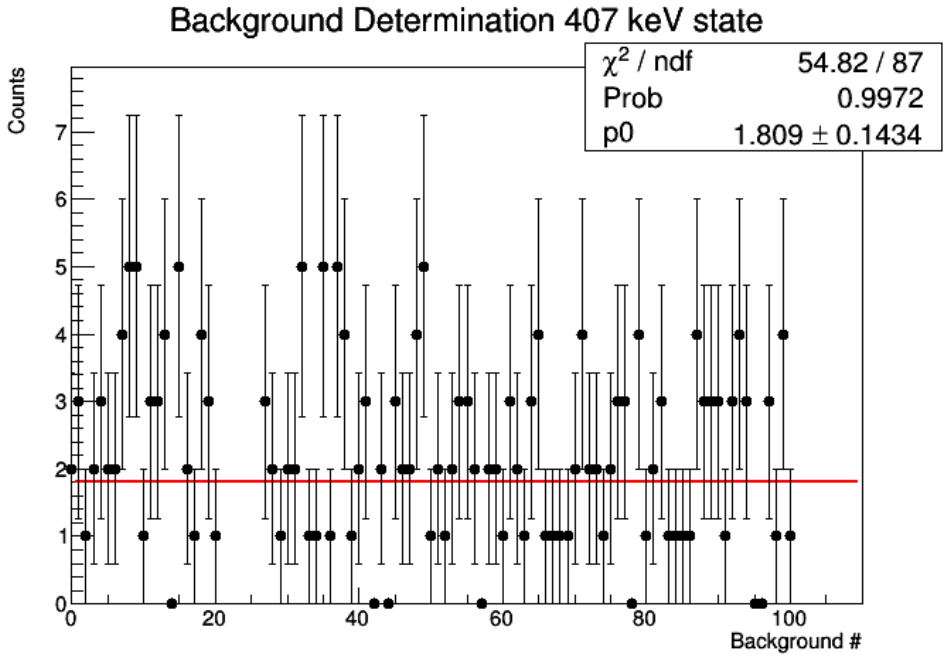

Figure 5.7: Background sideband analysis for 407 keV runs to determine background contribution in signal region.

5.1.5 303 keV (E_x = 6.674 MeV)

The 303 keV state has not been previously measured and was determined to be a potential resonant state by the Gillespie measurement. The prediction from this measurement was a resonance strength of $\omega\gamma$= 0.024-4.1 meV. During our measurements beam was taken for approximately 12 hours at 10^{11} pps which amounted to a total beam on target of $3.51(11)\times10^{15}$. The selected recoil charge state was 5+, which was measured to have 42.4(47)% of the recoil total. As can be seen in the separator TOF spectra, Figure 5.8, there is no noticeable peak correlating to the recoil nuclei for this state. According to the expected kinematics, the recoil peak was expected to be seen at 2800 ns. Using a signal region of 200 ns we find a background contribution of 90.8 counts, as seen in Figure 5.9 an upper limit of 9.7 recoil counts was used. This resulted in a 1σ upper limit for the strength of this state to be 5.82 μeV.

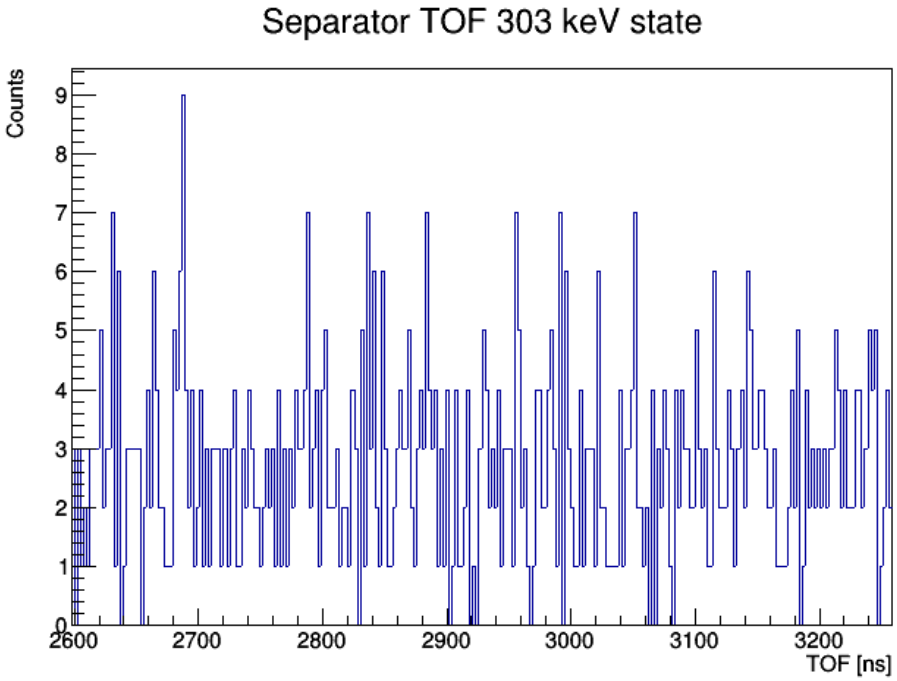

Figure 5.8: Separator TOF spectra for 303 keV runs with no obvious recoil peaks in the expected TOF region of 2800 ns.

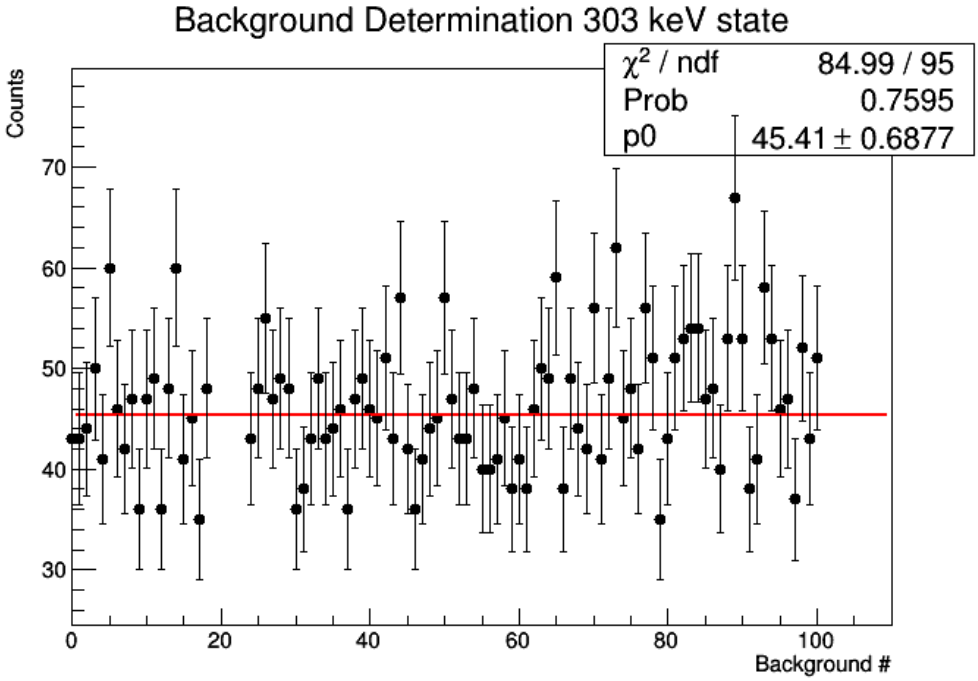

Figure 5.9: Background sideband analysis for 303 keV runs to determine background contribution in signal region.

5.1.6 452 keV (E_x = 6.823 MeV)

The 452 keV state has no previous direct measurements and was proposed as a potential resonant state by Gillespie et al.. They attributed a possible resonance strength for this state of $\omega\gamma = 2.7$ meV. During our measurements we had $1.04(2)\times10^{15}$ beam particles and target pressures constant at 6 Torr H_2. The 8+ charge state was again used to avoid decreasing the quality of the EMS beam suppression. This was measured to have 16.9(27)% of the recoil total. PID was done by viewing the separator TOF peak and removing any accidental background as has been previously done for the other states. The spectrum can be seen in Figure 5.10 and no peak is distinguishable from the background. An upper limit of 2.5 counts were attributed to this due to a background contribution of 4.7 counts in the expected signal region, as seen in Figure 5.11, and the result was a 1σ upper limit for this state at 23.9 μeV.

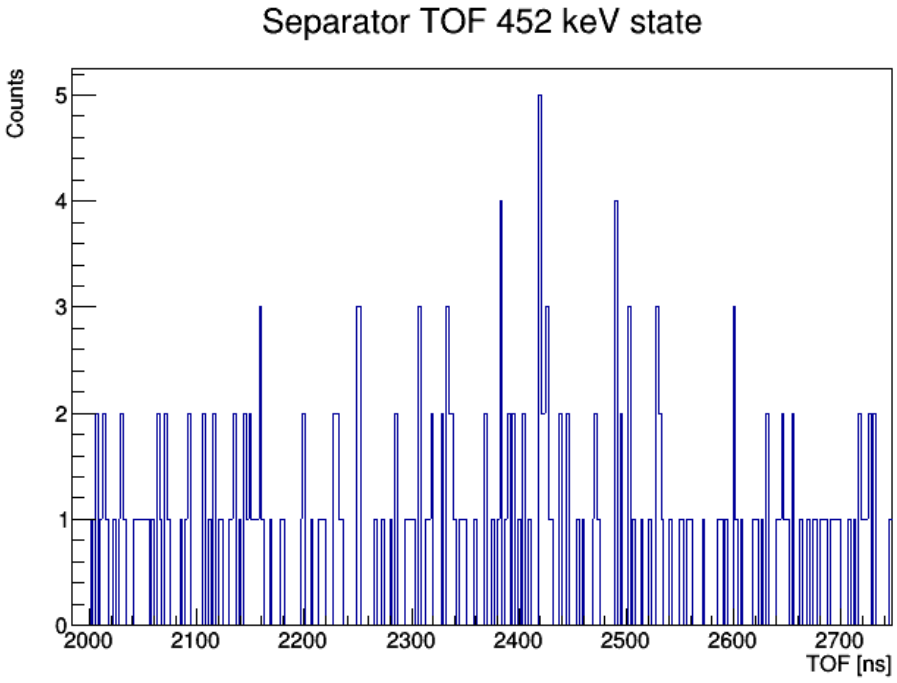

Figure 5.10: Separator TOF spectra for 452 keV runs with no peaks visible in the expected recoil TOF region, 2250 ns.

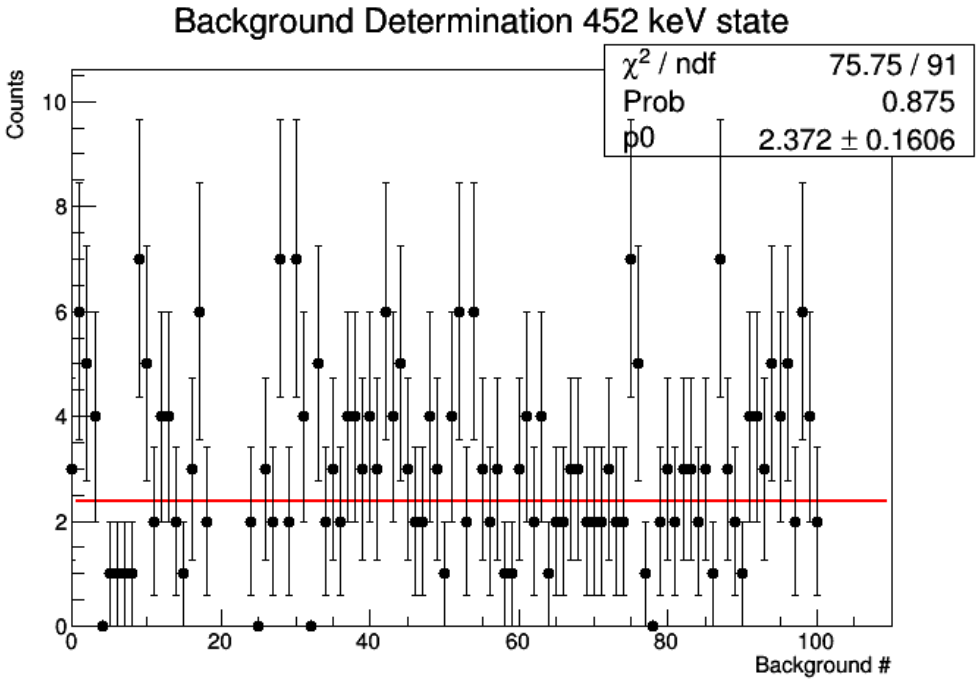

Figure 5.11: Background sideband analysis for 452 keV runs to determine background contribution in expected signal region.

5.1.7 471 keV (E_x = 6.842 MeV)

The 471 keV state had not been previously directly measured and had only been seen as a potential state by the Gillespie measurements. They attributed a possible resonance strength to this state of $\omega\gamma = 33 - 700$ μeV. During our measurements we had $1.64(4) \times 10^{15}$ beam particles on target and target pressures constant at about 6 Torr. The 8+ charge state was measured to have 22.3(22)% of the recoil total. As can be seen in the separator TOF spectra Figure 5.12, there are two small peaks which can be attributed to the recoil nuclei and after background subtraction, seen in Figure 5.13, 29.8 counts remain. This results in a resonance strength of $\omega\gamma = 93.6(280)$ μeV for this state.

5.1.8 431 keV (E_x = 6.802 MeV)

Due to the beam intensity being nearly 10 times what was expected, there was extra time after finishing our desired measurements. We were then able to probe an extra state

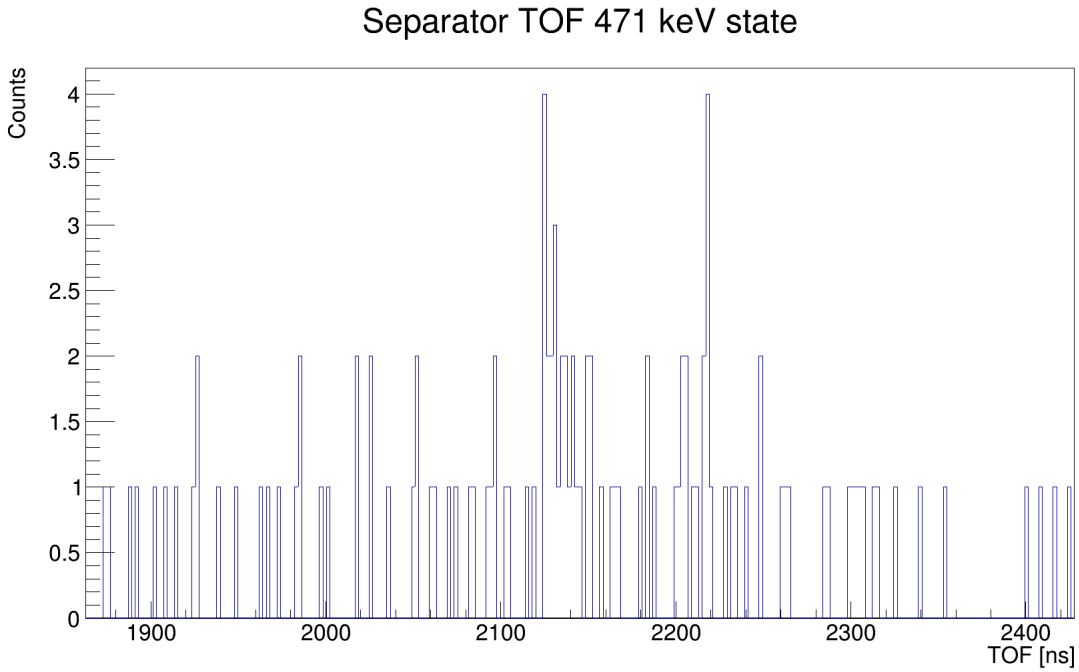

Figure 5.12: Separator TOF spectra for 471 keV runs with two small peaks visible due to the electronic's settings the MCP and hybrid detector triggered separately.

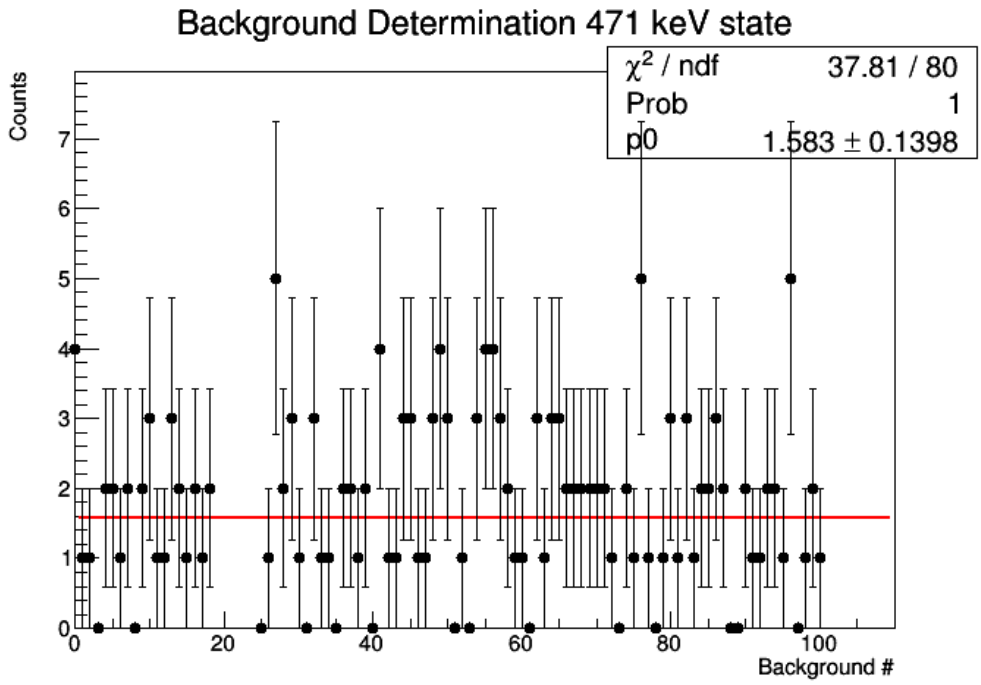

Figure 5.13: Background sideband analysis for 471 keV runs to determine background contribution.

to determine the possibility of a resonance. This was the 431 keV state seen in the Endt compilation [44] but not identified as a potential excited or resonant state by the Gillespie experiment. PID proceeded in the same manner as all previous states and with $7.47(10)\times10^{14}$ incoming particles there were no positively detected recoil nuclei in the expected signal region of 2300 ns, which can be seen in Figure 5.14. The 8+ charge state was expected to contain 12.3(34)% of the recoil total. Due to background in the expected signal region of approximately 2.6 counts, seen in Figure 5.15, 2 recoil counts were used for a 1σ upper limit, which resulted in a strength for this state of 33.8 μeV.

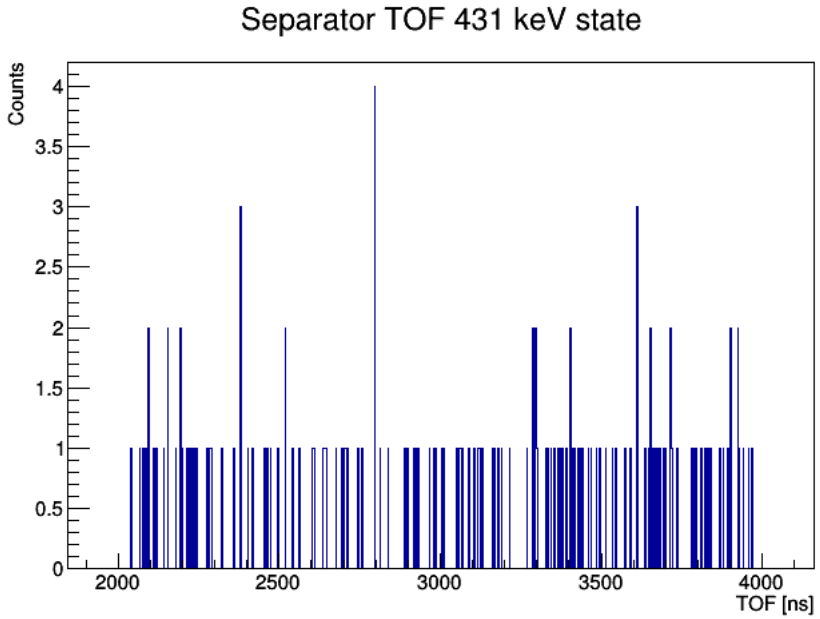

Figure 5.14: Separator TOF spectra for 431 keV runs with no visible peaks in the expected recoil TOF region of 2300 ns.

5.1.9 Resonance Strength Summary

The ^{34}S(p,γ)^{35}Cl experiment, S1686, was conducted at the DRAGON facility located at the TRIUMF National Lab in Vancouver Canada. During the experiment 8 potential resonances were measured to determine the resonance strength and potential astrophysical impact. Of theses 8 states 1 had been previously measured, 6 had been determined to be potential resonances from the measurement by Gillespie et al. and the final state was found

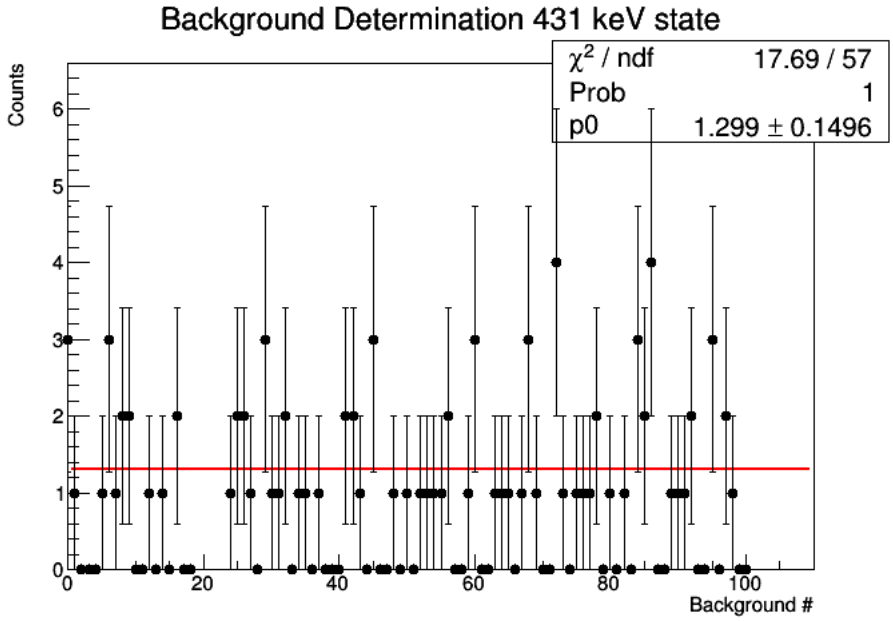

Figure 5.15: Background sideband analysis for 431 keV runs to determine background contribution in expected signal region.

as a part of a recent Endt compilation. A summary of the results of the resonance strength measurements and comparisons to the results of the Gillespie measurement can be seen in Table 5.1. From our measurements we have found that the 495 keV state was approximately half the previously listed resonance strength. This leads to the future need to remeasure the 1177 keV state and conduct the first independent measurement of the 695 keV state directly at DRAGON. In order to be able to clear up the history of the previous measured strengths the S1686 experiment had originally planned to measure the 1177 keV and 695 keV states, however the measurements were not feasible because at the time of the experiment the DRAGON electric dipoles could not reach the voltage to bend the beam at the energies required and one tank of the ISAC DTL was not functioning properly, meaning the beam could not be accelerated to the required energies. Of the other remaining states measured, 4 upper limits were set with a 1 σ confidence due to no positive detection of any recoil products and 3 were for the first time established as resonances in the ^{34}S(p,γ)^{35}Cl reaction.

Table 5.1: Results of S1686 experiment

	E_{lab} [keV/u]			Previous[1]		Current Work
E_{CM} [keV]	E_{rxn}	E_{in}	E_{out}	$\omega\gamma_{low}$ [eV]	$\omega\gamma_{high}$ [eV]	S1686 $\omega\gamma$ [eV]
495.5(6)	505.7	518.6	485.2	$3.0(3)\times10^{-2}$	$4.7(5)\times10^{-2}$	$1.38(23)\times10^{-2}$
272(2)	277.9	287.3	263.9	$8.5(10)\times10^{-6}$	$8.9(10)\times10^{-6}$	$1.26(32)\times10^{-5}$
390(2)*	398.5	409.7	381.4	$2.4(3)\times10^{-4}$	$1.5(1)\times10^{-3}$	$\leq5.63\times10^{-6}$
407(2)	415.8	426.7	398.2	$9.4(12)\times10^{-4}$	$1.0(1)\times10^{-3}$	$8.11(193)\times10^{-4}$
303(2)*	309.6	318.7	294.5	$2.4(2)\times10^{-8}$	$4.1(8)\times10^{-6}$	$\leq5.82\times10^{-6}$
452(2)*	461.8	472.5	441.7	$2.7(3)\times10^{-3}$	$2.7(3)\times10^{-3}$	$\leq2.39\times10^{-5}$
471(2)	481.2	492.5	460.0	$3.3(1)\times10^{-5}$	$7.0(3)\times10^{-4}$	$9.36(280)\times10^{-5}$
431(4)*	440.3	451.6	422.6	-	-	$\leq3.38\times10^{-5}$

[1] Values from work by Gillespie

$*$ Upper limit only

5.2 Recommended Resonance Strengths

Many methods of determining resonance strengths rely upon reference states as has been mentioned previously in this thesis. The 1177 keV resonance has been previously used as the characteristic reference state in the ^{34}S(p,γ)^{35}Cl reaction. This has led to issues because there have been several measurements of this state which have yielded strengths that vary by up to a factor of 6. The highest energy resonance measured in this work was the 495 keV resonance which had been previously measured relative to the 695 keV state, which itself had been measured relative to the 1177 keV state. This leads to issues because the strength found in previous measurements of the 495 keV state is directly related to the strength of the reference state. The recent work by Gillespie et al. listed a strength for the 495 keV state of 0.025(12) eV by using a resonance strength of 10.5(15) eV for the reference state [7]. When compared to the direct results from this work we find the 495 keV state to have a strength of 0.0138(23) eV, roughly half that found by Gillespie. If we use this as a means of finding the recommended resonance strength for the 1177 keV reference state we end up with a recommended strength of 5.8(13) eV. This result agrees well with the most recent measurements of the 1177 keV resonance strength of 4.95(35) eV [67]. By using our recommended resonance strength for the characteristic reference state, 1177 keV,

we can then re-normalize many of the previous indirect measurements found in [68]. The results of these, along with the recommended resonance strength, can be seen in Table 5.2. To calculate the re-normalized data, the value used for the 1177 keV reference strength was found for each measurement and was re-normalized using the results from this present work. Several measurement sets did not contain errors and were excluded from the average used to calculate the recommended strength. If no measurements with error exist then the recommended strength was left blank.

Table 5.2: Resonance strengths of previous relative measurements re-normalized to the results by this work.

		Resonance Strength $\omega\gamma$ [eV]		
E_{CM} [keV]	E_x [keV]	Previous	Re-normalized	Recommended
495.7(6)	6866.7(6)	0.025(12)[1]	0.0138(23)	0.0138(23)
695.2(4)	7066.2(4)	0.10(5)[2]	0.06(3)	0.072(34)
		0.15(6)[3]	0.083(36)	
732.3(4)	7103.3(4)	0.04[4]	0.116	0.138(72)
		0.3(2)[2]	0.138(95)	
		0.25(8)[3]	0.138(50)	
807.6(3)	7178.6(3)	0.2(1)[2]	0.11(6)	0.092(34)
		0.15(4)[3]	0.083(26)	
		0.07(1)[5]	0.083(18)	
814.0(4)	7185.0(4)	0.056[4]	0.163	-
823.5(3)	7194.5(3)	0.17[4]	0.49	0.32(12)
		0.6(2)[2]	0.30(11)	
		0.6(2)[3]	0.33(12)	
854.5(3)	7225.5(3)	0.073[4]	0.212	0.097(44)
		0.2(1)[2]	0.11(6)	
		0.15(5)[3]	0.083(31)	
863.0(3)	7234.0(3)	0.23[4]	0.67	0.45(15)
		0.7(2)[2]	0.36(12)	
		1.0(3)[3]	0.53(18)	
901.6(3)	7272.6(3)	0.31[4]	0.90	0.50(19)
		0.7(2)[2]	0.39(13)	
		1.1(4)[3]	0.60(24)	
991.0(3)	7362.0(3)	0.48[4]	1.39	0.88(31)
		1.6(5)[2]	0.89(32)	
		1.3[6]	0.69	
		1.6(5)[3]	0.86(31)	
1025.0(3)	7396.0(3)	0.067[4]	0.194	0.124(54)

Table 5.2: Continued.

		$0.2(1)^2$ 0.2^6 $0.25(8)^3$	0.11(6) 0.11 0.138(50)	
1070.0(5)	7451.0(5)	$0.15(1)^2$ 0.15^6 $0.20(6)^3$	0.083(15) 0.166 0.110(38)	0.097(26)
1130.1(8)	7501.1(8)	0.3^2 0.05^6	0.166 0.28	-
1131.9(7)	7502.9(7)	0.13^6 $0.2(1)^3$	0.138 0.22(12)	0.22(12)
1147.7(4)	7518.7(4)	$0.10(5)^2$ 0.15^6 $0.20(6)^3$	0.06(3) 0.083 0.110(38)	0.085(35)
1177.2(3)	7548.2(3)	2^4 $10.5(15)^7$ $10.5(15)^3$ $4.95(35)^5$	5.8 5.8(13) 5.8(13) 5.8(11)	5.8(12)

[1] from [2] [2] from [69] [3] from [41] [4] from [6] [5] from [67] [6] from [70] [7] from [7]

5.3 Astrophysical Reaction Rate

After calculating the resonance strength for the individual states the astrophysical reaction rate and therefore astrophysical significance of each state can be calculated using Equation 2.75, and the total rate can be calculate by simply summing the individual contributions of each state. The results of this calculation can be seen in Figure 5.16. It can be seen that the total reaction rate seen in black is dominated by the 272 keV resonance (green) until 0.3 GK when the 407 keV resonance in red begins to contribute. Eventually the 495 keV resonance takes over around 0.4 GK, which is approximately the peak temperature reached in O-Ne novae. This means the newly measured 272 keV resonance almost solely determines the production rate of ^{35}Cl in O-Ne novae environments. In Figure 5.17 we have normalized each state by the total reaction rate to see the percent contribution for each state individually. It can again be seen that the 272 keV state dominates the reaction rate until 0.3 GK when the 495 and 407 keV states begin to take over. These results can be directly

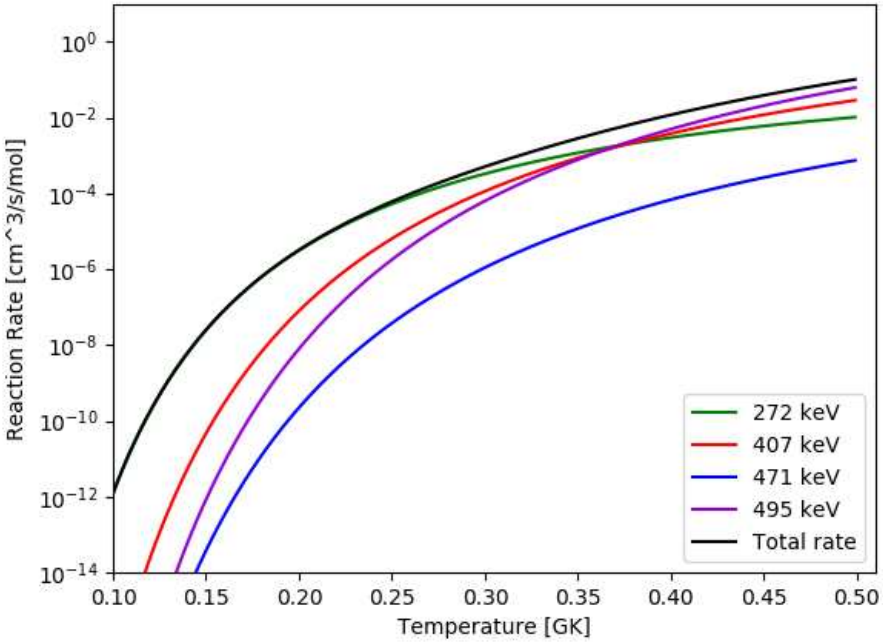

Figure 5.16: Astrophysical reaction rates calculated using the measured strengths for detected recoil states. Total reaction rate is shown in black.

compared to the results from the work by Gillespie to see how the astrophysical reaction rate has changed. In Figure 5.18 we took the ratio of the results by Gillespie to the results by this work.

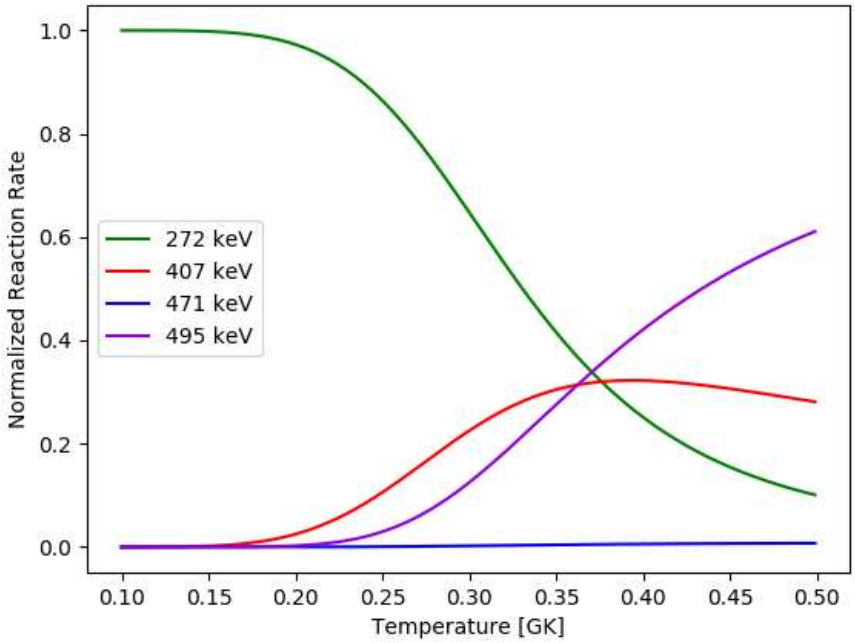

Figure 5.17: Reaction rate ratio normalized to the total reaction rate.

In this figure we plot only the two highest contributing states, the 272 keV and the 495 keV and the total rates using the 407 keV and 471 keV states as well. The individual rates are only scaled by the changing resonance strength but the total rates compared to both upper and lower limits from Gillespie have an underproduction at temperatures below 0.3 GK and an overproduction at temperatures above 0.3 GK. This is because the strength measured for the 272 keV state is roughly twice that found by Gillespie and the 495 keV strength was half that found by Gillespie.

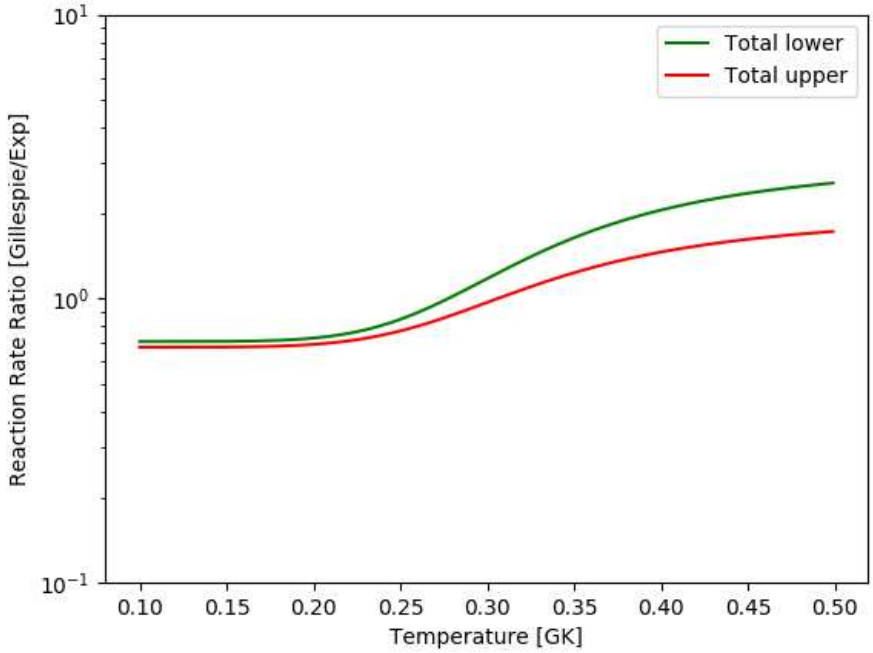

Figure 5.18: Reaction rate ratio compared to Gillespie's upper and lower limits.

5.4 Charge State Distributions

As mentioned earlier the separating stages of DRAGON allow only one recoil charge state to pass through to the end detectors so precise knowledge of the charge state distributions is needed for proper analysis. Due to the complicated series of charge changing reactions that occur, theoretical calculations of the charge state distributions are generally inaccurate. These distributions can be easily measured at DRAGON and this is done for each experiment when possible. An additional part of this thesis was to sort through old experimental information to catalog all the charge state distribution measurements done at DRAGON. Also, the semi-empirical formula developed by Liu was fit using limited data available at the time and could be improved upon by refitting with new data that spans a wider range of energies and Z values.

These distributions are fit with a Gaussian distribution and can be parameterized by the width d and center $\overline{q}$ as was done previously when using the semi-empirical formula

developed by Liu et al and work by Betz [62, 71]. Most of the distribution measurements did not include the uncertainty in the individual charge state fractions as this is generally not recorded in the electronic and paper logs so an uncertainty of 10% was attributed to each fraction when experimental information was not available. This is the uncertainty attributed to the semi-empirical CSD's so is an expected upper limit for the experimental measurement's uncertainty.

5.4.1 Charge State Mean

Attempts to theoretically calculate the average charge state of ions passing through matter were first done separately by Bohr [72, 73], Lamb [74], and Knipp and Teller [75, 76]. These were primarily done to more precisely calculate the energy loss for uranium fission fragments based on the most likely equilibrium charge states and as a result focus more on high energy and large Z nuclei. Bohr based his work on the assumption that all electrons with orbital velocities below the velocity of the ion would be lost through collisions, while those with higher velocities would be less likely to be lost. This leads to the need for a relation between the given ion and orbital velocities. Bohr began with the electronic velocity,

$$\mu = Z^* \frac{v_0}{v^*} \tag{5.1}$$

where v^* is the effective quantum number, v_0 is the Thomas-Fermi velocity ($e^2/\hbar$=2.188×10^8 cm/sec) and Z^* is a measure of the field strength where the electron is bound and is roughly equal to the number of electrons with velocity lower than μ, according to Bohr. This means that $Z^* \approx \overline{q}$ and by enforcing $\mu = v$, Bohr's resulting expression,

$$\overline{q} = v^* \frac{v}{v_0} \tag{5.2}$$

should, over a large intermediate region of q, have a flat maximum of v^* which corresponds to values close to $Z^{1/3}$. This result has been confirmed by analysis of electron binding by the Thomas-Fermi model [77, 78]. For values of $q \leq Z/2$ this leads to the result,

$$\overline{q}/Z = \frac{v}{v_0 Z^{2/3}}. \tag{5.3}$$

Where v is the ion velocity. Due to the reliance of q* on q, this expression is unreliable for q $\geq$ Z/2 and only provides a rough estimate for values below. Separate from the work by Bohr, Lamb based his considerations on energy in determining the average charge state. He assumed that fission fragments would lose electrons until the next ionization potential was larger than the kinetic energy of the fragment electrons. This method provided too low of ionization potentials and had to rely on empirical data for q $\leq$ 6. Another attempt at theoretical calculations of the mean charge was done by Knipp, Teller and Brunnings, where like Bohr, they assumed a dependence of $\overline{q}$ on the ratio of electronic and ionic velocities. In their work they introduce a more general relation between the characteristic electron velocity and the ion velocity of $\mu = \gamma v$. Where γ is an adjustable parameter not to be confused with the γ parameter in the semi-empirical formula, and is meant to correct for unknown effects in Bohr's model. A later attempt to theoretically calculate the mean charge was done by Bell [79], where he numerically calculated the average electron loss and capture cross sections. These results are very similar to those found by Lamb and a resulting comparison between these 4 theoretical models and experimental results can be seen in Figure 5.19, which was taken from the work by Betz [62]. It can be seen that the Lamb and Bell results agree well with experimental results over a wide range of reduced velocities but neither can capture the full trend.

This led to the need for semi-empirical methods in calculating the mean charge. Early work on semi-empirical formulae began with Papineau et al. [80]. Several others followed, also basing their work on the Thomas-Fermi model. Heckmann et al. indicated that $\overline{q}$/Z could be approximated by a linear function f(vZ^{ϵ}), where ϵ ranges from 0.55-0.58 [81]. It is also noted that $\epsilon = 2/3$ is of use for heavy ions. Dimitriev et al. did the first analytical semi-empirical formula for the mean charge, which improved upon their previous work [82, 83]. They generalized the Thomas-Fermi model and assumed that $\mu \approx Z^{\alpha} F(\overline{q}/Z)$. The result was for ions passing through gas,

$$\overline{q}/Z = ln\Big(\frac{v}{m_1 Z^{\alpha_1}}\Big)/ln(n_1 Z^{\alpha_2}) \tag{5.4}$$

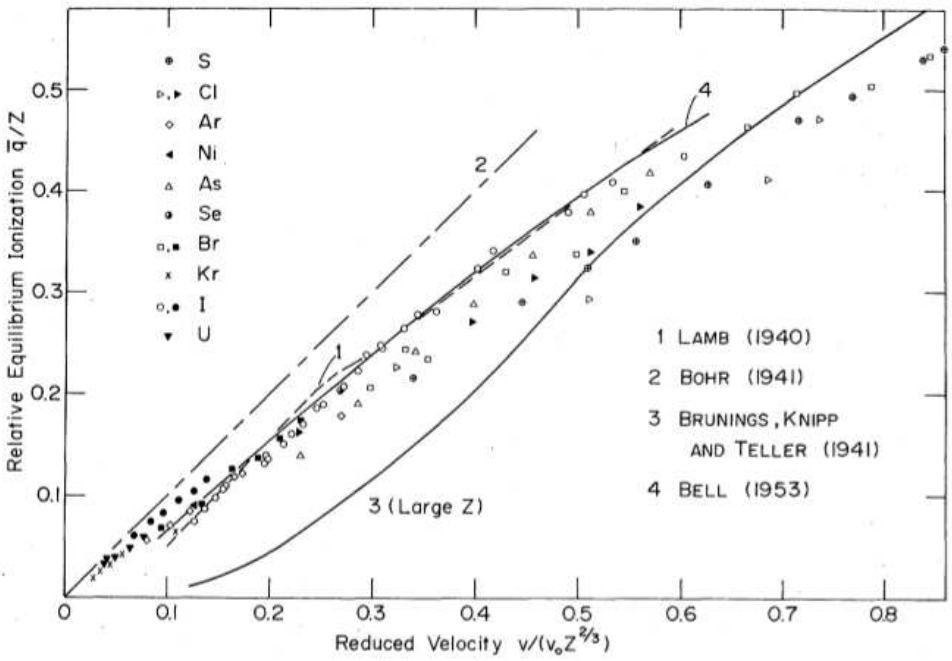

Figure 5.19: Comparison between various theoretical calculations of the mean charge and experimental data from [62].

for $0.3 \leq \overline{q}/Z \leq 0.9$, where m_1, α_1, α_2, and n_1 are all fit parameters. For values of $\overline{q}/Z \leq 0.3$ they suggest using,

$$\overline{q}/Z = AvZ^{1/2} \tag{5.5}$$

where A is a fit parameter. This equation has also been shown to be of use for solid targets as well but requires an independent fit. Further work by Betz et al. [71] saw that from the work by Heckmann for $\overline{q}/\mathrm{Z} \leq 0.9$, ln(1-$\overline{q}$/Z) could be approximated by the linear function $\mathrm{vZ}^{-0.55}$. A fit of the low energy data from Dimitriev by Heckmann yielded a value of $\epsilon = 0.45$. This then led to the development of the semi-empirical formula from Betz,

$$\overline{q}/Z = 1 - C\mathrm{Exp}[-v/(v_0 Z^{\gamma})] \tag{5.6}$$

where C and γ are fit parameters for each target and ion combination. In 1968 Dimitriev et al. developed an expression for the mean charge above energies of 100 MeV for ions in solid targets of [84],

$$\overline{q}/Z = [1 + (Z^{-\alpha}v/v')^{-1/k}]^{-k} \tag{5.7}$$

where v ' is 3.6×10^8 cm/sec and k and α are fit parameters. For the work done by Dimitriev α was found to be 0.45. No detail is given for the switch from v_0 to v'. It should also be noted that no detail is given about how the α parameter varies with target composition. The work by Liu in developing her semi-empirical formula expands on the formula by Betz, Equation 5.6. She adds two new free parameters to fit to the experimental data, A and B which are the slope and intercept of ln(1-$\overline{q}$/Z) vs v/(v 'Z$^\gamma$). She also changes velocity to energy per nucleon for the convenience of use with DRAGON where beam energy is dealt with in this format. Overall, the effect of this is that A can vary to find the ideal characteristic velocity and improve the experimental fit compared to Betz. Liu used the same value of γ or α for both hydrogen and helium targets.

5.4.2 Distribution Width

Some work has also been done by Dimitriev [83] on determining the width of the charge state distribution. The width shows little variation overall and almost no variation for different energies for a given Z value. From this Dimitriev came up with the semi-empirical formula for the width,

$$d = d_1 Z^w \tag{5.8}$$

where d_1 and w are fit parameters equal to 0.32 and 0.45 respectively for gaseous targets and 0.38 and 0.4 respectively for solid targets. Dimitriev then expanded on this formula for solid targets [84], coming to the expression,

$$d = d_2\left[\overline{q}\left(1 - (\overline{q}/Z)^{1/k}\right)\right]^{1/2} \tag{5.9}$$

with d_2 and k being fit parameters. Liu used the first formula, Equation 5.8, fit for her data to determine the distribution widths.

5.4.3 Asymmetry

In the work by Betz, he acknowledged that some of the measured charge state distributions, specifically high Z and low energies, showed a large amount of asymmetry in the charge state fractions. He noted that the fractions for $q \geq \overline{q}$ showed a slower decrease the farther the charge state was from the mean. Betz concludes that the cause is due to the multiple electron loss cross sections which are much larger in heavy targets compared to light targets. A measure of the asymmetry of the distributions was introduced as the skew,

$$S = \Sigma_i^{Z_p}(q_i - \overline{q})^3 * Fq_i/d^3 \tag{5.10}$$

where i iterates through all measurable charge states, Fq_i is the charge state fraction for the charge state i, and d is the measured distribution width. This formula is only applicable for measurements which capture the full distribution as missing charge state fractions due to magnetic constraints or other factors will artificially skew the distribution. A figure of the resulting S values for several measured distributions by Betz can be seen in Figure 5.20.

It can be seen that higher Z targets and lower energies tend to show the largest values of S. A similar effect has also been seen by Ryding et al. [85] where a high charge state tail has been seen. These were high precision measurements that were able to measure charge state fractions as low as 10^{-6}. These fractions are outside the range of use with DRAGON with current beam intensities but this demonstrates the extent of the asymmetry in the distributions. A figure of the resulting measured distributions can be seen in Figure 5.21.

5.4.4 CSD Results

The results for the cataloging of CSD details can be seen below in Table 5.3 and Table 5.4. The first set of $\overline{q}$ and d values are the experimental Gaussian fits to the distribution data. The second set of distribution parameters are calculated using the Liu semi-empirical formula with the previously mentioned fit values. The final set are from the updated fit values which will be discussed later in this section. Since these are fractional distributions the total sum of the individual charge state fractions should sum to 1. This could be enforced by

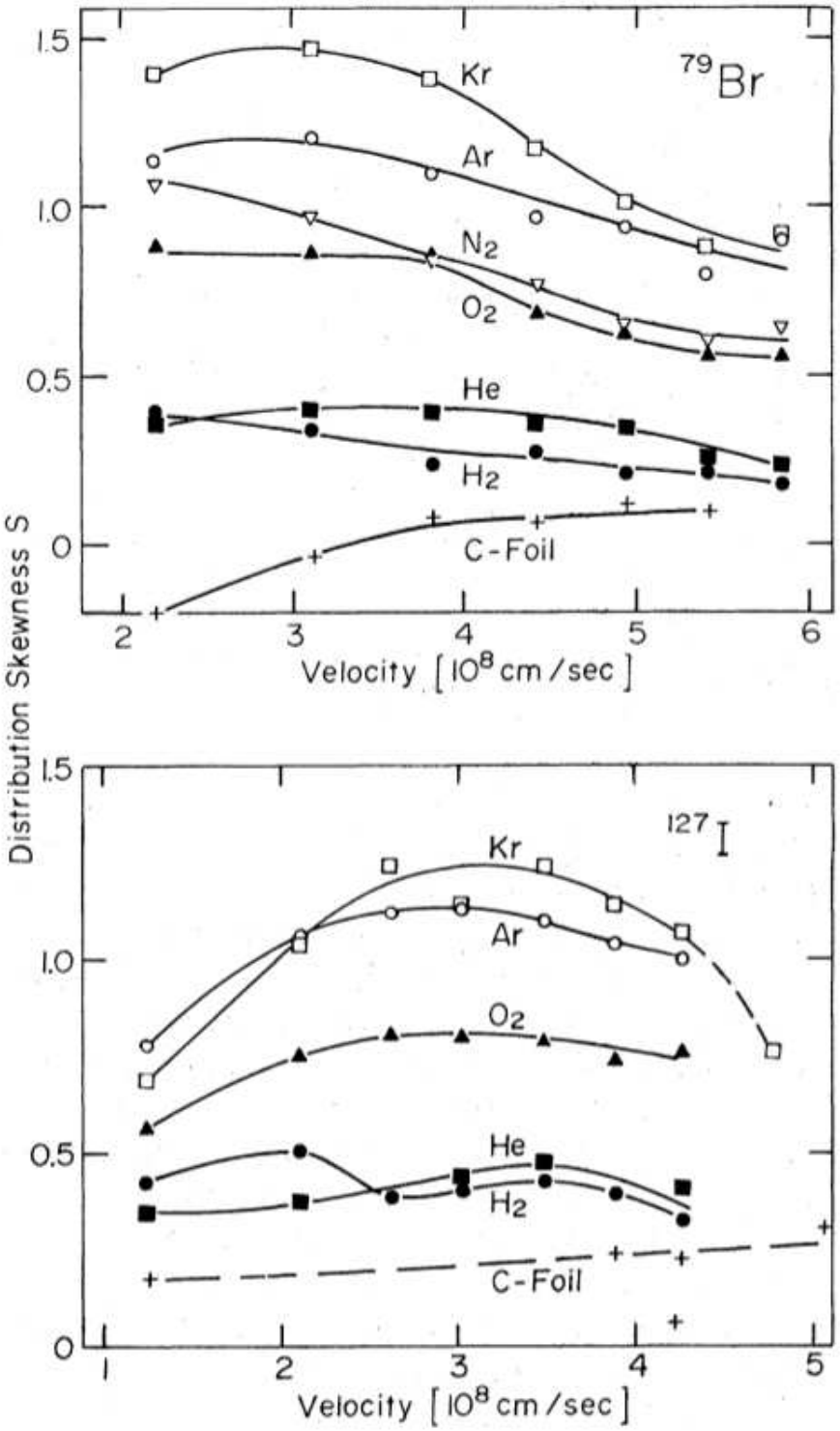

Figure 5.20: Charge state distribution skew for bromine and iodine passing through various gas targets and a carbon foil [62].

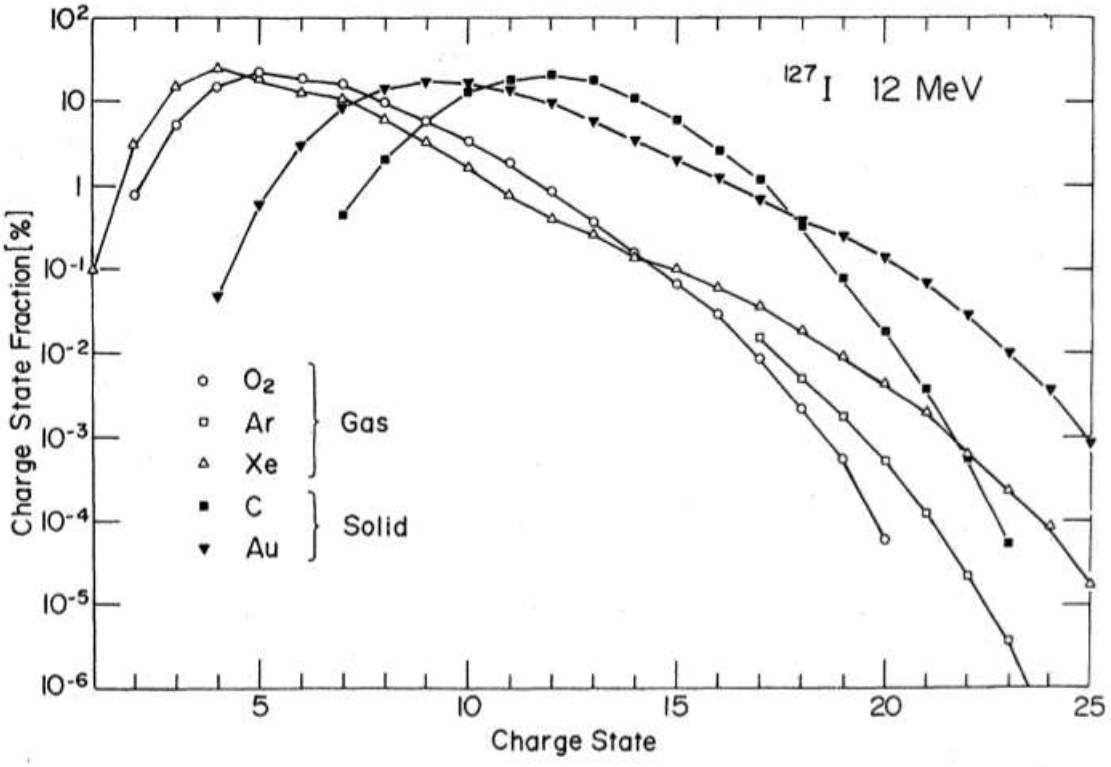

Figure 5.21: Charge state distributions showing pronounced asymmetry measured by Ryding et al. [85].

normalizing all measured distributions by the sum of the fractions but since the full range of charge states has not been measured for all distributions this cannot be done systematically. Instead, the requirement was made that the experimental fit needed to be normalized to sum to 1. This was done by scaling the experimental data points until the resulting fit was properly normalized. It should be noted that this causes some experimental distributions to sum to more than 1 which is physically incorrect but the fit mean, $\overline{q}$, and width d are independent of this scaling. This is done purely for ease of comparing fit widths in the figures as unknown charge state fractions could also cause the experimental sum to be larger than 1. To directly use the measured charge state fractions in future work, the distributions may need to be re-normalized to physically realistic values. The semi-empirical formula also needs to be properly normalized but this can be done by using a normalized Gaussian with the prefactor $\frac{1}{d\sqrt{2\pi}}$ as is customary.

New data was found for ions in hydrogen for values of Z ranging from 6 to 19 and at energies from 162 to 1173 keV/u. Liu's previous data only spanned from Z values of 7 to 12 and energies of 138 to 800 keV/u. For Helium, Liu only had data for ^{16}O from 138 to 875 keV/u but with the new measurements this now ranges from Z values of 4 to 22 and energies of 138 to 1093 keV/u.

Table 5.3: Charge state distributions for previous DRAGON experiments for Hydrogen gas targets

		Experimental		Liu		Modified	
Reaction	E_{lab} [keV/u]	$\overline{q}$	d	$\overline{q}$	d	$\overline{q}$	d
$^{13}C+H_2$	544	4.47(6)	0.636(31)	4.46	0.632	4.49	0.816
	558	4.62(5)	0.645(33)	4.50	0.632	4.53	0.816
	572	4.50(6)	0.645(33)	4.54	0.632	4.56	0.816
$^{15}N+H_2$	435*†	5.61(1)	0.603(11)	4.59	0.687	4.59	0.830
$^{16}O+H_2$	138*	2.43(1)	0.796(4)	2.39	0.739	2.30	0.843
	200*	3.18(1)	0.800(9)	3.24	0.739	3.17	0.843
	325*	4.29(1)	0.781(6)	4.35	0.739	4.31	0.843
	500*	5.51(3)	0.719(37)	5.29	0.739	5.27	0.843
	588*	5.71(1)	0.588(17)	5.62	0.739	5.60	0.843
	800*	6.17(1)	0.586(1)	6.12	0.739	6.18	0.843
$^{18}O+H_2$	706	6.10(3)	0.629(31)	5.97	0.739	5.96	0.843
	819	6.39(2)	0.654(14)	6.23	0.739	6.23	0.843
	842	6.44(2)	0.654(14)	6.28	0.739	6.27	0.843
	1044	6.61(6)	0.681(42)	6.63	0.739	6.63	0.843
	1077	6.67(5)	0.686(40)	6.67	0.739	6.67	0.843
$^{20}Ne+H_2$	1150†	7.78(5)	0.624(13)	8.09	0.836	8.05	0.864
	1165†	8.03(2)	0.526(18)	8.11	0.836	8.07	0.864
	1173†	8.13(2)	0.641(14)	8.12	0.836	8.09	0.864
$^{21}Ne+H_2$	274	4.17(5)	0.964(45)	4.38	0.836	4.26	0.864
	282	4.18(4)	0.870(33)	4.47	0.836	4.34	0.864
	410	5.53(9)	0.830(70)	5.53	0.836	5.43	0.864
	770†	7.28(3)	0.623(14)	7.19	0.836	7.13	0.864
$^{22}Ne+H_2$	196	2.83(2)	1.014(53)	3.42	0.836	3.27	0.864
	265	4.07(5)	0.898(36)	4.29	0.836	4.16	0.864
	343	4.86(6)	0.877(34)	5.03	0.836	4.92	0.864
	536	6.47(3)	0.860(32)	6.27	0.836	6.19	0.864
	661†	7.00(3)	0.838(22)	6.82	0.836	6.75	0.864
$^{21}Na+H_2$	1150†	8.48(6)	0.632(43)	8.70	0.880	8.64	0.873
$^{23}Na+H_2$	175	2.99(18)	0.827(70)	3.14	0.880	2.94	0.873
	200*	3.48(1)	0.780(11)	3.56	0.880	3.37	0.873

Table 5.3: Continued.

	238	3.86(5)	0.847(30)	4.11	0.880	3.93	0.873
	269	3.98(16)	1.005(51)	4.49	0.880	4.32	0.873
	297	4.69(3)	0.912(20)	4.81	0.880	4.65	0.873
	312	4.63(9)	0.955(44)	4.96	0.880	4.81	0.873
	374*	5.38(1)	0.897(7)	5.54	0.880	5.39	0.873
	435	5.64(3)	0.950(23)	6.01	0.880	5.87	0.873
	478*	6.30(1)	0.937(8)	6.30	0.880	6.17	0.873
	484	6.02(3)	0.920(22)	6.34	0.880	6.21	0.873
	505	6.42(2)	0.874(11)	6.46	0.880	6.34	0.873
	515	6.77(6)	0.858(32)	6.52	0.880	6.40	0.873
	524	6.63(26)	0.870(81)	6.58	0.880	6.46	0.873
	686†	7.71(5)	0.619(14)	7.36	0.880	7.26	0.873
$^{24}Mg+H_2$	200*	3.68(2)	0.758(21)	3.62	0.923	3.38	0.882
	227	3.88(5)	0.823(68)	4.05	0.923	3.82	0.882
	438	5.79(10)	1.109(71)	6.31	0.923	6.14	0.882
	500*	6.75(1)	0.949(6)	6.76	0.923	6.60	0.882
	800*	8.44(1)	0.839(5)	8.27	0.923	8.14	0.882
$^{26}Mg+H_2$	206	3.18(18)	0.916(94)	3.72	0.923	3.48	0.882
$^{26}Al+H_2$	470	6.51(4)	0.946(42)	6.84	0.965	6.62	0.890
$^{27}Al+H_2$	210	3.52(9)	0.805(64)	3.84	0.965	3.55	0.890
$^{35}Cl+H_2$	173	3.51(45)	1.097(162)	3.00	1.117	2.49	0.917
	259	4.47(47)	1.103(165)	4.88	1.117	4.40	0.917
	294	5.34(11)	0.943(42)	5.49	1.117	5.03	0.917
	377†	6.61(6)	0.698(40)	6.70	1.117	6.26	0.917
	393	6.41(10)	0.910(38)	6.90	1.117	6.47	0.917
	478	7.31(4)	0.918(39)	7.86	1.117	7.45	0.917
$^{39}K+H_2$	335	6.23(3)	0.993(13)	6.31	1.188	5.74	0.928
	417	6.93(63)	0.966(23)	7.50	1.188	6.96	0.928
	545	8.20(51)	0.948(43)	8.96	1.188	8.46	0.928
	610	9.07(53)	0.953(44)	9.58	1.188	9.09	0.928
	667	9.45(13)	1.056(59)	10.06	1.188	9.59	0.928
	731	9.88(34)	1.029(31)	10.55	1.188	10.09	0.928

*Values from Liu paper

†Values excluded from fit

The newly compiled data can be seen below in several figures arranged by reaction. Several $^{21}Ne + H_2$ CSD's can be seen in Figure 5.22, looking at the 3 lowest energy distributions they appear to be approximated well by the semi-empirical formula. The means are within 1/3 of a charge state. For the higher energy distribution, the 8+ charge state seems to be significantly overproduced relative to the expectations from Liu's formula and as a result

Table 5.4: Charge state distributions for previous DRAGON experiments for Helium gas targets

		Experimental		Liu		Modified	
Reaction	E_{lab} [keV/u]	$\overline{q}$	d	$\overline{q}$	d	$\overline{q}$	d
^{9}Be+He	275	2.33(9)	0.697(41)	2.36	0.506	2.33	0.780
	278	2.35(8)	0.682(39)	2.37	0.506	2.34	0.780
	285	2.28(11)	0.766(55)	2.40	0.506	2.37	0.780
	422	2.84(4)	0.722(46)	2.78	0.506	2.75	0.780
	523†	3.16(4)	0.738(49)	2.98	0.506	2.95	0.780
^{11}B+He	194	2.40(12)	0.565(28)	2.25	0.572	2.21	0.800
	213	2.48(12)	0.576(29)	2.37	0.572	2.33	0.800
^{12}C+He	162	2.05(15)	0.794(61)	2.17	0.632	2.13	0.816
	167	2.01(17)	0.811(66)	2.22	0.632	2.18	0.816
	194	2.28(11)	0.580(24)	2.45	0.632	2.41	0.816
	1466†	5.54(6)	0.617(29)	5.22	0.632	5.20	0.816
^{15}N+He	563	2.41(5)	0.748(22)	4.52	0.687	4.48	0.830
^{16}O+He	138*	2.12(2)	0.885(11)	2.08	0.739	2.04	0.848
	200*	2.77(3)	0.838(24)	2.81	0.739	2.77	0.848
	325*	3.66(1)	0.877(5)	3.81	0.739	3.76	0.848
	371*	3.92(1)	0.841(8)	4.08	0.739	4.04	0.848
	588*	4.98(1)	0.842(8)	5.02	0.739	4.98	0.848
	750*	5.62(3)	0.735(34)	5.49	0.739	5.46	0.848
	875*	5.78(1)	0.635(5)	5.78	0.739	5.74	0.848
^{18}O+He	526	4.57(8)	0.877(34)	4.80	0.739	4.76	0.848
^{19}F+He	190	2.92(15)	0.915(46)	2.81	0.789	2.77	0.854
	239	3.41(10)	0.845(36)	3.33	0.789	3.28	0.854
	259	3.55(6)	0.869(23)	3.52	0.789	3.47	0.854
	346	4.13(2)	0.864(8)	4.19	0.789	4.14	0.854
	626	5.52(1)	0.898(8)	5.56	0.789	5.52	0.854
	638	5.54(3)	0.950(32)	5.60	0.789	5.56	0.854
^{20}Ne+He	290	3.79(8)	0.983(47)	3.96	0.836	3.91	0.864
	304	4.13(5)	0.995(42)	4.08	0.836	4.03	0.864
	502	5.15(6)	0.976(47)	5.38	0.836	5.33	0.864
	642	5.84(3)	0.944(28)	6.01	0.836	5.96	0.864
	714†	7.39(8)	0.809(65)	6.27	0.836	6.23	0.864
	1093†	6.84(2)	0.526(18)	7.28	0.836	7.25	0.864
^{40}Ar+He	484	6.96(21)	0.899(89)	7.09	1.153	7.06	0.923
	540	7.24(11)	0.923(39)	7.60	1.153	7.57	0.923
^{44}Ti+He	537†	9.97(2)	0.585(25)	8.25	1.287	8.23	0.944
	706	10.07(11)	0.827(29)	9.80	1.287	9.79	0.944

$*$Values from Liu paper

†Values excluded from fit

the distribution does not agree well with a Gaussian and the width is much less than expected from the Liu formula. The charge state overproduction does not drastically change the fit as the result agrees very well with the expected $\overline{q}$ but again the width is significantly less. The distributions for all other energies are recreated very well by the semi-empirical formula using both the updated and previous parameters and are well described by a Gaussian. An explanation for this overproduction could be that the resulting $^{21}Ne^{+8}$ ion has only two remaining electrons that close the 1s shell. This electronic structure is very similar to the noble gas helium. As a result, this would cause the next ionization energy to be much larger and result in an overproduction of the 8+ charge state and an underproduction in the 9+ charge state as it takes significantly more energy to remove the 9th electron and break that shell closure. A table of the ionization energies up to Fe^{+26} can be seen in Table B.3, Table B.4, and Table B.5 located in Appendix B. Looking at the +9 ionization energy for Ne, which correlates to breaking the helium like structure, it is 5 times the 8+ ionization energy. Looking through the ionization energies for other elements discontinuities can be seen in ions where the resulting iso-electronic series is a noble gas. That means any Ne CSD measurements that extend past the 8+ charge state should show similar effects. Since Ne is a noble gas itself it can be seen that the 1st ionization energy is higher for Ne than for both of its neighbors F and Na. This does not seem to have a noticeable effect on the resulting Ne CSD's compared to the Liu formula.

Looking at Figure 5.23, $^{20}Ne + H_2$, the 8+ charge state is overproduced relative to the Liu formula for all three energies measured. The resulting mean of the distributions is not changed very much as the $\overline{q}$ is very close to the 8+ charge state, only the distribution widths end up decreasing compared to expectations. Also, looking at $^{22}Ne + H_2$, Figure 5.24, at 661 keV/u the 8+ charge state does not agree well with the expected Gaussian as it is again overproduced. The 7+ charge state also does not agree well with the Gaussian expectation but is much closer to the fit than the 8+. This discrepancy might be explained by an issue with the measurement itself, such as operator error. In this case, the resulting fit again agrees

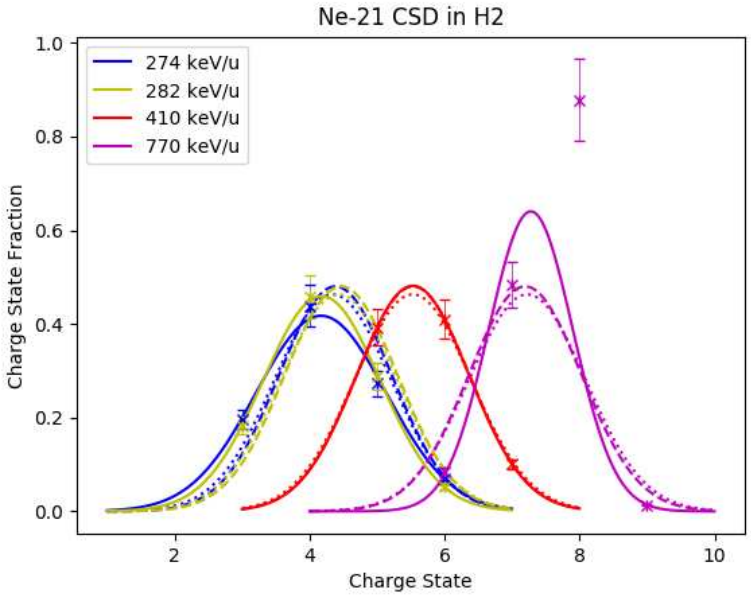

Figure 5.22: Charge state distributions for ^{21}Ne in hydrogen. The solid lines are experimental fits, the dashed lines are the semi-empirical formula using the parameters found by Liu and the dotted lines are from the semi-empirical formula using updated parameters.

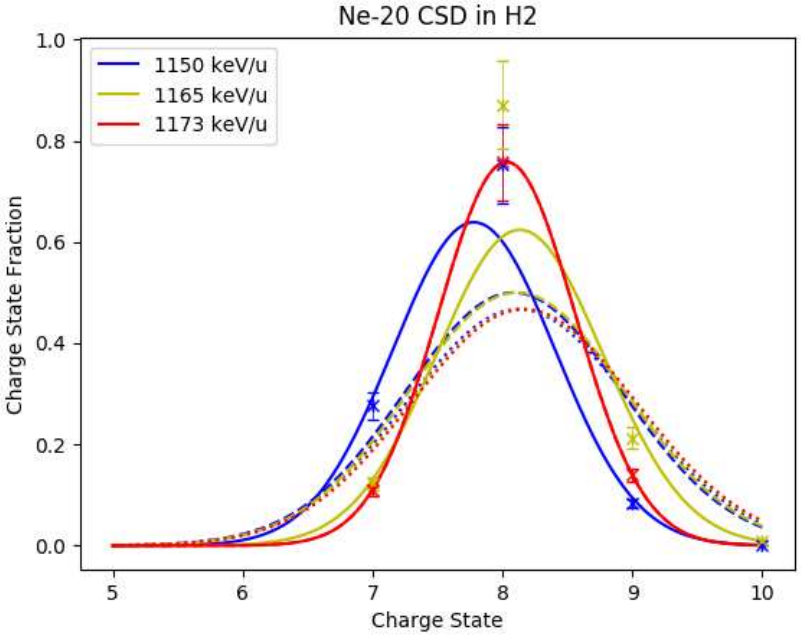

Figure 5.23: Charge state distributions for ^{20}Ne in hydrogen. The solid lines are experimental fits, the dashed lines are the semi-empirical formula using the parameters found by Liu and the dotted lines are from the semi-empirical formula using updated parameters.

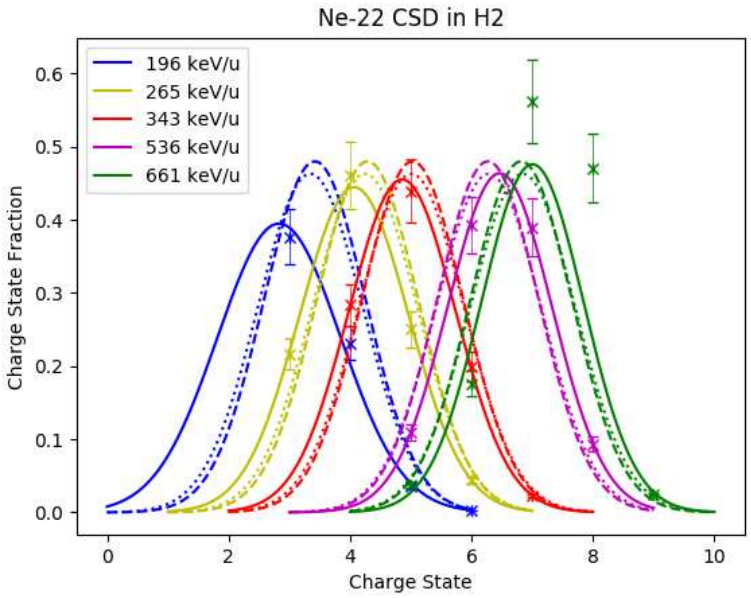

Figure 5.24: Charge state distributions for ^{22}Ne in hydrogen. The solid lines are experimental fits, the dashed lines are the semi-empirical formula using the parameters found by Liu and the dotted lines are from the semi-empirical formula using updated parameters.

well with the expectations. The overproduction can also be seen in ^{20}Ne + ^{4}He in Figure 5.25 at 1093 keV/u and could be the explanation for the poor agreement between experiment and the formula for the 714 keV/u measurement. For the 1093 keV/u measurement the 8+ charge state is overproduced but since the expected mean was approximately 8+ this doesn't change the mean much and mostly causes the width to go down. Looking at the 714 keV/u measurement the 8+ charge state is roughly equal to the 7+ and the resulting mean is 7.4 which agrees poorly with the estimated 6.2. If the 8+ was not enhanced due to the helium like effects the mean would likely then be close to 7 and the expected distribution would agree much better with the measured distribution. All other Ne distribution measurements that don't span to the 8+ charge state or have no expected 9+ contribution do not show this effect and all measured $\overline{q}$ agree within a half charge state. Due to the nature of the semi-empirical formula, these iso-electronic series effects are unable to be accounted for. As a result, the Ne CSD measurements mentioned specifically to show this effect have been

removed from the parameter fit which will be discussed later in this section.

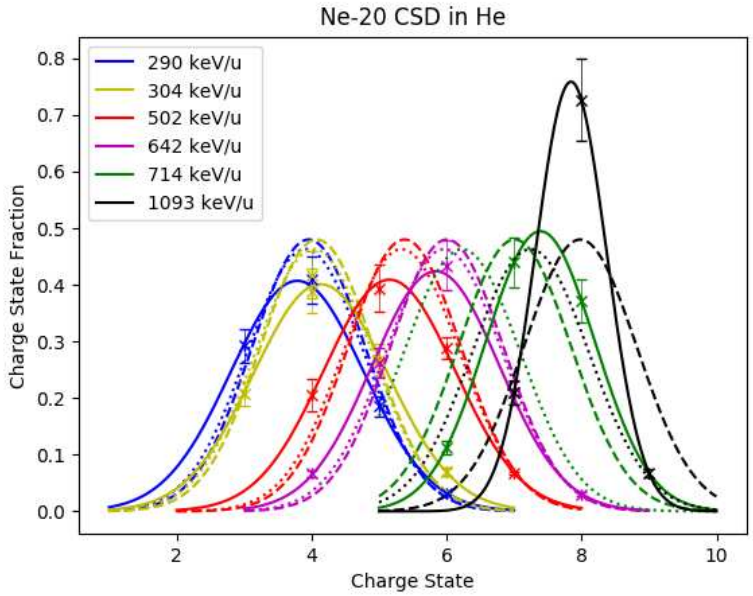

Figure 5.25: Charge state distributions for ^{20}Ne in helium. The solid lines are experimental fits, the dashed lines are the semi-empirical formula using the parameters found by Liu and the dotted lines are from the semi-empirical formula using updated parameters.

This effect should be apparent in elements other than Ne too, but at different charge states which correlate to a resulting noble gas iso-electronic series. This could be the potential cause of the poor agreement between experiment and the semi-empirical formula in the ^{23}Na distribution at 686 keV/u, see Figure 5.26. Na^{+9} looks like ^{4}He electronically, so it would be expected that the 9+ charge state would be enhanced in any Na CSDs. For the 686 keV/u measurement it is enhanced by a factor of 2 compared to the experimental Gaussian fit and the semi-empirical formula. This causes the $\overline{q}$ to be shifted towards the 9+ charge state and the width to be decreased. The 8+ charge state also appears to be enhanced but not nearly as drastically as the 9+. Looking at the 1150 keV/u distribution the 9+ charge state is again enhanced but the mean is not changed much as it was expected at approximately 9+. These two CSD measurements were also excluded from the final fit. Additional Na CSD measurements can be seen in the Appendix.

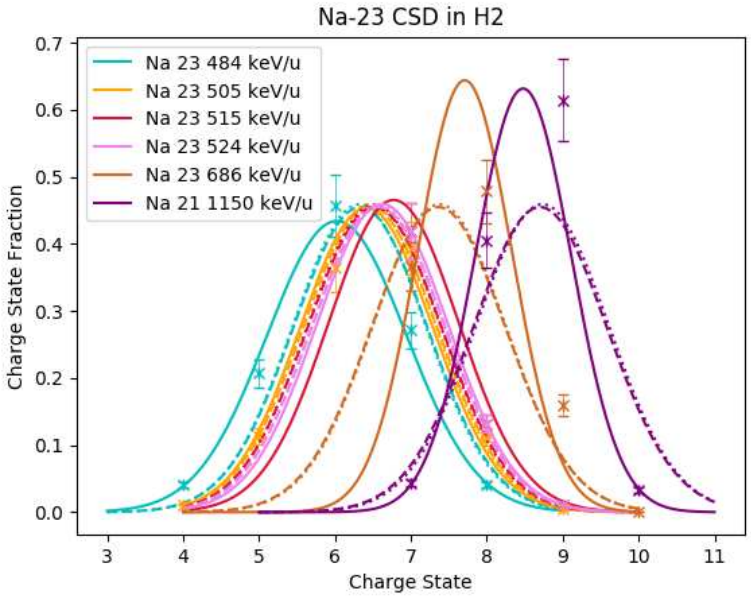

Figure 5.26: Charge state distributions for ^{23}Na in hydrogen. The solid lines are experimental fits, the dashed lines are the semi-empirical formula using the parameters found by Liu and the dotted lines are from the semi-empirical formula using updated parameters.

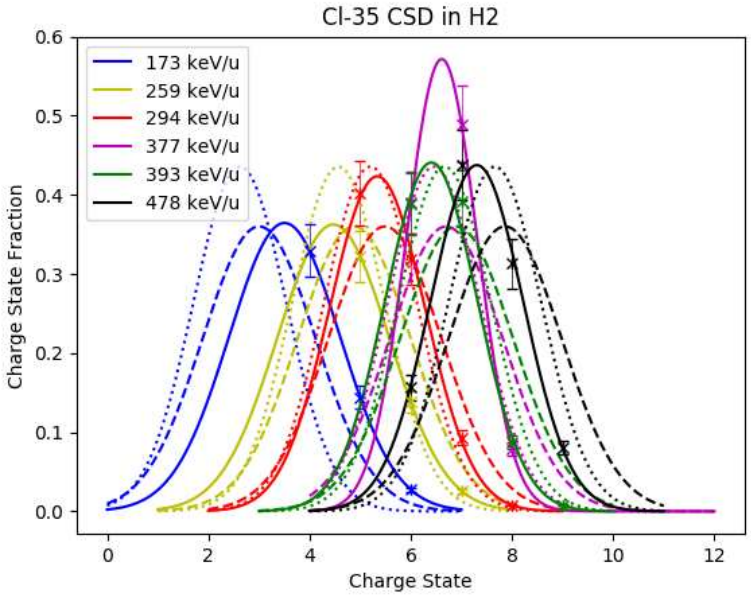

Figure 5.27: Charge state distributions for ^{35}Cl in hydrogen. The solid lines are experimental fits, the dashed lines are the semi-empirical formula using the parameters found by Liu and the dotted lines are from the semi-empirical formula using updated parameters.

For the element Cl which has 17 electrons, the Cl^{+7} ion looks like Ne and correlates to the closure of the 2p shell and has an ionization energy into the 8+ state about 3 times larger than the previous ionization energy. Also the Cl^{+12} ion looks like He and its next ionization energy is almost 5 times larger than the previous one. This shows that the 1s shell closure is much more tightly bound than the 2p shell closure. The result should be the enhancement of any 7+ and 12+ charge state fractions for the Cl measurements. For the Cl CSD's seen in Figure 5.27, in the measurements below 300 keV/u there is very little expected in the 7+ and 8+ charge states so these distribution means are not effected and therefore agree well with expectations. The 377 keV/u measurement looks like 7+ charge state is enhanced but the expected mean is approximately 7+ so this is not effected much. The resulting width is less and the 8+ charge state is underproduced relative to expectation. Looking at the next highest energy distribution, 393 keV/u, the 7+ charge state is enhanced slightly compared to the expected but not outside of the bounds of error. This CSD should show similar effects to the 377 keV/u distribution but the width is not decreased relative to the other measurements. In the 478 keV/u measurement the 7+ charge state is enhanced relative to the Liu formula and the mean is also shifted down towards 7+. The differences in expected width will be discussed later in this section. Only the 377 keV/u state was excluded from the final fit because the 478 keV/u measurements agreed with the overall trend in the final fits while the 377 keV/u measurement was an obvious outlier.

The distribution measurements for C + ^{4}He can be seen in Figure 5.28 and the 3 low energy measurements agree fairly well with expectation. The distribution widths are varied compared to expectation but generally within error and the means agree well. There are no expected iso-electronic effects for these distributions as the 4+ charge state correlates to He and none of the distributions have a significant 4+ contribution. For the higher energy distribution at 1466 keV/u the measured distribution agrees poorly with what was measured. This is due to the complete ionization of the C ion which is outside the scope of the semi-empirical formula. The resulting distribution has a larger contribution in the 6+ charge

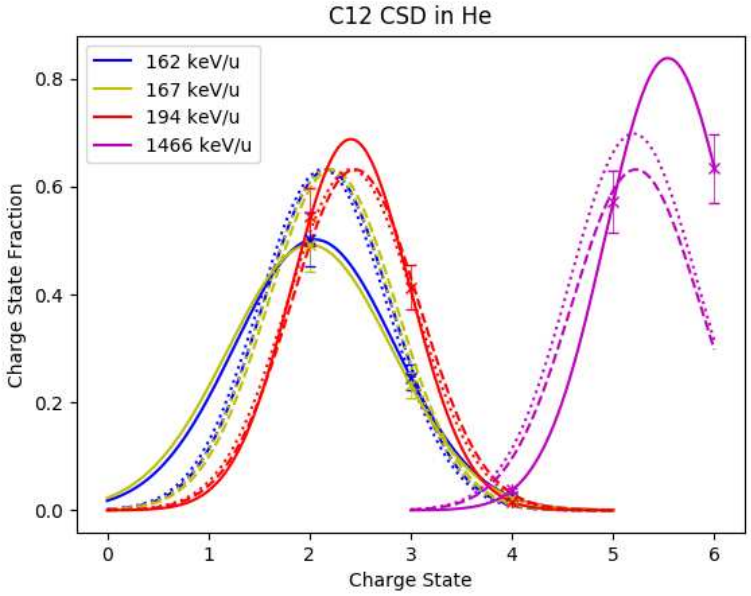

Figure 5.28: Charge state distributions for ^{12}C in helium. The solid lines are experimental fits, the dashed lines are the semi-empirical formula using the parameters found by Liu and the dotted lines are from the semi-empirical formula using updated parameters.

state as the ion no longer has any remaining electrons. It is mentioned in the paper by Betz [62], that these semi-empirical formulae are not accurate for values of $\overline{q}/Z$ close to 1, likely because of this effect. This CSD measurement was also excluded from the final fit as this effect cannot currently be accounted for using the semi-empirical formula.

CSD's for ^{9}Be can be seen in Figure 5.29 for energies from 275 keV/u to 523 keV/u. The measured means agree very well with the expected for all but the 523 keV/u measurement but the widths agree poorly compared to the results from Liu's formula. This is likely because Liu only had data that ranged from $7 \leq Z \leq 12$ so this is outside the range of those parameters. For the 523 keV/u measurement the 4+ charge state is enhanced compared to expectations because the 4+ charge state is completely ionized. This causes the mean to be shifted upwards towards 4+ and this measurement was excluded from the final fit as a result. It should be expected that the 2+ charge state, which correlates to the He iso-electronic series, would be enhanced but all the data are fit very well by a Gaussian. The

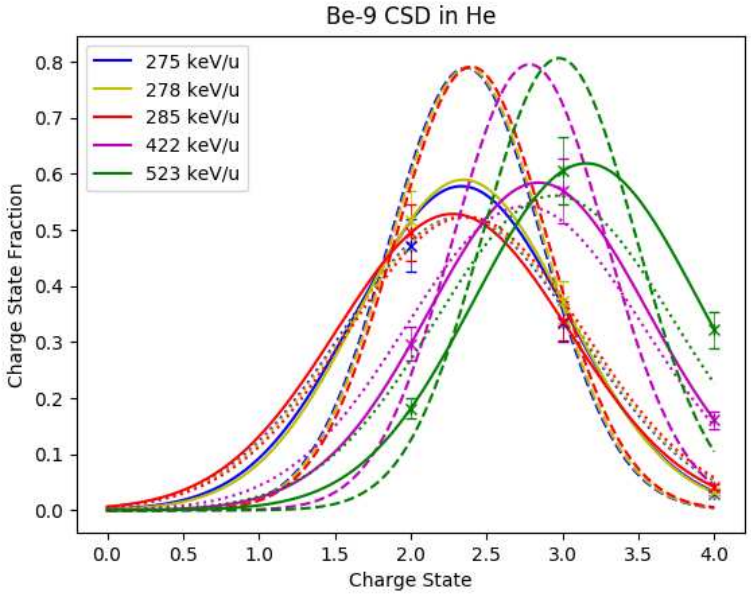

Figure 5.29: Charge state distributions for ^{9}Be in helium. The solid lines are experimental fits, the dashed lines are the semi-empirical formula using the parameters found by Liu and the dotted lines are from the semi-empirical formula using updated parameters.

lack of enhancement might be explained by the fact that the expected mean is above the 2+ charge state so the majority of the electrons have more kinetic energy than the discontinuity which lessens the effect.

Measured CSD's for ^{44}Ti can be seen in Figure 5.30 at energies of 537 and 706 keV/u. The 537 keV/u data appears to be shifted towards higher charge states and agrees very poorly with the expectation from the Liu formula and is off by nearly 2 full charge states. This appears to be some error with the measurements itself as the 706 keV/u measurement agrees well with the expected charge state mean but the width is off again as this was outside the previous range of data available for Liu. The 537 keV/u measurement may have been mislabeled as the wrong energy or possibly the wrong charge states recorded. This measurement was found recorded in an old paper log book with minimal details so this distribution was also excluded from the final fit and the direct measurement itself should not be used.

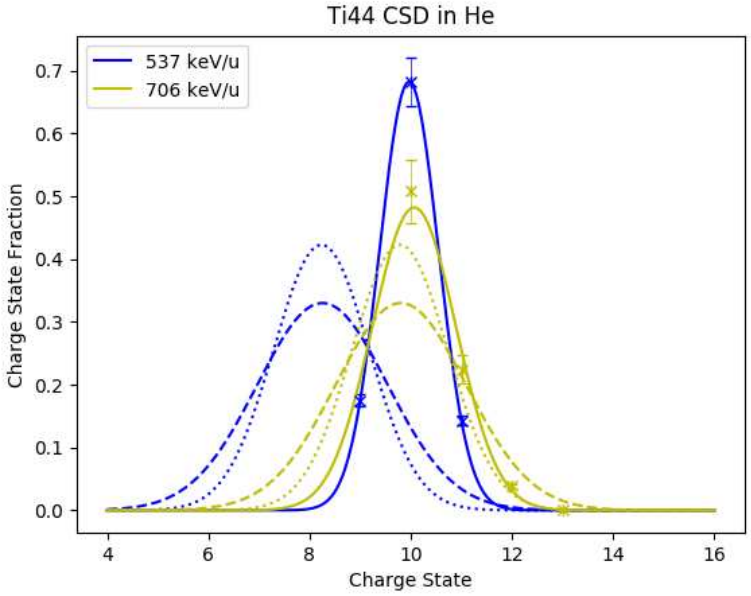

Figure 5.30: Charge state distributions for ^{44}Ti in helium. The solid lines are experimental fits, the dashed lines are the semi-empirical formula using the parameters found by Liu and the dotted lines are from the semi-empirical formula using updated parameters.

When Liu fit her data she used a γ of 0.44515 for both hydrogen and helium targets, which was found in the work by Betz. Using the same value of γ we plotted the reduced parameters ln(1-$\overline{q}$/Z) vs v/(v$_o Z^{\gamma}$) and saw that our data also followed a linear trend with a non zero intercept, B, and slope, A. We then fit this data individually for hydrogen and helium targets using least squares minimization to determine the optimal linear fit for this γ. In order to quantify the improvement of the updated parameters we calculated the reduced chi squared for each fit,

$$\chi^2_{red} = \frac{1}{K}\Sigma_i^N \frac{(\overline{q}_{fit} - \overline{q}_{exp})^2}{\sigma_{exp}} \tag{5.11}$$

where K is the number of degrees of freedom which for a linear fit is N-2. The resulting fit for both hydrogen and helium were visually very similar to the fits found by Liu and can be seen in Figure 5.31 and Figure 5.32. In order to quantify the improvement in the semi-empirical formula by using the updated parameters we calculate the relative difference in the χ^2_{red} value for each fit. For the hydrogen fit the updated parameters gave a χ^2_{red} of

34.32 which compared to the χ^2_{red} from Liu's parameter set of 41.32 is an improvement of 16.7%. The resulting fit parameters for hydrogen and a γ value of 0.44515 was A = 1.4598 and B = 0.4868. For the helium data the updated parameter χ^2_{red} was found to be 22.1 which when compared to the results using Liu's parameter set for helium, which had a χ^2_{red} of 22.4, is an improvement of 1.7%. The resulting fit parameters were for a γ of 0.44515, A = 1.1315 and B = 0.3466.

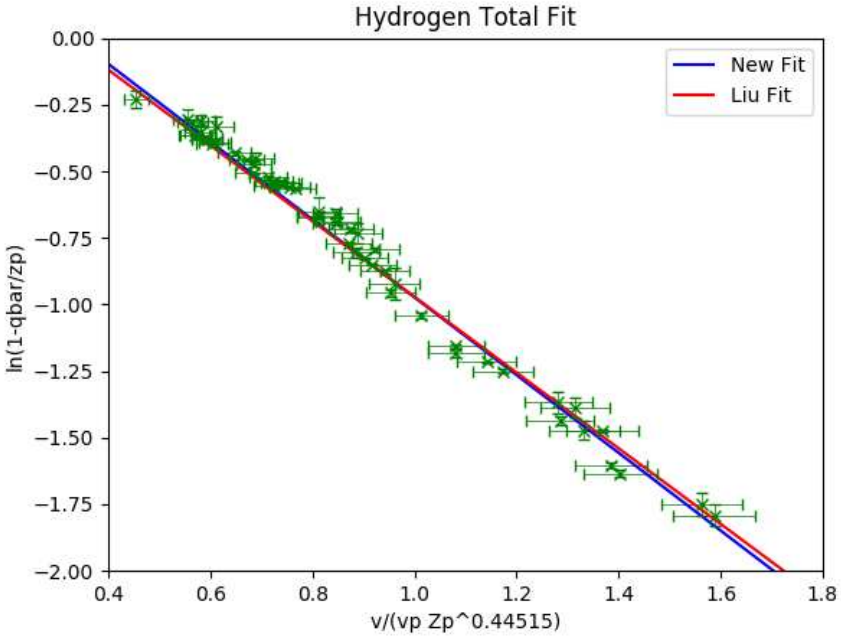

Figure 5.31: Parameter fit for hydrogen CSD data for a γ value of 0.44515. The vp in the reduced velocity is v′ mentioned in previous section.

A further improvement on the updated parameters was done by allowing γ to be a free parameter. In going through the work by Betz it was seen that originally γ was a free parameter and the value used by Liu corresponded to the best fit for carbon foil targets. We then performed a linear fit for each value of γ in the likely range of γ values and calculated the χ^2_{red} for each. The resulting parameters that minimized the χ^2_{red} were for hydrogen targets A = 1.55563, B = 0.48386, and γ = 0.47299. For helium, the resulting best fit was A = 1.10101, B = 0.34635, and γ = 0.43236. With the updated parameters, the χ^2_{red}=21.9

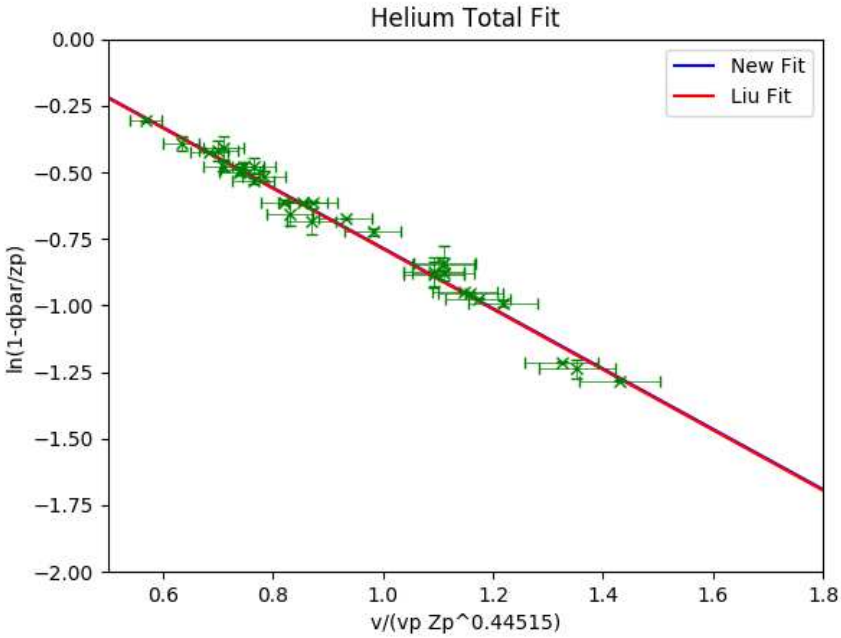

Figure 5.32: Parameter fit for helium CSD data for a γ value of 0.44515.

for helium targets, which is an improvement of 2.2%. For hydrogen the χ^2_{red}=31.61 using the updated parameters. Which corresponds to an improvement of 23.5% on average. The resulting fits can be seen below in Figure 5.33 for hydrogen and Figure 5.34 for helium. Liu's data is shown in red to emphasize the addition of new data. These can't be visually compared to Liu's results because the reduced velocity depends on γ and would not fit the data in these figures. The excluded CSD's mentioned earlier are in yellow to highlight them as outliers in either the width or mean figures. A ^{15}N CSD at 435 keV/u, which was a part of Liu's original data set, was excluded as well because it was an outlier in the mean charge state plot as mentioned in the work by Liu. This was the first CSD measured at DRAGON and could likely have contained a systematic error in the measurement. Thus by allowing γ to be a free parameter we have improved even further on the previous work and have arrived at the currently recommended parameter set.

After fitting the mean charge data the distribution width parameters needed to be updated as well. The new data spans a larger range of Z values compared to the previous

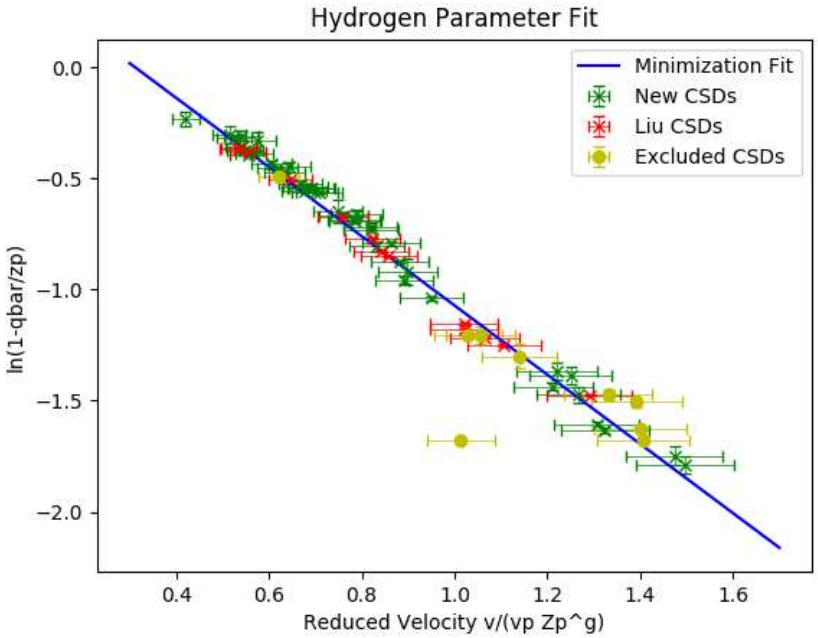

Figure 5.33: Parameter fit for hydrogen CSD data where γ is a free parameter. Liu's data is in red, the new data is in green and any excluded CSDs are in yellow.

data available to Liu. The width in the semi-empirical formula depends only on the atomic number Z and is the same for both hydrogen and helium targets. In Figure 5.35, the newly added data can be seen compared with both fits. The result allows this to be used for a much wider range of Z values and shows that the distribution width changes much more slowly for large values of Z than from Liu's fit. The best fit parameters were found to be d_1 = 0.66826284 and w = 0.11161432. This shows why the estimations from Liu's parameters had too small of a width for ions such as Be and too large of a width for ions like Cl. It is suggested that the updated parameters for both the mean and width be used for atomic numbers of 4 to 22 and energies of 138 to 1100 keV/u.

In order to confirm the assumption that a Gaussian distribution properly models the measured charge state distributions the skew or s was calculated via Equation 5.10 for all measured distributions where missing measurements would not artificially skew the distribution. Several distributions were also excluded because of the electronic structure effect which

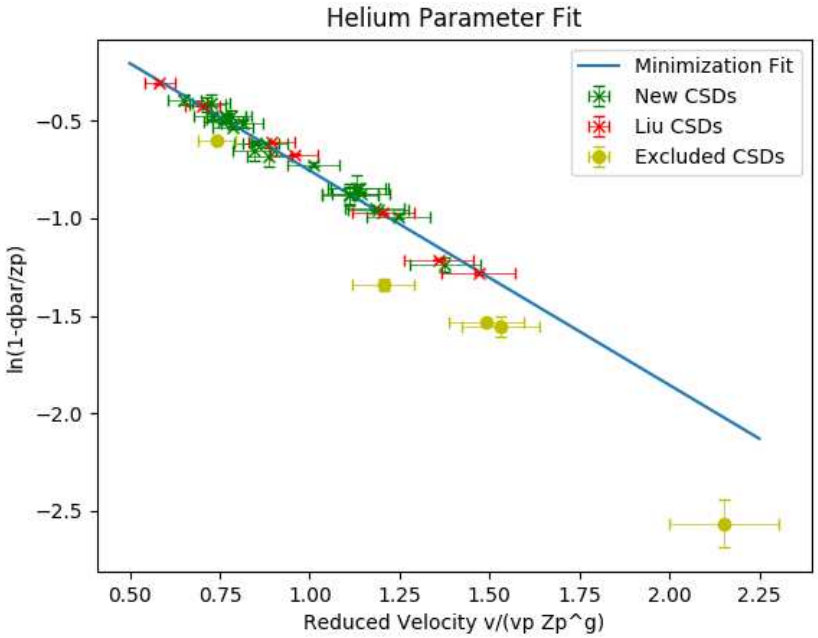

Figure 5.34: Parameter fit for helium CSD data where γ is a free parameter. Liu's data is in red, the new data is in green and any excluded CSDs are in yellow.

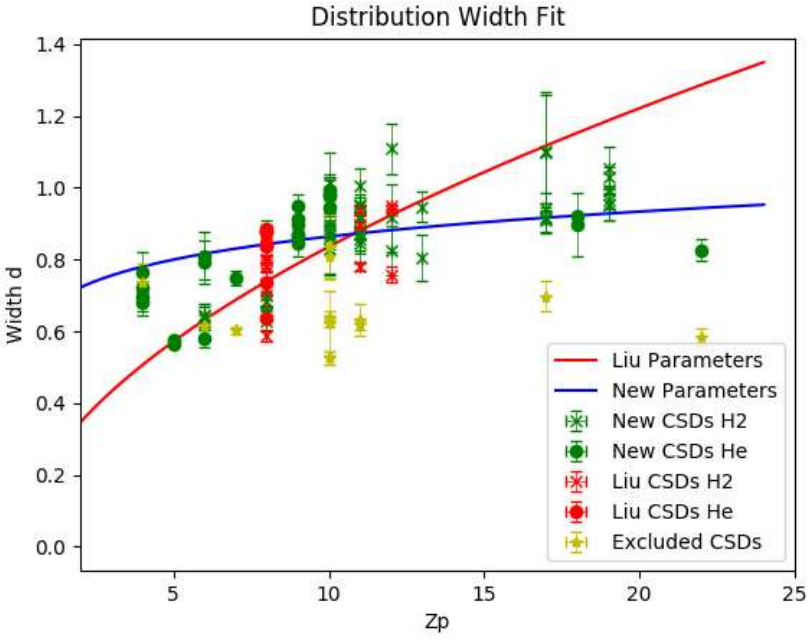

Figure 5.35: Parameter fit for helium CSD data.

enhanced specific charge states and would artificially cause the distribution to be skewed. The results can be seen in Figure 5.36. All values of skew fall below 0.3 which shows that

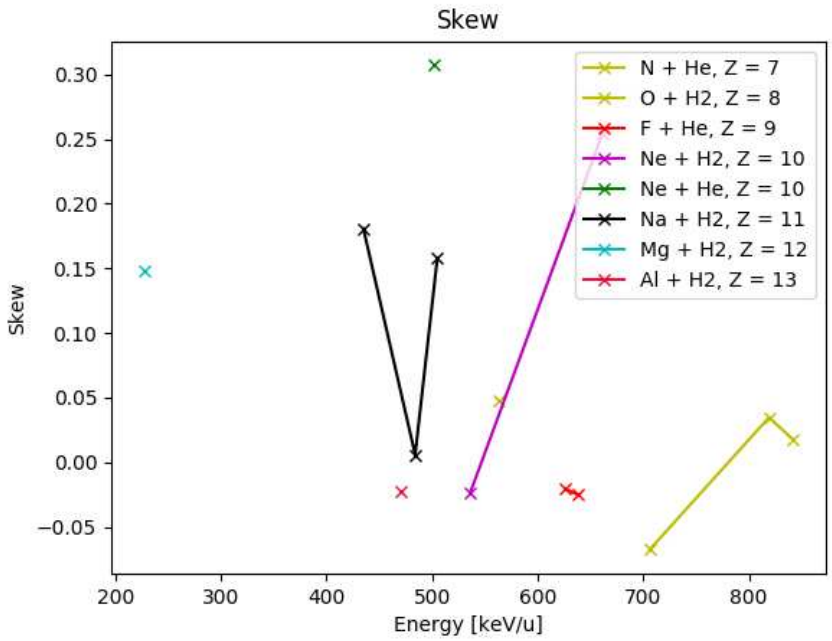

Figure 5.36: Calculated skews for measured charge state distributions. Solid lines are to show the trend of specific elements with energy.

the measured distributions are very symmetric and approximating them with a Gaussian is appropriate.

Codes such as CASP (Convolution Approximation for Swift Particles), which are primarily used to calculate stopping power, also can calculate charge state distributions. We decided to compare the results from CASP to the experimentally measured data. The code outputs charge state fractions and calculates the stopping power for each charge state so these values were recorded for each corresponding distribution and were fit with a Gaussian to get the mean and width. These were then taken and fit in the same manner as the experimental data with a γ value of 0.44515, as the reduced parameters also followed a linear trend for the CASP CSDs. The resulting comparison for hydrogen can be seen in Figure 5.37 where the values can be seen to agree at lower values of the reduced velocity but begins to

disagree significantly at higher values. The best fit parameters for hydrogen with a fixed γ=0.44515 were A=1.0324 and B=0.2237. We also wanted to see if CASP could capture the enhancement in various charge states due to noble gas iso-electronic series so we plotted and fit the CASP CSD's which can be seen in Figure 5.38. These are fit with a Gaussian and it can be seen that they agree perfectly. This shows that the CASP CSD is likely calculated in a similar manner to Liu's formula, by calculating the mean and width of the resulting Gaussian and calculating the fractions from that distribution. As a result CASP is unable to account for the iso-electronic effects seen in the experimental measurements.

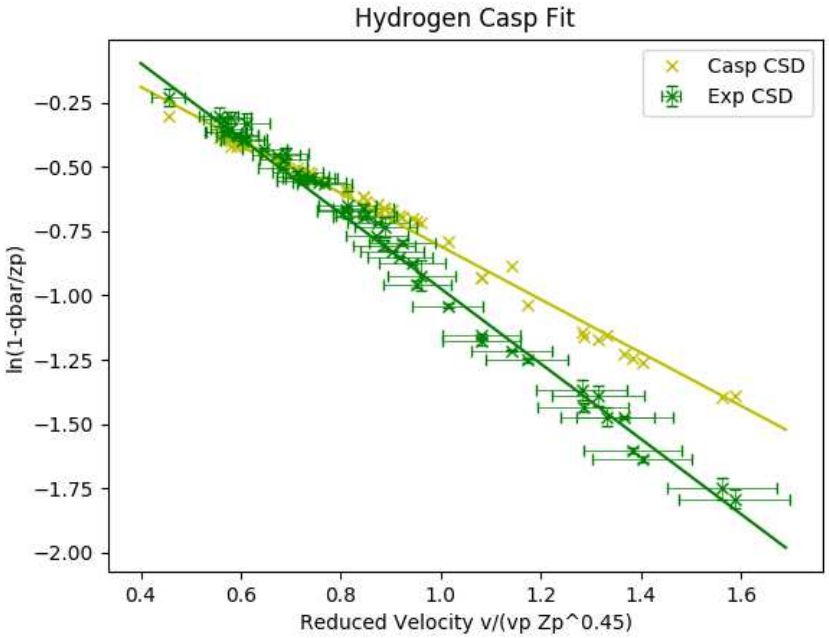

Figure 5.37: CSD reduced parameter fit for a γ value of 0.44515 for CASP hydrogen values in yellow and experimental values in green.

The same fit for CASP distributions in helium can be seen in Figure 5.39 where the two data sets have nearly the same slope but a slightly different offset but overall the two sets agree very well. The best fit parameters for helium for a fixed $\gamma = 0.44515$ were found to be A = 1.0728 and B = 0.2292.

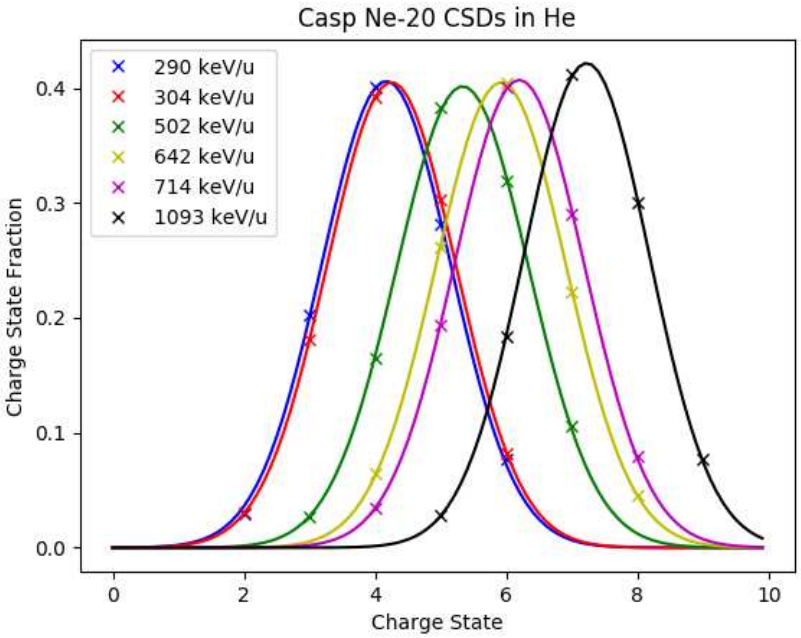

Figure 5.38: Parameter fit for Casp ^{20}Ne+He CSD data.

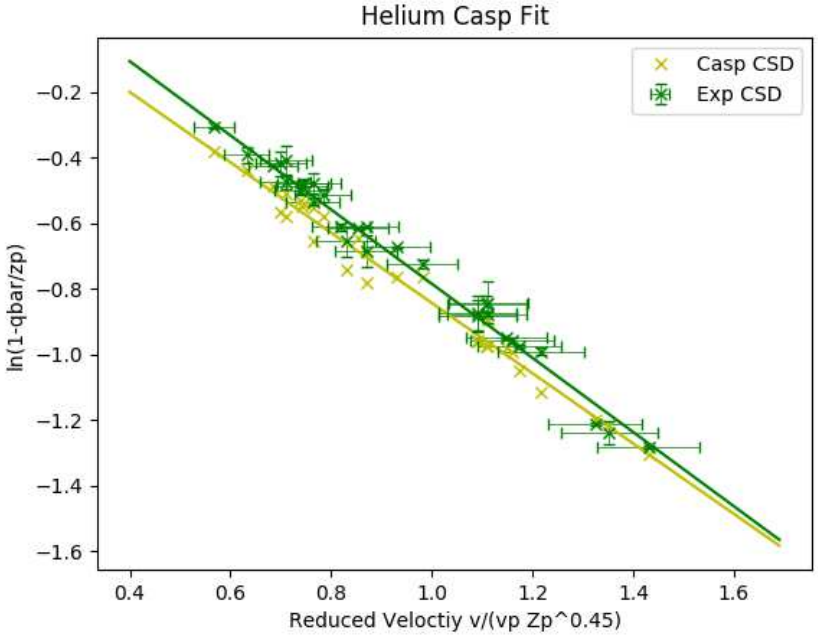

Figure 5.39: CSD reduced parameter fit for a γ value of 0.44515 for CASP helium values in yellow and experimental values in green.

5.5 Stopping Powers

The beam stopping power is indirectly measured at every recoil measurement done at DRAGON. The incoming and outgoing beam energy is measured to determine the position of the resonance in the gas target and the stopping power can be calculated from this information. These measurements are less precise than the usual stopping power measurements which utilize multiple pressures and provide more than 2 points to fit but are done for every experiment. Again a backlog of information existed with previous DRAGON experiments so as an additional part of this work we have gone through the paper and electronic logs of past experiments to extract the stopping power information where possible. This information is presented in a condensed format below in the Appendix, organized by the beam and target. If a reaction has enough data to be properly fit then a complete comparison to the results of SRIM can be done and can be seen in a series of plots discussed individually below. The error in each individual measurement is mostly dependent on the ratio of the uncertainty in the energy measurement to the total energy lost through the target. Some of the values found in the paper logs had small energy losses relative to the uncertainty and error for these points reaches up to 50%.

All stopping power distributions with enough data to be properly fit were fit to a modified Gaussian function defined as,

$$f(x) = A * \mathrm{Exp}[-\frac{(log10(x) - \mu)^2}{2d^2}]. \tag{5.12}$$

To determine the goodness of the fit, the reduced χ^2 was calculated using Equation 5.11 with $\overline{q}$ replaced with the stopping power.

The experimental data for the Na+H_2 agrees fairly well with the results from SRIM for lower energies but appears to peak about 20% lower than SRIM and is not as wide of a distribution as can be seen in Figure 5.40. More experimental data could be used at energies below about 2×10^2 and above 1×10^3 keV/u to confirm a total comparison to the results from SRIM. It should be noted that when sufficient experimental data existed the stopping power

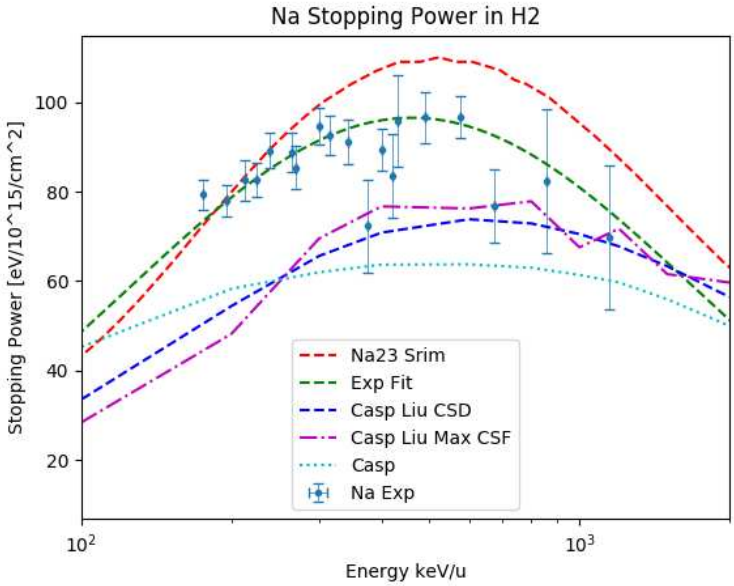

Figure 5.40: Stopping power as a function of energy for Na+H_2 compared to SRIM in red. Experimental fit is in green. The light blue line is the result from CASP, the purple is the stopping power of the maximum charge state from the updated Liu formula, and the dark blue is using the complete distribution from the updated Liu formula.

was averaged over multiple measurements for a small range of energies. Because these plots are done with a logarithmic scaling there is no easy systematic range of energies to average over so this was done visually for each plot. This is done mostly for the ease of viewing these plots and comparing overall trends between experiment, SRIM and CASP. The experimental fits are done using all of the available experimental data, which again can be found in the Appendix. The results from the fit are A = 96.50, μ = 2.663, and d = 0.568 which resulted in a χ^2_{red} of 8.76.

We decided to also compare the results from the code CASP, which calculates the stopping power for ions in gaseous targets. This is done by calculating the stopping power for each individual charge state then using the charge state distribution a total stopping power is calculated. It was found that CASP tends to underestimate the charge state mean and therefore estimate a smaller total stopping power. The light blue dotted curve in Figure 5.40 is the direct result from CASP and peaks at roughly half the height of that expected by

SRIM. We decided to use the stopping power for the maximum charge state found by the updated Liu formula to see if this could more closely recreate the stopping power found experimentally. While this did slightly improve the agreement as can be seen by the purple curve, this made the distribution have discontinuities which correspond to changes in the maximum charge state which have a significantly different stopping power. We then decided to calculate the total stopping power using the full distribution found by the updated Liu formula in the same manner as CASP and this was plotted as the dark blue dashed curve. It can be seen that this smooths out the discontinuities but does not better predict the stopping power compared to experiment.

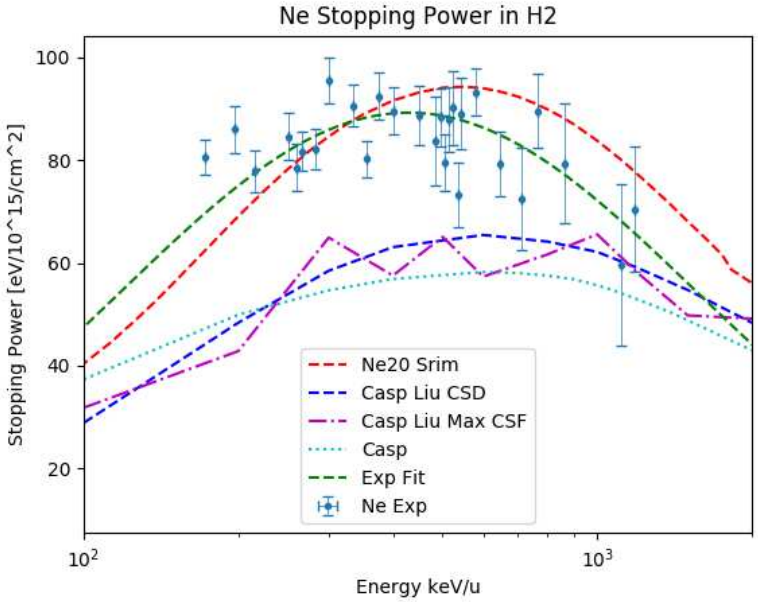

Figure 5.41: Stopping power as a function of energy for Ne+H_2 compared to SRIM in red. Results directly from CASP are in light blue. Results from CASP re-normalized to the CSD from the updated Liu formula are in dark blue. The experimental fit is in green.

For the Ne+H_2 data it appears to agree well with SRIM. The fitted experimental data peaks about 10% lower than the results from SRIM and are shifted slightly to the left and can be seen in Figure 5.41. The fitted width seems to agree well with the results from SRIM but due to the shift the overall agreement is poor. The resulting fit parameters are A =

89.25, $\mu = 2.633$, and d = 0.5635 which results in a χ^2_{red} of 10.76 due significant fluctuations between subsequent measurements. Again, more experimental data is needed at higher and lower energies to improve the overall comparison. CASP again significantly underestimates the stopping power at lower energies but appears to overestimate the stopping power above about 2×10^3 keV/u but no direct experimental evidence is present for those energies. The modified CASP results, using the updated Liu formula, agree slightly better than the results purely from CASP but neither is a useful approximation of the stopping power.

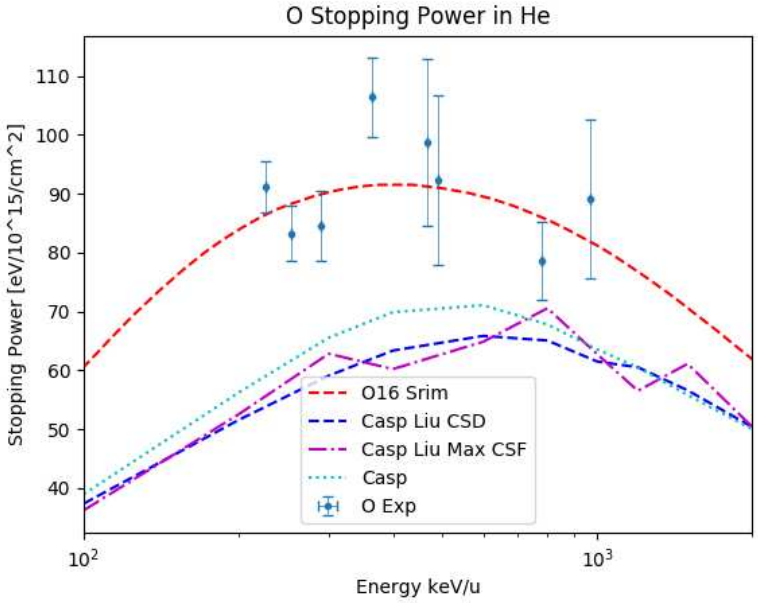

Figure 5.42: Stopping power as a function of energy for O+He compared to SRIM in red. Results directly from CASP are in light blue. Results from CASP re-normalized to the CSD from the updated Liu formula are in dark blue.

For the O+He reaction there was only limited data and no experimental fit could be done, see Figure 5.42. It does seem that SRIM is a very close approximation for the stopping power near the Bragg peak but nothing can be said about the stopping power away from this peak. The direct CASP approximation actually agrees better than the modified CASP curve but by only a very small relative amount. This points to CASP producing similar CSD for O+He to the updated Liu formula but the individual charge state stopping powers are significantly

underestimated.

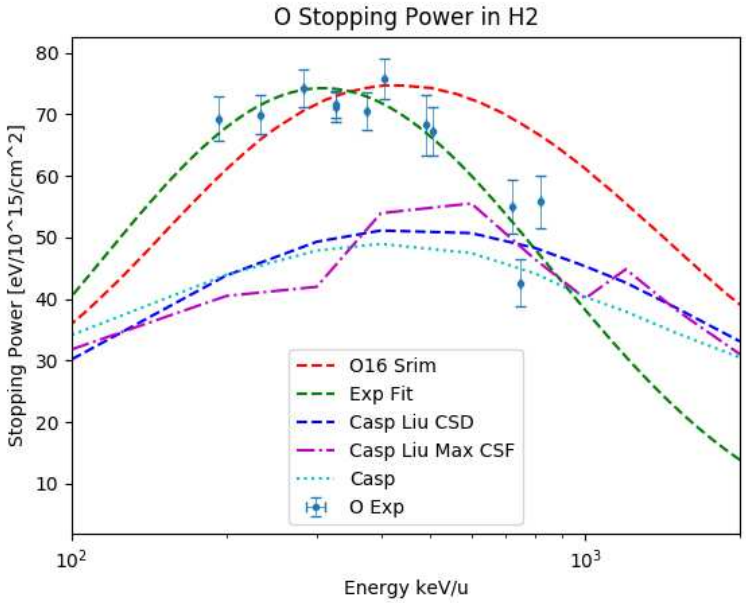

Figure 5.43: Stopping power as a function of energy for O+H_2 compared to SRIM in red. Results directly from CASP are in light blue. Results from CASP re-normalized to the CSD from the updated Liu formula are in dark blue. The experimental fit is in green.

The O+H_2 reaction had more available experimental data and the resulting fit agrees fairly well at low energies with the results from SRIM but begins to deviate significantly at energies above the Bragg peak, see Figure 5.43. The results from the fit are A = 74.26 μ = 2.489, and d = 0.4436 with a χ^2_{red} of 12.97. The experimental distribution seems to be shifted slightly toward lower energies but peaks at the same overall stopping power. SRIM appears to be a good estimate up to energies of about 500 keV/u. CASP again significantly underestimates the stopping power over the relevant region but the distribution width is much larger so would overestimate at higher and lower energies. CASP slightly underestimates the charge state mean for energies above the Bragg peak but overestimates at energies below.

Only a small amount of data existed for C+H_2 but mostly agrees well with the expectation from SRIM, see Figure 5.44. Due to the limited range of data, again, no attempt was made to fit the experimental data. CASP again agrees with the CSD's calculated using the Liu

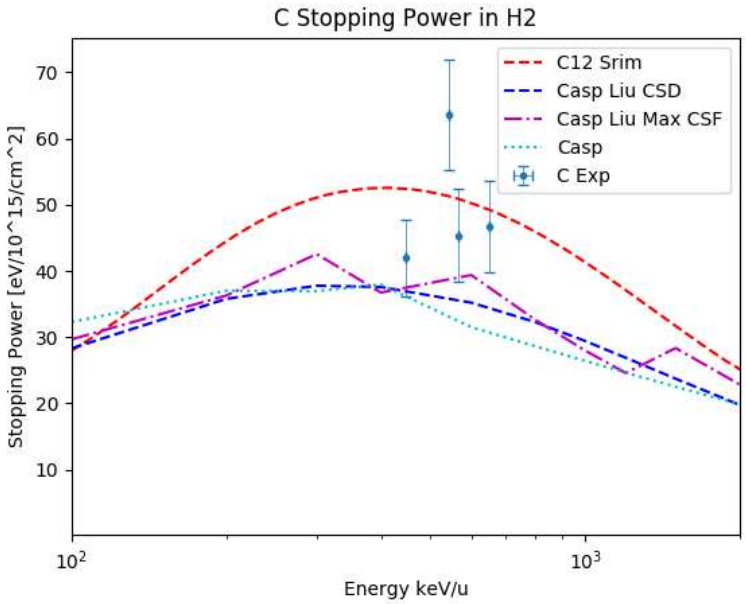

Figure 5.44: Stopping power as a function of energy for C+H_2 compared to SRIM in red. Results directly from CASP are in light blue. Results from CASP re-normalized to the CSD from the updated Liu formula are in dark blue.

formula as the modified CASP values are roughly equivalent to the direct CASP results but still underestimate the maximum stopping power at the Bragg peak.

There existed a large amount of C+He data in the old paper experimental logs but mostly at energies above 1 $\times 10^3$ keV/u. These mostly were done at low pressures or charge states such that the incoming energy could not be directly measured. This meant the measured energy loss was less and the error was much higher in many of these points. As a result most of the experimental points agree very well with the SRIM estimate as can be seen in Figure 5.45. The resulting experimental fit agrees very nicely with SRIM but is shifted up to slightly higher stopping powers and overall is a wider distribution. The fit parameters are A = 67.78 μ = 2.558, and d = 0.8126 with a χ^2_{red} of 15.71. For C+He SRIM is a very close estimate of the experimental stopping power over the range of available data.

Data was found for Mg+H_2 primarily for about 220 keV/u and a couple of other limited energies below 1×10^3 keV/u. The data seems to be fairly well approximated by SRIM but

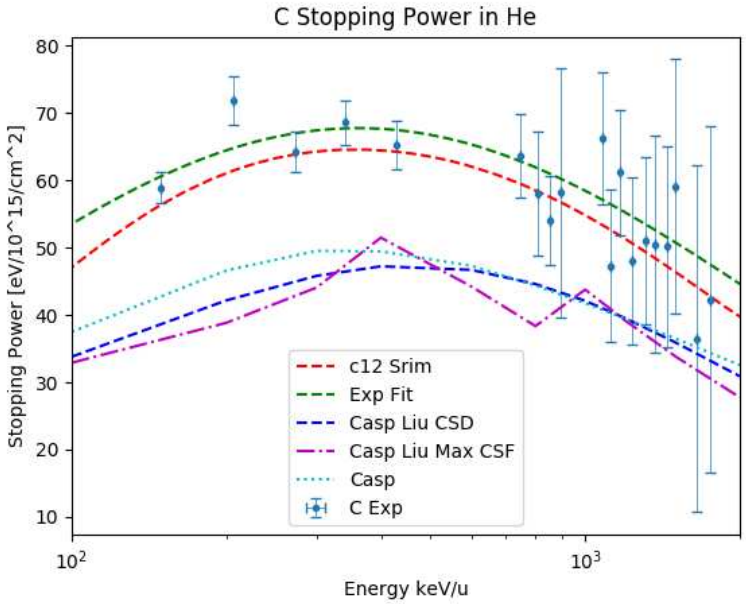

Figure 5.45: Stopping power as a function of energy for C+He compared to SRIM in red. Results directly from CASP are in light blue. Results from CASP re-normalized to the CSD from the updated Liu formula are in dark blue. The experimental fit is in green.

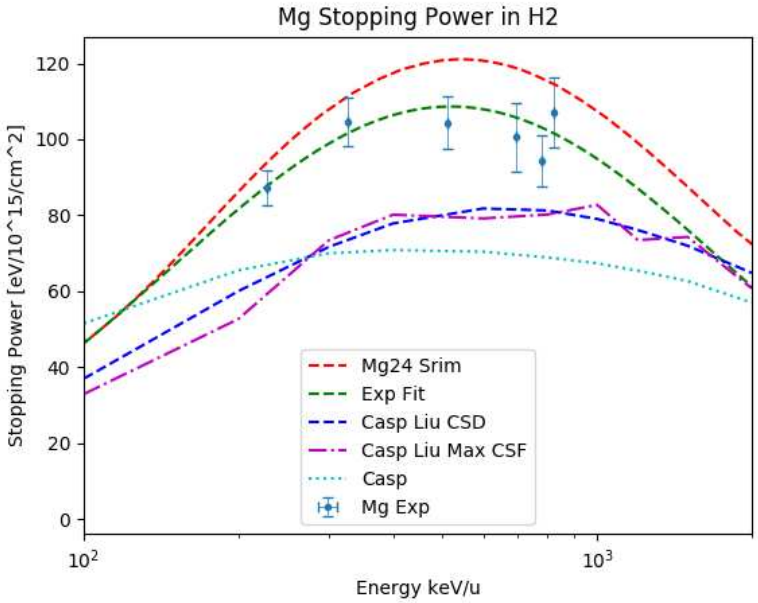

Figure 5.46: Stopping power as a function of energy for Mg+H_2 compared to SRIM in red. Results directly from CASP are in light blue. Results from CASP re-normalized to the CSD from the updated Liu formula are in dark blue. The experimental fit is in green.

is outside of the bounds of error for most energies. The experimental fit matches SRIM perfectly at low energies outside of the range of data but begins to deviate by about 20% around the Bragg peak as can be seen in Figure 5.46. The resulting fit parameters are A = 108.63 μ = 2.715, and d = 0.5473 with a χ^2_{red} of 9.36. CASP again underestimates the stopping power over the relevant region but has a much wider distribution.

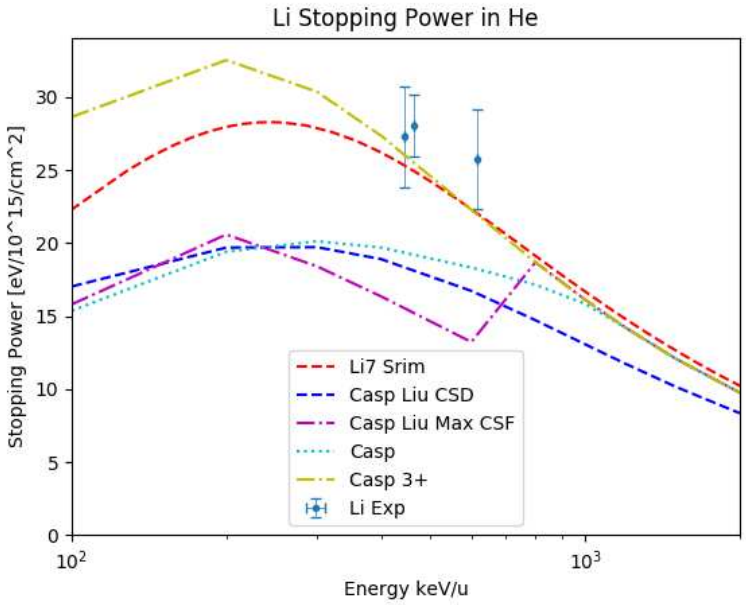

Figure 5.47: Stopping power as a function of energy for Li+He compared to SRIM in red. Results directly from CASP are in light blue. Results from CASP re-normalized to the CSD from the updated Liu formula are in dark blue. Yellow curve is the stopping power for the 3+ charge state.

Only a small amount of data was found for the Li+He reaction but again seems to match SRIM fairly well. SRIM seems to underestimate the stopping power as seems to be the trend for all ions in He that have been considered so far. CASP does not agree well as it significantly underestimates the stopping power but does begin to agree with SRIM when the 3+ charge state has 100% of the ions around 10^3 keV/u. We then decided to investigate whether the stopping power for the 3+ charge state found by CASP agreed with SRIM over the full distribution. In Figure 5.47 the yellow curve shows the CASP stopping power for the 3+ charge state only and above the Bragg peak this trend agrees very well with

SRIM but deviates significantly with the stopping power at lower energies. Several other sets of data were found for the stopping power of other ions in hydrogen and helium gas but followed similar trends as discussed previously in this section. They have been included in the Appendix because little additional insight is gained by discussing them individually.

A feature that was noticed during these measurements and analysis was that the stopping power increases with increasing charge state. This has been noted previously [86, 87] and is also seen in the code CASP which calculates the CSD and stopping power for each charge state. The increase in stopping power with charge state is likely due to the change in the charge changing cross section with charge state and the increased electron screening effective potential [88]. Examples of this feature can be seen for various reactions and energies in Figure 5.48, Figure 5.49, and Figure 5.50.

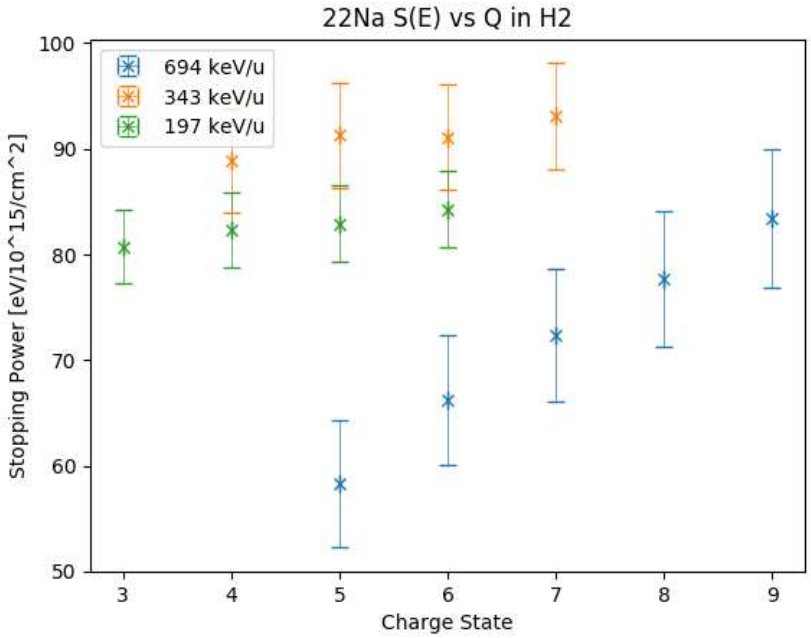

Figure 5.48: Stopping power as a function of charge state for various energies of $^{22}Na+H_2$.

On average, for the large number of particles those which exit in a particular charge state will have spent on average more time in that charge state and each individual charge state's stopping power can be measured by focusing on the charge state of interest. This

is particularly easy to measure at DRAGON as the energy is measured after the charge selecting magnet, MD1.

In Figure 5.48 the trend can be seen for various energies of the $^{22}Na+H_2$ reaction, that for increasing charge state the stopping power increases as well. This can also be seen for several other reactions and energies in Figure 5.49 and Figure 5.50 which show the $^{23}Na+H_2$ and $^{22}Ne+H_2$ reactions respectively. Additional figures can be seen in the Appendix. This effect tends to not be an issue at DRAGON because the stopping power is usually measured in the charge state of interest but is worth noting for high precision measurements where error below 5-10% is desired.

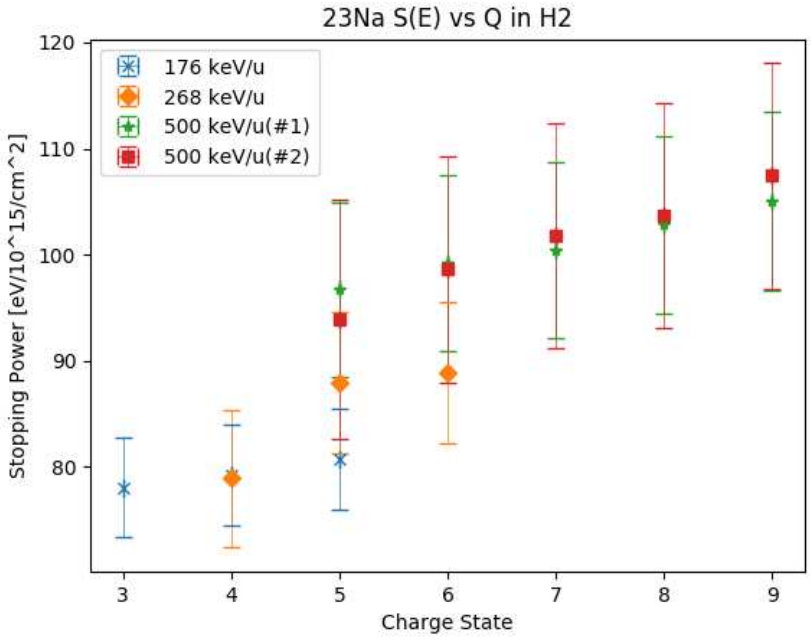

Figure 5.49: Stopping power as a function of charge state for various energies of $^{23}Na+H_2$.

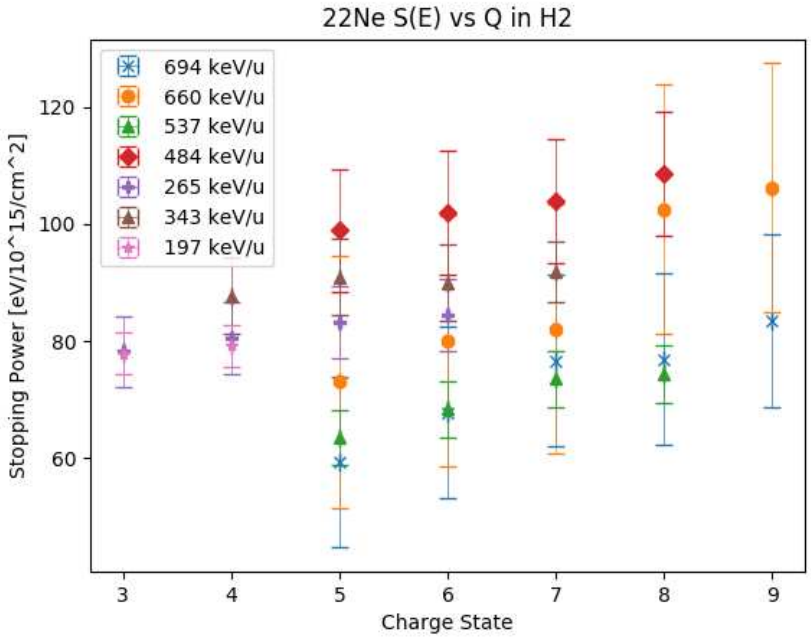

Figure 5.50: Stopping power as a function of charge state for various energies of $^{22}Ne+H_2$.

CHAPTER 6

SUMMARY & OUTLOOK

To summarize, in this present work we have performed the measurement of 8 resonance strengths in the ^{34}S(p,γ)^{35}Cl reaction at energies within the Gamow window relevant for astrophysical scenarios at the DRAGON facility located at the TRIUMF lab in Vancouver, Canada. Of the resonances measured, the E_{CM}=495 keV state had been previously measured relative to a specific reference state. The measurement for this work constitutes the first direct absolute measurement of the 495 keV resonance strength which significantly cuts down the potential for systematic error and removes the need for unnecessary theoretical considerations. We have also performed the first direct measurements of the E_{CM}=272, 407, and 471 keV states, and confirmed them to be resonant states which significantly contribute to the overall astrophysical reaction rate, with the 272 keV state dominating the astrophysical reaction rate over the majority of the peak nova burning temperatures. For the remaining states measured, E_{CM}=303, 390, 431, 452 keV, upper limits were set for the resonance strength due to no positively detected recoils. This work has provided a means to evaluate the potential systematic error in the strength of the characteristic reference state used in previous measurements of the 495 keV state. To correct for this we have provided an adjusted list of resonance strengths measured relative to this reference state based on the results of the present work. A future direct measurement of the characteristic 1177 keV reference state at DRAGON is recommended to confirm the predicted resonance strengths from this present work.

Additionally, we have analyzed the measurement of the E_{CM}=258.6 keV resonance of the ^{21}Ne(p,γ)^{22}Na reaction performed at DRAGON to evaluate the discrepancy between literature and the DRAGON calibration measurement's results. This work resolved the discrepancy and measured a resonance strength that agreed very well with the previous

literature value.

The final portion of this work was to catalog all previous CSD and stopping power measurements conducted at DRAGON and condense them into a more readily available form for the use by future experimenters. The CSD results were compared to the semi-empirical formula established by Liu to predict the CSD for ions of atomic charge 7-12, and energies of 138-875 keV/u in hydrogen and helium gas. This new data was used to update the fit parameters for the semi-empirical formula to provide a more accurate estimate of experimental CSDs. With the updated parameters the semi-empirical formula is now recommended to be used with ions of atomic charge 4-22 and energies of 138-1093 keV/u in hydrogen and helium gas. The compiled stopping power data was compared to the results from the codes SRIM and CASP which provide estimates of the experimental stopping power. It was shown that SRIM tends to over predict the stopping power but is generally within 20% of the experimental results and can be used as a reasonable estimate. CASP tends to under predict the results by as much as 50% and is not recommended to be used as an estimate of the stopping power. Experimental fits were performed when enough data was found to properly constrain the fit. These can be used to interpolate the stopping power where experimental data does not currently exist. For high precision measurements with desired error below 15-20% direct measurements of the stopping power are needed to ensure this level of accuracy.

REFERENCES CITED

[1] C. Iliadis et al. The effects of thermonuclear reaction rate variations on nova nucleosynthesis: A sensitivity study. *The Astrophysical Journal Supplement Series*, 142:105–137, 2002.

[2] O. V. Pruissen. Primary gamma-ray transitions of mixed e1 m2 character. *Nuclear Physics A*, 480:77–84, 1988.

[3] A. Janiuk. Nucleosynthesis of elements in gamma-ray burst engines. *Astronomy and Astrophysics*, 568, 2014.

[4] E. Bravo. Sensitivity study of explosive nucleosynthesis in type ia supernovae: Modification of individual thermonuclear reactions rates. *Physical Review C*, 85, 2012.

[5] J. Jose. The imprint of nova nucleosynthesis in presolar grains. *AIP Conference Proceedings*, 2002.

[6] N. Hazewindus. *Experiments on Nuclear Levels in 35Cl*. PhD thesis, 1963.

[7] G. Engelbertink and P. Endt. Measurements of (p,gamma) resonance strengths in the s-d shell. *Nuclear Physics*, 88:12–20, 1966.

[8] B. Paine. (p,gamma) resonance strengths in the s-d shell. *Nuclear Physics A*, 331: 389–400, 1979.

[9] S. A. Gillespie. First measurement of the s34(p,gamma)35cl reaction rate through indirect methods for presolar nova grains. *Physical Review C*, 96, 2017.

[10] C. Iliadis. *Nuclear physics of the stars*. Weinheim, Germany, 2015.

[11] W. Fowler. Completion of the proton-proton reaction chain and the possibility of energetic neutrino emission by hot stars. *Astrophysical Journal*, 127:551–556, 1958.

[12] R. Kippenhahn. *Stellar Structure and Evolution*. Springer, New York, 2012.

[13] National Nuclear Data Center. Interactive chart of nuclides, 2019. URL `nndc.bnl.gov`.

[14] K.Nomoto. Triple alpha reaction at low temperatures in accreting white dwarfs and neutron stars. *Astronomy and Astrophysics*, pages 239–245, 1985.

[15] R. Napiwotzki. White dwarfs in old planetary nebulae. *Acta Astrominica*, 43. 4:343–352, 1993.

[16] B. Paczyński. Stellar evolution from main sequence to white dwarf or carbon ignition. *Acta Astrominica*, 20. 2:47–58, 1970.

[17] K. Lodders. Presolar grains from meteorites: Remnants from the early times of the solar system. *Chemie der Erde*, 65:93–166, 2005.

[18] H. Tsuda. Thermonuclear reactions in stars involving heavy ions up to the formation of iron nuclei. *Volume of Theoretical Physics*, 29. 1:29–43, 1963.

[19] S. Chandrasekhar. The maximum mass of ideal white dwarfs. *Astrophysical Journal*, 71:81–82, 1931.

[20] A. Z. Mekjian. Explosive nucleosynthesis, equilibrium thermodynamics, and relativistic heavy-ion collisions. *Phys. Rev. C*, 17:1051–1070, Mar 1978. doi: 10.1103/PhysRevC.17.1051. URL `https://link.aps.org/doi/10.1103/PhysRevC.17.1051`.

[21] S.E. Woosley and T.A. Weaver. The evolution and explosion of massive stars ii: Explosive hydrodynamics and nucleosynthesis. 8 1995.

[22] J. R. Wilson et al. Stellar core collapse and supernova. *New York Academy of Sciences*, pages 267–293.

[23] C. Fyer. Mass limits for black hole formation. *Astrophysical Journal*, 522:413–418, 1999.

[24] Crenshaw. Novae, 2012.

[25] J. Jose. Nucleosynthesis in classical novae: Co versus one white dwarfs. *The Astrophysical Journal*, 494:680–690, 1998.

[26] B. Schaefer. Comprehensive photometric histories of all known galactic recurrent novae. *Astrophysical Journal Supp.*, 187:275–373, 2010.

[27] M. Wiescher. Explosive hydrogen burning in novae. *Astronomy and Astrophysics*, 160: 56–7, 1986.

[28] J. D'Auria et al. The 21na(p,gamma)22mg reaction from ecm = 200 to 1103 kev in novae and x-ray bursts. *Phys. Rev. C*, 69, 2004.

[29] Chart of nuclides, 2015. URL `https://wwwndc.jaea.go.jp/CN14/sp/`.

[30] F. K. Thielemann. Hydrostatic nucleosynthesis. ii. core neon to silicon burning and presupernova abundance yields of massive stars. *The Astrophysical Journal*, 295:604–619, 1985.

[31] R. Perna et al. Short gamma-ray bursts from the merger of two black holes. *The Astrophysical Journal Letters*, 821:L18, 2016.

[32] I. Banerjee et al. Nucleosynthesis in the outflows associated with the accretion disks of type ii collapsars. *The Astrophysical Journal*, 778:8–20, 2013.

[33] A. MacFayden et al. Collapsars: gamma-ray burst and explosions in failed supernovae. *The Astrophysical Journal*, 524:262–289, 1999.

[34] A. MacFayden et al. Supernovae, jets, and collapsars. *The Astrophysical Journal*, 550: 410–425, 2001.

[35] I. Banerjee et al. Nucleosynthesis in the accretion disks of type ii collapsars. *ArXiv:1305.1755*, 2013.

[36] I. Banerjee et al. Nucleosynthesis in the gamma-ray burst accretion disks and associated outflows. *ArXiv:1302.3067*, 2013.

[37] Sachiko Amari, Xia Gao, Larry R. Nittler, Ernst Zinner, Jordi Jose, Margarita Hernanz, and Roy S. Lewis. Presolar grains from novae. *The Astrophysical Journal*, 551(2):1065–1072, apr 2001. doi: 10.1086/320235.

[38] S. Amari et al. Presolar grains from novae. *The Astrophysical Journal*, 551:1065–1072, 2001.

[39] L.R. Nittler et al. Astrophysics with extraterrestrial materials. *Annu. Rev. Astron. Astrophys.*, 54:53–93, 2016.

[40] M. Aléonard. Strengths of (p,gamma) resonances in 33cl, 35cl, and 28si. *Physics Letters B*, 49:40–42, 1974.

[41] M. Meyer. Energy levels of 35cl. *Nuclear Physics A*, 264:13–29, 1976.

[42] A. Graue et al. A study of the 35cl levels by means of the 34s(3he,d)35cl reaction. *Nucl. Phys. A*, 136:577–591, 1969.

[43] K. Setoodehnia et al. Experimental study of 35cl excited states via 32s(a,p). *Phys. Rev. C*, 99, 2019.

[44] P.M Endt. Energy levels of a = 21-44 nuclei (vii). *Nuclear Physics A*, 521:1–830, 1990.

[45] R. Laxdal. Acceleration of radioactive ions. *Nuclear Instruments and Methods B.*, 204: 400–409, 2003.

[46] D. Connolly. *Radiative alpha capture on 34S at astrophysically relevant energies and design of a scattering chamber for high precision elastic scattering measurements for the dragon experiment.* PhD thesis, Colorado School of Mines, 2015.

[47] TRIUMF. Isac facilities for rare-isotope beams. URL `https://www.triumf.ca/research-program/research-facilities/isac-facilities`.

[48] K. Jayamanna. A multicharge ion source (supernanogan) for the olis facility at isac/triumf. *Review of Scientific Instruments*, 81, 2010.

[49] D. Hutcheon et al. The dragon facility for nuclear astrophysics at triumf-isac: design, construction and operation. *Nuclear Instruments and Methods A.*, 498:190–210, 2003.

[50] D. Hutcheon et al. The dragon facility for nuclear astrophysics at triumf-isac. *Nuclear Physics A*, 718:515–517, 2003.

[51] D. Gigliotti. *Efficiency calibration measurement and GEANT simulation of the DRAGON BGO gamma ray array at TRIUMF.* PhD thesis, UNBC, 2000.

[52] D. Gigliotti. Calibration and simulation of a gamma array for dragon at isac. *Nuclear Instruments and Methods B*, 204:671–677, 2003.

[53] C. Vockenhuber. Improvements of the dragon recoil separator at isac. *Nuclear Instruments and Methods B.*, 266:4167–4170, 2008.

[54] C. Brune. Radiative capture reactions in astrophysics. *Annu. Rev. Nucl. Part. Sci.*, 1056-8700/97/0610-00, 2015.

[55] Dataplot reference manual. *NIST*, 2:66–67.

[56] D. Hutcheon. Measurement of radiative capture resonance energies with an extended gas target. *Nuclear Instruments and Methods in Physics Research A*, 689:70–74, 2012.

[57] U. Greife. Energy loss around the stopping power maximum of ne, mg, and na ions in hydrogen gas. *National Institutes of Methods B*, pages 1–6, 2003.

[58] J.F. Ziegler. The stopping range of ions in matter. *Nuclear Instruments and Methods*, page URL http://www.srim.org, 2014.

[59] W. Liu. Charge state studies of low energy heavy ions passing through hydrogen and helium gas. *Nuclear Instruments and Methods A*, 496:198–214, 2003.

[60] W. Liu. *Charge State Studies of Heavy Ions Passing Through Matter*. PhD thesis, Simon Fraser University, 11 2001.

[61] J. Zylberberg. Charge-state distributions after radiative capture. 2006.

[62] H. D. Betz. The average charge of stripped heavy ions. *Phys. Lett*, 22:643–644, 1966.

[63] K. Shima. Systematics of equilibrium charge distributions of ions passing through a carbon foil over the ranges z=4-92 and e=0.02-6 mev/u. *Phys. Rev*, 40A:3557–3570, 1989.

[64] V. S. Nikolaev. On the equilibrium charge distribution in heavy element ion beams. *Phys. Lett*, 28A:277–278, 1968.

[65] S. Engel. *Awakening of the DRAGON*. PhD thesis, Ruhr-Universitat Bochum, 2003.

[66] J. Gorres et al. Search for low energy resonance in 21ne(p,gamma)22na and 22ne(p,gamma)23na. *Nuclear Physics A*, 385:57–75, 1982.

[67] V.N. Vodin et al. *Bull.Rus.Acad.Sci.Phys*, 64:327, 2001.

[68] J. Chen et al. Nuclear data sheets for a = 35. *Nuclear Data Sheets*, 112:2715–2850, 2011.

[69] P. Hubert. Etude des états exités du noyau 35cl. *Nuclear Physics A*, 195:485–501, 1972.

[70] B. Fant et al. Investigations of gamma ray transtitions and lifetimes in 35cl. *Z. Physik*, 260:185–196, 1973.

[71] H. D. Betz. *Review of Modern Phys.*, 44:3:465–539, 1972.

[72] N. Bohr. *Phys Rev*, 58:654, 1940.

[73] N. Bohr. *Phys Rev*, 59:270, 1940.

[74] N. Bohr. *Phys Rev*, 58:669, 1940.

[75] E. Teller J.K. Knipp. *Phys Rev*, 59:659, 1941.

[76] E. Teller J.H. Brunnings, J.K. Knipp. *Phys Rev*, 60:657, 1941.

[77] L.H. Thomas. *Proc. Camb. Phil. Soc.*, 23:542, 1927.

[78] E. Fermi. *Z Phys.*, 48:73, 1927.

[79] G.I. Bell. *Phys Rev*, 90:548, 1953.

[80] A. Papineau. *Compt. Rend*, 242:2933, 1956.

[81] H. H. Heckmann. *Phys. Rev*, 117:544, 1963.

[82] I. S. Dimitriev. *Zh. Eksperim. i. Teor. Fiz*, 32:570, 1957.

[83] V. S. Nikolaev I. S. Dimitriev. *Zh, Eksperim, i Teor. Fiz.*, 47:615, 1964.

[84] V. S. Nikolaev I. S. Dimitriev. *Phys Letters*, 28A:277, 1968.

[85] G. Ryding et al. *Phys Rev*, A3:1658, 1971.

[86] C. Frey. Charge state dependence of the stopping power of 1 mev/a 58ni ions. *Nuclear Instruments and Methods B*, 107:31–35, 1996.

[87] J. Juaristi. Charge state dependence of the energy loss of slow ions in metals. *Phys. Rev. Letters*, 82-5:1048–1051, 1999.

[88] A. Blazevic. Stopping power of swift neon ions in dependence on the charge state in the non-equilibrium regime. *Nuclear Instruments and Methods in Physics Research B*, 190:64–68, 2002.

[89] NIST. Atomic spectra database. URL `https://physics.nist.gov/PhysRefData/ASD/ionEnergy.html`.

APPENDIX A

REACTION RATE RESONANT

In order to solve the integral in Equation 2.74, several substitutions need to be made. If we let a = $\Gamma/2$ and x = $(E_r - E)$, this results in dE = -dx and the integral now spans $-E_r, \infty$ and if we look specifically at the integrand,

$$\int_0^{\infty} \frac{\Gamma/2}{(E_r - E)^2 + \Gamma^2/4} = -\int_{-E_r}^{-\infty} \frac{a}{x^2 + a^2}. \tag{A.1}$$

This can be solved with another substitution, if we let x = atan(θ) and assume $\Gamma \gg 1$.

$$\begin{cases} \frac{dx}{d\theta} = asec^2(\theta) & \implies dx = asec^2(\theta)d\theta \\ \theta_0 = tan^{-1}(\frac{E_r}{a}) & \approx \frac{\pi}{2} \\ \theta_f = tan^{-1}(\frac{-\infty}{a}) & = -\frac{\pi}{2} \end{cases} \tag{A.2}$$

This results in,

$$\int_0^{\infty} \frac{\Gamma/2}{(E_r - E)^2 + \Gamma^2/4} dE = \int_{-\pi/2}^{\pi/2} \frac{a^2 sec^2(\theta)}{a^2 sec^2(\theta) + a^2} d\theta = \int_{-\pi/2}^{\pi/2} d\theta = \pi. \tag{A.3}$$

So the result of the integral in Equation 2.74 is,

$$N_A < \sigma\nu >= N_A \frac{\sqrt{2\pi}\hbar^2}{(m_{01}kT)^{3/2}} e^{-E_r/kT} \omega \frac{\Gamma_a \Gamma_b}{\Gamma} 2\pi = N_A \Big(\frac{2\pi}{m_{01}kT}\Big)^{\frac{3}{2}} \hbar^2 e^{-\frac{E_r}{kT}} \omega\gamma. \tag{A.4}$$

APPENDIX B

CHARGE STATE DISTRIBUTIONS

This section includes additional charge state distribution information which did not add any additional insight or is included as a reference for future experiments.

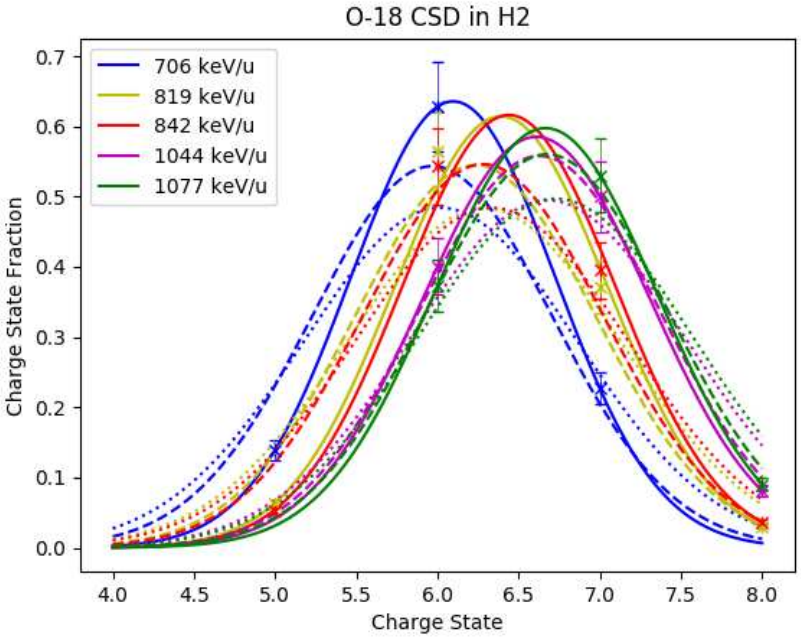

Figure B.1: Charge state distributions for ^{18}O in hydrogen. The solid lines are experimental fits, the dashed lines are the semi-empirical formula using the parameters found by Liu and the dotted lines are from the semi-empirical formula using updated parameters.

The measured CSD's for $^{18}O+H_2$ can be seen in Figure B.1 for energies from 706 to 1093 keV/u. The O^{+6} ion is a part of the He iso-electronic series and would be expected to be enhanced. This could be the explanation for the smaller width of the 706 keV/u measurement but since the mean charge is approximately 6+ this does not skew the distribution. The other measurements have a mean charge above 6+ but are actually skewed towards higher charges which implies that the noble gas like effects are minimal in these measurements. These

measurements also do not appear as outliers in the final parameter fit so all measurements were included in that fit.

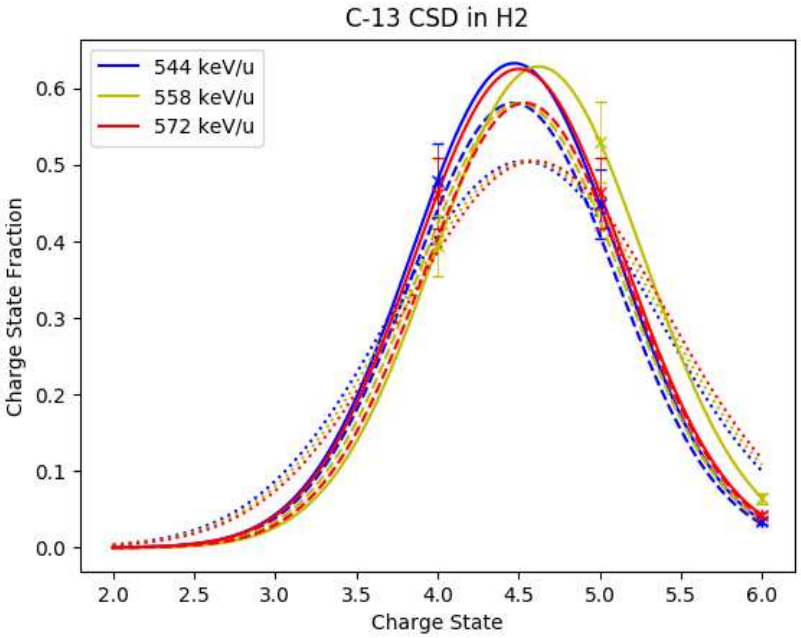

Figure B.2: Charge state distributions for ^{13}C in hydrogen. Solid lines are experimental fits, dashed lines are CSD's from Liu's formula and dotted lines are from Liu's formula with updated parameters.

Measurements for several $^{13}C+H_2$ CSD's can be seen in Figure B.2 and all charge state means are well approximated by the semi-empirical formula with either parameter set. Liu actually approximates the widths closer for $C+H_2$ as these widths appear to be smaller than expected but this is due to chance as there was no available C CSD data for Liu. The 558 keV/u measurement actually peaks at a higher charge state than the 572 keV/u measurement, likely due to experimental error or systematic uncertainty.

The remaining $^{23}Na+H_2$ CSD measurements can be seen in Figure B.3. The measurements seems to be well approximated by the semi-empirical formula as there are no expected 9+ contributions which would be enhanced by the iso-electronic effects.

The $^{15}N+He$ CSD measurement can be seen in Figure B.4 at 563 keV/u. It appears that the 5+ charge state is enhanced compared to a regular Gaussian which is explainable due to

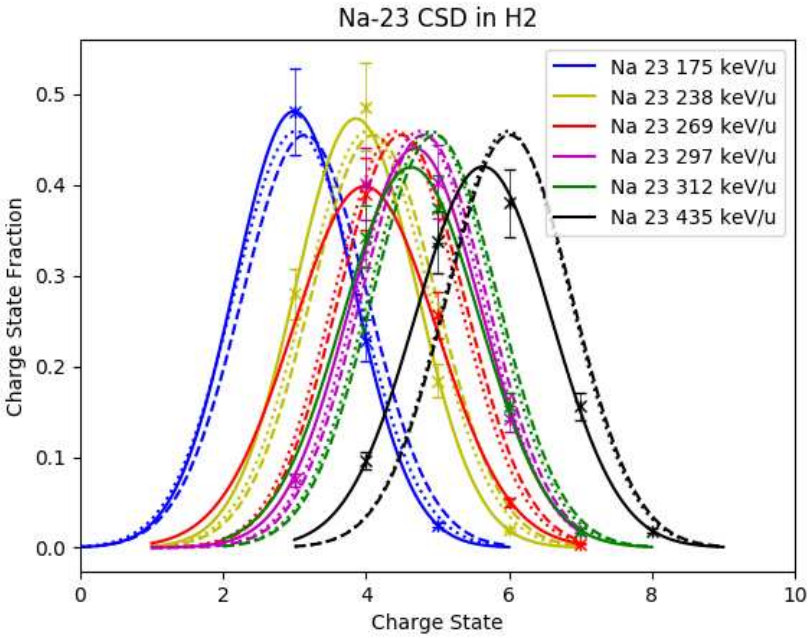

Figure B.3: Charge state distributions for ^{23}Na in hydrogen. The solid lines are experimental fits, the dashed lines are the semi-empirical formula using the parameters found by Liu and the dotted lines are from the semi-empirical formula using updated parameters.

the N^{+5} ion being a part of the He iso-electronic series. This does not change the resulting fit much as both parameter sets approximate the distribution well. This point did not appear as an outlier in the final fit and was therefore included.

The Mg+H_2 CSD's can be seen in Figure B.5 for both ^{24}Mg and ^{26}Mg. For the 227 and 206 keV/u measurements the distribution is well fit by a gaussian and the distribution means are slightly lower than predicted but not outside of expectations. The 438 keV/u measurements appear to match the updated parameter semi-empirical formula very well but the resulting fit agrees poorly, likely due to statistical variation as the resulting fit has a large error. This CSD was included in the final fit as this point did not appear as an outlier.

The measured CSD's for Al+H_2 can be seen in Figure B.6 for both ^{26}Al and ^{27}Al. The 210 keV/u distribution is fit well by a gaussian but the 3+ charge state is enhanced slightly compared to the expectations, possibly because of the He iso-electronic effects but not enough to consider this distribution an outlier. The 470 keV/u measurement agrees very well with

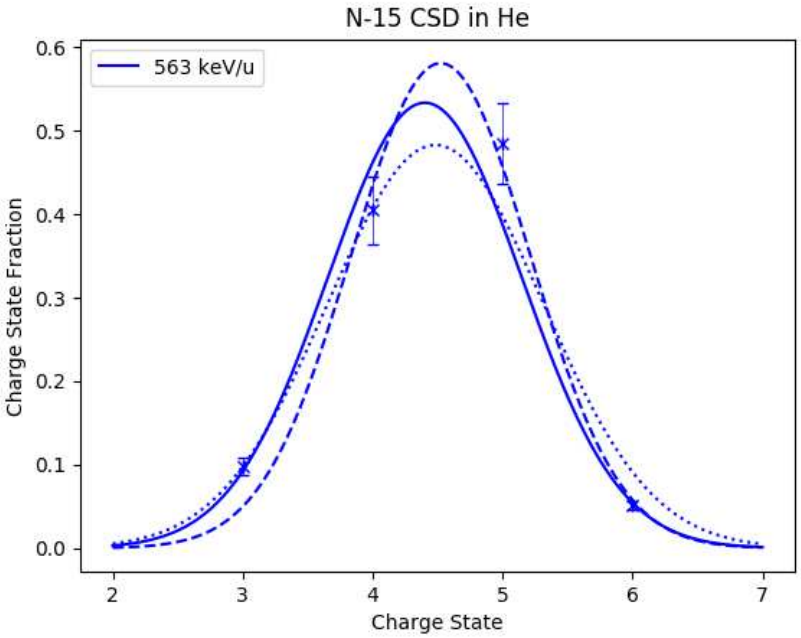

Figure B.4: Charge state distribution for ^{15}N in helium. The solid line is experimental fits, the dashed lines is the semi-empirical formula using the parameters found by Liu and the dotted line is from the semi-empirical formula using updated parameters.

the updated parameter semi-empirical formula.

Several ^{39}K CSD's can be seen in Figure B.7. All of the measured charge state means agree well with the expectations. K^{+9} ions are a part of the Ne iso-electronic series so it should be expected that they are slightly enhanced as the Ne series discontinuity is less than the He series as can be seen in Table B.3, Table B.4, and Table B.5. This can be clearly seen in the 610 keV/u distribution where the 9+ peak is larger than anticipated by the Liu formula. The remaining distributions with a significant 9+ contribution do not show this same enhancement. Liu's parameters overestimate the distribution width as is to be expected by the comparative fits seen in Figure 5.35. All K distributions were included in the final fit as none of them appeared to be outliers.

An ^{18}O+He distribution can be seen in Figure B.8 at 526 keV/u. The charge state mean is approximated well by the Liu formula with the updated parameters but the previous parameter set is approximately half a charge state too high. The data is fit within error as

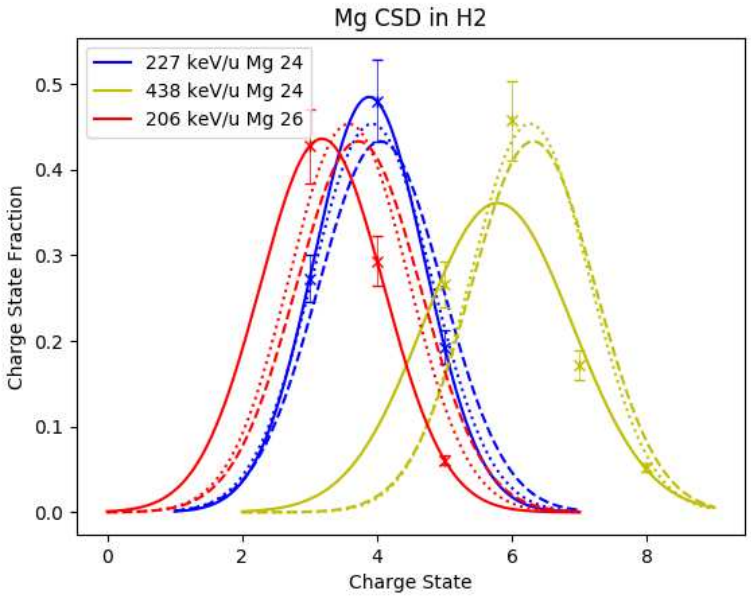

Figure B.5: Charge state distributions for Mg in hydrogen. The solid lines are experimental fits, the dashed lines are the semi-empirical formula using the parameters found by Liu and the dotted lines are from the semi-empirical formula using updated parameters.

a Gaussian except for the 6+ state which is just outside the bounds of error. This could be expected though as O^{+6} is a part of the He iso-electronic series.

Two distributions for ^{40}Ar can be seen in Figure B.9. Both are fit very well by a Gaussian and are well approximated by the Liu formula with the updated parameter set. The 8+ charge state resembles Ne and is expected to be enhanced but this does not appear to be the case.

Several ^{19}F+He distributions can be seen in Figure B.10 and all are fit very well by the Gaussian distribution. The widths are underestimated by both parameter sets but the charge state means are all recreated very closely by either set. The 7+ charge state resembles He but due to this small expected 9+ contribution in the 638 keV/u distribution this does not appear to effect the overall distribution.

It was seen that in the work by Betz [62] that the ideal γ value for gaseous targets was 0.55 and no mention of why 0.44515 was chosen was found in the work by Liu. As a result

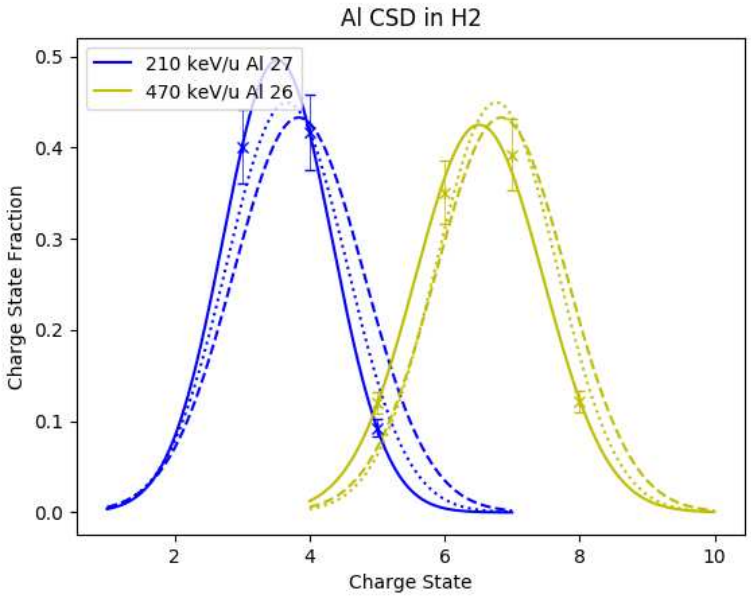

Figure B.6: Charge state distributions for Al in hydrogen. The solid lines are experimental fits, the dashed lines are the semi-empirical formula using the parameters found by Liu and the dotted lines are from the semi-empirical formula using updated parameters.

we decided to find the minimizing parameters for a γ value of 0.55. These can be seen in Figure B.11 for hydrogen targets and Figure B.12 for helium targets. The χ^2_{red} was found to be minimized for hydrogen at a A = 1.8441 and B = 0.4690. These parameters resulted in a χ^2_{red} of 51.6 which is 25% worse than the original parameter set by Liu. For helium targets this was found to be A = 1.4137 and B = 0.3471, which corresponded to a χ^2_{red} of 31.84. This again is worse than the previous parameter set by Liu and therefore not suggested for use.

The tables Table B.1 and Table B.2 contain the fitted means and widths from the CASP CSD's in hydrogen and helium. Errors are not listed for the fits because no error estimate exists for the individual charge state fractions from CASP and the fractions themselves likely are directly from a Gaussian distribution and the fit would have a very small but meaningless error as a result.

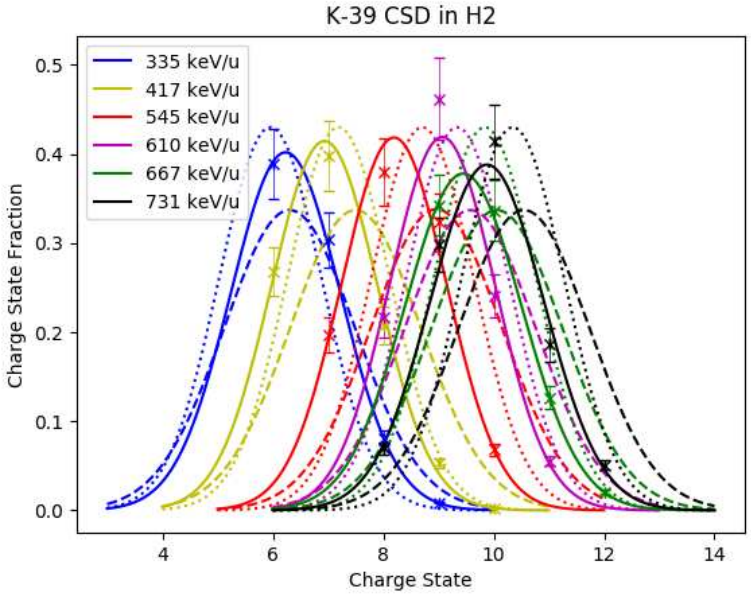

Figure B.7: Charge state distributions for ^{39}K in hydrogen. The solid lines are experimental fits, the dashed lines are the semi-empirical formula using the parameters found by Liu and the dotted lines are from the semi-empirical formula using updated parameters.

Table B.1: Charge state distributions for previous DRAGON experiments for Hydrogen gas targets compared to CASP

		Experimental		CASP	
Reaction	E_{lab} [keV/u]	$\overline{q}$	d	$\overline{q}$	d
$^{13}C+H_2$	544	4.47(6)	0.636(31)	4.08	0.827
	558	4.62(5)	0.645(33)	4.11	0.822
	572	4.50(6)	0.645(33)	4.14	0.822
$^{15}N+H_2$	435*†	5.61(1)	0.603(11)	4.30	0.901
$^{16}O+H_2$	138*	2.43(1)	0.796(4)	2.51	0.929
	200*	3.18(1)	0.800(9)	3.07	0.921
	325*	4.29(1)	0.781(6)	3.95	0.934
	500*	5.51(3)	0.719(37)	4.85	0.924
	588*	5.71(1)	0.588(17)	5.17	0.915
	800*	6.17(1)	0.586(1)	5.66	0.898
$^{18}O+H_2$	706	6.10(3)	0.629(31)	5.49	0.912
	819	6.39(2)	0.654(14)	5.69	0.892
	842	6.44(2)	0.654(14)	5.73	0.890
	1044	6.61(6)	0.681(42)	6.01	0.969
	1077	6.67(5)	0.686(40)	6.00	0.902
$^{20}Ne+H_2$	1150†	7.78(5)	0.624(13)	7.29	0.969
	1165†	8.03(2)	0.526(18)	7.32	0.969

Table B.1: Continued.

	1173†	8.13(2)	0.641(14)	7.34	0.969
$^{21}Ne+H_2$	274	4.17(5)	0.964(45)	4.02	1.012
	282	4.18(4)	0.870(33)	4.07	1.009
	410	5.53(9)	0.830(70)	4.82	1.023
	770†	7.28(3)	0.623(14)	6.35	1.011
$^{22}Ne+H_2$	196	2.83(2)	1.014(53)	3.42	1.009
	265	4.07(5)	0.898(36)	3.95	1.010
	343	4.86(6)	0.877(34)	4.45	1.082
	536	6.47(3)	0.860(32)	5.45	1.036
	661†	7.00(3)	0.838(22)	5.94	1.011
$^{21}Na+H_2$	1150†	8.48(6)	0.632(43)	7.69	1.026
$^{23}Na+H_2$	175	2.99(18)	0.827(70)	3.44	1.041
	200*	3.48(1)	0.780(11)	3.63	1.044
	238	3.86(5)	0.847(30)	3.99	1.032
	269	3.98(16)	1.005(51)	4.22	1.051
	297	4.69(3)	0.912(20)	4.43	1.069
	312	4.63(9)	0.955(44)	4.51	1.131
	374*	5.38(1)	0.897(7)	4.88	1.061
	435	5.64(3)	0.950(23)	5.23	1.066
	478*	6.30(1)	0.937(8)	5.47	1.083
	484	6.02(3)	0.920(22)	5.50	1.086
	505	6.42(2)	0.874(11)	5.54	1.083
	524	6.63(26)	0.870(81)	5.59	1.079
	686†	7.71(5)	0.619(14)	6.33	1.068
$^{24}Mg+H_2$	200*	3.68(2)	0.758(21)	3.87	1.069
	227	3.88(5)	0.823(68)	4.11	1.075
	438	5.79(10)	1.109(71)	5.52	1.075
	500*	6.75(1)	0.949(6)	5.82	1.106
	800*	8.44(1)	0.839(5)	7.04	1.101
$^{26}Mg+H_2$	206	3.18(18)	0.916(94)	3.92	1.200
$^{26}Al+H_2$	470	6.51(4)	0.946(42)	5.97	1.069
$^{27}Al+H_2$	210	3.52(9)	0.805(64)	4.21	1.139
$^{35}Cl+H_2$	173	3.51(45)	1.097(162)	4.41	1.112
	259	4.47(47)	1.103(165)	5.46	1.667
	294	5.27(19)	1.001(123)	5.83	1.200
	377†	6.61(6)	0.698(40)	6.53	1.218
	393	6.41(10)	0.910(38)	6.65	1.216
	478	7.31(4)	0.918(39)	7.20	1.221
$^{39}K+H_2$	335	6.23(3)	0.993(13)	6.46	1.234
	417	6.93(63)	0.966(23)	7.21	1.283
	545	8.20(51)	0.948(43)	8.14	1.296
	610	9.07(53)	0.953(44)	8.56	1.300
	667	9.45(13)	1.056(59)	8.90	1.262

Table B.1: Continued.

	731	9.88(34)	1.029(31)	9.17	1.288

∗Values from Liu paper
†Excluded from final fit

Table B.2: Charge state distributions for previous DRAGON experiments for Helium gas targets compared to CASP

		Experimental		CASP	
Reaction	E_{lab} [keV/u]	$\overline{q}$	d	$\overline{q}$	d
^{9}Be+He	275	2.33(9)	0.697(41)	2.46	0.689
	278	2.35(8)	0.682(39)	2.47	0.691
	285	2.28(11)	0.766(55)	2.49	0.690
	422	2.84(4)	0.722(46)	2.81	0.667
	523	3.16(4)	0.738(49)	2.99	0.651
^{11}B+He	194	2.40(12)	0.565(28)	2.61	0.770
	213	2.48(12)	0.576(29)	2.71	0.770
^{12}C+He	162	2.05(15)	0.794(61)	2.59	0.827
	167	2.01(17)	0.811(66)	2.64	0.828
	194	2.28(11)	0.580(24)	2.88	0.838
	1466	5.54(6)	0.617(29)	5.17	0.668
^{15}N+He	563	2.41(5)	0.748(22)	4.70	0.864
^{16}O+He	138*	2.12(2)	0.885(11)	2.54	0.909
	200*	2.77(3)	0.838(24)	3.09	0.903
	325*	3.66(1)	0.877(5)	3.99	0.915
	371*	3.92(1)	0.841(8)	4.27	0.918
	588*	4.98(1)	0.842(8)	5.20	0.895
	750*	5.62(3)	0.735(34)	5.58	0.886
	875*	5.78(1)	0.635(5)	5.83	0.895
^{18}O+He	526	4.57(8)	0.877(34)	4.99	0.901
^{19}F+He	190	2.92(15)	0.915(46)	3.19	0.939
	239	3.41(10)	0.845(36)	3.59	0.989
	259	3.55(6)	0.869(23)	3.72	0.957
	346	4.13(2)	0.864(8)	4.29	0.962
	626	5.52(1)	0.898(8)	5.61	0.953
	638	5.54(3)	0.950(32)	5.66	0.949
^{20}Ne+He	290	3.79(8)	0.983(47)	4.17	0.985
	304	4.13(5)	0.995(42)	4.25	0.984
	502	5.15(6)	0.976(47)	5.33	1.007
	642	5.84(3)	0.944(28)	5.92	0.992
	714	7.39(8)	0.809(65)	6.19	0.988
	1093	7.84(2)	0.526(18)	7.22	0.953
^{40}Ar+He	484	6.96(21)	0.899(89)	7.58	1.237

Table B.2: Continued.

	540	7.24(11)	0.923(39)	7.92	1.308
^{44}Ti+He	537	9.97(2)	0.585(25)	8.71	1.346
	706	10.07(11)	0.827(29)	9.95	1.373

∗Values from Liu paper
†Excluded from final fit

Table B.3: Ionization energies up to Fe^{+10} in unit of eV from [89]

Z	Symbol	1+	2+	3+	4+	5+	6+	7+	8+	9+	10+
1	H	13.6									
2	He	24.6	54.4								
3	Li	5.4	75.6	122.5							
4	Be	9.3	18.2	153.9	217.7						
5	B	8.29	25.2	37.9	259.4	340.2					
6	C	11.3	24.4	47.9	64.5	392.1	490.0				
7	N	14.5	29.6	47.4	77.5	97.9	552.1	667.0			
8	O	13.6	35.1	54.9	77.4	113.9	138.1	739.3	871.4		
9	F	17.4	35.0	62.7	87.2	114.2	157.2	185.2	953.9	1103	
10	Ne	21.6	41.0	63.4	97.2	126.2	158.0	207.3	239.1	1196	1362
11	Na	5.1	47.3	71.6	98.9	138.4	172.2	208.5	264.2	299.9	1465
12	Mg	7.6	15.0	80.1	109.3	141.3	186.8	225.0	328.0	367.5	1762
13	Al	6.0	18.8	28.4	120.0	153.8	190.5	241.8	284.6	330.2	398.7
14	Si	8.2	16.3	33.5	45.1	166.8	205.3	246.6	303.6	351.3	401.4
15	P	10.5	19.8	30.2	51.4	65.0	220.4	263.6	309.6	372.3	424.4
16	S	10.4	23.3	34.9	47.2	72.6	88.1	281.0	328.8	379.8	447.7
17	Cl	13.0	23.8	39.8	53.2	67.7	96.9	114.2	348.3	400.9	456.7
18	Ar	15.8	27.6	40.7	59.6	74.8	91.3	124.4	143.5	422.6	479.8
19	K	4.3	31.6	45.8	60.9	82.7	99.4	117.6	154.9	175.8	503.7
20	Ca	6.1	11.9	50.9	67.3	84.3	108.8	127.2	147.2	188.5	211.3
21	Sc	6.6	12.8	24.8	73.5	92.0	110.7	138.0	158.1	180.0	225.2
22	Ti	6.8	13.6	27.5	43.3	99.3	119.5	140.7	170.5	192.1	215.9
23	V	6.7	14.6	29.3	46.7	65.3	128.1	150.7	173.6	206.0	230.5
24	Cr	6.8	16.5	31.0	49.2	69.5	90.6	160.3	184.8	209.5	244.5
25	Mn	7.4	15.6	33.7	51.2	72.4	95.6	119.2	195.5	221.9	248.6
26	Fe	7.9	16.2	30.7	54.9	75.0	99.0	125.0	151.1	233.6	262.1

Table B.4: Ionization energies up to Fe^{+20} in unit of eV from [89]

Z	Symbol	11+	12+	13+	14+	15+	16+	17+	18+	19+	20+
11	Na	1649									

Table B.4: Continued.

12	Mg	1762	1963								
13	Al	442.0	2086	2304							
14	Si	476.3	523.4	2438	2673						
15	P	479.4	560.6	611.7	2817	3070					
16	S	504.6	564.4	652.0	707.0	3224	3494				
17	Cl	530.0	591.6	656.3	750.2	809.2	3658	3946			
18	Ar	540.4	619.0	685.5	755.1	855.5	918.4	4121	4426		
19	K	565.6	631.1	714.7	786.3	860.9	967.7	1035	4611	4934	
20	Ca	591.6	658.2	728.6	817.2	894.0	973.7	1087	1158	5129	5470
21	Sc	249.8	687.4	757.7	833.2	926.5	1009	1094	1213	1288	5675
22	Ti	265.1	291.5	787.7	864.0	944.5	1043	1130	1220	1346	1425
23	V	254.8	308.5	336.3	896.0	977.2	1063	1165	1259	1354	1487
24	Cr	270.8	296.7	354.7	384.2	1012	1097	1188	1295	1395	1495
25	Mn	286.1	314.4	343.6	403.0	435.2	1134	1224	1320	1431	1537
26	Fe	290.9	330.8	361.0	392.2	456.2	489.3	1263	1358	1460	1576

Table B.5: Ionization energies up to Fe^{+26} in unit of eV from [89]

Z	Symbol	21+	22+	23+	24+	25+	26+
21	Sc	6034					
22	Ti	6249	6626				
23	V	1570	6851	7246			
24	Cr	1634	1721	7482	7895		
25	Mn	1643	1789	1880	8141	8572	
26	Fe	1687	1798	1950	2046	8828	9278

Table B.6: CSD measurements in hydrogen gas.

Beam	E_{out} [keV/u]	3+	4+	5+	6+	7+	8+	9+	10+	11+	12+
^{13}C	544		48.0	44.9	3.53						
	558		39.4	53.0	6.45						
	572		46.2	46.4	4.19						
^{18}O	706			13.9	62.8	22.6					
	819			6.23	56.4	37.1	3.08				
	842			5.30	54.3	39.5	3.67				
	1044				40.0	50.0	8.05				
	1077				37.3	53.0	9.02				
^{20}Ne	1150				27.6	75.3	8.35	0.12			
	1165				12.3	87.0	21.2	0.97			
	1173				11.0	75.7	13.9				

Table B.6: Continued.

^{21}Ne	274	19.6	43.9	27.3	7.02						
	282	18.3	45.8	28.9	5.17						
	410			39.3	41.0	10.1					
	770				8.55	48.5	87.7	1.31			
^{22}Ne	196	37.6	23.2	3.65	0.31						
	265	21.7	46.1	25.0	4.46						
	343		28.4	44.0	20.0	2.29					
	536			11.0	39.3	39.0	9.38				
	661			3.68	17.6	56.2	47.0	2.47			
^{21}Na	1150					4.39	40.6	61.4	3.29		
^{23}Na	175	48.1	22.8	2.52							
	238	28.0	48.6	18.4	1.95						
	269		39.0	25.6	4.99						
	297	7.5	40.1	40.3	14.3	1.88					
	312		34.3	37.4	15.6	1.89					
	435		9.54	33.7	38.0	15.6	1.88				
	484		4.14	20.7	45.7	27.1	4.14				
	505		1.09	11.4	36.4	39.4	11.1	0.52			
	515				31.1	44.5	17.0	1.60			
	524					41.9	13.2	1.11			
	686					36.7	47.8	15.9	0.06		
^{24}Mg	227	27.3	48.0	19.3							
	438			26.6	45.7	17.2	5.24				
^{26}Mg	206	42.7	29.3	6.11							
^{26}Al	470			12.0	35.1	39.2	12.2				
^{27}Al	210	40.1	41.7	9.26							
^{35}Cl	173		32.9	14.4	2.74						
	259			32.3	13.8	2.60					
	294			40.2	31.9	9.32	0.78				
	377				39.0	48.9	7.91				
	393				38.9	39.2	8.80	0.77			
	478				15.7	43.8	31.3	8.09			
^{39}K	335				38.9	30.4	8.12	0.83			
	417				26.8	39.8	20.8	5.34	0.25		
	545					19.6	38.0	32.3	6.81		
	610						21.6	46.1	24.0	5.53	
	667							34.3	33.7	12.7	2.07
	731						6.94	29.8	41.4	18.6	5.08

Table B.7: CSD measurements in helium gas. Energy is in units of keV/u.

Beam	E_{out}	2+	3+	4+	5+	6+	7+	8+	9+	10+	11+	12+	13+

Table B.7: Continued.

^{9}Be	275	47.2	33.5	3.04									
	278	51.9	37.3	3.13									
	285	49.5	33.8	4.19									
	422	29.7	57.0	16.1									
	523	18.2	60.5	32.2									
^{11}B	194	55.3	40.7	1.30									
	213	49.5	46.5	2.14									
^{12}C	162	50.1	24.7	2.48									
	167	49.2	23.2	2.39									
	194	54.4	41.4	1.61									
	1466			3.73	57.2	63.4							
^{15}N	563		9.79	40.5	48.5	5.19							
^{18}O	526			38.6	36.6	13.9	0.94						
^{19}F	190		43.5	21.7	3.27								
	239		43.3	34.5	8.78	0.42							
	259		38.3	38.3	11.9	0.84							
	346		19.7	45.4	27.1	4.76	0.19						
	626			10.7	37.0	39.1	11.4						
	638			11.2	37.9	35.7	13.2						
^{20}Ne	290		29.3	40.9	18.5	3.26							
	304		20.8	40.4	26.8	6.92							
	502			20.5	39.4	28.8	6.77						
	642			6.64	26.3	20.9	3.01						
	714					11.3	44.0	37.2					
	1093						20.9	72.6	6.77				
^{40}Ar	484						44.4	22.7	3.38				
	540						41.9	30.9	7.05	0.50			
^{44}Ti	537								17.5	68.2	14.3		
	706									50.8	22.5	3.85	0.08

Table B.8: CSD measurements in hydrogen gas, un-normalized data.

Beam	E_{out} [keV/u]	3+	4+	5+	6+	7+	8+	9+	10+	11+	12+
^{13}C	544		59.2	55.4	4.36						
	558		39.8	53.4	6.50						
	572		46.9	47.0	4.25						
^{18}O	706			9.30	41.9	15.1					
	819			4.27	38.6	25.4	2.11				
	842			3.26	33.4	24.3	2.26				
	1044				26.5	33.1	5.33				
	1077				23.3	33.1	5.63				
^{20}Ne	1150					24.8	67.6	7.5	0.11		

Table B.8: Continued.

	1165					10.1	71.7	17.5	0.8		
	1173					10.7	73.4	13.5			
^{21}Ne	274	18.6	41.7	25.9	6.67						
	282	18.6	46.7	29.5	5.27						
	410			39.8	41.6	10.2					
	770				5.86	33.2	60.1	0.9			
^{22}Ne	196	50.9	31.3	4.94	0.42						
	265	21.9	46.6	25.3	4.5						
	343		36.0	55.7	25.3	2.9					
	536			10.7	38.4	38.1	9.16				
	661			2.90	13.9	44.3	37.0	1.94			
^{21}Na	1150					4.00	37.0	56.0	3.0		
^{23}Na	175	55.8	26.5	2.92							
	238	44.5	77.2	29.2	3.1						
	269		50.6	33.2	6.47	0.58					
	297	7.20	38.5	38.7	13.7	1.80					
	312		38.5	42.0	17.5	2.12					
	435		7.11	25.1	28.3	11.6	1.40				
	484		5.74	28.7	63.3	37.6	5.74				
	505		1.04	10.8	34.6	37.4	10.5	0.50			
	515				33.0	47.2	18.0	1.70			
	524					37.8	11.9	1.00			
	686					29.0	37.8	12.6	0.05		
^{24}Mg	227	25.6	45.0	18.1							
	438			26.0	44.7	16.9	5.13				
^{26}Mg	206	35.0	24.0	5.00							
^{26}Al	470			12.0	35.1	39.2	12.2				
^{27}Al	210	26.0	27.0	6.00							
^{35}Cl	173		48.0	21.0	4.00						
	259			61.2	26.2	4.93					
	294			72.0	57.1	16.7	1.39				
	377				35.1	44.1	7.13				
	393				38.4	38.7	8.96	0.77			
	478				13.7	38.3	27.4	7.08			
^{39}K	335				46.6	36.4	9.73	1.00			
	417				29.6	43.9	22.9	5.89	0.28		
	545					18.4	35.6	30.3	6.38		
	610						17.1	36.5	19.0	4.38	
	667							34.1	33.5	12.6	2.06
	731						8.95	38.5	53.4	24.0	6.55

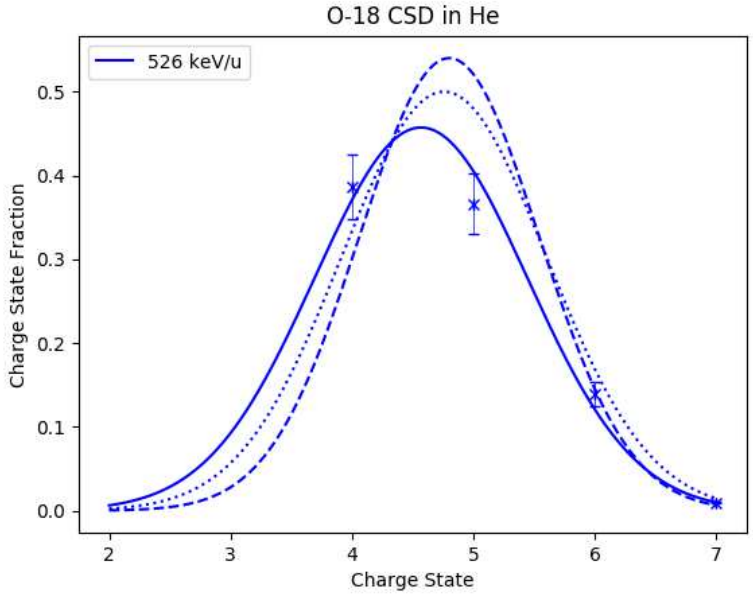

Figure B.8: Charge state distribution for ^{18}O in helium. The solid lines is experimental fits, the dashed line is the semi-empirical formula using the parameters found by Liu and the dotted line is from the semi-empirical formula using updated parameters.

Table B.9: CSD measurements in helium gas un-normalized data. Energy is in units of keV/u.

Beam	E_{out}	2+	3+	4+	5+	6+	7+	8+	9+	10+	11+	12+	13+
^{9}Be	275	47.2	33.5	3.04									
	278	50.3	36.2	3.04									
	285	62.4	42.6	5.28									
	422	34.8	66.9	18.9									
	523	12.7	42.3	22.5									
^{11}B	194	49.3	36.3	1.16									
	213	47.6	44.7	2.06									
^{12}C	162	46.6	22.9	2.30									
	167	47.3	22.3	2.30									
	194	33.4	25.4	0.99									
	1466			3.00	46.0	51.0							
^{15}N	563		9.11	37.7	45.2	4.83							
^{18}O	526				30.8	29.2	11.1	0.75					
^{19}F	190		70.4	35.1	5.3								
	239		57.7	46.0	11.7	5.60							
	259		45.8	45.9	14.3	1.01							
	346		24.5	56.5	33.7	5.92	0.23						
	626			8.45	29.3	31.0	9.01						

Table B.9: Continued.

	638			9.25	31.4	29.6	10.9						
^{20}Ne	290		35.2	49.2	22.3	3.92							
	304		19.4	37.7	25.0	6.46							
	502			18.0	34.5	25.3	5.93						
	642			6.64	26.3	43.5	20.9	3.01					
	714					6.77	26.4	22.3					
	1093						10.7	37.1	3.46				
^{40}Ar	484						13.8	7.07	1.05				
	540						40.1	29.6	6.75	0.48			
^{44}Ti	537								17.5	68.2	14.3		
	706									65.8	29.1	4.99	0.11

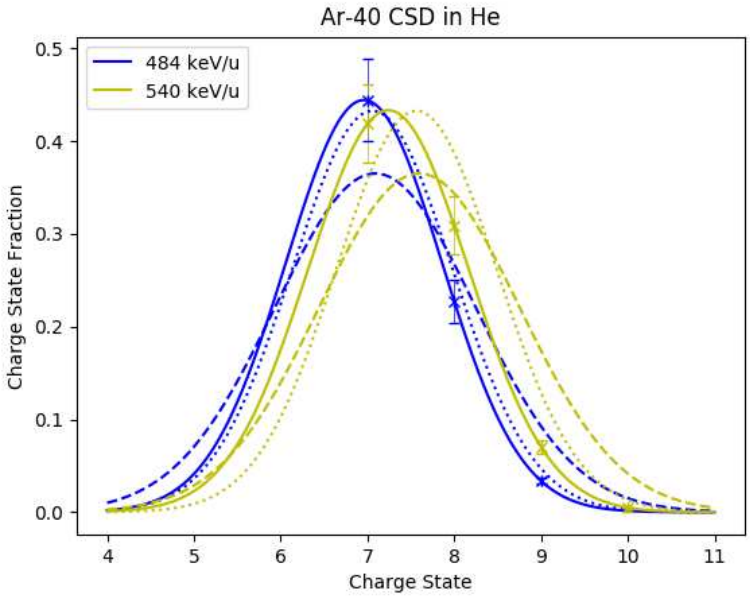

Figure B.9: Charge state distributions for ^{40}Ar in helium. The solid lines are experimental fits, the dashed lines are the semi-empirical formula using the parameters found by Liu and the dotted lines are from the semi-empirical formula using updated parameters.

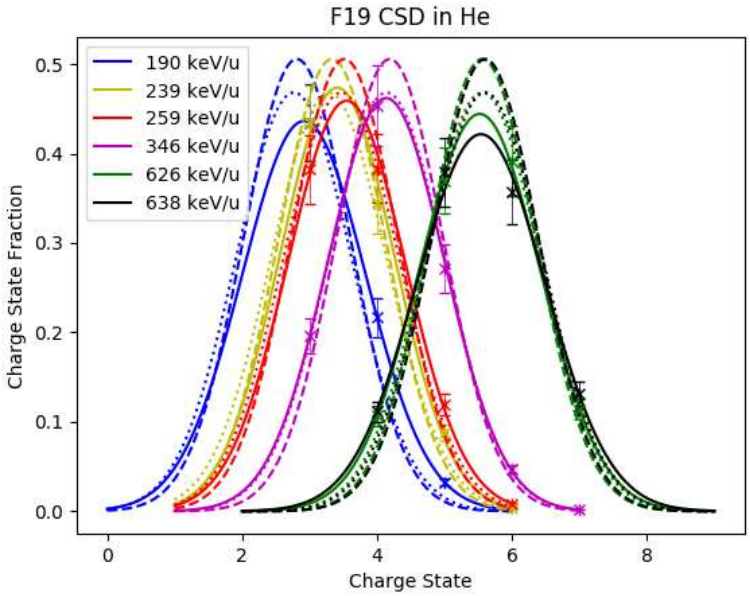

Figure B.10: Charge state distributions for ^{19}F in helium. The solid lines are experimental fits, the dashed lines are the semi-empirical formula using the parameters found by Liu and the dotted lines are from the semi-empirical formula using updated parameters.

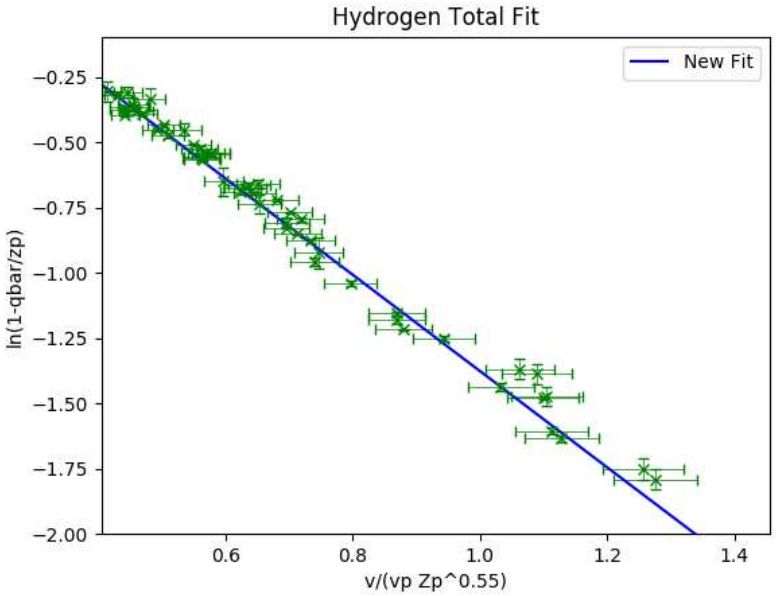

Figure B.11: Parameter fit for hydrogen CSD data for a γ value of 0.55. Liu's data is in red and the new data is in green. The vp in the reduced velocity is v′ mentioned in Results section.

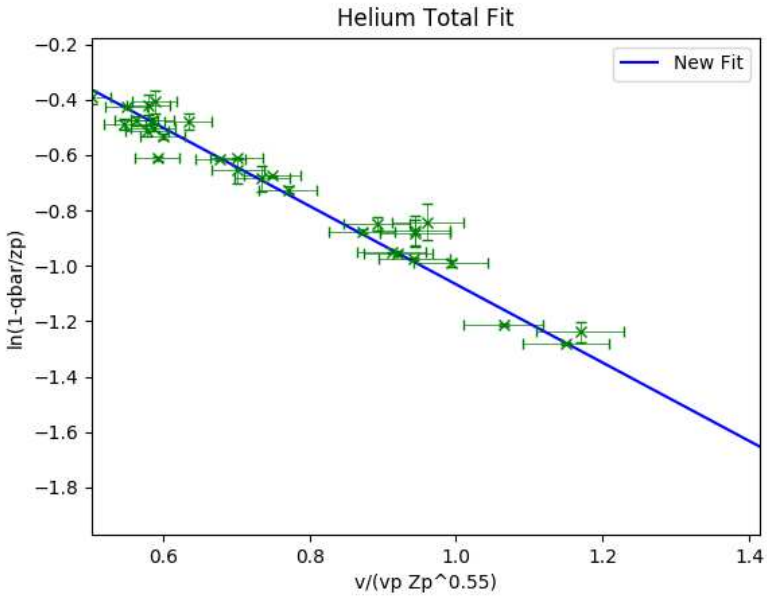

Figure B.12: Parameter fit for helium CSD data for a γ value of 0.55. Liu's data is in red and the new data is in green.

Table B.10: CSD measurements from Liu's work[59]. Energy is in units of keV/u.

Beam	E_{out}	1+	2+	3+	4+	5+	6+	7+	8+	9+	10+
^{15}N	435				3.70(22)	34.32(90)	57.57(95)	4.41(26)			
^{16}O	138	10.46(56)	43.30(121)	38.99(118)	7.01(46)	0.33(5)					
	200		17.59(71)	48.78(121)	30.17(105)	3.41(27)	0.05(1)				
	325		1.10(9)	13.41(56)	47.59(122)	34.19(113)	3.71(29)				
	325			7.37(41)	50.07(94)	37.51(91)	5.05(35)				
	500			0.50(6)	10.00(44)	44.50(127)	43.50(126)	1.50(9)			
	500			0.35(4)	9.89(54)	41.88(95)	46.77(96)	1.11(7)			
	588			0.112)	3.50(29)	32.23(117)	59.85(124)	4.31(30)			
	800				0.36(4)	8.93(51)	65.81(84)	23.78(72)	1.12(14)		
^{23}Na	200		7.39(49)	42.51(121)	40.78(120)	8.72(57)	0.60(7)				
	374			1.01(11)	13.25(54)	40.90(115)	34.69(109)	9.44(50)	0.71(8)		
	478			0.10(2)	2.18(15)	16.74(66)	40.18(114)	32.81(106)	7.50(48)	0.49(8)	
^{24}Mg	200			36.17(88)	48.72(94)	14.03(44)	1.07(6)	0.01(1)			
	500				0.66(8)	8.92(40)	30.45(76)	40.81(85)	17.66(51)	2.13(12)	
	800						1.40(8)	10.51(33)	41.64(89)	37.78(86)	8.67(42)
^{16}O	138	20.78(79)	44.96(118)	27.69(97)	6.31(35)	0.26(4)					
	200	0.020(3)	33.04(110)	46.31(122)	18.64(74)	1.92(15)	0.07(1)				
	325		7.90(43)	34.48(110)	42.28(117)	14.61(59)	0.73(8)				
	371		4.28(27)	25.56(93)	47.21(147)	20.31(78)	2.10(12)				
	588			3.90(22)	24.45(90)	47.52(119)	23.31(87)	0.82(9)			
	750				9.00(59)	37.38(119)	48.11(125)	5.51(31)			
	875					29.88(111)	59.44(122)	10.68(59)			

APPENDIX C

STOPPING POWER

Several additional figures of stopping power in hydrogen and helium gas are contained in this section, along with tables of all data relating to stopping powers. In Figure C.1 the Ca+He stopping power data can be seen compared to SRIM and several variations of CASP as previously done in earlier sections. The few data points agree with SRIM almost perfectly and are close to the Bragg peak. Too few data exist to properly fit so no attempt was made to fit the data. Again CASP appears to underestimate the stopping power compared to SRIM and experiment. Data for K+H_2 can be seen in Figure C.2 compared to SRIM and

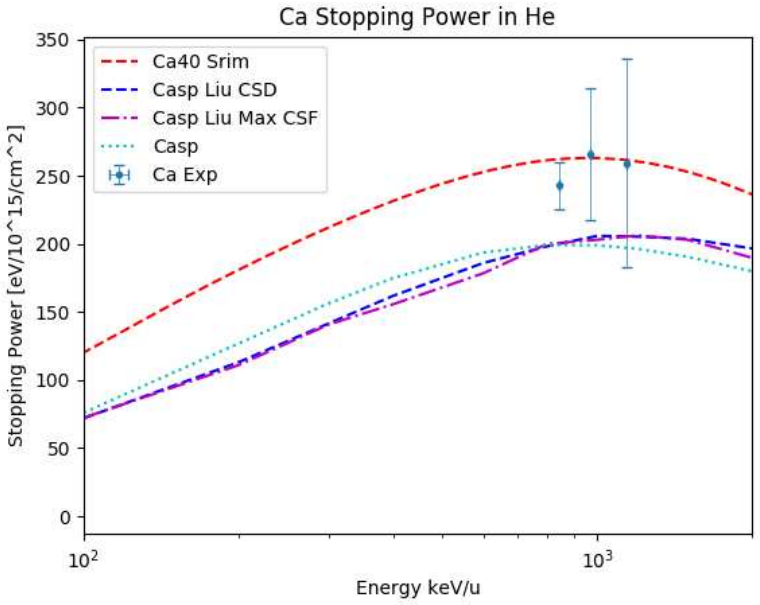

Figure C.1: Stopping power as a function of energy for Ca+He compared to SRIM in red. Results directly from CASP are in light blue. Results from CASP re-normalized to the CSD from the updated Liu formula are in dark blue.

CASP. Too few data exists to rely on the experimental fit away from the Bragg peak but SRIM seems to be a reasonable estimate at approximately 15% too high as seems to be the

case for most hydrogen targets. The modified CASP appears to overestimate the energy of the Bragg peak which causes poor agreement with experiment but approximates the peak height within about 14 %.

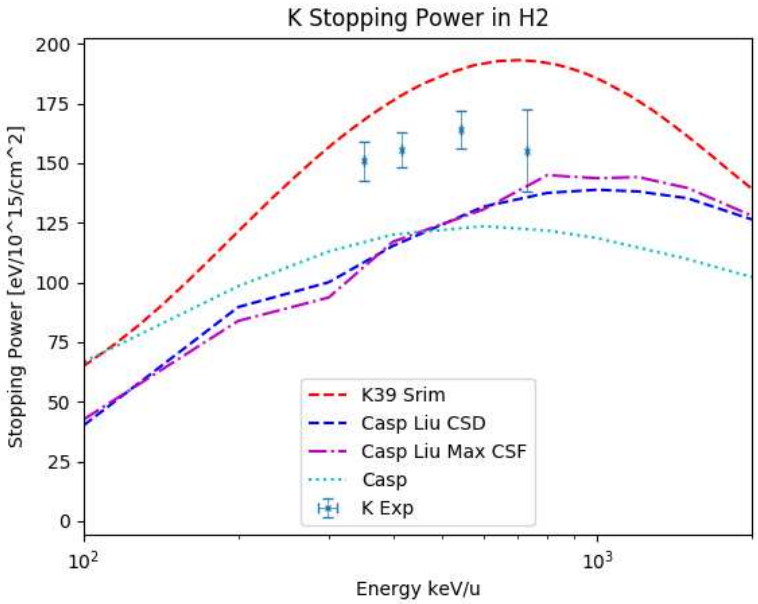

Figure C.2: Stopping power as a function of energy for K+H_2 compared to SRIM in red. Results directly from CASP are in light blue. Results from CASP re-normalized to the CSD from the updated Liu formula are in dark blue.

Compiled data for F+H_2 can be seen in Figure C.3. Only a few energies were found so no experimental fit was attempted. The limited data that exists agrees well with SRIM which could be a reliable estimate of the stopping power where no data currently exists. CASP predicts similar CSD's for this reaction as the semi-empirical formula as the modified CASP agrees with the regular CASP results. CASP appears to be a very poor estimator as a whole though, as it predicts the stopping power to be roughly half of what was measured.

In Figure C.4 the F+He stopping power can be seen for several energies. These agree with the results by SRIM very closely but not enough data exists to properly fit the entire distribution. CASP's CSD prediction agrees with that from the Liu formula but the stopping power peak height is significantly less than SRIM or the experimental data.

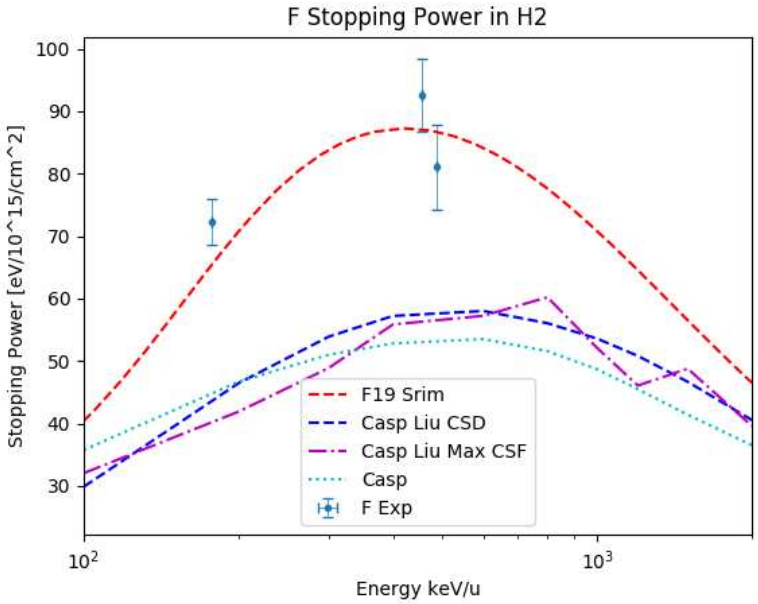

Figure C.3: Stopping power as a function of energy for F+H_2 compared to SRIM in red. Results directly from CASP are in light blue. Results from CASP re-normalized to the CSD from the updated Liu formula are in dark blue.

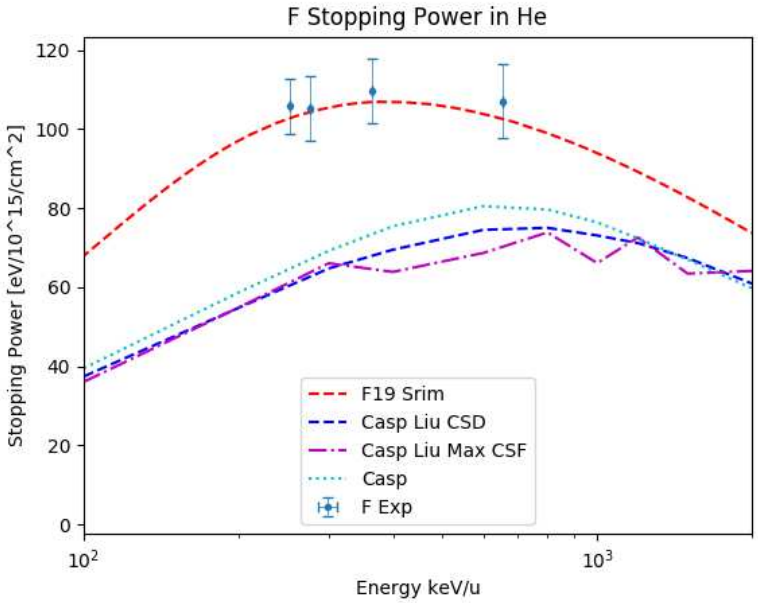

Figure C.4: Stopping power as a function of energy for F+He compared to SRIM in red. Results directly from CASP are in light blue. Results from CASP re-normalized to the CSD from the updated Liu formula are in dark blue.

The compiled data for S+H_2 can be seen in Figure C.5 at energies from 200 to 500 keV/u. No attempt was made to fit due to the limited range of data. SRIM overestimates the stopping power for most the measured values and CASP underestimates all measured values. CASP also predicts a lower energy Bragg peak compared to the Liu formula results.

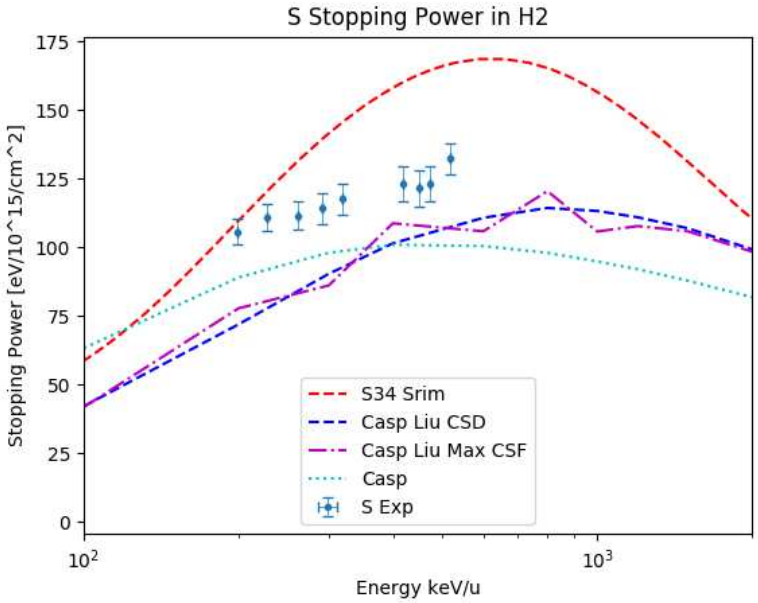

Figure C.5: Stopping power as a function of energy for S+H_2 compared to SRIM in red. Results directly from CASP are in light blue. Results from CASP re-normalized to the CSD from the updated Liu formula are in dark blue.

Stopping power data for S+He can be seen Figure C.6 for a small range of energies near the estimated Bragg peak. Too few data existed to properly fit so this was not done. SRIM overestimates the stopping power but just outside of error for most points measured so this could be a reliable means of estimating the stopping power. CASP again underestimates the stopping power but appears to have very similar results for the CSD compared to the semi-empirical formula as the modified CASP matches the regular CASP results. No new additional Cl+H_2 data was found outside of the stopping powers measured while taking CSD measurements for this work, as can be seen in Figure C.7. SRIM does not deviate far

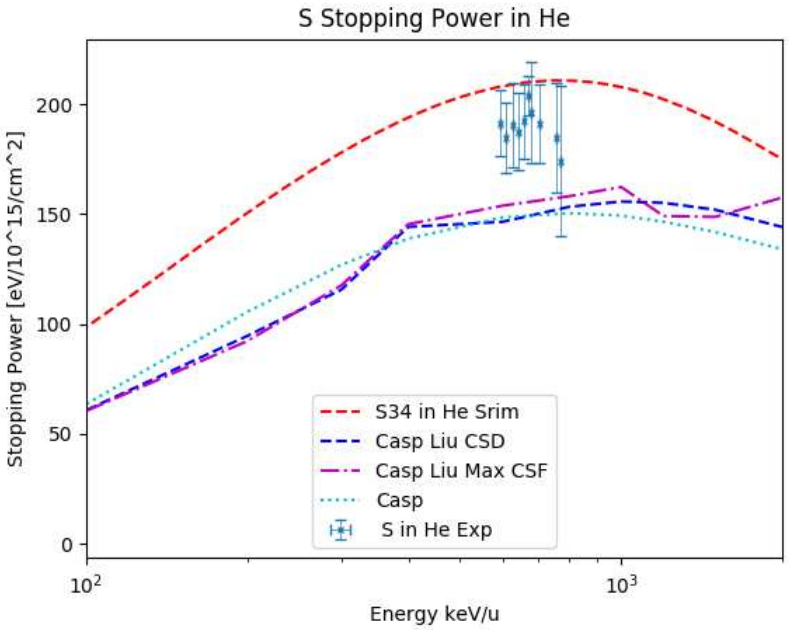

Figure C.6: Stopping power as a function of energy for S+He compared to SRIM in red. Results directly from CASP are in light blue. Results from CASP re-normalized to the CSD from the updated Liu formula are in dark blue.

from the measured stopping powers but more data is needed for a proper comparison. The regular CASP results peak at almost half the result by SRIM and the experimental data falls roughly in between for energies close to the Bragg peak.

A few points of Ar+H_2 data were found during this work, see Figure C.8, at energies near the approximated Bragg peak. SRIM overestimates the stopping power as is the case for most H_2 targets and CASP underestimates as is the case for all data found so far. The experimental data deviates from the SRIM approximation by roughly 20%.

In Figure C.9 the Al+H_2 stopping power can be seen. For most of the data found the stopping power is fairly well approximated by SRIM which overestimates by approximately 5%. Not enough data exists to properly fit the entire distribution so this was not done. All CASP estimates are approximately the same which shows that the CSD found by CASP agrees fairly well with the Liu formula results.

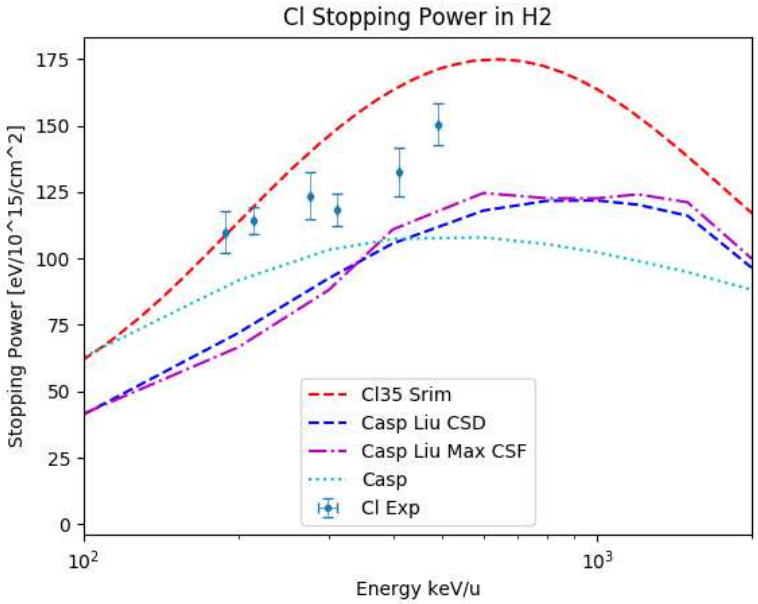

Figure C.7: Stopping power as a function of energy for Cl+H_2 compared to SRIM in red. Results directly from CASP are in light blue. Results from CASP re-normalized to the CSD from the updated Liu formula are in dark blue.

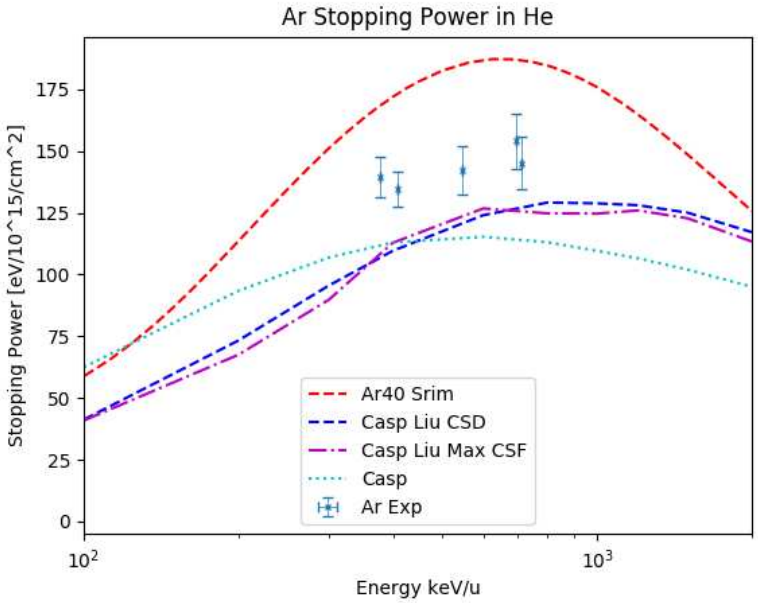

Figure C.8: Stopping power as a function of energy for Ar+He compared to SRIM in red. Results directly from CASP are in light blue. Results from CASP re-normalized to the CSD from the updated Liu formula are in dark blue.

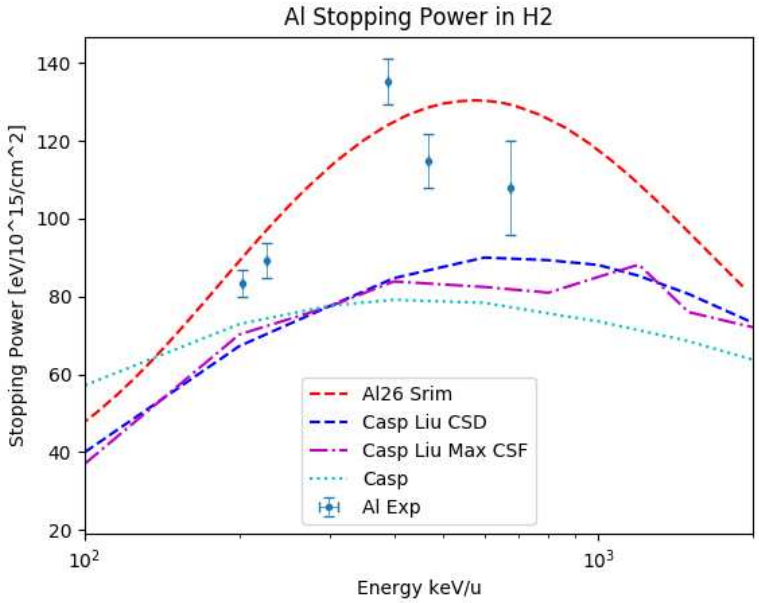

Figure C.9: Stopping power as a function of energy for Al+H_2 compared to SRIM in red. Results directly from CASP are in light blue. Results from CASP re-normalized to the CSD from the updated Liu formula are in dark blue.

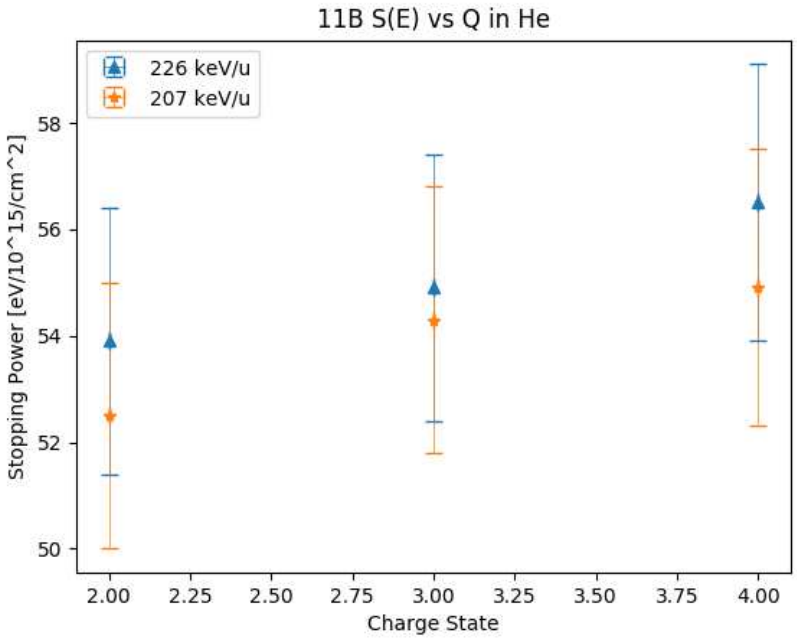

Figure C.10: Stopping power as a function of charge state for various energies of ^{11}B+He.

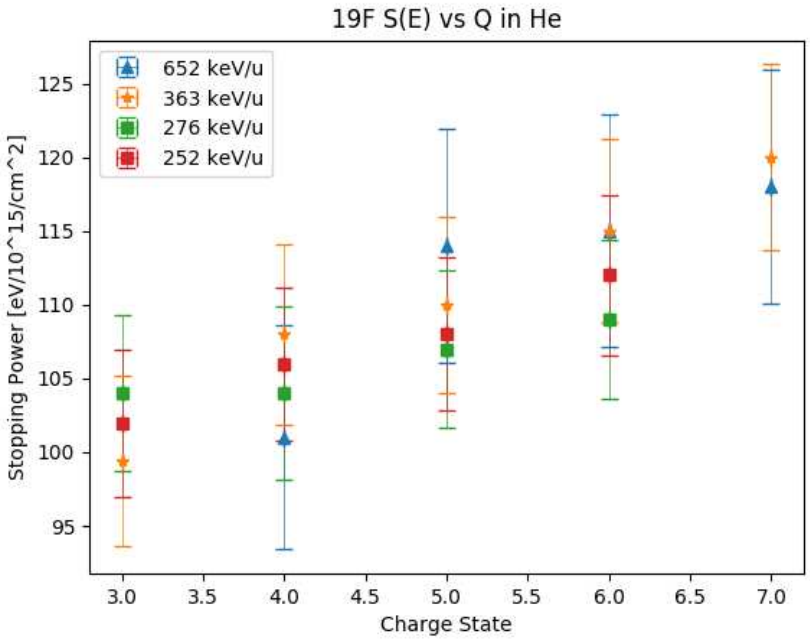

Figure C.11: Stopping power as a function of charge state for various energies of ^{19}F+He.

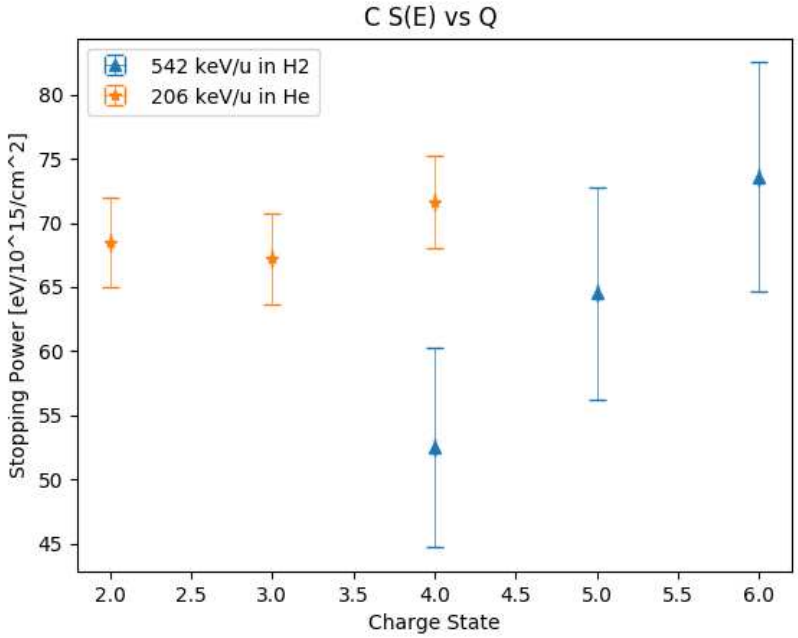

Figure C.12: Stopping power as a function of charge state for various energies of ^{12}C in both hydrogen and helium.

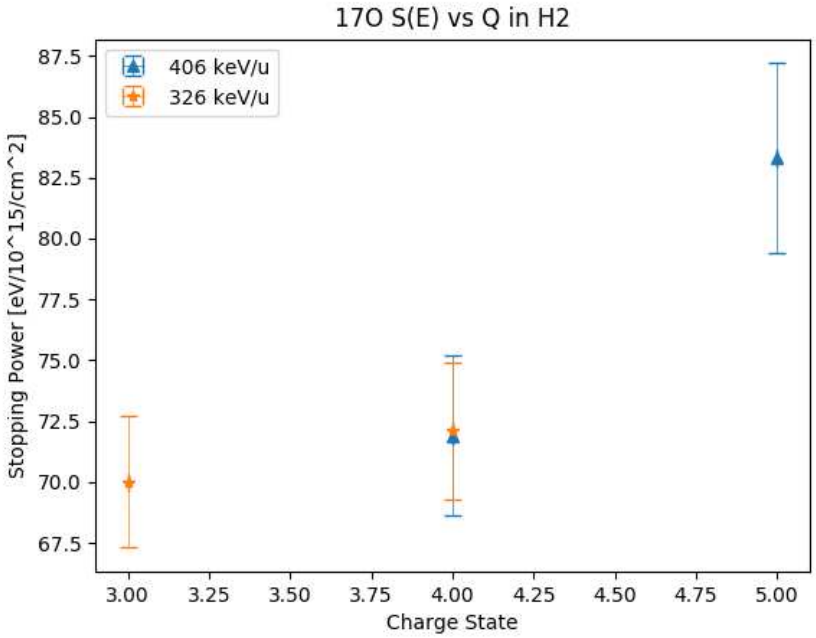

Figure C.13: Stopping power as a function of charge state for various energies of $^{17}O+H_2$.

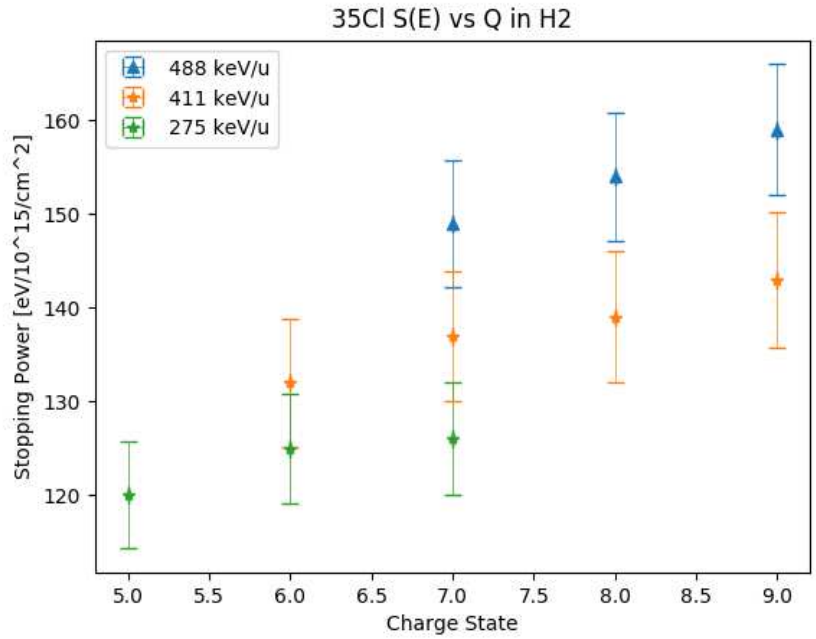

Figure C.14: Stopping power as a function of charge state for various energies of $^{35}Cl+H_2$.

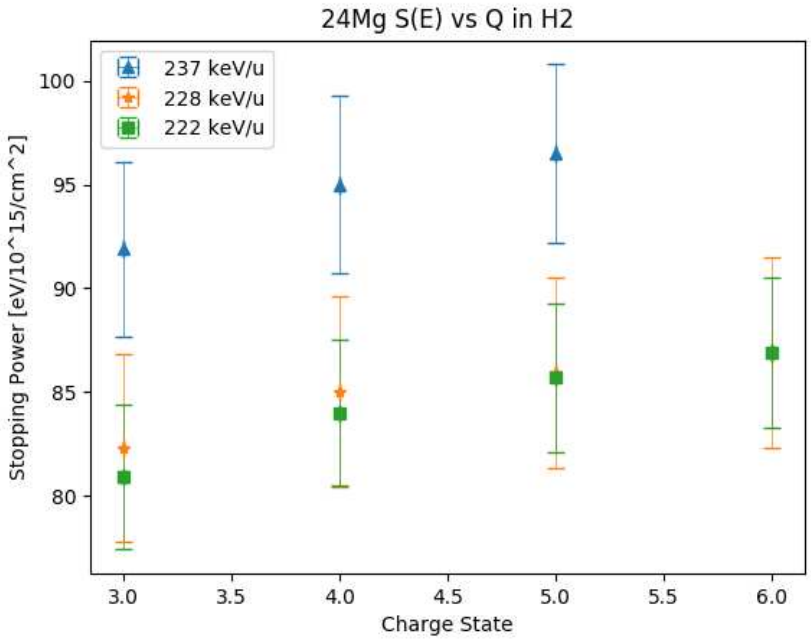

Figure C.15: Stopping power as a function of charge state for various energies of $^{24}Mg+H_2$.

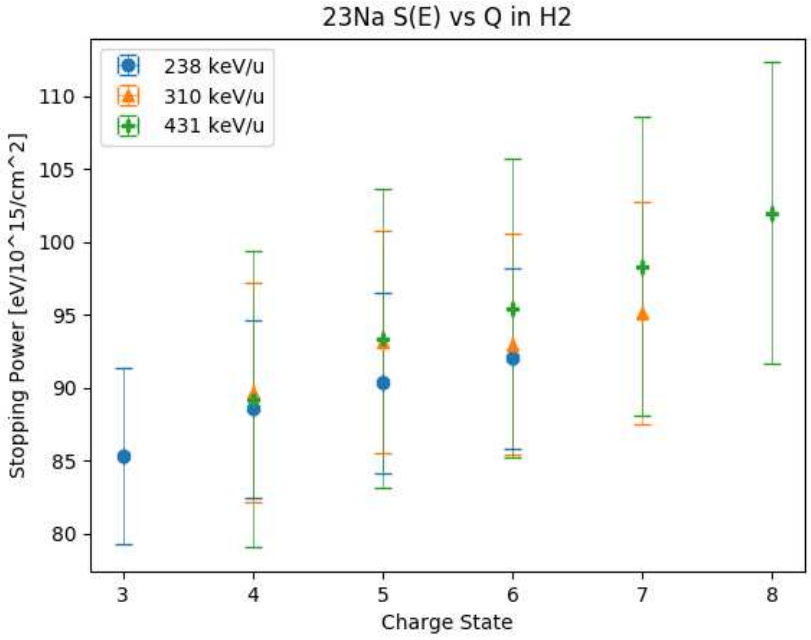

Figure C.16: Additional stopping power as a function of charge state measurements for various energies of $^{23}Na+H_2$.

Table C.1: Aluminum in hydrogen stopping powers

Energy [keV/u]	Target	Charge	S(E) $[\frac{eV}{10^{15}cm^2}]$	S(E) error
226.02	H	6.00	93.96	4.84
226.22	H	6.00	94.23	4.66
226.50	H	6.00	75.33	4.04
226.60	H	6.00	93.96	4.64
389.79	H	6.00	135.20	5.80
455.75	H	-	116.22	6.46
455.75	H	6.00	117.78	6.74
458.50	H	6.00	113.36	6.45
459.10	H	-	109.98	11.84
468.62	H	6.00	108.16	5.09
469.35	H	6.00	121.16	6.76
484.19	H	6.00	117.78	6.74

Table C.2: Argon in helium stopping powers

Energy [keV/u]	Target	Charge	S(E) $[\frac{eV}{10^{15}cm^2}]$	S(E) error
378.00	H	8.00	139.60	8.29
407.30	H	6.00	134.52	7.2
545.33	H	8.00	142.40	9.82
696.00	H	10.00	154.00	11.38
713.00	H	10.00	145.16	10.54

Table C.3: Calcium in helium stopping powers

Energy [keV/u]	Target	Charge	S(E) $[\frac{eV}{10^{15}cm^2}]$	S(E) error
829.00	He	11.00	260.00	45.80
841.00	He	10.00	243.00	17.30
968.00	He	12.00	266.00	48.60
1120.00	He	11.00	200.00	82.10
1120.00	He	11.00	347.00	146.00
1130.00	He	11.00	246.00	91.60
1130.00	He	11.00	213.00	67.60
1130.00	He	12.00	259.00	56.80
1130.00	He	12.00	158.00	52.10
1150.00	He	12.00	249.00	54.40
1150.00	He	13.00	220.00	55.90
1150.00	He	13.00	238.00	54.80
1160.00	He	12.00	224.00	58.10

Table C.4: Carbon in hydrogen stopping powers

Beam	Energy [keV/u]	Target	Charge	S(E) $[\frac{eV}{10^{15}cm^2}]$	S(E) error
C13	447.97	H	3.00	41.99	5.78
C13	542.87	H	4.00	52.52	7.76
C13	542.87	H	6.00	73.58	8.85
C13	542.89	H	5.00	64.48	8.32
C13	556.67	H	5.00	45.11	3.40
C13	571.14	H	5.00	40.56	7.65
C13	571.14	H	6.00	52.91	8.65
C13	571.14	H	7.00	42.77	8.36
C13	649.00	H	5.00	38.87	8.81
C13	650.09	H	5.00	51.87	8.85
C13	651.63	H	3.00	49.27	3.15

Table C.5: Carbon in helium stopping powers

Energy [keV/u]	Target	Charge	S(E) $[\frac{eV}{10^{15}cm^2}]$	S(E) error
148.00	He	2.00	58.92	2.35
149.00	He	2.00	58.92	2.35
206.00	He	2.00	69.12	3.55
206.00	He	3.00	74.76	3.69
272.00	He	2.00	64.22	2.98
338.00	He	3.00	67.34	3.35
341.00	He	3.00	66.95	3.25
343.00	He	-	71.50	3.42
405.00	He	-	64.22	3.48
442.00	He	3.00	67.47	3.75
442.00	He	3.00	64.35	3.63
747.00	He	6.00	63.60	6.18
810.00	He	6.00	58.08	9.22
856.00	He	6.00	54.00	6.65
881.00	He	5.00	53.28	21.02
895.00	He	5.00	63.24	18.36
896.00	He	5.00	58.44	15.90
902.00	He	5.00	47.88	17.59
905.00	He	5.00	58.92	18.31
906.00	He	5.00	67.32	19.55
1070.00	He	5.00	64.80	6.40
1070.00	He	5.00	50.76	7.53
1080.00	He	5.00	53.76	8.91
1080.00	He	5.00	48.84	16.48

Table C.5: Continued.

1080.00	He	6.00	91.44	7.37
1090.00	He	5.00	54.96	7.59
1090.00	He	6.00	68.64	9.49
1100.00	He	5.00	45.24	12.28
1100.00	He	6.00	96.96	14.71
1100.00	He	6.00	50.52	7.27
1130.00	He	5.00	40.92	18.03
1130.00	He	6.00	52.68	7.76
1160.00	He	6.00	90.60	10.90
1160.00	He	6.00	41.04	8.01
1180.00	He	6.00	52.08	9.04
1220.00	He	6.00	60.00	9.55
1220.00	He	6.00	35.64	16.39
1240.00	He	6.00	50.04	15.44
1250.00	He	6.00	46.32	8.41
1300.00	He	6.00	46.08	10.01
1300.00	He	6.00	55.92	31.03
1300.00	He	6.00	49.68	9.19
1300.00	He	6.00	51.96	11.32
1300.00	He	6.00	82.56	11.59
1310.00	He	6.00	46.92	10.32
1310.00	He	6.00	49.32	9.32
1320.00	He	6.00	41.04	14.53
1320.00	He	6.00	43.32	10.58
1330.00	He	6.00	48.36	10.54
1340.00	He	6.00	46.20	7.98
1360.00	He	6.00	80.64	9.74
1360.00	He	6.00	43.68	9.46
1370.00	He	6.00	52.44	30.46
1380.00	He	6.00	45.72	11.29
1400.00	He	6.00	30.24	19.70
1410.00	He	6.00	36.84	8.21
1410.00	He	6.00	42.24	17.24
1430.00	He	6.00	52.08	10.91
1430.00	He	6.00	49.92	10.67
1430.00	He	6.00	47.40	12.90
1430.00	He	6.00	46.80	11.18
1460.00	He	6.00	43.08	10.55
1460.00	He	6.00	47.88	20.12
1460.00	He	6.00	45.00	10.65
1460.00	He	6.00	60.84	9.62
1470.00	He	6.00	75.96	12.13

Table C.5: Continued.

1470.00	He	6.00	54.72	44.62
1480.00	He	6.00	45.48	19.43
1480.00	He	6.00	39.36	21.42
1480.00	He	6.00	84.48	36.11
1480.00	He	6.00	75.84	10.10
1480.00	He	6.00	37.80	16.41
1490.00	He	6.00	23.64	11.06
1500.00	He	6.00	79.44	11.56
1510.00	He	6.00	76.08	13.59
1520.00	He	6.00	75.84	13.46
1520.00	He	6.00	36.72	24.34
1540.00	He	6.00	45.36	21.32
1550.00	He	6.00	89.40	27.85
1630.00	He	6.00	39.36	23.49
1630.00	He	6.00	39.00	31.49
1640.00	He	6.00	33.60	24.97
1640.00	He	6.00	42.84	21.61
1670.00	He	6.00	33.24	31.48
1690.00	He	6.00	30.72	21.63
1720.00	He	6.00	35.16	21.28
1720.00	He	6.00	55.92	31.44
1760.00	He	6.00	39.12	25.21
1810.00	He	6.00	39.00	25.14

Table C.6: Fluorine in hydrogen stopping powers

Energy [keV/u]	Target	Charge	S(E) $[\frac{eV}{10^{15}cm^2}]$	S(E) error
167.43	H	-	71.25	3.61
186.85	H	-	73.34	3.77
454.77	H	-	92.53	5.77
485.00	H	6.00	81.13	6.68
487.00	H	6.00	80.94	7.09

Table C.7: Chlorine in hydrogen stopping powers

Energy [keV/u]	Target	Charge	S(E) $[\frac{eV}{10^{15}cm^2}]$	S(E) error
188.00	H	4.00	109.55	4.93
188.00	H	5.00	109.20	4.92
188.00	H	6.00	110.95	14.26
214.00	H	5.00	115.15	5.29
214.00	H	6.00	113.40	5.22
276.00	H	5.00	123.55	8.92
311.00	H	6.00	120.75	6.14
311.00	H	7.00	122.15	6.17
311.00	H	8.00	112.35	5.88
412.00	H	6.00	132.30	9.13
488.00	H	7.00	149.45	6.78
488.00	H	8.00	154.00	6.87
488.00	H	9.00	159.25	6.99
498.00	H	8.00	139.30	10.59

Table C.8: Fluorine in helium stopping powers

Energy [keV/u]	Target	Charge	S(E) $[\frac{eV}{10^{15}cm^2}]$	S(E) error
252.00	He	4.00	104.88	8.80
252.00	He	4.00	106.92	5.18
276.00	He	4.00	104.50	10.86
277.00	He	4.00	106.02	5.47
364.00	He	4.00	110.50	6.06
364.00	He	4.00	108.68	10.17
653.00	He	4.00	112.01	7.83
653.00	He	4.00	102.22	11.00

Table C.9: Potassium in helium stopping powers

Energy [keV/u]	Target	Charge	S(E) $[\frac{eV}{10^{15}cm^2}]$	S(E) error
351.00	H	-	150.93	8.21
416.45	H	7.00	155.61	7.22
543.57	H	8.00	164.19	7.75
730.00	H	10.00	155.22	17.18

Table C.10: Sodium in hydrogen stopping powers

Beam	Energy [keV/u]	Target	Charge	S(E) $[\frac{eV}{10^{15}cm^2}]$	S(E) error	
21Na	210.00	H	4.00	83.00	3.67	
21Na	213.00	H	4.00	86.10	4.34	
21Na	213.00	H	5.00	85.30	4.31	
21Na	214.00	H	4.00	76.40	6.06	
21Na	214.00	H	4.00	82.10	4.15	
21Na	215.00	H	5.00	82.10	4.13	
21Na	220.00	H	4.00	83.20	3.76	
21Na	221.00	H	4.00	83.00	3.71	
21Na	222.00	H	4.00	100.00	5.02	
21Na	225.00	H	4.00	83.60	3.77	
21Na	225.00	H	6.00	73.30	3.44	
21Na	230.00	H	8.00	73.30	3.47	
21Na	471.00	H	6.00	104.00	5.58	
21Na	480.00	H	7.00	96.20	5.89	
21Na	487.00	H	6.00	102.00	4.41	
21Na	492.00	H	6.00	94.30	4.24	
21Na	496.00	H	6.00	101.00	4.57	
21Na	496.00	H	7.00	103.00	4.65	
21Na	569.00	H	7.00	95.10	4.60	
21Na	570.00	H	6.00	98.30	4.25	
21Na	579.00	H	7.00	94.50	4.64	
21Na	582.00	H	7.00	98.50	5.36	
21Na	825.00	H	8.00	89.00	14.70	
21Na	838.00	H	8.00	82.10	9.57	
21Na	862.00	H	8.00	89.90	26.20	
21Na	874.00	H	8.00	81.50	13.50	
21Na	884.00	H	8.00	68.90	16.50	
21Na	1150.00	H	9.00	70.40	23.60	
21Na	1150.00	H	9.00	71.40	12.30	
21Na	1160.00	H	8.00	68.00	12.50	
22Na	191.00	H	3.00	79.90	3.72	
22Na	196.00	H	4.00	71.70	3.13	
22Na	197.00	H	-	82.10	3.52	
22Na	265.00	H	4.00	88.90	4.37	
22Na	300.00	H	5.00	86.20	4.14	
22Na	343.00	H	-	91.10	4.96	
22Na	400.00	H	5.00	89.30	4.65	
22Na	421.00	H	-	83.60	11.20	
22Na	486.00	H	6.00	109.00	6.00	
22Na	660.00	H	7.00	82.10	9.86	

Table C.10: Continued.

22Na	694.00	H	-	71.60	6.30	
23Na	175.00	H	-	79.30	3.34	
23Na	238.00	H	-	89.10	3.94	
23Na	269.00	H	-	85.40	3.95	
23Na	310.00	H	-	86.40	4.37	
23Na	373.00	H	6.00	96.60	8.81	
23Na	374.00	H	6.00	72.20	7.87	
23Na	377.00	H	6.00	76.80	15.60	
23Na	382.00	H	6.00	80.00	15.90	
23Na	431.00	H	-	95.70	10.20	
23Na	501.00	H	-	101.00	10.70	
23Na	508.00	H	6.00	96.10	6.95	

Table C.11: Neon in hydrogen stopping powers

Beam	Energy [keV/u]	Target	Charge	S(E) $[\frac{eV}{10^{15}cm^2}]$	S(E) error
20Ne	275.00	H	4.00	84.50	3.53
20Ne	275.00	H	4.00	84.80	3.51
20Ne	332.00	H	4.00	88.30	3.79
20Ne	460.00	H	5.00	92.20	5.13
20Ne	461.00	H	6.00	94.40	4.31
20Ne	522.00	H	6.00	91.60	4.85
20Ne	541.00	H	5.00	88.90	4.48
20Ne	541.00	H	5.00	90.20	5.46
20Ne	927.00	H	8.00	79.40	11.70
20Ne	1150.00	H	8.00	41.60	4.48
20Ne	1150.00	H	9.00	67.60	10.20
20Ne	1150.00	H	9.00	70.00	8.71
20Ne	1160.00	H	8.00	64.20	15.40
20Ne	1160.00	H	8.00	65.20	14.20
20Ne	1160.00	H	8.00	108.00	16.10
20Ne	1160.00	H	8.00	106.00	16.00
20Ne	1160.00	H	8.00	68.80	13.10
20Ne	1160.00	H	8.00	75.80	11.40
20Ne	1160.00	H	8.00	71.80	14.00
20Ne	1160.00	H	8.00	65.40	15.50
20Ne	1160.00	H	8.00	58.80	6.72
20Ne	1160.00	H	8.00	60.80	21.50
20Ne	1160.00	H	8.00	60.80	19.10
20Ne	1160.00	H	8.00	61.20	31.40
20Ne	1160.00	H	8.00	60.40	21.30

Table C.11: Continued.

20Ne	1160.00	H	9.00	57.60	10.70
20Ne	1160.00	H	9.00	62.60	16.90
20Ne	1160.00	H	9.00	58.20	10.70
20Ne	1160.00	H	9.00	60.00	10.80
20Ne	1160.00	H	9.00	68.60	6.92
20Ne	1160.00	H	9.00	66.60	6.49
20Ne	1160.00	H	9.00	69.00	6.48
20Ne	1160.00	H	9.00	68.40	6.48
20Ne	1160.00	H	9.00	70.00	9.19
20Ne	1170.00	H	7.00	62.80	7.40
20Ne	1170.00	H	8.00	66.40	14.60
20Ne	1170.00	H	8.00	66.20	13.60
20Ne	1170.00	H	8.00	113.00	14.60
20Ne	1170.00	H	8.00	64.00	16.10
20Ne	1170.00	H	8.00	66.40	16.90
20Ne	1170.00	H	8.00	61.20	16.90
20Ne	1170.00	H	8.00	76.80	14.50
20Ne	1170.00	H	8.00	62.40	14.70
20Ne	1170.00	H	8.00	62.20	8.77
20Ne	1170.00	H	8.00	66.40	16.90
20Ne	1170.00	H	8.00	96.20	14.90
20Ne	1170.00	H	8.00	65.60	14.80
20Ne	1170.00	H	8.00	94.60	9.94
20Ne	1170.00	H	9.00	67.20	7.55
20Ne	1170.00	H	9.00	65.60	7.80
20Ne	1170.00	H	9.00	47.40	11.40
20Ne	1170.00	H	9.00	54.40	9.91
20Ne	1170.00	H	9.00	49.40	17.00
20Ne	1180.00	H	8.00	68.20	15.10
20Ne	1180.00	H	8.00	92.80	19.50
20Ne	1180.00	H	9.00	66.80	6.75
20Ne	1180.00	H	9.00	65.20	6.83
20Ne	1250.00	H	8.00	59.40	9.86
20Ne	1250.00	H	8.00	58.20	13.20
20Ne	1470.00	H	8.00	81.00	11.50
20Ne	1470.00	H	8.00	88.60	23.10
21Ne	215.00	H	4.00	77.90	4.07
21Ne	272.00	H	4.00	83.00	4.39
21Ne	273.00	H	4.00	84.20	7.36
21Ne	273.00	H	5.00	89.50	6.84
21Ne	274.00	H	4.00	83.40	5.41
21Ne	275.00	H	4.00	83.60	4.68

Table C.11: Continued.

21Ne	275.00	H	4.00	84.40	4.51
21Ne	275.00	H	5.00	86.30	4.61
21Ne	276.00	H	4.00	84.80	4.49
21Ne	276.00	H	4.00	90.90	4.82
21Ne	277.00	H	4.00	86.30	4.48
21Ne	277.00	H	4.00	76.20	2.95
21Ne	279.00	H	4.00	86.30	4.60
21Ne	279.00	H	5.00	88.40	4.25
21Ne	279.00	H	-	89.70	5.43
21Ne	281.00	H	5.00	85.90	4.24
21Ne	282.00	H	-	89.00	4.80
21Ne	285.00	H	4.00	71.80	2.97
21Ne	285.00	H	4.00	84.20	3.59
21Ne	356.00	H	6.00	80.20	3.52
21Ne	488.00	H	5.00	89.30	5.85
21Ne	491.00	H	6.00	90.10	5.84
21Ne	492.00	H	6.00	91.80	5.89
21Ne	493.00	H	6.00	85.70	5.71
21Ne	494.00	H	6.00	87.80	5.67
21Ne	495.00	H	6.00	86.90	5.72
21Ne	495.00	H	6.00	83.60	5.65
21Ne	496.00	H	5.00	92.20	5.99
21Ne	496.00	H	6.00	85.30	5.68
21Ne	499.00	H	6.00	88.00	5.83
21Ne	499.00	H	6.00	86.90	5.80
21Ne	500.00	H	6.00	93.70	4.33
21Ne	501.00	H	6.00	82.30	5.72
21Ne	503.00	H	6.00	81.50	5.63
21Ne	509.00	H	6.00	88.80	5.94
21Ne	511.00	H	6.00	89.90	5.97
21Ne	513.00	H	6.00	73.30	5.40
21Ne	513.00	H	6.00	78.80	5.57
21Ne	514.00	H	6.00	90.50	6.04
21Ne	516.00	H	6.00	85.50	5.80
21Ne	516.00	H	6.00	86.10	8.07
21Ne	519.00	H	6.00	96.60	6.21
21Ne	519.00	H	6.00	103.00	6.44
21Ne	520.00	H	6.00	92.20	8.58
21Ne	521.00	H	6.00	85.90	5.86
21Ne	524.00	H	6.00	92.00	8.41
21Ne	524.00	H	6.00	87.40	6.04
21Ne	526.00	H	6.00	86.50	8.30

Table C.11: Continued.

21Ne	527.00	H	6.00	95.80	8.66
21Ne	579.00	H	7.00	93.20	4.61
21Ne	760.00	H	8.00	89.30	7.51
21Ne	762.00	H	8.00	86.50	7.49
21Ne	763.00	H	8.00	90.10	7.63
21Ne	772.00	H	8.00	94.10	7.78
21Ne	773.00	H	8.00	95.80	7.77
21Ne	774.00	H	7.00	81.70	4.80
21Ne	860.00	H	8.00	77.10	9.94
21Ne	867.00	H	8.00	81.70	13.30
21Ne	1130.00	H	8.00	91.80	9.65
21Ne	1140.00	H	9.00	74.60	14.50
21Ne	1150.00	H	9.00	64.10	11.90
22Ne	251.00	H	-	84.60	4.52
22Ne	266.00	H	-	81.70	3.75
22Ne	300.00	H	3.00	95.90	4.38
22Ne	300.00	H	5.00	95.10	4.36
22Ne	328.00	H	5.00	92.40	4.40
22Ne	328.00	H	5.00	92.40	4.40
22Ne	343.00	H	-	91.00	4.13
22Ne	375.00	H	5.00	92.50	4.58
22Ne	400.00	H	5.00	89.60	4.49
22Ne	440.00	H	7.00	85.40	9.28
22Ne	443.00	H	4.00	82.70	4.02
22Ne	482.00	H	6.00	87.80	7.77
22Ne	536.00	H	6.00	73.30	6.28
22Ne	545.00	H	5.00	88.20	10.50
22Ne	643.00	H	-	77.20	8.79
22Ne	660.00	H	-	89.10	8.91
22Ne	695.00	H	-	72.90	7.46
22Ne	711.00	H	5.00	62.50	10.60
22Ne	723.00	H	5.00	82.00	11.90
22Ne	1280.00	H	9.00	55.20	19.80
22Ne	1510.00	H	8.00	46.60	13.80

Table C.12: Nitrogen in helium stopping powers

Energy [keV/u]	Target	Charge	S(E) $[\frac{eV}{10^{15}cm^2}]$	S(E) error
387	He	3.00	78.2	4.63
426	He	3.00	79.4	4.41
430	He	-	79.5	5.65
874	He	-	63.5	14.3
876	He	-	66.6	13.9
879	He	-	68.4	14.5
882	He	5.00	65.6	14.5
883	He	5.00	68.4	12.2
1000	He	6.00	67.8	11.3
1000	He	6.00	69.9	11.3
1010	He	6.00	67.5	11.3
1020	He	6.00	65.7	11.4
1030	He	6.00	68.1	11.5
1110	He	-	68.1	23.6
1120	He	-	48.6	23.2
1140	He	-	56.9	8.4

Table C.13: Oxygen in hydrogen stopping powers

Beam	Energy [keV/u]	Target	Charge	S(E) $[\frac{eV}{10^{15}cm^2}]$	S(E) error
O17	187	H	3.00	67.8	3.47
O17	198	H	-	70.7	3.72
O17	233	H	-	71.6	2.85
O17	233	H	-	68.3	3.52
O17	283	H	4.00	74.3	3.05
O17	327	H	3.00	70	2.7
O17	327	H	4.00	72.1	2.78
O17	375	H	-	70.6	2.97
O17	407	H	4.00	71.9	3.3
O17	407	H	5.00	83.3	3.91
O17	486	H	4.00	68.3	4.86
O17	495	H	4.00	68.2	4.91
O17	505	H	-	70.9	3.51
O18	714	H	4.00	43.5	4.52
O18	716	H	6.00	66.4	3.95
O18	716	H	6.00	66.4	3.95
O18	729	H	6.00	44	5.08
O18	734	H	6.00	43.2	4.61
O18	739	H	4.00	42.2	3.35
O18	768	H	5.00	42.6	3.46
O18	818	H	7.00	55.8	4.23

Table C.14: Oxygen in helium stopping powers

Beam	Energy [keV/u]	Target	Charge	S(E) $[\frac{eV}{10^{15}cm^2}]$	S(E) error
O17	223	He	-	89.4	3.67
O17	255	He	-	102	6.14
O17	261	He	3.00	98.6	6.21
O17	363	He	3.00	113	7.42
O17	366	He	3.00	104	7.44
O16	776	He	6.00	84.5	8.04
O16	776	He	6.00	88.8	7.22
O16	782	He	6.00	62.6	4.67
O16	969	He	6.00	84.3	15.4
O16	974	He	6.00	93.9	11.4

Table C.15: Sulfur in hydrogen stopping powers

Energy [keV/u]	Target	Charge	S(E) $[\frac{eV}{10^{15}cm^2}]$	S(E) error
194.24	H	6.00	104.28	4.58
194.87	H	4.00	102.96	4.53
208.58	H	6.00	109.23	4.83
227.49	H	6.00	110.88	4.95
259.00	H	6.00	111.87	5.25
261.88	H	6.00	108.24	5.02
262.00	H	6.00	114.18	5.38
287.00	H	5.00	110.47	5.78
296.84	H	6.00	117.81	5.55
309.66	H	6.00	113.85	5.46
315.08	H	6.00	119.13	5.62
318.70	H	5.00	114.38	6.17
318.80	H	6.00	122.43	5.80
327.90	H	7.00	117.81	5.65
409.70	H	6.00	125.06	6.55
420.32	H	7.00	124.74	6.31
426.87	H	6.00	119.64	6.82
450.30	H	7.00	121.44	6.62
451.60	H	8.00	113.82	5.94
472.50	H	8.00	122.38	6.43
492.50	H	8.00	133.16	6.95
518.40	H	8.00	132.22	5.50

Table C.16: Sulfur in helium stopping powers

Energy [keV/u]	Target	Charge	S(E) $[\frac{eV}{10^{15}cm^2}]$	S(E) error
595.00	He	7.00	191.42	15.14
610.09	He	7.00	184.62	15.90
628.35	He	7.00	190.40	19.04
641.00	He	7.00	187.34	17.54
658.00	He	8.00	192.10	16.88
670.00	He	8.00	203.66	8.89
678.18	He	-	196.18	22.82
705.00	He	8.00	191.08	17.72
758.20	He	-	184.96	24.94

APPENDIX D

COPYRIGHT PERMISSIONS

This section includes all permissions for copyrighted images used throughout the body of the thesis.

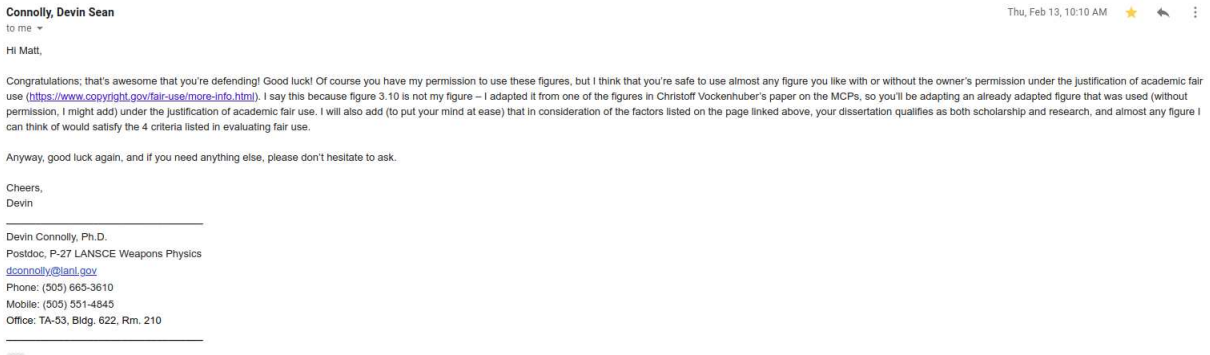

Connolly, Devin Sean Thu, Feb 13, 10:10 AM

to me

Hi Matt,

Congratulations; that's awesome that you're defending! Good luck! Of course you have my permission to use these figures, but I think that you're safe to use almost any figure you like with or without the owner's permission under the justification of academic fair use (https://www.copyright.gov/fair-use/more-info.html). I say this because figure 3.10 is not my figure – I adapted it from one of the figures in Christoff Vockenhuber's paper on the MCPs, so you'll be adapting an already adapted figure that was used (without permission, I might add) under the justification of academic fair use. I will also add (to put your mind at ease) that in consideration of the factors listed on the page linked above, your dissertation qualifies as both scholarship and research, and almost any figure I can think of would satisfy the 4 criteria listed in evaluating fair use.

Anyway, good luck again, and if you need anything else, please don't hesitate to ask.

Cheers,
Devin

Devin Connolly, Ph.D.
Postdoc, P-27 LANSCE Weapons Physics
dconnolly@lanl.gov
Phone: (505) 665-3610
Mobile: (505) 551-4845
Office: TA-53, Bldg. 622, Rm. 210

JAEA Nuclear Data Center <jendl@jaea.go.jp> Tue, Jan 28, 5:38 PM

to me

Dear Matthew,

Thank you for your inquiry.

Of course, you can reuse the image of our chart of nuclides 2014.
We hope that the contents of our website are useful for you.

Best Regards,

Shinsuke Nakayama
Nuclear Data Center, Japan Atomic Energy Agency

2020-01-28 (火) の 13:43 -0700 に Matthew Lovely さんは書きました:

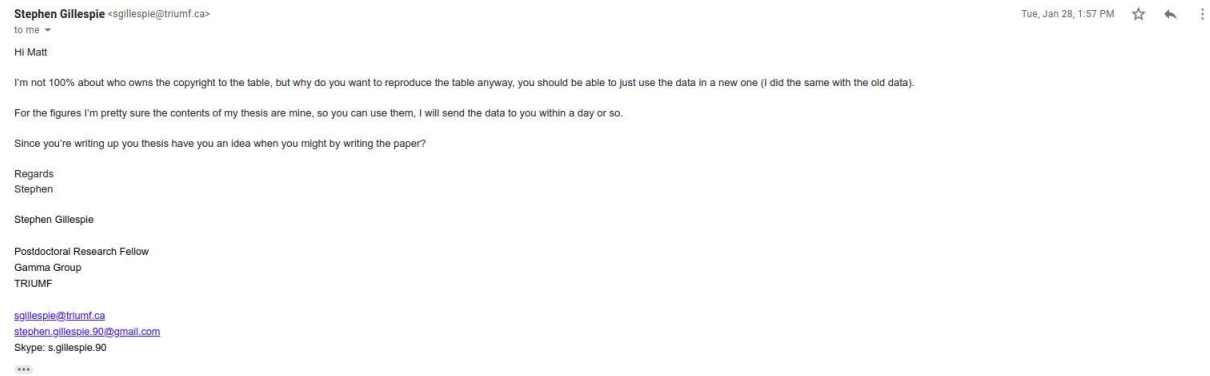

Stephen Gillespie <sgillespie@triumf.ca> Tue, Jan 28, 1:57 PM

to me

Hi Matt

I'm not 100% about who owns the copyright to the table, but why do you want to reproduce the table anyway, you should be able to just use the data in a new one (I did the same with the old data).

For the figures I'm pretty sure the contents of my thesis are mine, so you can use them, I will send the data to you within a day or so.

Since you're writing up you thesis have you an idea when you might by writing the paper?

Regards
Stephen

Stephen Gillespie

Postdoctoral Research Fellow
Gamma Group
TRIUMF

sgillespie@triumf.ca
stephen.gillespie.90@gmail.com
Skype: s.gillespie.90

American Physical Society
Reuse and Permissions License

28-Jan-2020

This license agreement between the American Physical Society ("APS") and Matthew Lovely ("You") consists of your license details and the terms and conditions provided by the American Physical Society and SciPris.

Licensed Content Information

License Number:	**RNP/20/JAN/022310**
License date:	28-Jan-2020
DOI:	10.1103/PhysRevC.96.025801
Title:	First measurement of the $^{34}\mathrm{S}(p,g)^{35}\mathrm{Cl}$ reaction rate through indirect methods for presolar nova grains
Author:	S. A. Gillespie et al.
Publication:	Physical Review C
Publisher:	American Physical Society
Cost:	USD $ 0.00

Request Details

Does your reuse require significant modifications: No

Specify intended distribution locations:	Worldwide
Reuse Category:	Reuse in a thesis/dissertation
Requestor Type:	Student
Items for Reuse:	Figures/Tables
Number of Figure/Tables:	1
Figure/Tables Details:	Table II
Format for Reuse:	Print and Electronic
Total number of print copies:	Up to 1000

Information about New Publication:

University/Publisher:	Colorado School of Mines
Title of dissertation/thesis:	Proton Capture on 34S in the Astrophysical Energy Regime
Author(s):	Matthew Lovely
Expected completion date:	Apr. 2020

License Requestor Information

Name:	Matthew Lovely
Affiliation:	Individual
Email Id:	mlovely@mymail.mines.edu
Country:	United States

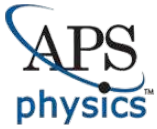

American Physical Society
Reuse and Permissions License

TERMS AND CONDITIONS

The American Physical Society (APS) is pleased to grant the Requestor of this license a non-exclusive, non-transferable permission, limited to Print and Electronic format, provided all criteria outlined below are followed.

1. You must also obtain permission from at least one of the lead authors for each separate work, if you haven't done so already. The author's name and affiliation can be found on the first page of the published Article.
2. For electronic format permissions, Requestor agrees to provide a hyperlink from the reprinted APS material using the source material's DOI on the web page where the work appears. The hyperlink should use the standard DOI resolution URL, http://dx.doi.org/{DOI}. The hyperlink may be embedded in the copyright credit line.
3. For print format permissions, Requestor agrees to print the required copyright credit line on the first page where the material appears: "Reprinted (abstract/excerpt/figure) with permission from [(FULL REFERENCE CITATION) as follows: Author's Names, APS Journal Title, Volume Number, Page Number and Year of Publication.] Copyright (YEAR) by the American Physical Society."
4. Permission granted in this license is for a one-time use and does not include permission for any future editions, updates, databases, formats or other matters. Permission must be sought for any additional use.
5. Use of the material does not and must not imply any endorsement by APS.
6. APS does not imply, purport or intend to grant permission to reuse materials to which it does not hold copyright. It is the requestor's sole responsibility to ensure the licensed material is original to APS and does not contain the copyright of another entity, and that the copyright notice of the figure, photograph, cover or table does not indicate it was reprinted by APS with permission from another source.
7. The permission granted herein is personal to the Requestor for the use specified and is not transferable or assignable without express written permission of APS. This license may not be amended except in writing by APS.
8. You may not alter, edit or modify the material in any manner.
9. You may translate the materials only when translation rights have been granted.
10. APS is not responsible for any errors or omissions due to translation.
11. You may not use the material for promotional, sales, advertising or marketing purposes.
12. The foregoing license shall not take effect unless and until APS or its agent, Aptara, receives payment in full in accordance with Aptara Billing and Payment Terms and Conditions, which are incorporated herein by reference.
13. Should the terms of this license be violated at any time, APS or Aptara may revoke the license with no refund to you and seek relief to the fullest extent of the laws of the USA. Official written notice will be made using the contact information provided with the permission request. Failure to receive such notice will not nullify revocation of the permission.
14. APS reserves all rights not specifically granted herein.
15. This document, including the Aptara Billing and Payment Terms and Conditions, shall be the entire agreement between the parties relating to the subject matter hereof.

American Physical Society
Reuse and Permissions License

05-Feb-2020

This license agreement between the American Physical Society ("APS") and Matthew Lovely ("You") consists of your license details and the terms and conditions provided by the American Physical Society and SciPris.

Licensed Content Information

License Number:	**RNP/20/FEB/022544**
License date:	05-Feb-2020
DOI:	10.1103/RevModPhys.44.465
Title:	Charge States and Charge-Changing Cross Sections of Fast Heavy Ions Penetrating Through Gaseous and Solid Media
Author:	HANS-DIETER BETZ
Publication:	Reviews of Modern Physics
Publisher:	American Physical Society
Cost:	USD $ 0.00

Request Details

Does your reuse require significant modifications: No

Specify intended distribution locations:	United States,Canada
Reuse Category:	Reuse in a thesis/dissertation
Requestor Type:	Student
Items for Reuse:	Figures/Tables
Number of Figure/Tables:	3
Figure/Tables Details:	Figure 5.8, Figure 5.24, and Figure 5.29
Format for Reuse:	Print and Electronic
Total number of print copies:	Up to 1000

Information about New Publication:

University/Publisher:	Colorado School of Mines
Title of dissertation/thesis:	Proton Capture on 34S in the Astrophysical Energy Regime
Author(s):	Matthew Lovely
Expected completion date:	Apr. 2020

License Requestor Information

Name:	Matthew Lovely
Affiliation:	Individual
Email Id:	mlovely@mymail.mines.edu
Country:	United States

ELSEVIER LICENSE
TERMS AND CONDITIONS

Feb 05, 2020

This Agreement between Colorado School of Mines -- Matthew Lovely ("You") and Elsevier ("Elsevier") consists of your license details and the terms and conditions provided by Elsevier and Copyright Clearance Center.

License Number	4762590662162
License date	Feb 05, 2020
Licensed Content Publisher	Elsevier
Licensed Content Publication	Nuclear Instruments and Methods in Physics Research Section B: Beam Interactions with Materials and Atoms
Licensed Content Title	Acceleration of radioactive ions
Licensed Content Author	R.E. Laxdal
Licensed Content Date	May 1, 2003
Licensed Content Volume	204
Licensed Content Issue	n/a
Licensed Content Pages	10
Start Page	400
End Page	409

Type of Use	reuse in a thesis/dissertation
Portion	figures/tables/illustrations
Number of figures/tables/illustrations	1
Format	both print and electronic
Are you the author of this Elsevier article?	No
Will you be translating?	No
Title	Proton Capture on 34S in the Astrophysical Energy Regime
Institution name	Colorado School of Mines
Expected presentation date	Apr 2020
Portions	Figure 1
Requestor Location	Colorado School of Mines 1500 Illinois St Golden, CO 80401 United States Attn: Colorado School of Mines
Publisher Tax ID	98-0397604
Total	0.00 USD
Terms and Conditions	

INTRODUCTION

ELSEVIER LICENSE
TERMS AND CONDITIONS

Feb 05, 2020

This Agreement between Colorado School of Mines -- Matthew Lovely ("You") and Elsevier ("Elsevier") consists of your license details and the terms and conditions provided by Elsevier and Copyright Clearance Center.

License Number	4762591033881
License date	Feb 05, 2020
Licensed Content Publisher	Elsevier
Licensed Content Publication	Nuclear Instruments and Methods in Physics Research Section B: Beam Interactions with Materials and Atoms
Licensed Content Title	Commissioning and operation of DRAGON
Licensed Content Author	Sabine Engel
Licensed Content Date	May 1, 2003
Licensed Content Volume	204
Licensed Content Issue	n/a
Licensed Content Pages	5
Start Page	154
End Page	158

Type of Use	reuse in a thesis/dissertation
Portion	figures/tables/illustrations
Number of figures/tables/illustrations	1
Format	both print and electronic
Are you the author of this Elsevier article?	No
Will you be translating?	No
Title	Proton Capture on 34S in the Astrophysical Energy Regime
Institution name	Colorado School of Mines
Expected presentation date	Apr 2020
Portions	Figure 1
Requestor Location	Colorado School of Mines 1500 Illinois St Golden, CO 80401 United States Attn: Colorado School of Mines
Publisher Tax ID	98-0397604
Total	0.00 USD
Terms and Conditions	

INTRODUCTION

ELSEVIER LICENSE
TERMS AND CONDITIONS

Feb 05, 2020

This Agreement between Colorado School of Mines -- Matthew Lovely ("You") and Elsevier ("Elsevier") consists of your license details and the terms and conditions provided by Elsevier and Copyright Clearance Center.

License Number	4758390290247
License date	Jan 29, 2020
Licensed Content Publisher	Elsevier
Licensed Content Publication	Chemie der Erde - Geochemistry
Licensed Content Title	Presolar grains from meteorites: Remnants from the early times of the solar system
Licensed Content Author	Katharina Lodders,Sachiko Amari
Licensed Content Date	May 23, 2005
Licensed Content Volume	65
Licensed Content Issue	2
Licensed Content Pages	74
Start Page	93
End Page	166
Type of Use	reuse in a thesis/dissertation

Portion	figures/tables/illustrations
Number of figures/tables/illustrations	2
Format	both print and electronic
Are you the author of this Elsevier article?	No
Will you be translating?	No
Title	Proton Capture on 34S in the Astrophysical Energy Regime
Institution name	Colorado School of Mines
Expected presentation date	Apr 2020
Portions	Figure 1 and Figure 23
Requestor Location	Colorado School of Mines 1500 Illinois St Golden, CO 80401 United States Attn: Colorado School of Mines
Publisher Tax ID	98-0397604
Total	0.00 USD

Terms and Conditions

INTRODUCTION

1. The publisher for this copyrighted material is Elsevier. By clicking "accept" in connection with completing this licensing transaction, you agree that the following terms and conditions apply to this transaction (along with the Billing and Payment terms and conditions

ELSEVIER LICENSE
TERMS AND CONDITIONS

Feb 05, 2020

This Agreement between Colorado School of Mines -- Matthew Lovely ("You") and Elsevier ("Elsevier") consists of your license details and the terms and conditions provided by Elsevier and Copyright Clearance Center.

License Number	4762590662162
License date	Feb 05, 2020
Licensed Content Publisher	Elsevier
Licensed Content Publication	Nuclear Instruments and Methods in Physics Research Section B: Beam Interactions with Materials and Atoms
Licensed Content Title	Acceleration of radioactive ions
Licensed Content Author	R.E. Laxdal
Licensed Content Date	May 1, 2003
Licensed Content Volume	204
Licensed Content Issue	n/a
Licensed Content Pages	10
Start Page	400
End Page	409

Type of Use	reuse in a thesis/dissertation
Portion	figures/tables/illustrations
Number of figures/tables/illustrations	1
Format	both print and electronic
Are you the author of this Elsevier article?	No
Will you be translating?	No
Title	Proton Capture on 34S in the Astrophysical Energy Regime
Institution name	Colorado School of Mines
Expected presentation date	Apr 2020
Portions	Figure 1
Requestor Location	Colorado School of Mines 1500 Illinois St Golden, CO 80401 United States Attn: Colorado School of Mines
Publisher Tax ID	98-0397604
Total	0.00 USD
Terms and Conditions	

INTRODUCTION

ELSEVIER LICENSE
TERMS AND CONDITIONS

Feb 05, 2020

This Agreement between Colorado School of Mines -- Matthew Lovely ("You") and Elsevier ("Elsevier") consists of your license details and the terms and conditions provided by Elsevier and Copyright Clearance Center.

License Number	4758390426337
License date	Jan 29, 2020
Licensed Content Publisher	Elsevier
Licensed Content Publication	Nuclear Instruments and Methods in Physics Research Section A: Accelerators, Spectrometers, Detectors and Associated Equipment
Licensed Content Title	The DRAGON facility for nuclear astrophysics at TRIUMF-ISAC: design, construction and operation
Licensed Content Author	D.A Hutcheon,S Bishop,L Buchmann,M.L Chatterjee,A.A Chen,J.M D'Auria,S Engel,D Gigliotti,U Greife,D Hunter,A Hussein,C.C Jewett,N Khan,M Lamey,A.M Laird,W Liu,A Olin,D Ottewell,J.G Rogers,G Roy,H Sprenger,C Wrede
Licensed Content Date	Feb 11, 2003
Licensed Content Volume	498
Licensed Content Issue	1-3
Licensed Content Pages	21
Start Page	190

End Page	210
Type of Use	reuse in a thesis/dissertation
Portion	figures/tables/illustrations
Number of figures/tables/illustrations	5
Format	both print and electronic
Are you the author of this Elsevier article?	No
Will you be translating?	No
Title	Proton Capture on 34S in the Astrophysical Energy Regime
Institution name	Colorado School of Mines
Expected presentation date	Apr 2020
Portions	Figure 1, Figure 2, Figure 4, Figure 5, Figure 6
Requestor Location	Colorado School of Mines 1500 Illinois St Golden, CO 80401 United States Attn: Colorado School of Mines
Publisher Tax ID	98-0397604
Total	0.00 USD
Terms and Conditions	

Copyright Clearance Center Marketplace™

Annual Reviews, Inc. - License Terms and Conditions

Order Date	28-Jan-2020
Order license ID	1015555-1
ISSN	1545-4282
Type of Use	Republish in a thesis/dissertation
Publisher	ANNUAL REVIEWS
Portion	Chart/graph/table/figure

LICENSED CONTENT

Publication Title	Annual review of astronomy and astrophysics	Rightsholder	Annual Reviews, Inc.
		Publication Type	e-Journal
Date	12/31/1962	URL	http://arjournals.annualreviews.org/loi/astro
Language	English		
Country	United States of America		

REQUEST DETAILS

Portion Type	Chart/graph/table/figure	Distribution	Worldwide
Number of charts / graphs / tables / figures requested	2	Translation	Original language of publication
		Copies for the disabled?	No
Format (select all that apply)	Print, Electronic	Minor editing privileges?	No
Who will republish the content?	Publisher, not-for-profit	Incidental promotional use?	No
Duration of Use	Life of current edition	Currency	USD
Lifetime Unit Quantity	Up to 499		
Rights Requested	Main product		

NEW WORK DETAILS

Title	Proton Capture on 34S in the Astrophysical Energy Regime	Institution name	Colorado School of Mines
		Expected presentation date	2020-04-06
Instructor name	Uwe Greife		

ADDITIONAL DETAILS

Order reference number	N/A	The requesting person / organization to appear on the license	Matthew Lovely/Colorado School of Mines

REUSE CONTENT DETAILS

Title, description or numeric reference of the portion(s)	Figure 5	**Title of the article/chapter the portion is from**	3.3.1 Asymptotic Giant Branch Stardust
Editor of portion(s)	n/a	**Author of portion(s)**	Larry Nittler
Volume of serial or monograph	2016:54	**Issue, if republishing an article from a serial**	N/A
Page or page range of portion	63	**Publication date of portion**	2016-06-27

CCC Republication Terms and Conditions

1. Description of Service; Defined Terms. This Republication License enables the User to obtain licenses for republication of one or more copyrighted works as described in detail on the relevant Order Confirmation (the "Work(s)"). Copyright Clearance Center, Inc. ("CCC") grants licenses through the Service on behalf of the rightsholder identified on the Order Confirmation (the "Rightsholder"). "Republication", as used herein, generally means the inclusion of a Work, in whole or in part, in a new work or works, also as described on the Order Confirmation. "User", as used herein, means the person or entity making such republication.

2. The terms set forth in the relevant Order Confirmation, and any terms set by the Rightsholder with respect to a particular Work, govern the terms of use of Works in connection with the Service. By using the Service, the person transacting for a republication license on behalf of the User represents and warrants that he/she/it (a) has been duly authorized by the User to accept, and hereby does accept, all such terms and conditions on behalf of User, and (b) shall inform User of all such terms and conditions. In the event such person is a "freelancer" or other third party independent of User and CCC, such party shall be deemed jointly a "User" for purposes of these terms and conditions. In any event, User shall be deemed to have accepted and agreed to all such terms and conditions if User republishes the Work in any fashion.

3. Scope of License; Limitations and Obligations.

    3.1. All Works and all rights therein, including copyright rights, remain the sole and exclusive property of the Rightsholder. The license created by the exchange of an Order Confirmation (and/or any invoice) and payment by User of the full amount set forth on that document includes only those rights expressly set forth in the Order Confirmation and in these terms and conditions, and conveys no other rights in the Work(s) to User. All rights not expressly granted are hereby reserved.

    3.2. General Payment Terms: You may pay by credit card or through an account with us payable at the end of the month. If you and we agree that you may establish a standing account with CCC, then the following terms apply: Remit Payment to: Copyright Clearance Center, 29118 Network Place, Chicago, IL 60673-1291. Payments Due: Invoices are payable upon their delivery to you (or upon our notice to you that they are available to you for downloading). After 30 days, outstanding amounts will be subject to a service charge of 1-1/2% per month or, if less, the maximum rate allowed by applicable law. Unless otherwise specifically set forth in the Order Confirmation or in a separate written agreement signed by CCC, invoices are due and payable on "net 30" terms. While User may exercise the rights licensed immediately upon issuance of the Order Confirmation, the license is automatically revoked and is null and void, as if it had never been issued, if complete payment for the license is not received on a timely basis either from User directly or through a payment agent, such as a credit card company.

    3.3. Unless otherwise provided in the Order Confirmation, any grant of rights to User (i) is "one-time" (including the editions and product family specified in the license), (ii) is non-exclusive and non-transferable and (iii) is subject to any and all limitations and restrictions (such as, but not limited to, limitations on duration of use or circulation) included in the Order Confirmation or invoice and/or in these terms and conditions. Upon completion of the licensed use, User shall either secure a new permission for further use of the Work(s) or immediately cease any new use of the Work(s) and shall render inaccessible (such as by deleting or by removing or severing links or other locators) any further copies of the Work (except for copies printed on paper in accordance with this license and still in User's stock at the end of such period).